INFORMATION TO USERS

This manuscript has been reproduced from the microfilm master. UMI films the text directly from the original or copy submitted. Thus, some thesis and dissertation copies are in typewriter face, while others may be from any type of computer printer.

The quality of this reproduction is dependent upon the quality of the copy submitted. Broken or indistinct print, colored or poor quality illustrations and photographs, print bleedthrough, substandard margins, and improper alignment can adversely affect reproduction.

In the unlikely event that the author did not send UMI a complete manuscript and there are missing pages, these will be noted. Also, if unauthorized copyright material had to be removed, a note will indicate the deletion.

Oversize materials (e.g., maps, drawings, charts) are reproduced by sectioning the original, beginning at the upper left-hand corner and continuing from left to right in equal sections with small overlaps.

Photographs included in the original manuscript have been reproduced xerographically in this copy. Higher quality 6" x 9" black and white photographic prints are available for any photographs or illustrations appearing in this copy for an additional charge. Contact UMI directly to order.

ProQuest Information and Learning
300 North Zeeb Road, Ann Arbor, MI 48106-1346 USA
800-521-0600

UMI®

DISSERTATION

A NEW TECHNIQUE FOR OBTAINING AEROSOL SIZE DISTRIBUTIONS WITH APPLICATIONS TO ESTIMATES OF AEROSOL PROPERTIES

Submitted by

Jennifer L. Hand

Department of Atmospheric Science

In partial fulfillment of the requirements

for the Degree of Doctor of Philosophy

Colorado State University

Fort Collins, Colorado

Summer, 2001

ProQuest Information and Learning Company
300 North Zeeb Road
P.O. Box 1346
Ann Arbor, MI 48106-1346

COLORADO STATE UNIVERSITY

June 8, 2001

WE HEREBY RECOMMEND THAT THE DISSERTATION PREPARED UNDER OUR SUPERVISION BY JENNIFER L. HAND ENTITLED A NEW TECHNIQUE FOR OBTAINING AEROSOL SIZE DISTRIBUTIONS WITH APPLICATIONS TO ESTIMATES OF AEROSOL PROPERTIES BE ACCEPTED AS FULFILLING IN PART REQUIREMENTS FOR THE DEGREE OF DOCTOR OF PHILOSOPHY.

Committee on Graduate Work

Wayne Schubert

Adviser

Department Head

ABSTRACT OF DISSERTATION

A NEW TECHNIQUE FOR OBTAINING AEROSOL SIZE DISTRIBUTIONS WITH APPLICATIONS TO ESTIMATES OF AEROSOL PROPERTIES

The **B**ig **B**end **R**egional **A**erosol **V**isibility and **O**bservation study (BRAVO) was conducted from July to October 1999. The park is located in a remote region of southwest Texas on the border with Mexico but still has some of the poorest visibility of any Class 1 monitored area in the western United States. The park is frequently influenced by air masses carrying pollutants from Mexico and eastern Texas. Continuous physical, optical and chemical aerosol measurements were performed in an effort to understand the sources and contributions to haze in the park.

Dry aerosol size distributions were measured over the size range of $0.05 < D_p < 20$ μm. Three instruments were used to cover this range, each having a different measurement technique. A new method was developed to align the size distributions in the instrument overlap regions, allowing for the retrieval of aerosol real refractive index and effective density as well as size parameters for accumulation and coarse particle modes.

The combined size distributions were used to calculate particle light scattering coefficients (b_{sp}) for the total distribution and to investigate periods with significant fractional contributions by accumulation and coarse mode particles to total b_{sp}. Calculated and measured b_{sp} from a nephelometer were highly correlated and agreed within the uncertainties of the measurements and uncertainties due to particle losses in the instrument inlets. The agreement between measured and calculated light scattering coefficients supported the accuracy of the size distributions and refractive indices retrieved with the alignment method.

Aerosol chemical composition measured daily during BRAVO suggested that the fine aerosol ionic composition was generally acidic with sulfate and ammonium as the dominant species. During certain periods fine organic carbon and soil fractional contributions to fine aerosol mass concentrations were significant. Retrieved refractive index and density were compared with computed values using these fine ($D_p < 2.5$ μm) and coarse ($2.5 < D_p < 10$ μm) aerosol compositions. These estimates agreed well, with average retrieved and computed refractive indices of $m = 1.566 \pm 0.012$ and $m = 1.56 \pm 0.02$, respectively. The average retrieved effective density was $\rho_e = 1.56 \pm 0.12$ g cm^{-3} and included the effects of dynamic shape factor. The average computed fine bulk density was $\rho_e = 1.85 \pm 0.14$ g cm^{-3}.

Finally, surface-based measurements of aerosol optical properties were related to properties derived from ground-based remote sensing from the USDA UVB radiometer network site located in the park, approximately 30 miles from the BRAVO site. A correlation in aerosol optical depth of $R^2 = 0.691$ was observed between the two methods, and they agreed within 40 %. Ångstrom wavelength exponents were computed to characterize the spectral variations of aerosol optical depth over the wavelength range of 415 – 860 nm. Variations in Ångstrom exponents were observed in both estimates and corresponded to changing aerosol properties as seen in the composition and size distribution data sets. A correlation of $R^2 = 0.755$ was observed between the *in-situ* and remote sensing methods of estimating Ångstrom exponents, and the estimates agreed within 30 %.

These results were encouraging because they provided insight into the relationships between surface-based measurements of aerosol physical and chemical properties and optical properties retrieved by remote sensing techniques.

Jennifer L. Hand
Atmospheric Science Department
Colorado State University
Fort Collins, CO 80523
Summer 2001

ACKNOWLEDGMENTS

It is impossible to list everyone with whom I've had the pleasure of working during my time at CSU. First and foremost I want to express my gratitude to my advisor, Sonia Kreidenweis. She has been a constant source of support, availability, enthusiasm and scientific ideas. She is an outstanding role model and I will always be grateful for the many opportunities that she provided. My committee members: Jeff Collett, Wayne Schubert, Sue James and Lorraine Remer are thanked for the time and energy they invested; their ideas and input greatly improved the quality of this work. The invaluable discussions over the years with Bill Malm have been indispensable.

Eli Sherman was largely responsible for the high level of success of the measurements performed by CSU during the BRAVO study and I cannot overemphasize how grateful I am to have worked with him. Taehyoung Lee, Mike Hannigan and Jill Reilly also contributed to the success of the study. Air Resources Specialists were vital to the study and I appreciate their efforts. I would like to thank Derek Day for nephelometer data. I am grateful to Jim Slusser and Gwen Scott from the USDA UVB program at NREL for providing the remote sensing data presented in this work.

I am very fortunate to have been a part of the Atmospheric Chemistry group and have enjoyed and appreciated their friendship and support. Specifically, the friendship of Sandy Progen is greatly appreciated. I am also forever grateful for the incredible support and love from my family. Finally, I would like to thank Ross. Without his love, humor, intellectual and emotional support, I would not have finished this work. This research was fully funded by the National Park Service, grant number CA238099001.

TABLE OF CONTENTS

1 **INTRODUCTION** 1

1.1 Big Bend National Park: A Historic Perspective 2

1.2 Overview of the 1999 BRAVO Study 3

1.3 Novel Approach to Aligning Size Distributions 6

1.4 Column- versus Surface-Based Estimates of Aerosol Optical Properties 7

2 **EXPERIMENTAL** 12

2.1 TSI Aerodynamic Particle Sizer 3320 13

2.2 PMS Optical Particle Counter: LASAIR 1003 17

2.3 TSI Differential Mobility Analyzer 19

2.4 DMPS/OPC Drying System 23

2.5 TSI Condensation Particle Counter 3010 and 3025 25

3 **INSTRUMENT CALIBRATION** 28

3.1 Single Jet Atomizer Calibration 29

3.2 Post-Field Study Calibration 30

3.3 Calibration Results: PMS LASAIR 1003 35

3.4 OPC Channel Diameter Scaling Method 37

3.5 Calibration Results: TSI APS 3320 39

4 **ALIGNMENT METHOD: PARTICLE REFRACTIVE INDEX AND DENSITY RETRIEVAL** 50

4.1 Previous Measurements of Refractive Index and Density 51

4.2 Twomey Inversion of Size Distributions 53

4.3 Retrieving Particle Refractive Index: Alignment Method Part 1 58

4.3.1 Inverting DMA data 59

4.3.2 Data Smoothing Using the Twomey Inversions 61
4.3.3 Distribution Comparison: Least-Squares Fit..... 62
4.4 Retrieving Particle Effective Density: Alignment Method Part 2 64

5 SENSITIVITY STUDIES FOR ALIGNMENT METHOD 75
5.1 Fixed Case: Experimental Kernels..... 75
5.2 Sensitivity to the Form of Kernel Applied in Twomey Inversion 77
5.3 Sensitivity to Kernel Weighting in Twomey Inversion 78
5.4 Sensitivity to DMA-OPC Overlap Region..... 79
5.5 Sensitivity to OPC-APS Overlap Region..... 81
5.6 Sensitivity to Complex Refractive Index 82
5.7 Discussion..... 85

6 AEROSOL PHYSICAL AND CHEMICAL PROPERTIES..... 99
6.1 Aerosol Size Distributions Statistics..... 102
6.2 Aerosol Composition 106
6.3 Retrieved Refractive Index and Effective Density 110

7 DERIVED AEROSOL OPTICAL PROPERTIES AND VISIBILITY ESTIMATES 137
7.1 Calculations of Optical Properties 139
7.2 Mass Scattering Efficiencies 147
7.3 Estimates of Particle Extinction and Absorption..... 153
7.4 Summary and Discussion 156

8 AEROSOL OPTICAL PROPERTIES FROM GROUND-BASED REMOTE SENSING 179
8.1 Ground-Based Remote Sensing of Aerosol Optical Properties..... 181
8.2 Cloud-Contamination Removal 186
8.3 Comparisons of Surface- and Column-Based Aerosol Optical Properties..... 188

8.4 Effects of Relative Humidity Correction on Aerosol Optical Depth and Ångstrom Wavelength Exponent 193
8.5 Summary and Discussion 194

9 SUMMARY AND FUTURE WORK 208
9.1 Summary 208
9.2 Future Work 214

REFERENCES 217

A THEORETICAL LOSS CALCULATIONS 229

B EXPERIMENTAL UNCERTAINTY CALCULATIONS 238

C DMA CHARGE CORRECTION MATRIX 245

LIST OF TABLES

1.1 Conversion between Day of Year (DOY) and date 10
3.3.1 PMS LASAIR 1003 diameter channel limits 45
3.4.1 PMS LASIAR 1003 channel scaling polynomial coefficients 45
6.6.1 Average accumulation mode size parameters 119
6.1.2 Average coarse mode size parameters 119
6.2.1 Average fine ($PM_{2.5}$) chemistry mass fractions 120
6.2.2 Average coarse ($PM_{10} - PM_{2.5}$) chemistry mass fractions 120
6.3.1 Physical constants for species used in refractive index and density Calculations 121
6.3.2 Average retrieved dry refractive index and effective density from the alignment method 121
7.1.1 Average calculated dry light scattering coefficients with contributions from accumulation mode and coarse mode particles and the full distribution 158
7.1.2 Average size parameters derived from dry light scattering distributions 158
7.2.1 Average dry mass scattering efficiencies for the accumulation and coarse particle modes 158
7.3.1 Average estimated dry light extinction coefficients 159
7.3.2 Average estimated dry light absorption coefficients 159
7.3.3 Average estimated dry single-scattering albedo1 159
8.3.1 Average estimates of ambient aerosol optical depth and Ångstrom exponents for surface-based and remote sensing measurements 196
8.3.2 Correlations between ambient surface- and column-based properties 196
8.3.3 Percent differences in ambient surface- and column-based properties 196
8.3.4 Average estimates of dry aerosol optical depth and Ångstrom exponents for surface-based and remote sensing measurements 197
8.3.5 Correlations between dry surface- and column-based properties 197
8.3.6 Percent differences in dry surface- and column-based properties 197

LIST OF FIGURES

1.1 Map of Big Bend National Park, Texas 11
2.1 Experimental set-up of the DMPS/OPC drying system 27
3.2 Experimental set-up of the DMA calibration system 46
3.3.1 PMS LASAIR 1003 experimental kernels for $(NH_4)_2SO_4$ 47
3.3.2 PMS LASAIR 1003 experimental kernels for oleic acid 47
3.4.1 PMS LASAIR 1003 diameter scaling polynomials 48
3.4.2 PMS LASAIR 1003 dD_g/dm for the scaling polynomials 48
3.5.1 TSI APS 3320 collection efficiency for $(NH_4)_2SO_4$ and oleic acid 49
3.5.2 TSI APS 3320 and TSI 3010 total number concentrations for $(NH_4)_2SO_4$ 49
4.3.1 Flow chart of the alignment method 68
4.3.3.1.a Scatter plot of aligned OPC and DMA $dV/dlogD_p$ on October 8 69
4.3.3.1.b Scatter plot of unaligned OPC and DMA $dV/dlogD_p$ on October 8 69
4.3.3.2 Slope versus applied refractive index on October 8 70
4.3.3.3 χ^2 versus applied refractive index on October 8 70
4.3.3.4 Unaligned OPC and DMA volume distributions on October 8 71
4.3.3.5 Aligned OPC and DMA volume distributions on October 8 71
4.4.1 The APS-OPC overlap range for the "fixed" case 72
4.4.2.a Scatter plot of aligned OPC and APS $dV/dlogD_p$ on October 12 72
4.4.2.b Scatter plot of unaligned OPC and APS $dV/dlogD_p$ on October 12 73
4.4.3 Slope versus applied effective density on October 8 73
4.4.4 χ^2 versus applied effective density on October 8 74
4.4.5 Complete volume distribution on October 8 74
5.1.1 Hourly retrieved refractive indices for the "fixed" case 88
5.1.2 Slopes corresponding to retrieved refractive index for the "fixed" case ... 88
5.1.3 χ^2 corresponding to retrieved refractive indices for the "fixed" case 89
5.1.4 Hourly retrieved effective densities for the "fixed" case 89
5.1.5 Slopes corresponding to retrieved effective density for the "fixed" case .. 90

5.1.6 χ^2 corresponding to retrieved effective densities for the "fixed" case..... 90
5.2.1 Percent difference in refractive index between the "fixed" case and the perfect kernel case..... 91
5.2.2 Percent difference in effective density between the "fixed" case and the perfect kernel case..... 91
5.2.3 Aligned volume distributions for the "fixed" case on September 12 92
5.2.4 Aligned volume distributions for the perfect kernel case on September 12..... 92
5.3.1 Percent difference in refractive index between the "fixed" case and the Twomey weight parameter case 93
5.3.2 Percent difference in effective density between the "fixed case and the Twomey weight parameter case 93
5.4.1 Percent difference in refractive index between the "fixed" case and the adjusted DMA-OPC overlap range case 94
5.4.2 Aligned volume distributions for the "fixed" case on October 12 94
5.4.3 Aligned volume distributions for the adjusted DMA-OPC overlap range case on October 12..... 95
5.4.4 Percent difference in effective density between the "fixed" case and the adjusted DMA-OPC overlap range case 95
5.5.1 Percent difference in effective density between the "fixed" case and the adjusted APS-OPC overlap range case 96
5.5.2 Aligned volume distributions for the "fixed" case on October 12 96
5.5.3 Aligned volume distributions for the adjusted APS-OPC overlap range Case on October 12..... 97
5.6.1 Theoretical instrument response for different refractive indices..... 97
5.7.1 Surface area distribution for September 12..... 98
6.1.1 Dry total number concentrations..... 122
6.1.2 Dry volume concentrations for the accumulation mode, coarse mode and total distribution..... 122
6.1.3 Fractional contributions to total volume concentrations from coarse and accumulation mode particles 123

6.1.4 Timeline of dry accumulation mode volume geometric mean diameters .. 123
6.1.5 Scatter plot of accumulation mode volume geometric mean diameters and volume concentrations 124
6.1.6 Timeline of dry coarse mode volume geometric mean diameters 124
6.1.7 Scatter plot of coarse mode volume geometric mean diameters and volume concentrations 125
6.1.8 Timeline of accumulation mode geometric standard deviation 125
6.1.9 Scatter plot of accumulation mode geometric standard deviation and volume geometric mean diameter 126
6.1.10 Timeline of coarse mode geometric standard deviation 126
6.1.11 Hourly contours of volume size distributions for the entire study 127
6.2.1 Timeline of $PM_{2.5}$ ammonium to sulfate molar ratios 128
6.2.2 Timeline of fine ($PM_{2.5}$) chemical composition 128
6.2.3 Timeline of fine ($PM_{2.5}$) chemistry mass fractions 129
6.2.4 Timeline of fine ($PM_{2.5}$) soil mass concentrations 129
6.2.5 Timeline of fine ($PM_{2.5}$) mineral ratios of Al/Ca and Si/Al 130
6.2.6 Timeline of coarse (PM_{10} - $PM_{2.5}$) chemical composition 130
6.2.7 Timeline of coarse (PM_{10} - $PM_{2.5}$) chemistry mass fractions 131
6.2.8 Timeline of coarse (PM_{10} - $PM_{2.5}$) soil mass concentrations 131
6.3.1 Timeline of retrieved and computed dry refractive indices 132
6.3.2 Timeline of computed fine and coarse imaginary part of refractive index 132
6.3.3 Timeline of fine and coarse dry soil refractive indices 133
6.3.4 Timeline of retrieved and computed density 133
6.3.5 Timeline of derived dynamic shape factor 134
6.3.6 Timeline of computed refractive index with different assumption of chemical components 134
6.3.7 Timeline of computed density with different assumptions of chemical Components 135
6.3.8 Timeline of total mass concentrations 135
6.3.9.a MOUDI mass distributions and estimated mass distributions derived from volume distributions on August 15 136

6.3.9.b MOUDI mass distributions and estimated mass distributions derived from volume distributions on September 14 136
7.1.1 Timeline of calculated dry light scattering coefficients 160
7.1.2 Fractional contribution of light scattering from accumulation mode and coarse mode particles to total light scattering coefficients 160
7.1.3 Accumulation mode volume ratios versus light scattering coefficient ratio 161
7.1.4 Coarse mode volume ratios versus light scattering coefficient ratio 161
7.1.5 Light scattering coefficients due to accumulation mode particles versus accumulation mode volume concentrations 162
7.1.6 Light scattering coefficients due to coarse mode particles versus coarse Mode volume concentrations 162
7.1.7 Light scattering distribution on July 6 163
7.1.8 Light scattering distribution on October 12 163
7.1.9 Timeline of dry accumulation mode volume geometric mean diameter and light scattering geometric mean diameter 164
7.1.10 Light scattering distribution on July 25 164
7.1.11 Accumulation mode volume geometric mean diameter versus light scattering geometric mean diameter 165
7.1.12 Timeline of dry coarse mode volume geometric mean diameter and light scattering geometric mean diameter 165
7.1.13 Coarse mode volume geometric mean diameter versus light scattering geometric mean diameter 166
7.1.14 Accumulation mode light scattering coefficient versus light scattering geometric mean diameter 166
7.1.15 Coarse mode light scattering coefficient versus light scattering geometric mean diameter 167
7.1.16 Contours of light scattering coefficient distributions for the entire study . 167
7.1.17 Timeline of NPS $PM_{2.5}$ nephelometer-measured dry light scattering coefficients with calculated values 168

7.1.18 Calculated dry accumulation mode light scattering coefficients versus NPS $PM_{2.5}$ nephelometer-measured light scattering coefficients 168
7.1.19 Calculated dry $PM_{2.5}$ light scattering coefficients versus NPS $PM_{2.5}$ nephelometer-measured light scattering coefficients 169
7.2.1 Timeline of dry accumulation mode mass scattering efficiencies 170
7.2.2 Dry accumulation mode mass scattering efficiency versus derived accumulation mode mass concentrations 170
7.2.3 Dry accumulation mode mass scattering efficiency versus volume geometric mean diameter 171
7.2.4 Timeline of dry coarse mass scattering efficiencies 171
7.2.5 Dry coarse mode mass scattering efficiency versus derived coarse mass . 172
7.2.6 Dry coarse mode mass scattering efficiency versus volume geometric mean diameter 172
7.2.7 Reconstructed fine light scattering coefficient versus calculated accumulation mode light scattering coefficient 173
7.2.8 Reconstructed coarse light scattering coefficient versus calculated coarse mode light scattering coefficient 173
7.2.9 Reconstructed total light scattering coefficient versus calculated total Light scattering coefficient 174
7.2.10 Reconstructed fine light scattering coefficient versus nephelometer-measured fine light scattering coefficient 174
7.3.1 Light extinction, scattering and absorption distributions on July 6 175
7.3.2 Light extinction, scattering and absorption distributions on October 12 ... 175
7.3.3 Mie scattering, extinction and absorption efficiencies 176
7.3.4 Ratio of Mie absorption to Mie extinction efficiency 176
7.3.5 Timeline of dry light absorption coefficients 177
7.3.6 Timeline of black carbon concentrations 177
7.3.7 Timeline of single-scattering albedo 178
8.1.1 Solar irradiance from MODTRAN 198
8.1.2 Chappius band ozone cross sections 198

8.1.3 Filter functions for visible channels of the VIS-MFRSR 199
8.1.4 Rayleigh and ozone optical depths for visible wavelengths 199
8.3.1 Timeline of ambient aerosol optical depths 200
8.3.2 Surface-based versus column-based ambient aerosol optical depth 200
8.3.3 Ambient light extinction coefficient versus ambient column-based aerosol optical depth 201
8.3.4 Timeline of ambient Ångstrom wavelength exponents 201
8.3.5 Surface-based versus column-based ambient Ångstrom exponents 202
8.3.6 Fractional contribution of accumulation mode volume to total volume concentrations versus surface-based ambient Ångstrom exponents 202
8.3.7 Fractional contribution of accumulation mode volume to total volume concentrations versus column-based ambient Ångstrom exponents 203
8.3.8 Fractional contribution of coarse mode volume to total volume concentrations versus surface-based ambient Ångstrom exponents 203
8.3.9 Fractional contribution of coarse mode volume to total volume concentrations versus column-based ambient Ångstrom exponents 204
8.3.10 Dry accumulation mode volume geometric mean diameter versus ambient surface-based Ångstrom exponents 204
8.3.11 Dry accumulation mode volume geometric mean diameter versus ambient column-based Ångstrom exponents 205
8.3.12 Dry coarse mode volume geometric mean diameter versus ambient surface-based Ångstrom exponents 205
8.3.13 Dry coarse mode volume geometric mean diameter versus ambient column-based Ångstrom exponents 206
8.3.14 Timeline of dry Ångstrom exponents 206
8.3.15 Surface-based dry aerosol optical depth versus ambient optical depths 207
8.3.16 Surface-based dry Ångstrom exponents versus ambient Ångstrom exponents 207
A.1 Particle losses for the DMA experimental set-up 236
A.2 Particle losses for the OPC experimental set-up 236
A.3 Particle losses for the APS experimental set-up 237

CHAPTER 1. INTRODUCTION

The Big Bend Regional Aerosol and Visibility Observational Study (BRAVO) was conducted from July through October 1999 in Big Bend National Park, Texas. The park is located in southwest Texas along the Rio Grande River on the border between Mexico and Texas (see map in Figure 1.1). The study was motivated by historic data that demonstrated that Big Bend National Park has the poorest visibility of any Class 1 area in the western United States, a surprising find given the remote location of the park. The IMPROVE network (Interagency Monitoring of Protected Visual Environments, *Malm et al.*, 1994) has been monitoring fine particulate matter and visibility in the park since 1988. Before this, fine particle data were collected there as early as 1982 as a part of the National Park Service (NPS) Fine Particle Network (*Eldred et al.*, 1986). Because of the political implications of trans-border pollution, in September and October of 1996 an international visibility scoping study was conducted by the NPS and PROFEPA of Mexico (Procuraduria Federal de Proteccion al Ambiente) to measure fine particular matter at nineteen sites in Mexico and Texas. The first part of this chapter describes the typical particle chemical composition, visibility and air mass flow patterns observed during these earlier measurements. Later sections of this chapter address similar measurements performed during the BRAVO study and their implications for visibility estimates in the park.

1.1 BIG BEND NATIONAL PARK: A HISTORICAL PERSPECTIVE

Results from the 1996 scoping study were consistent with the historical database and demonstrated that sulfate was the major contributor to fine mass (*Gebhart et al.*, 2001). Seasonally, fine particulate sulfate concentrations were highest during summer and autumn when back trajectories suggested air masses predominantly originating from the southeast, passing over Mexico. Industrial regions of Mexico, including two coal-fired power plants (Carbon I and Carbon II) and other Mexican cities, are located in this area. Although less frequently, other areas contributing to high sulfur concentrations were east Texas and possibly as far away as the Ohio River Valley. Light extinction was also observed to be highest in summer and lowest during winter, with fine sulfate as the major contributor to light extinction during summer months.

On average, organic carbon (OC) and soil did not contribute significantly to light extinction at Big Bend National Park, however, episodically they could be important. The highest organic carbon concentrations were observed during the spring (especially in May) when flow from the south was believed to be transporting smoke from seasonal agricultural burning in Mexico. Fine soil concentrations were highest in July when back trajectories were exclusively associated with flow from the southeast, suggesting transport of air masses from Africa and mineralogical ratios (aluminum to calcium) suggestive of Saharan dust (*Perry et al.*, 1997). Elevated fine soil concentrations during other seasons of the year were associated with flow from the west and southwest and were probably associated with local sources (*Gebhart et al.*, 2001).

Some of the issues identified in previous data were lack of closure between reconstructed extinction (computed by summing estimated contributions from each species) and extinction measured directly with transmissometers. Coarse particle scattering coefficients were underestimated by as much as a factor of two (*Malm*, personal communication). However, reasonable closure was achieved between reconstructed and gravimetric fine mass and reconstructed and measured scattering. The discrepancy in extinction could be due to incorrect estimates of coarse particle scattering, misapplied relative humidity correction factors or incorrect assumptions of absorption or scattering efficiencies. For instance, *Malm and Day* (2000) measured coarse mass scattering efficiencies at Grand Canyon National Park near 1.0 $m^2 g^{-1}$, much higher than the 0.4 – 0.6 $m^2 g^{-1}$ typically assumed in reconstructed scattering calculations. Although the 1996 scoping study provided more spatially and temporally resolved measurements than the typical IMPROVE historical data, these questions regarding lack of closure for some measurements remained unanswered and the 1999 BRAVO study was designed to further investigate these issues.

1.2 OVERVIEW OF THE 1999 BRAVO STUDY

The Environmental Protection Agency and the National Park Service sponsored the BRAVO study to provide an in depth investigation into the physio-chemical characteristics of particles that contribute to visibility degradation in the park. Approximately forty sites were operated continuously throughout Texas in an effort to understand the spatial and temporal distribution of the particulate matter in the transport pathway of the park during the season of historically high light extinction. This

dissertation focuses on the measurements performed at one of these sites, located at Kbar Ranch inside the park. Continuous measurements of aerosol chemical composition, size distributions, visibility, and absorption were performed at the site. Several investigators were responsible for these measurements and although the experiments will be described here, results corresponding to only some of these experiments will be presented in this work.

Of the many sites operated during the study, the Kbar Ranch site included the most extensive instrumentation. Colorado State University (CSU) collected daily samples of $PM_{2.5}$ and size resolved (MOUDI impactor) aerosol for detailed chemical analysis perfomed on site. Bulk samples were analyzed for Cl^-, SO_4^{-2}, NO_3^-, Na^+, NH_4^+, K^+, Mg^{+2}, Ca^{+2} and aerosol acidity. University of California at Davis (UCD) operated IMPROVE samplers with 2.5 μm and 10 μm size cuts to determine the chemical speciation of fine and coarse particle modes. UCD samples were analyzed for the above-mentioned ions as well as organic carbon, elemental carbon and elements. The measured fine aerosol composition was generally acidic with sulfate and ammonium as the dominant species. On average organic carbon was the next most abundant species contributing to fine mass, although periods existed when fine soil was a major contributor to fine mass; these periods were associated with suspected Saharan dust episodes. Elemental carbon was only a small fraction of fine mass. On average coarse particle mass consisted of approximately equal contributions of soil and organic carbon, although episodes did occur when coarse mass was comprised mainly of crustal material. MOUDI measurements suggested that nitrate was associated with the coarse mode and that sulfate was typically associated with the fine mode.

The NPS directly measured aerosol optical properties with transmissometers located in the park and several nephelometers operating at the Kbar Ranch site. Dry and ambient relative humidity light scattering coefficients were measured with a relative humidity controlled nephelometer system to estimate humidity growth correction factors. Nephelometers were also operated with size selective inlets to investigate contributions of coarse particle scattering to visibility degradation. Aerosol light absorption was measured by CSU with an aethalometer. Reconstructed scattering and extinction estimates were made by combining scattering and absorption efficiencies with 24 hour chemical compositions measured by CSU and UCD.

Dry aerosol number distribution measurements were made by CSU to characterize the full aerosol spectrum from 50 nm to 20 micrometers using three instruments, each utilizing a different measurement technique. By applying Mie theory to the size distributions, light scattering coefficients were calculated and fractional contributions of the accumulation and coarse particle modes to total scattering were determined. Nephelometer-measured light scattering coefficients compared well to these estimates. Coarse particle scattering proved to be important in the early part of the study (July-August) with periods typically associated with suspected Saharan dust events. Accumulation mode scattering was dominant during September and October. Accumulation and coarse mode aerosol size parameters were determined from these size distributions and used to identify periods when coarse mode volume concentrations were the major contributor to total integrated volume. These periods coincided with the suspected Saharan dust events. Accumulation mode volume concentrations dominated total integrated volumes during other periods; these episodes corresponded to periods

with high fine sulfate concentrations and relatively high accumulation mode scattering coefficients.

1.3 NOVEL APPROACH TO ALIGNING SIZE DISTRIBUTIONS

In order to construct a complete size distribution from the different instruments used to measure size distributions, an alignment method was developed that allowed for reconciliation of size distributions in overlapping size ranges as well as retrieval of particle refractive index and effective density. A differential mobility analyzer (DMA), optical particle counter (OPC), and aerodynamic particle sizer (APS) were used to obtain dry size distributions. The DMA measured a "true" size assuming spherical particles. The OPC measured an optical size that depended on particle optical properties such as refractive index, and the APS measured aerodynamic size, dependent on particle density and dynamic shape factor. Based on work by *Stolzenburg et al.* (1998), the DMA was used to calibrate several OPC channels simultaneously and in doing so retrieved particle real refractive index. Once the OPC size distributions were calibrated with DMA distributions, they were used to simultaneously calibrate APS channels and retrieve particle effective density.

To construct a complete size distribution from instruments having overlapping size ranges, other researchers have applied a piece-wise calculation in the overlap range by using data from only one instrument up to a given diameter, and data from a different instrument beyond it (*Eldering et al.*, 1994; *Wilson et al.*, 1988). The novelty of the approach described here was the incorporation of data in the overlap regions to derive information about the particle optical and physical properties, as well as utilization of all of the data to construct a complete size distribution. Dry particle refractive index and

effective density were derived for each size distribution, resulting in hourly averaged values for the entire study. As will be shown in Chapter 6, the daily averaged retrieved refractive indices and densities agreed within experimental uncertainty with values calculated using chemical compositions. Higher values of refractive index ($m \sim 1.58$) were retrieved during periods corresponding to suspected Saharan dust episodes and relatively larger fine soil mass fractions while smaller values ($m \sim 1.54$) were retrieved during periods with high sulfate mass fractions, consistent with particles dominated by ammoniated sulfate.

1.4 COLUMN- VERSUS SURFACE-BASED ESTIMATES OF AEROSOL OPTICAL PROPERTIES.

The presence of a USDA UV-B network at Big Bend National Park allowed for the opportunity to compare surface measurements of aerosol optical properties to estimates derived by remote sensing techniques. Performing these types of comparisons is important because radiative forcing effects of aerosols have previously relied on surface measurements with the assumption that these represent the tropospheric column (*Charlson et al.*, 1992; *IPCC*, 1995). The BRAVO study provided an excellent opportunity to investigate to what extent the chemical, optical and physical measurements made at the surface related to optical properties derived by remote sensing. *Kreidenweis et al.* (2001) recently demonstrated the need for including aerosol chemistry to gain better insight into remote sensing aerosol measurements. In this work, the variations observed in the aerosol properties derived from remote sensing were related to the changes observed in aerosol chemical composition and size measured at the Kbar Ranch site.

A fully instrumented UVB network site operates continuously near Castalon in Big Bend National Park, approximately 30 miles from the Kbar Ranch site (*Bigelow et al.*, 1998). The site includes Multi-Filter Rotating Shadowband Radiometers (MFRSR) that measure irradiances in both UV and visible wavelengths, however only visible wavelengths were investigated in this work. Aerosol optical depths (aerosol extinction integrated over a vertical column, τ_a) were derived from irradiance measurements by removing Rayleigh scattering and gaseous absorption at 5 wavelengths ranging from 415-860 nm. Calculations of aerosol optical depths from surface estimates of light scattering coefficients were made at the same wavelengths, assuming a well mixed column and boundary layer heights derived from transport layer models (*Gebhart*, personal communication). Correlations were observed between the column and point measurements for the entire study.

Spectral parameters were estimated from both the surface and column measurements. Angstrom wavelength exponents were calculated from measured size distributions and from the variation in radiometer aerosol optical depth over the wavelength range of 415-860 nm. Large values of Angstrom exponents were expected for aerosols dominated by accumulation mode sizes. Smaller values of Angstrom exponents correspond to larger particles such as dust (*Eck et al.*, 1999; *Reid et al.*, 1999). Good agreement between the two datasets was observed, and differences in Angstrom exponents corresponded to changing aerosol properties. These results were encouraging because they provided insight into the relationships between measured aerosol physio-chemical properties with optical properties retrieved by remote sensing techniques.

The remaining chapters cover the topics described in this Introduction with increased detail. Chapter 2 presents the details of the experimental set up and field campaign. Chapter 3 describes instrument calibrations and how these were applied to the size distribution data. Chapters 4 and 5 present the alignment method used to retrieve refractive index and particle density, as well as studies performed to test the sensitivity of assumptions in the method. Chapter 6 presents results of size parameters derived from size distributions as well as comparisons between different data sets to demonstrate consistency in measured and derived parameters. Calculations of light scattering coefficients and comparisons with measured values can be found in Chapter 7, and column aerosol optical properties can be found in Chapter 8. Chapter 9 will present plans for future work. The timelines in this work will be presented in terms of Day of Year (DOY). Table 1.1 provides the conversion between DOY in 1999 and actual date for the reader's convenience.

Table 1.1 Conversion between date and Day of Year for July through October.

Date	July	August	September	October
1	182	213	244	274
2	183	214	245	275
3	184	215	246	276
4	185	216	247	277
5	186	217	248	278
6	187	218	249	279
7	188	219	250	280
8	189	220	251	281
9	190	221	252	282
10	191	222	253	283
11	192	223	254	284
12	193	224	255	285
13	194	225	256	286
14	195	226	257	287
15	196	227	258	288
16	197	228	259	289
17	198	229	260	290
18	199	230	261	291
19	200	231	262	292
20	201	232	263	293
21	202	233	264	294
22	203	234	265	295
23	204	235	266	296
24	205	236	267	297
25	206	237	268	298
26	207	238	269	299
27	208	239	270	300
28	209	240	271	301
29	210	241	272	302
30	211	242	273	303
31	212	243		304

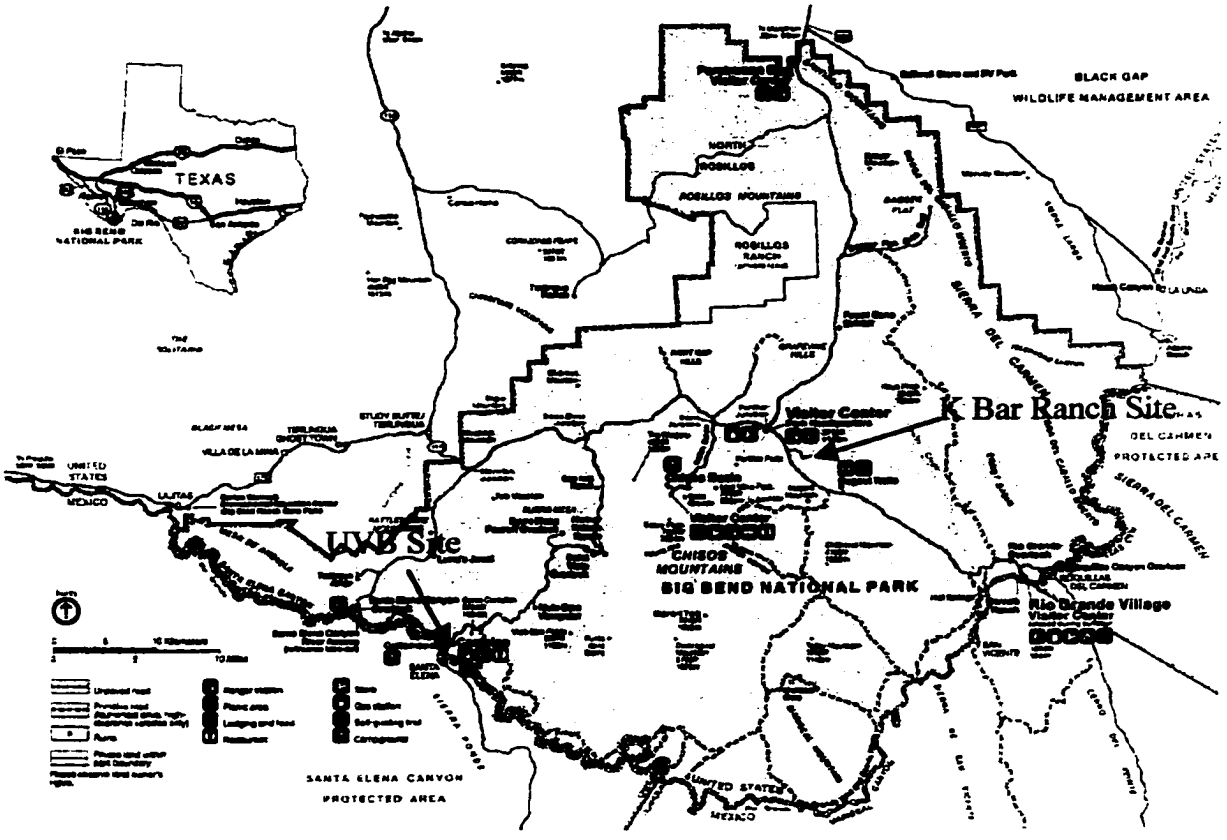

Figure 1.1 Map of Big Bend National Park, Texas. The park's location in Texas is shown in the smaller map in the corner (www.nps.gov/bibe/pphtml/maps/html).

CHAPTER 2. EXPERIMENTAL

The sampling site was located in a clearing at the end of an approximately 0.7 mile long service road near the Kbar ranch, on the east side of highway 118, 2 miles southeast from Park Headquarters at Panther Junction. Particle sampling instrumentation was located inside a construction trailer with inlet ports positioned through the roof. Two other trailers were co-located at the site, with one housing analytical chemistry equipment (CSU), and the second housing particle light scattering measurements (NPS). Scaffolding located between the trailers supported filter samplers. Vehicle traffic was kept to a minimum at the site with the exception of daily visits from the NPS service personnel.

The full aerosol size spectrum was of interest in characterizing total light scattering, therefore the aerosol physical measurements were designed to characterize the aerosol size spectrum from 50 nm to 20 μm. In order to cover this wide size range, three instruments with different measurement techniques were utilized. The experimental set-up was designed to maximize particle counting statistics by minimizing particle losses and measurement biases, with isokinetic sampling techniques and minimal bends in the sampling tubing. This design included choosing the sampling time of each instrument to improve counting statistics. In order to avoid uncertain particle sizing from changing relative humidities both in the ambient and sampled air, aerosol measurements were made at low relative humidity. The aerosol sample was dried either by passing it through a Perma Pure dryer (Perma Pure Inc., Toms River, NJ) or, for large particles subject to

significant losses in the Perma Pure dryer, by heating the aerosol. Sensors in the sample lines monitored relative humidity and temperature. In the following sections each instrument will be described as well as its associated plumbing and drying systems.

Checks on instrument operation and flow rates were performed on a daily basis and recorded in logbooks during the field study. Flow rate measurements were performed using a NIST traceable primary volumetric flow meter (Gilian Gilibrator, Sensidyne Inc., Clearwater, FL). For each instrument the daily recorded values are listed in each section. All of the instruments were integrated and monitored by a data acquisition computer running LabView (National Instruments, Austin, TX) and therefore all of the sample times were synchronized.

2.1 TSI AERODYNAMIC PARTICLE SIZER 3320

The TSI Aerodynamic Particle Sizer (APS) 3320 (TSI, Minneapolis, MN) is a time-of-flight spectrometer that estimates aerosol aerodynamic size by measuring the velocity of a particle in an accelerating air stream. The stated size range of the instrument is 0.5 – 20 μm with 52 total channels, the first channel measuring total number of particles from 0.3-0.5 μm. The logarithmic bin width for each bin is 0.03. The APS sample time was five minutes. Large particles are relatively few in number, therefore statistics in this size range may be poor. For the majority of the study, the APS sampled from its own inlet that consisted of 1/2 inch outer-diameter (OD) stainless steel (SS) tubing that extended through the roof. A stainless steel inlet cap and screen were connected to the top of the inlet to protect the plumbing from insects and precipitation. Bends with respect to the horizontal were avoided in the APS tubing to reduce the

gravitational particle losses in the lines. The aerosol sample was dried using a 12 inch fiber coil heater (Cole Parmer, Vernon Hills, IL) wrapped tightly around approximately 19 inches of SS tubing and maintained at a temperature of 50 degrees Celsius. The heater was wrapped with fiberglass insulation and aluminum foil.

The flow system in the APS consists of 5.0 ± 0.2 liters per minute (LPM) total flow drawn into the instrument and split into 4.0 ± 0.1 LPM sheath flow by an outer nozzle and 1.0 ± 0.1 LPM aerosol sample flow by an inner nozzle (TSI APS 3320 instrument manual). The pressure drop is converted to volumetric flow while compensating for atmospheric pressure. The inlet pressure, total, aerosol and sheath flows were recorded from the instrument display by the operator on a daily basis. The actual flows could not be measured without removing the outer casing of the instrument and therefore were not measured to avoid disrupting the instrument alignment. The monthly averaged display values of the aerosol flow were July: 0.998 ± 0.012 LPM, August: 1.0 ± 0.2 LPM, September: 0.99 ± 0.16 LPM and October: 1.010 ± 0.300 LPM. Auxiliary data files recorded instrument variables on a 5 minute sample period and included inlet pressure, total flow, sheath flow, laser power (% maximum), laser current, sheath pump voltage, total pump voltage, inlet temperature and internal box temperature.

After the total flow has been split between the aerosol and sheath flow, the sheath flow is filtered and drawn by its own pump and controlled by determining a pressure drop through an orifice. The sheath flow is reunited with the sample flow, focusing the aerosol sample to the center of the stream. The sample flow is therefore accelerated and smaller particles with less inertia are accelerated with it. Larger particles with more inertia lag behind, according to their aerodynamic diameter. The particle velocity is measured in the

optics chamber. Following the optics chamber the flow exits the instrument, drawn by the total flow pump.

The optics chamber contains a 28 mW, 675-nm laser diode and collimating lens. The laser beam is split into 2 separate beams spaced by 90-100 μm. A calcite plate splits the beam and the plate thickness controls the beam spacing. The sample stream passes through the two beams and side-scattered light from particles interacting with the incident beam is collected by an elliptical mirror and focused on a solid-state avalanche photodiode detector (APD). The scattered light is converted to an electrical signal by the detector. When a particle passes through each laser beam the resulting scattered light is detected and related to particle velocity.

The velocity of the particle can be determined because the distance between the two laser beams is known and the time between each scattering event is recorded. The gas velocity (v_g) of the centerline at the exit of the nozzle is given as Equation 2.1.1 (*Chen et al, 1985*):

$$v_g = \left[\frac{2RT}{M}\ln\left(\frac{P}{P-\Delta P}\right)\right]^{1/2} \tag{2.1.1}$$

where R is the gas constant and M is the molecular weight of air. The ambient pressure and temperature are given as P and T, respectively. The pressure drop across the nozzle is denoted as ΔP. The average particle velocity between the laser beams can be calculated from Equation 2.1.2:

$$v_p = \frac{v_g t_{\min}}{t} \tag{2.1.2}$$

where t is the transit time of the particle between the two laser beams and t_{min} is the minimum transit time for small particles observable by the APS (*Baron et al., 1993*).

Particles with different density or shape will accelerate differently in the flow field and therefore be sized differently by the APS. Aerodynamic diameter can be converted to an actual diameter by Equation 2.1.3 (*Hinds*, 1999). The subscript "*p*" refers to the physical particle while "*ae*" refers to the aerodynamic particle.

$$D_p = D_{ae}\left[\frac{C_{ae}}{\rho_e C_p}\right]^{1/2} \tag{2.1.3}$$

In Equation (2.1.4), the effective density, ρ_e, is defined as the ratio of the particle density (ρ_p) to the particle dynamic shape factor, χ. The dynamic shape factor is defined as the ratio of the actual resistance force of a nonspherical particle to the resistance force of a sphere having the same velocity and volume (*Hinds*, 1999).

$$\rho_e = \frac{\rho_p}{\chi} \tag{2.1.4}$$

The Cunningham correction factor (C_p or C_{ae}) takes into account that small particles with diameters approaching the mean free path of air no longer satisfy the Stokes equation. The relative velocity of air at the surface of the spherical particle is no longer zero and the particles can settle faster than Stoke's law predicts. The Cunningham factor corrects for this effect. The form of the slip correction factor used is given as Equation 2.1.5 *(Hinds*, 1999)

$$C_p = 1 + \frac{2}{PD_p}\left[6.32 + 2.01\exp(-1.1095PD_p)\right] \tag{2.1.5}$$

where P is pressure in cm Hg and D_p is particle diameter in micrometers. Equations 2.1.3 and 2.1.5 are solved iteratively because the slip correction factor is also a function of diameter. Converting aerodynamic diameter to actual or true diameter requires some knowledge of the particle effective density.

The signal processing in the APS 3320 takes into account four different types of events that can occur during sampling. Event 1 occurs when the scattered light from a particle passing through the first beam can be detected, but the scattered light from the second beam passage is not detectable over the threshold detection limit. The result is a false large particle detection (also referred to as phantom counts, see *Heitbrink and Baron, 1992; Heitbrink et al., 1991*) because a following particle passing through the initial beam can be interpreted as the scattering from a second beam passage. Event 2 is a valid event and occurs when two scattering events are detected over the threshold detection of the instrument. Event 3 is a coincidence event and occurs when a second particle enters the measurement area before the first particle has left. Event 4 occurs when a second scattering event never occurs and the instrument timer exceeds its 4.096 μs limit. This can happen when a very large particle or a recirculating particle travels through the measurement area. Each event is recorded in its own memory location, with event 2 being recorded as the actual time-of-flight data. By recording these events, coincidence issues are automatically resolved with the APS 3320 (TSI APS 3320 instrument manual).

2.2 PMS OPTICAL PARTICLE COUNTER: LASAIR 1003

A Particle Measuring Systems (PMS, Boulder, CO) optical particle counter (OPC) was used to measure dry aerosol size distributions. The LASAIR 1003 samples with a 0.028 LPM flow rate resulting in a maximum detectable concentration of 13,440 particles cm^{-3}. The instrument has 8 size channels with manufacturer calibration channel limit diameters corresponding to 0.1 - 0.2, 0.2 - 0.3, 0.3 - 0.4, 0.4 - 0.5, 0.5 - 0.7, 0.7 - 1.0, 1.0 -

2.0 and > 2.0 μm (PMS LASAIR 1003 instrument manual). Manufacturer calibrations were performed with polystyrene latex spheres (PSL, Interfacial Dynamics Corp, Portland, OR). The instrument flow system provides the sample flow and includes a pump, filters, flow meter, and inlet and outlet jets. The flow is volumetric and was adjusted for atmospheric pressure. The OPC flow was maintained by a mass flow meter inside the instrument that measures a pressure drop across a venturi and displays the volumetric flow on the instrument front panel. Instrument software corrects for site elevation. These values were recorded daily but the flow was not measured with a flow meter every day. Flow measurements were made during instrument calibration using a Gilibrator low flow cell (Model 17126, 1-250 cm^3 min^{-1}, precision of ± 0.82 %) and recorded, typically once per week. The monthly averaged values for the LASAIR 1003 were July: 0.030 ± 0.005 LPM, August: 0.029 ± 0.005 LPM, September: 0.029 ± 0.004 LPM, and October: 0.028 ± 0.005 LPM. The laser reference voltage was also recorded from the instrument display as an indication of the cleanliness of the optics. During the study, the laser voltage did not fall below 4.5 V, the recommended value. Clean optics were maintained by a purge flow drawn across the cavity mirrors. The LASAIR 1003 has a passive cavity with wide-angle 90-degree scattering collecting optics. The collecting optics included four Mangin mirrors and a solid state photodetector. A 10 mW helium neon (632.8 nm) laser is used as the illumination source. The position of the sample with respect to the laser beam was maintained by the jet tip. The particle sample passes through the optical chamber, scattering light as it passes through the laser beam. The scattered light is collected and converted to an electric signal, and this signal is proportional to the optical size of the particle. The data system bins the signals into

appropriate channels and records the number of particles measured. The manufacturer calibration relates the scattered light to an optical size.

2.3 TSI 3071 DIFFERENTIAL MOBILITY ANALYZER

The TSI 3071 Differential Mobility Analyzer (DMA) (TSI, Minneapolis, MN) is an electrostatic classifier that relies on the theory of electrophoresis to measure aerosol size. A known charge distribution is applied to sampled particles by passing the aerosol through a Kr-85 neutralizer. High concentrations of bipolar ions undergo frequent collisions with the aerosol due to random motions of the ions. After the particles reach a state of equilibrium with respect to the ion collisions, they carry a bipolar charge distribution. After the aerosol sample passes through the neutralizer, it enters the main section of the DMA containing two concentric cylinders. The outer cylinder is electrically grounded, while the inner collector rod is kept at a known negative voltage. The polydisperse aerosol sample and sheath flows enter the instrument at the top of the cylinders and travel down the cylinders in the annular region between. A potential difference exists between the inner and outer cylinders resulting in positively charged particles being attracted toward the center rod due to the induced electric field. Particle trajectories depend on the inner rod voltage and the particle electric mobility. Particles with a specific mobility exit the instrument through a slit at the bottom of the collecting rod with the monodisperse flow and then are counted by a TSI 3010 Condensation Particle Counter (CPC, TSI, Minneapolis, MN). The unselected remaining particles exit the instrument with the excess flow. Only a fraction of the sampled particles actually obtain a charge and of those roughly half are positively charged and counted.

In order to determine the size of particles that are selected by the DMA, the equations governing the DMA will be derived and discussed now. The electric mobility of a particle can be determined by examining the force balance on a particle. For a particle with n elementary charges, e, the electrostatic force (F_e) in an electric field E is given by Equation 2.3.1

$$F_e = neE \tag{2.3.1}$$

The particle velocity can be calculated under equilibrium conditions when the Stokes drag force and electrostatic force are equal (Equation 2.3.2)

$$neE = \frac{3\pi\eta v_t \chi D_p}{C_p} \tag{2.3.2}$$

where η is the viscosity of air, v_t is the particle terminal velocity, χ is the particle dynamic shape factor taking into account nonsphericity, D_p is particle diameter, and C_p is the Cunningham correction factor (see Equation 2.1.5). The terminal velocity can be determined from Equation (2.3.2). The particle mobility is described as the particle's velocity in an applied electric field. The mobility (Z_p) is calculated using Equation 2.3.3, with typical units of $m^2 V^{-1} s^{-1}$:

$$Z_p = \frac{v_t}{E} = \frac{neC_p}{3\pi\eta\chi D_p} \tag{2.3.3}$$

The range of diameters that can be sized depends on their mobility, the instrument geometry, and flow rates of the DMA. *Knutson and Whitby* (1975) developed the relationship between instrument parameters and electric mobility (Equation 2.3.4) and mobility bandwidth (Equation 2.3.5).

$$Z_p = \frac{[Q_t - 0.5(Q_m + Q_p)]}{2\pi VL} \ln\left(\frac{r_{out}}{r_{in}}\right) \tag{2.3.4}$$

$$\Delta Z_p = \frac{(Q_m + Q_s)}{2\pi VL} \ln(\frac{r_{out}}{r_{in}}) \qquad (2.3.5)$$

where Q_m, Q_p, Q_s and Q_e are the mondisperse flow, polydisperse flow, sheath flow, and excess flow, respectively. The total aerosol flow (Q_t) is given as $Q_t = Q_p + Q_s$ or $Q_t = Q_m + Q_e$. The outer cylinder radius (r_{out}) is 1.958 cm and the inner cylinder radius (r_{in}) is 0.937 cm. The voltage of the inner cylinder is V and the length (L) between the aerosol sample inlet and the exit slit is 44.44 cm (TSI DMA instrument manual). Combining Equations (2.3.3) and (2.3.4) provides the relationship between particle diameter (D_p) and collector rod voltage (Equation 2.3.6):

$$V = \frac{3\chi\eta D_p Q_s \ln(r_{out}/r_{in})}{2neC_p L} \qquad (2.3.6)$$

Depending on the desired particle size to be measured, a corresponding voltage is calculated from Equation 2.3.6 and applied to the collector rod of the DMA.

To measure a continuous aerosol size distribution, the DMA creates a mobility distribution that is later inverted to a size distribution. The mobility channels were forced to meet at the channel mobility limits, resulting in a simpler data inversion. To accurately size particles with the DMA it is important that the instrument flow rates be maintained at their nominal level. The flow rates used in this study were determined based on relationships obtained by manipulating Equations (2.3.4) and (2.3.5). A flow ratio of 10:1 ($Q_s = Q_e$ = 3.0 LPM and $Q_p = Q_m$ = 0.3 LPM) corresponds to a multiplicative factor between mobility channels of 1.222. For example, after choosing the largest sampled channel midpoint diameter (smallest mobility) the larger channel midpoint mobilities (smaller diameters) are 1.222 times the previous midpoint mobility. For a 10:1 flow ratio, the channel limits are just touching using this 1.222 factor. The total number of channels

for the distribution and sample time for each channel can be chosen depending on the user's application. For this study a total of 21 bins were used with a diameter range of $0.05 < D_p < 0.87$ μm and a sample time for each channel increased with larger size. The largest diameter channels sampled twice as long as the smaller diameter channels (up to 40 seconds per bin) in an attempt to improve Poisson counting statistics.

A particle with a given mobility may exist as a small particle with unit charge or a large particle with multiple charges. To obtain an accurate size distribution, the raw DMA data must be corrected for multiply charged particles. Particles with diameters smaller than 20 nm are mostly singly charged, where particles between 20 and 70 nm typically have double charges. Above 70 nm, particles can have a higher number of charges because of larger areas for ions to interact. The raw DMA data are inverted with a charge correction to correct the mobility distribution for multiply charged particles. In this study a full correction of up to 6 charges was applied to size distribution inversions.

Previous researchers have investigated the nature of the charge distribution (*Fuchs,* 1964*; Gunn and Woessner*, 1956; *Wiedensohler* 1988) and have demonstrated that it is not completely described by a Boltzmann equilibrium charge distribution. The charge distribution is not symmetric about zero but instead shows deviations between measured and calculated fractions of positive and negative charges, with deviations increasing with smaller diameter. Bipolar charging of submicron particles was investigated initially by *Gunn and Woessner* (1956) and *Fuchs* (1964). The fractions of particles with multiple charges applied in this study were determined following *Wiedensohler* (1988) who derived empirical expressions to approximate Fuch's model for fractions of particles with 3 or more charges. For approximating the charge distribution

for particles with 2 or less charges, Wiedensohler's least squares regression analysis was applied. Inverting raw DMA data with a multiple charge correction requires some knowledge of the largest expected diameter sampled by the DMA. Use of an impactor on the DMA inlet is suggested by the TSI DMA manual in order to avoid this issue. No impactor was used for this study because existing impactors had cut off diameters that were too small for this application. Discussions about how this issue was resolved can be found in Chapter 4.3.1.

2.4 DMPS/OPC DRYING SYSTEM

A TSI DMPS system (Differential Mobility Analyzer and associated Condensation Particle Counter) and PMS Optical Particle Counter sampled from the same drying inlet to measure 15 minute dry aerosol number distributions (see Figure 2.4.1 for experimental set up). The DMA and OPC resolution and instrument design and operation were described previously. Three critical orifices (O'Keefe Controls Co., Trumbull, CT) were used to maintain the dilution, sheath and excess flows in the DMA. The pressure drops across these orifices were logged and displayed on the data acquisition computer in order to detect any flow problems during instrument operation. A particle free dilution air source filtered with a HEPA filter (Gelman Scientific, Ann Arbor, MI) was plumbed into the DMA to make up the flow difference between the 0.3 LPM sample flow and 1.0 LPM CPC required flow rate. The sheath flow was also filtered with a HEPA filter. Air regulators were used to set the dilution and sheath air flow rates. Five mass flow meters were also plumbed into the DMA to monitor the flow rates of the sheath, excess, monodisperse/CPC, dilution and polydisperse flow rates by

computer in order to ascertain any problems with flows while the instruments were operating. Five check points were plumbed into the system with ball valves to check flows by a standard cell Gilibrator (Model 17218, 0.02-6 LPM, precision of ± 0.2 %). The polydisperse aerosol flow rate was measured daily and if variations of more than ±10% of the desired flow were observed, the dilution, sheath and excess flows were measured and adjusted. Flow measurements were performed on the TSI CPC 3010 daily also. All of the measured and adjusted flows were recorded in a logbook as well as the values of the mass flow meters at the moment before the flow rate checks. The monthly averaged measured flows for the polydisperse flow rate were (desired flow: 0.3 LPM) July: 0.307 ± 0.004 LPM, August: 0.307 ± 0.009 LPM, September: 0.302 ± 0.006 LPM, and October: 0.307 ± 0.008 LPM. The daily logged information for the OPC was discussed previously. The temperature and relative humidity of the excess flow were measured with a sensor (Humitter 50, Vaisala Inc., Woburn, MA) and average values were 25 ± 2 degrees Celsius and 1.7 ± 0.5 %, respectively. No problems with the DMA were encountered during the field study. It was dismantled and cleaned one time on August 25 1999.

The drying system consisted of a 4 foot long section of 1/8 inch inner diameter (ID) stainless steel Perma Pure (PP) dryer with a sheath flow held at a pressure of 10 pounds per square inch (PSI). A URG cyclone (Model 2000-30ED, URG, Chapel Hill, NC) with a D_{50} of 2.5 μm at 3 LPM was attached at the inlet. Between the cyclone and the PP dryer was a combined length of 27.5 inches of stainless steel (SS) tubing with two 90-degree bends with respect to horizontal. An isokinetic sampler allowed for matched velocities between the 3/8 outer diameter (OD) SS tubing and the 1/8 PP dryer. A bypass

of 2.4 LPM at the top of the PP was controlled by a critical orifice. The remaining flow (0.6 LPM) passed through the PP drier and then into 64.75 inches of SS 1/4 OD tubing with two 90-degree bends. Before being split between the DMA and the OPC, the relative humidity and temperature of the aerosol sample were measured with average values of 15 ± 9 % and 22 ± 8 degrees Celsius during the study. A brass Y designed with 20 degree and 70 degree bends with respect to horizontal split the sample flow for the DMA and OPC. Isokinetic samplers were included in each section of the Y. One side of the Y passed through 6.6 inches of 1/4 OD SS tubing before entering the polydisperse port of the DMA with 0.3 LPM of flow. The other side of the Y (and 0.3 LPM of the sample flow) led to the OPC with a 0.272 LPM bypass using a needle valve. The remaining sample with a 0.028 LPM flow rate passed through 9.65 inches of 1/4 OD SS and 5.3 inches of 1/8 OD flexible tubing before entering the OPC. The Y was designed for faster sampling with the OPC because the instrument has a relatively small sample flow. The total number of bends for the DMPS/OPC drying system was four 90-degree bends and one 20-degree bend and one 70-degree bend. Particle loss calculations were performed for this system and are described in Appendix A.

2.5 TSI CONDENSATION PARTICLE COUNTER 3010 AND 3025

Two TSI condensation particle counters (CPCs, TSI, Minneapolis, MN) sampled ambient air (no drying) on a one minute sampling period. A TSI 3010 (D_p > 15 nm) and a TSI UFCPC 3025 (D_p > 3 nm) shared 77.25 inches of 1/4 inch OD SS tubing. The tubing led through the side wall of the trailer and included a SS cap and screen at the end of the inlet. The total sample flow in this section of tubing was 2.5 LPM. The sample was split

in a brass Y two inches from the inlets of the instruments, with 1.5 LPM entering the CPC 3025 and 1.0 LPM entering the CPC 3010. The total number of bends in the tubing included two 90 degree bends and two 70 degree bends with respect to horizontal. The instrument display indicated whether a proper flow rate was maintained. The display was checked and flow rates were noted in the logbook daily. The working fluid of the instruments (1-Butanol, Fischer Scientific CO., Houston,TX) was also checked on a daily basis and filled if needed.

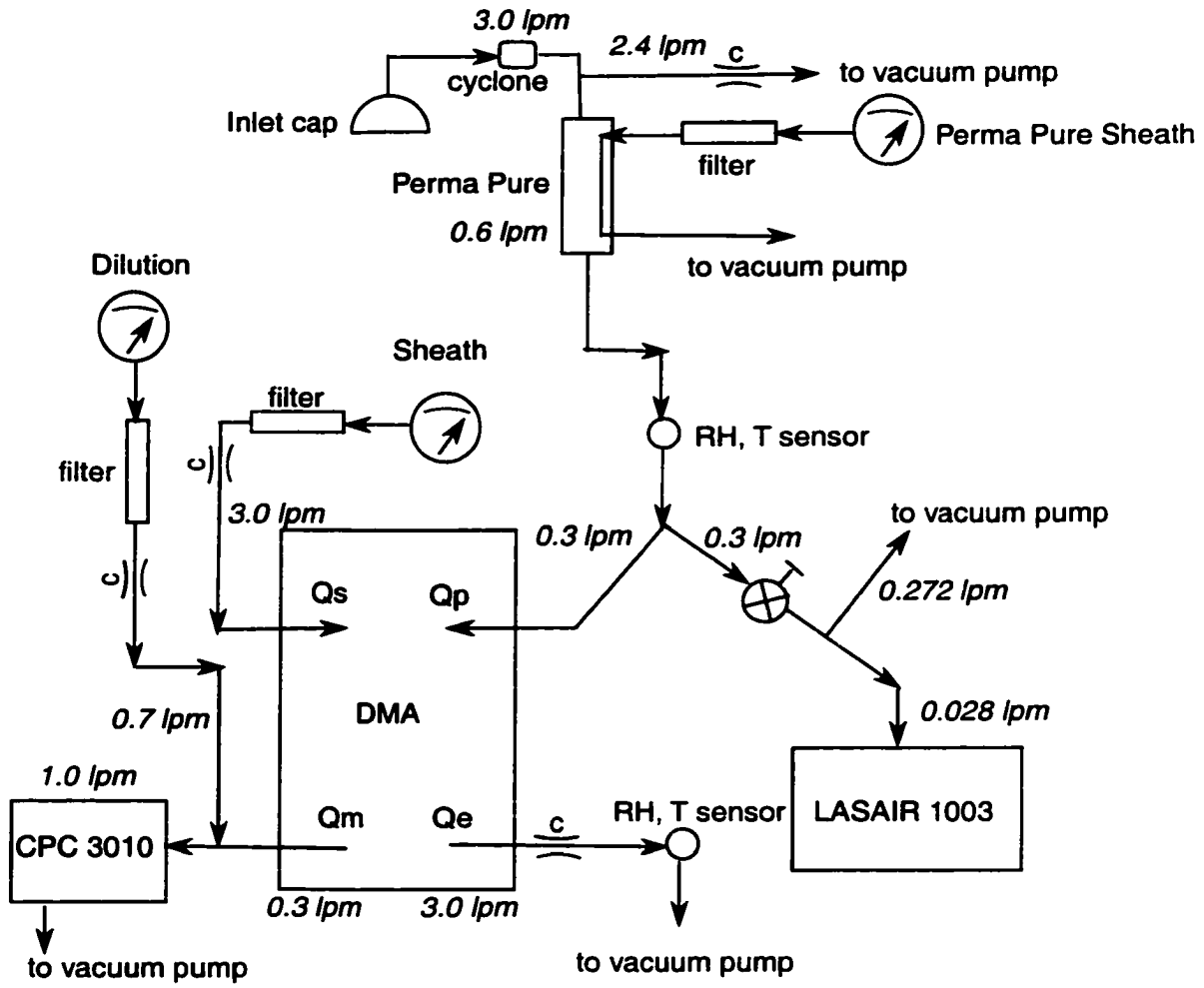

Figure 2.4.1 Experimental set-up of the DMPS-OPC drying system

CHAPTER 3. INSTRUMENT CALIBRATION

Aerosol size measurements do not necessarily reflect the physical size of the particle, depending on the measurement technique. The APS particle measurements depend on particle density and shape and the OPC measurements depend on the optical properties of the particles. Manufacturers typically calibrate instruments using particles of known size and physical, chemical or optical properties, such as polystyrene latex spheres (PSL). Aerosol properties can vary considerably on short time scales in the atmosphere and these properties typically do not reflect those of laboratory aerosols used for manufacturer calibration purposes. In order to invert measured data into aerosol size distributions that reflect the true nature of the aerosols in the atmosphere, sizing information must be corrected for varying aerosol properties. Many previous studies demonstrated significant under-estimations in volume concentrations derived from OPC measurements when no corrections for the particle *in-situ* optical properties were applied (*Pinnick et al.*, 2000; *Kim*, 1995; *Hering and McMurry*, 1991). Other studies have suggested methods for converting the APS aerodynamic diameter to true diameter (*Heidenreich,* 1995; *Peters et al.*, 1993; *Wang and John*, 1989 and *Baron*, 1986). Performing instrument calibrations with laboratory generated aerosols of known size and chemical composition is absolutely necessary for obtaining meaningful measurements of aerosols of differing chemical composition. As a part of this study, calibrations were

performed before, during and after the study period by three methods: single jet atomizer aerosol generation, monodisperse DMA aerosol generation, and monodisperse VOAG aerosol generation. The chemical species used were PSL, ammonium sulfate and oleic acid. Each type of calibration will be discussed here. In the following sections the results of these calibrations for the OPC and the APS will be presented, as well as how these results were used to obtain methods for inverting OPC and APS data for particles of any chemical composition.

3.1 SINGLE JET ATOMIZER CALIBRATION

A TSI 9302 A single jet atomizer (TSI, Minneapolis, MN) was used to generate PSL particles for calibration purposes during the field study. PSL solutions (PSL, Interfacial Dynamics Corp., Portland, OR) were created by adding 4 drops of PSL liquid to 125 mL deionized water. Compressed air cleaned with a HEPA filter delivered particle free air to the atomizer at 10 PSI. Aerosols that exited the atomizer were then sampled by the OPC. The diameters (in micrometers) of PSL used during the field study were 0.19 ± 4.8 %, 0.31 ± 2.0 %, 0.41 ± 1.9 %, 0.47 ± 4.6 %, 0.63 ± 1.9 %, 0.75 ± 2.8 %, 0.87 ± 1.5 %, 2.04 ± 2.8 % and 5.0 ± 6.2 %. PSL has refractive index (m) of 1.588 (Interfacial Dynamics Corp., Portland, OR). One-minute samples were recorded and the channel corresponding to the peak number concentration was recorded for each size atomized. The larger PSL sizes (2.04 μm and 5.0 μm) clogged the atomizer and were not observed by the OPC. All of the other sizes were binned according to the manufacturer calibration. Calibrations were performed on the OPC weekly. This same procedure was performed before and after the study to ensure consistency with the OPC calibration; no problems

were detected with OPC sizing. Attempts were made to calibrate the APS with this system, but because the larger PSL sizes clogged the atomizer, it was difficult to obtain a calibration using these sizes. The PSL 0.87 μm size was used and was observed with the APS (see Chapter 3.5).

3.2 POST-FIELD STUDY CALIBRATION

To perform an extensive instrument calibration on the OPC and APS, the instruments were reconfigured in the Atmospheric Simulation Laboratory at Colorado State University, Fort Collins, Colorado, after the study. The calibration was performed in two phases. The first phase incorporated the DMA and TSI 3075/3076 Aerosol Generation System (TSI, Minneapolis, MN) to select monodisperse particles of known chemical composition and size for smaller diameter ranges (D_p < 1 μm). The second phase incorporated the TSI 3450 Vibrating Orifice Aerosol Generator (VOAG) (TSI, Minneapolis, MN) to generate monodisperse particles of known composition for larger sizes (0.5 – 25 μm). Each phase required a different experimental set-up; they will be discussed separately.

Calibration Using the DMA

The DMA was used for calibration purposes because of its ability to select a monodisperse aerosol sample of any desired size under 1 μm. Ammonium sulfate and oleic acid were used as the calibration aerosol because their optical properties are typical of those observed in the atmosphere (*Hering and McMurry*, 1991). Dry $(NH_4)_2SO_4$ has a real refractive index (m) of 1.53 at 580 nm (*Tang*, 1996), and oleic acid has m = 1.46

(*CRC*, 1998-1999). Two PMS OPCs (LASAIR 1002 and LASAIR 1003) were calibrated with these species and differences in sizing were expected because of their different optical properties. A solution of 1% ammonium sulfate was made by weighing 5.00 g of dry $(NH_4)_2SO_4$ with a Mettler Analytical Balance (Model AG204) and adding it to 500 mL deionized water. Oleic acid solutions were made by pipetting 10 mL of oleic acid to 250 mL 2-propanol. A TSI 3075/3076 Aerosol Generation System was used to atomize these solutions to particles that were then dried by heating and drying systems before being deposited in a sample generation chamber. For an in-depth description of the generation system, see *Brechtel* (1998). Figure 3.2 depicts the experimental set up.

The dry particles were drawn from the generation chamber at 0.3 LPM to the polydisperse inlet port on the DMA after passing an overflow waste port. Critical orifices on the sheath and excess ports maintained a 10:1 flow rate ratio in the DMA. A monodisperse aerosol sample flow rate of 0.3 LPM exited the DMA and traveled into a manifold designed to minimize particle loss when sampling with several instruments. The manifold was built at CSU and consisted of a 2 inch diameter metal pipe with end caps. The manifold was supported vertically by ring stands and the DMA monodisperse sample entered an inlet port on the top end cap. The bottom end cap housed five exit ports, one in the center and four surrounding it. Four of the ports were connected to stainless steel 1/4 inch OD tubing and the center port was connected to 1/2 inch OD stainless steel tubing. Four of the five ports were connected to instruments, with the largest center port connected to the APS 3320. The other three smaller ports were used for two OPCs (LASAIR 1002 and 1003; PMS, Boulder, CO) and a TSI 3010 CPC. The fifth port was capped. A T-union plumbed in line with a HEPA filter provided clean particle free

dilution air (5.785 LPM) to make up the difference in the four instrument flows (a total of 6.085 LPM) and the DMA monodisperse flow rate. A critical orifice was used to control the dilution flow rate.

The voltages applied to the DMA were calculated from Equation 2.3.6, for diameters ranging from 0.05-0.940 μm in 5-10 nm increments. Sizes were also chosen that corresponded to PSL diameters. The voltage was dialed into the DMA, and the system was allowed to equilibrate for two minutes before sampling with the OPCs. Total number concentrations were monitored with a TSI 3010 CPC. For each DMA voltage the OPC channel with the maximum counts was recorded on an acquisition computer. The same voltages were used with both ammonium sulfate and oleic acid particles to obtain the OPC instrument response to particles of the same size but different optical properties. These particles were sized differently by the OPCs due to their different optical properties. Discussion of how these calibration data were applied to a new sizing method for the OPC can be found in the Chapter 3.3. Although the APS 3320 was also sampling particles during this calibration, its inlet was out of alignment causing a difference of one channel between the measured and expected maximum bin (see Chapter 3.5).

TSI 3054 Vibrating Orifice Aerosol Generation (VOAG) Calibration

A TSI 3450 Vibrating Orifice Aerosol Generation (VOAG) (TSI, Minneapolis, MN) was used to generate larger particles of known chemical composition. The VOAG generates a liquid jet through an orifice attached to a piezoelectric crystal that vibrates at set frequencies, creating droplets of known size due to instabilities and jet break-up. The solution droplets were composed of a nonvolatile solute and volatile solvent; after solvent

evaporation a solute aerosol particle of known size remained. Uniform drops were produced by applying a periodic signal of appropriate frequency to the jet. One droplet was produced per cycle of disturbance and therefore the droplet volume could be calculated. The VOAG system consisted of two major components: a droplet generation system and an aerosol flow system.

The droplet generation system included a syringe pump, orifice assembly, signal generator and liquid pressure system. A droplet solution was forced through a syringe at a constant flow rate into an orifice assembly. The assembly included an orifice disk held in an orifice cup by a Teflon O-ring. A liquid feed enters and a drain exits the orifice cup. When the drain was closed and the liquid feed was open, the chamber became pressurized and liquid was forced through the orifice as a jet. The signal generator induced a vibration in the piezoelectric ceramic glued to the orifice chamber. The vibration was transmitted directly to the orifice disk and the liquid jet. The frequency of the vibration was set on the instrument display and the value depended on the size of orifice used. A liquid pressure gauge on the instrument display detected any changes, such as a clogged orifice. A constant liquid pressure ensured ideal particle stability, therefore the gauge was also used to determine when the system was at equilibrium and measurements were performed. Typical equilibrium values used in this study were 17-18 PSI.

Once a jet had been maintained by the droplet generation system, a monodisperse aerosol sample was formed if no significant coagulation occurred. To avoid coagulation, the aerosol flow system provided dilution and dispersion air. Compressed air entered the back panel of the instrument and passed through a filter before it was split into dispersion

and dilution air sources. Typical values of dispersion and dilution air were 21-22 cm^3 min^{-1} and 50 LPM, respectively. The aerosols were dispersed before coagulation can occur by directing the aerosol stream into turbulent air. The aerosols were then mixed with dilution air that evaporates the volatile solvent, leaving the nonvolatile solute. No neutralizer was used. Both of these flows were controlled from the instrument panel.

The droplet volume can be calculated by Equation 3.2.1 (TSI VOAG instrument manual)

$$D_d = \left[\frac{6Q_L}{\pi f}\right]^{1/3} \tag{3.2.1}$$

where Q_L is the liquid flow rate and f is the disturbance frequency. For a 20 μm orifice and 20 mL syringe, a 60 kHz frequency was used and a 7.4×10^{-4} cm^2 s^{-1} flow rate was used. For the same 20 μm orifice a 60 mL syringe and a flow rate of 4.29×10^{-4} cm^2 s^{-1} were also used (TSI VOAG instrument manual). If the nonvolatile solvent has any impurities, these uncertainties affect the resulting aerosol size. The volume concentration of impurities (I) is included with the concentration of solute (C) in the calculation of aerosol drop size (Equation 3.2.2).

$$D_p = D_d(C + I)^{1/3} \tag{3.2.2}$$

Droplets of known size can be generated by the VOAG by either changing the frequency and liquid flow rate or by changing the concentration of the input solution. For this calibration, a different solution was created for each size calibrated, following the method of *Straub and Collett* (2001). Solutions of ammonium sulfate and oleic acid were created for calibration purposes. Deionized water was used for the volatile solvent for the

ammonium sulfate solution, and 2-propanol was used for a volatile solvent for oleic acid solutions.

The same manifold system described in the DMA calibration section was used with the VOAG set-up. Input to the manifold consisted of a one-inch outer diameter flexible tube that ran from the VOAG sampling chamber to the top end cap of the manifold. A filtered excess port was used for overflow. Two OPCs (PMS LASAIR 1002 and 1003, Boulder, CO), a TSI 3010 CPC and the TSI APS 3320 sampled from four of the five exit ports. The fifth port was left open for excess flow.

3.3 CALIBRATION RESULTS: PMS LASAIR 1003

Polystyrene latex sphere calibrations of the OPC proved to be consistent with the manufacturer calibration. Dry ammonium sulfate and oleic acid were used for extensive DMA calibrations. Monodisperse samples were generated with the DMA; 75 ammonium sulfate calibrations and 85 oleic acid calibrations were performed. Each monodisperse aerosol sample generated by the DMA was contaminated by multiply charged particles that were observed by the OPC. The diameters corresponding to the multiply charged particles were calculated with Equation 2.3.3. Ideally the initial polydisperse input size distribution would be scanned with the DMA in an effort to quantify the multiply charged particles. The distribution can partially be constructed by assuming a lognormal distribution and using a mean size and geometric standard deviation suggested by the TSI 3075/3076 Aerosol Generation System instrument manual (TSI, Minneapolis, MN). However the total number of the distribution was not measured and therefore the number

of doublets and triplets could not be quantified. The OPC channel where the multiply charged particles were observed was recorded and used as a check on assumed bin limits.

For each size measured, a TSI 3010 CPC was used to measure total number concentration. A collection kernel (K) was constructed by calculating the ratio of the OPC number concentration for each measured size in a given bin divided by the total number concentration counted. Figures 3.3.1 and 3.3.2 present results of the OPC calibration for ammonium sulfate and oleic acid presented as collection kernels. These data include only calibrations performed with the DMA. Aerosols generated with the VOAG corresponded to sizes that were measureable only with the largest size channels of the OPC (channel 7 and 8). The VOAG calibration method does not reasonably allow for a highly size resolved calibration as compared to the DMA. VOAG calibration data were used for consistency checks with DMA calibrations, but not for constructing collection kernels. Figures 3.3.1 and 3.3.2 demonstrate the sizes each bin was most efficient at collecting. For most bins a separate peak was observed at smaller diameters than the maximum peak. Figure 3.3.1 demonstrates that a given bin can have contributions from multiply charged particles. For example, the small peak of Bin 2 was positioned with the Bin 1 kernel, suggesting that mobility diameters sized by Bin 1 also had doublets that were sized in Bin 2. Because the number of these could not be quantified as doublets or triplets, no corrections were made for these peaks. Overlap between the collection kernels is obvious from Figures 3.3.1 and 3.3.2 therefore the OPC data inversion must include some corrections based on these kernels.

Efficiency curves for use in data inversion were derived as follows. The form of the collection efficiency used was based on work by *Winklmayr et al. (1990)* (Equation 3.3.1).

$$E_n(D_p) = \left[1 + \left(\frac{D_{50}}{D_p}\right)^{2s}\right]^{-1} \tag{3.3.1}$$

To construct efficiencies ($E_n(D_p)$) for any bin (n), the steepness (s) and the diameter for which 50% collection is expected (D_{50}) had to be obtained for each channel and for each calibration species. The steepness was determined by plotting calibration data as cumulative distributions. The assumed D_{50} for each bin and calibration species was consistent with the diameter corresponding to 50% collection of the experimental cumulative distribution curves for singly charged particles. Theoretical curves using these D_{50} were compared to the experimentally derived cumulative distributions for each bin and were used to obtain an initial guess of steepness, which was adjusted to match the calibration data. The theoretical kernels plotted with data on Figures 3.3.1 and 3.3.2 were obtained by converting efficiencies to kernels based on *Winklmayr et al. (1990)* (Equation 3.3.2):

$$K_n = E_n(D_p)$$

$$K_i(D_p) = E_i(D_p)[1 - E_{i+1}(D_p)] \times \ldots [1 - E_n(D_p)] \tag{3.3.2}$$

where n is the number of stages and $i=n-1, n-2, \ldots 1$. Each kernel was constructed such that at a given diameter the sum of all kernels gave 100% collection. Table 3.3.1 provides the values of D_{50} for each calibration aerosol species. The steepness derived for each bin for the LASAIR 1003 for ammonium sulfate and oleic acid was a consistent $s = 20$. The bin limits shifted to larger sizes for oleic acid compared to ammonium sulfate, as

expected for a species with lower refractive index. Bin 6 was only partially characterized by the calibration and bins 7 and 8 not at all because of the larger diameters to which they correspond. The next section will discuss determination of bin limits for channels 6 and 7 and also presents a method for obtaining channel limits for any chemical composition.

3.4 OPC CHANNEL DIAMETER SCALING METHOD

If every particle in the atmosphere had known optical properties that correspond to either dry ammonium sulfate or oleic acid, data inversion for this study would be simple. Unfortunately aerosol optical properties can vary significantly and the data inversion has to be prepared for any chemical composition. The OPC has been calibrated for three refractive indices: PSL (m = 1.588, corresponding to the manufacturer calibration), dry ammonium sulfate (m = 1.53) and oleic acid (m = 1.46). Using the information gained from these calibrations, a method was developed for scaling manufacturer calibration (MC) bin limits for any real refractive index of $1.46 < m < 1.588$. A ratio (f_D) was calculated of the PSL D_{50} over the ammonium sulfate or oleic acid D_{50}. Figure 3.4.1 presents these ratios for each bin versus the corresponding refractive index of the calibration species. A second order polynomial was fit to these data producing an equation that relates a scaling factor, f_D, to refractive index. Table 3.4.1 provides the polynomial coefficients for each bin. The resulting polynomials are plotted on Figure 3.4.1. For a given refractive index a scaling factor was derived and used to multiply the MC D_{50} limits to obtain a new set of D_{50} limits corresponding to that refractive index. Collection kernels for any refractive index were calculated with Equation 3.3.2 assuming a steepness of 20, similar to the other calibration species.

Investigations into changing diameter with refractive index for each bin polynomial were made to assure that the change in diameter with changing refractive index was always negative (e.g. $dD_{50}/dm < 0$) because as refractive index increases, diameter decreases. The polynomial for bin 2 produced a positive derivative, therefore to obtain a negative derivative the channel 2 D_{50} was adjusted from 0.23 μm to 0.226 μm, supported by calibration data. All other bin polynomials resulted in negative derivatives (see Figure 3.4.2).

As discussed previously, no calibration data were available to provide D_{50} limits for bin 6 or bin 7. Estimates were made based on the amount D_{50} shifted for each calibration species for each bin. No polynomials were derived for bin 8 because no upper diameter limit was available for that bin and therefore this bin was not included in the OPC data inversion.

3.5 CALIBRATION RESULTS: TSI APS 3320

The APS calibration was performed with the intent of confirming the theoretical relationship between aerodynamic and actual diameter (Equation 2.1.3). In addition to confirming this equation, the calibration revealed other issues with the APS. The instrument was found to be very sensitive to inlet alignment and this sensitivity caused sizing problems by shifting peak channels one to two sizes too small. The unaligned inlet problem was first observed during the field study when the APS was being calibrated with PSL (as discussed previously). Calibrations with the TSI 9302 A single jet atomizer were difficult because larger PSL clogged the atomizer. A PSL size of 0.87 μm (corresponding D_{ae} = 0.89 μm, ρ_{PSL} = 1.05 g cm^{-3}, Interfacial Dynamics Corp, Portland,

OR) was used although this size occurs at the lower measurement end of the APS 3320 where efficiency problems were observed (see the next section). Attempts were made to calibrate with a 2.0 μm PSL particle and these were intermittently successful.

On September 2, 1999 the APS 3320 was taken apart for routine maintenance following instructions in the instrument manual. The outer and inner nozzles were removed for cleaning. The bottom of the outer nozzle was coated with a brown particulate matter. Both the inner and the outer nozzles were cleaned with 2-propanol. After reassembling the APS 3320, it was discovered to be very sensitive to how tightly the rings and nozzle assembly were tightened. Sensitivity to the nozzle position under the APS sampling tubing was observed. Based on these observations a PSL calibration was performed on September 3, 1999. The 0.87 μm and 2.0 μm PSL particles were being sized two bins too small. To fix this alignment problem the fittings and instrument position were adjusted until the PSL particles were observed in the correct channels. These calibrations were performed almost half way through the study, calling into question the data from July- September. In an attempt to salvage these data, corrections were made to the APS 3320 data by shifting the channels of distributions two bins larger, consistent with sizing offsets observed during the calibration. For example, if N_1 corresponds to the number concentration measured in bin 1, the shift would result in N_1 now corresponding to bin 3. Shifting the data in this way resulted in a loss of 2 bins from the large end of the instrument.

Calibration Using the DMA

The APS 3320 sampled with the OPCs during the DMA calibration with ammonium sulfate and oleic acid; descriptions of the sizes sampled can be found in Section 2.3. Poorer counting efficiencies were observed during the field study for sizes smaller than 1 μm by comparing APS size distributions with distributions measured with the DMA. Poor counting efficiencies were also observed during the calibration studies. This decrease in counting efficiency at smaller sizes was also observed by *Leinert and Wiedensohler* (2000). Their efficiencies were created using data for PSL particles of several sizes.

The same type of alignment issues observed during the field study were experienced in the post calibration experiments. The instrument proved to be very sensitive to the degree of tightening of the outer nozzle ring and the position of the nozzle with respect to the sample tubing. The poor counting efficiencies and the presence of multiply charged particles produced uncertainties in deciphering the DMA calibration at the smaller (< 1 μm) diameter end of the APS. A shift of one bin was observed with the calibration, suggesting peak sizes of ammonium sulfate and oleic acid generated by the DMA were measured one bin too small by the APS. The instrument underwent inner and outer nozzle adjustments until the particles were sampled correctly.

Collection efficiencies similar to those produced by *Leinert and Wiedensohler* (2000) were constructed although multiply charged particles and alignment issues still affected the data. Figure 3.5.1 presents these efficiencies for ammonium sulfate and oleic acid as a function of aerodynamic diameter. These curves do not collapse when they are plotted with geometric diameter instead. This figure is included to demonstrate the

differences in efficiencies observed for two chemical species due to the difference in their optical properties, a somewhat surprising result suggesting that different efficiency corrections would be required for particles of differing chemical composition (also discussed by *Leinert and Wiedensohler*, 2000). The reader should be cautioned not to apply these efficiencies in any quantitative manner because the alignment conditions and multiply charged particles affect these curves. A small peak is noticeable with the ammonium sulfate curve at smaller sizes and corresponds to multiply charged particles. This peak is not observed with the oleic acid data and it is hypothesized that the reason was the differences in density for the two species. Oleic acid has a density of 0.89 g cm^{-3} (*CRC*, 1980-1981) and dry ammonium sulfate has a density of 1.76 g cm^{-3} (*Tang*, 1996). The smaller density of oleic acid results in smaller aerodynamic diameters and it is suspected that multiply charged particles were not observed by the APS for the smaller diameters. No shape factor (χ) was included for ammonium sulfate calibrations because previous work by *Brechtel* (1998) suggested that dry ammonium sulfate particles generated by this method did not require any shape correction.

Calibration Using the VOAG

The VOAG was used to generate larger diameter particles for APS calibration purposes. Both ammonium sulfate and oleic acid were used as calibration aerosol. Eight sizes were generated with the VOAG using a 20 μm orifice, a frequency of 60 kHz and a flow rate of 7.4×10^{-4} cm^2 s^{-1}. The solution concentrations were determined from Equation 3.2.2 and corresponded to aerosol diameters of 0.5, 0.75, 1.0, 2.0, 5.0, 10.0, 12.0, and 15 μm. Between each concentration sampled with the VOAG, 60 mL of deionized water

were run through the system to flush any remaining solution from the orifice assembly. The liquid jet was allowed to stabilize during each sample at a typical equilibrium value of 17 PSI. A TSI 3010 CPC also sampled during these calibrations and total number concentrations were recorded. Not until the CPC number concentrations were stable were measurements performed with the APS 3320. A five-minute sample period was maintained. All of the ammonium sulfate sizes were observed in the expected channels with the APS, confirming the theoretical relationship between aerodynamic and actual diameter (Equation 2.1.3). Comparisons between total number concentration measured with the CPC and the APS for a given diameter are presented in Figure 3.5.2. Good agreement between the two instruments was observed for smaller sizes (< 2 μm) after which poor counting efficiencies were observed with the CPC. Based on these results the acceptable lower diameter limit of the APS was assumed to be between 0.5 and 0.75 μm.

Seven sizes were generated for oleic acid calibrations. Concentrations corresponding to 1.0, 2.0, 5.0, 10.0, 12.0, 15.0, and 20.0 μm were used with a 20 μm orifice with the same settings as used with ammonium sulfate calibrations. Between each calibration size, 20 mL of 2-propanol were run through the system to flush any remaining oleic acid solution in the orifice. Three sizes were generated using a 10 μm orifice: 0.5, 0.75, and 1.0 μm but these sizes were not observed with the APS. All of the sizes calibrated with oleic acid were sized consistently small by one or two bins. No verification of sizes was made with a microscope. *Baron* (1986) demonstrated the difficulties in using oleic acid with the VOAG due to droplet deformation, however this tends to result in particles being sized larger than expected. Given the good results with ammonium sulfate and PSL, the problem was assumed to be with the oleic acid solutions.

The APS calibration revealed alignment issues that allowed for corrections to be made to data measured during the field study. The calibrations confirmed the theoretical equation that will be used to invert size distribution as will be discussed later (Chapter 4.4). Investigations into collection efficiencies at small diameters suggested difficulties when trying to correct for these efficiencies because of dependence on chemical composition. Constructing APS collection kernels similar to those derived for the OPC was difficult due to all of these issues. The method used for the OPCs was applied, but assumptions of the steepness of each channel were made based on the narrow channels of the APS (logarithmic width of 0.03). Instead of assuming perfect collection for each channel, a steepness of 100 for each was assumed. Ammonium sulfate calibration results suggested the manufacturer calibration D_{50} limits were acceptable and could be adjusted based on Equation 2.1.3, for different effective densities.

Table 3.3.1 PMS LASAIR 1003 channel D_{50} determined for different calibration aerosols.

Channel	PSL D_{50} (μm)	$(NH_4)_2SO_4$ D_{50} (μm)	Oleic Acid D_{50} (μm)
1	0.1	0.13	0.15
2	0.2	0.226	0.24
3	0.3	0.335	0.36
4	0.4	0.425	0.47
5	0.5	0.555	0.62
6	0.7	0.81	0.89
7	1.0	1.05	1.10

Table 3.4.1 PMS LASAIR 1003 channel scaling polynomial coefficients for the equation $f_D = am^2 + bm + c$ (see text).

Channel	*a*	*b*	*c*
1	19.637	-57.25	42.393
2	9.7348	-28.37	21.502
3	7.1322	-20.437	15.468
4	-2.1338	7.6673	-5.7949
5	2.8073	-7.0444	5.1074
6	9.6226	-27.662	20.661
7	1.5827	-4.1139	3.5417

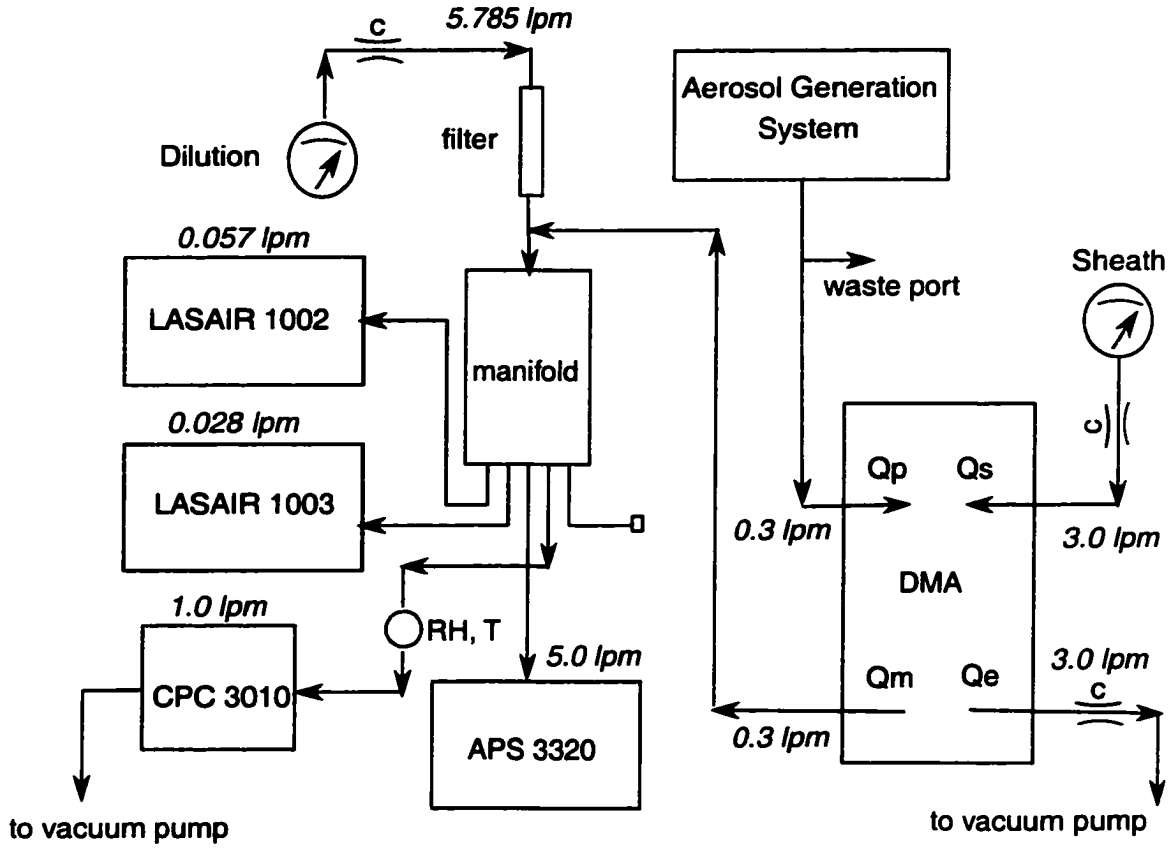

Figure 3.2 Experimental set-up of the DMA-OPC-APS calibration system.

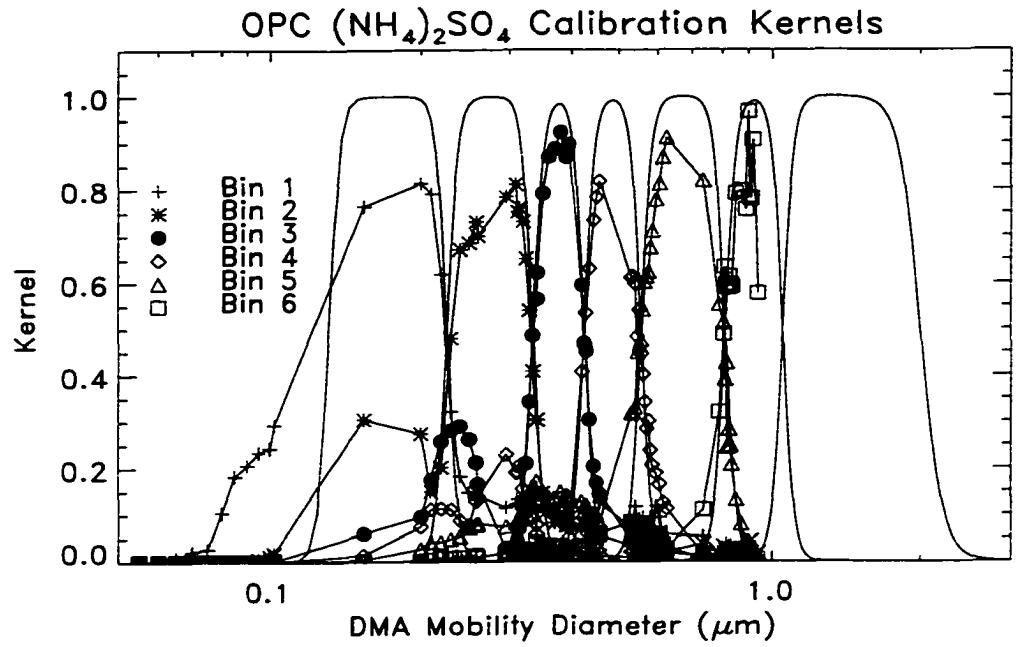

Figure 3.3.1 LASAIR 1003 experimental kernels plotted against DMA mobility diameter for $(NH_4)_2SO_4$ using the DMA calibration system.

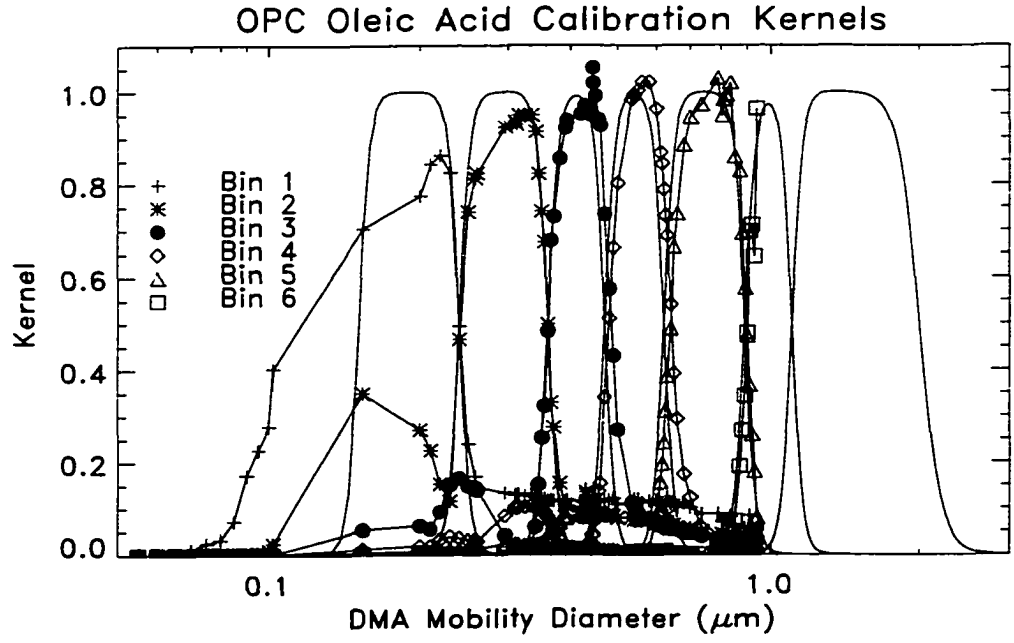

Figure 3.3.2 LASAIR 1003 experimental kernels plotted against DMA mobility diameters for oleic acid using the DMA calibration system.

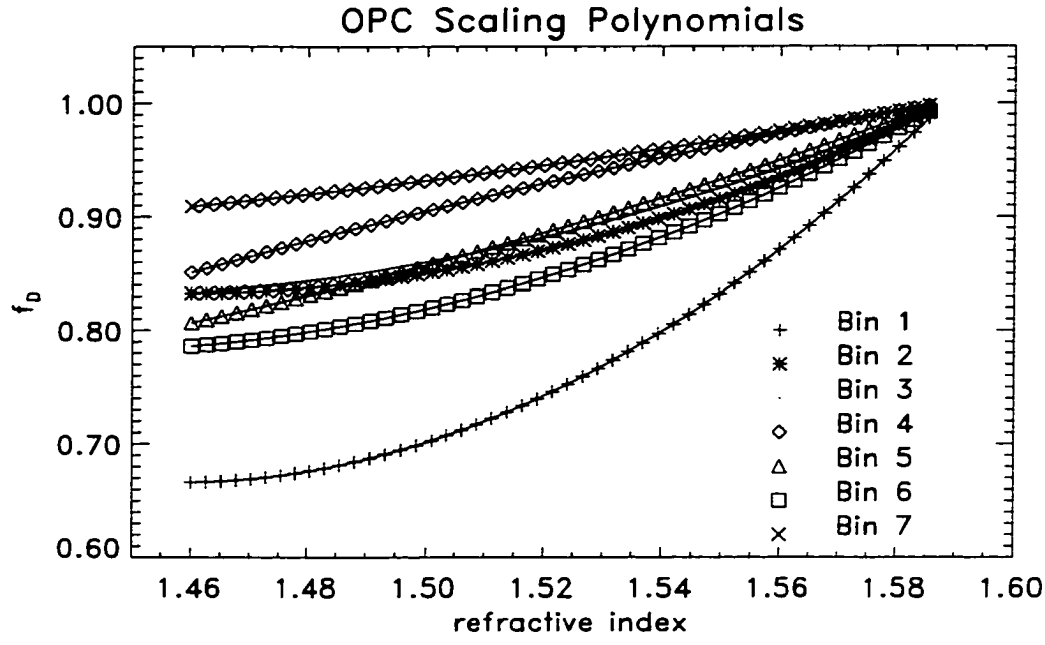

Figure 3.4.1 LASAIR 1003 scaling polynomials.

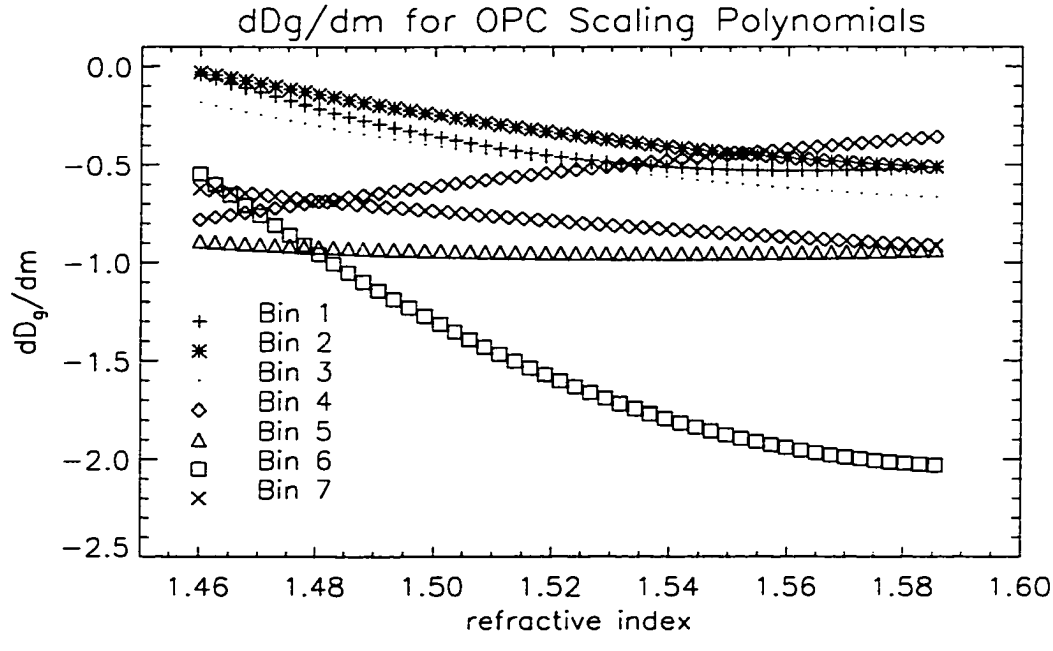

Figure 3.4.2 LASAIR 1003 dD_g/dm for the scaling polynomials in Figure 3.4.1.

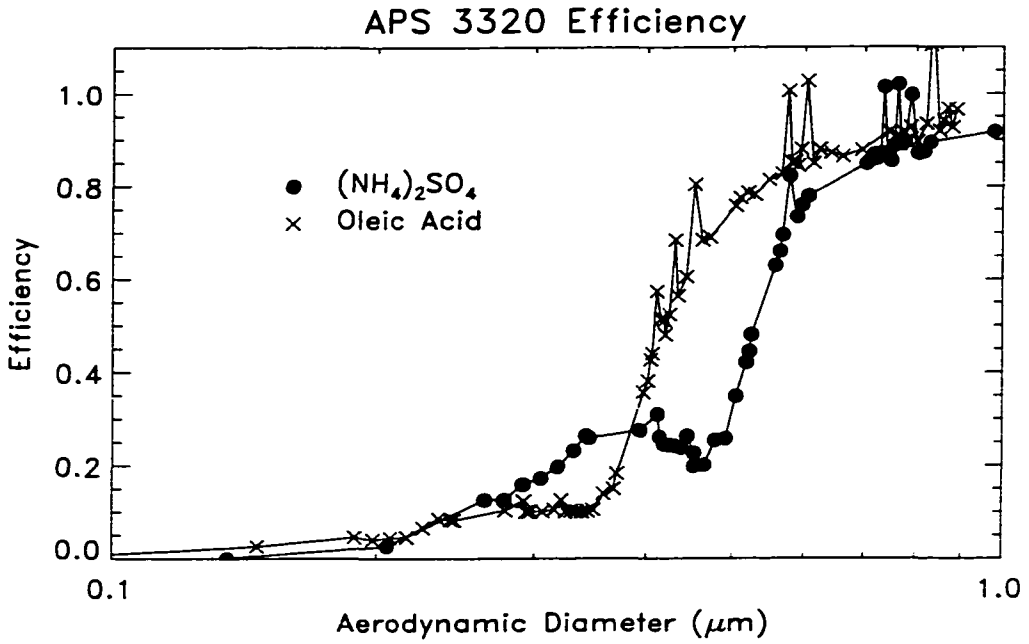

Figure 3.5.1 APS 3320 counting efficiencies plotted against aerodynamic diameter for $(NH_4)_2SO_4$ and oleic acid derived from DMA calibrations.

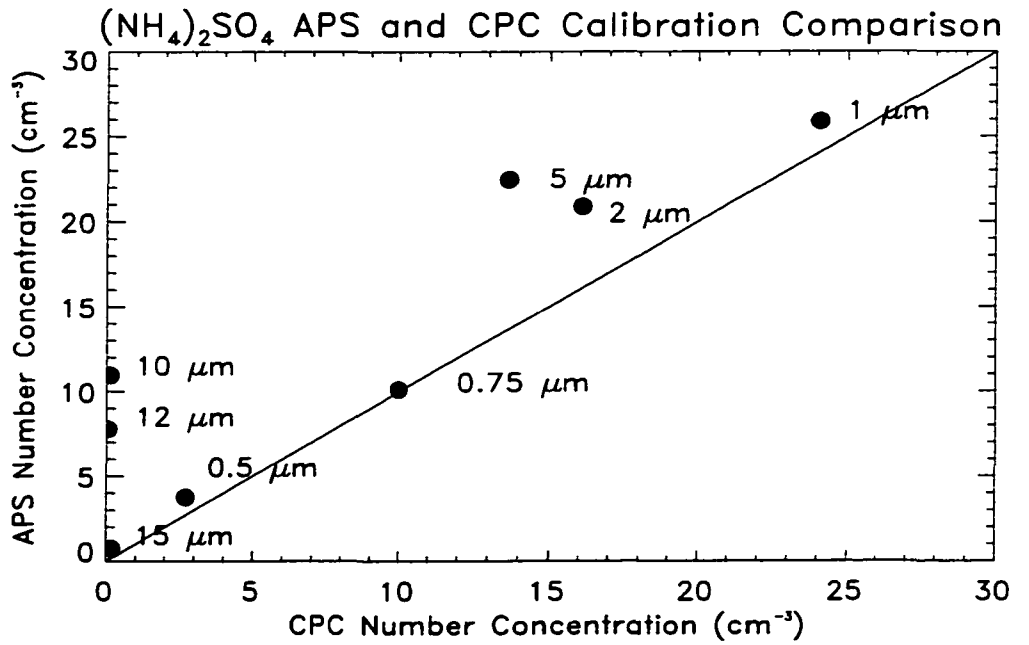

Figure 3.5.2 APS 3320 $(NH_4)_2SO_4$ total number concentrations compared to the TSI 3010 CPC using the VOAG calibration system.

CHAPTER 4. ALIGNMENT METHOD: PARTICLE REFRACTIVE INDEX AND DENSITY RETRIEVAL

The development of this alignment method was motivated by two major factors. The instruments used in this study have different measurement techniques, each depending on a different aerosol property. The DMA measures a mobility diameter that is a true diameter when spherical particles are assumed. The optical particle counter measures optical size, dependent on particle refractive index that is generally unknown for atmospheric particles. The aerodynamic particle sizer measurements depend on particle density and shape that also are generally unknown. Each of these instruments performs more optimally in different size ranges but overlap does occur between them. Constructing a complete size distribution using data from all three instruments requires that distributions be reconciled in the overlap size regions. Other researchers have approached this problem by choosing data from each instrument so that one instrument is used for a range of diameters and beyond them a different instrument would be used (*Eldering et al.*, 1994; *Wilson et al.*, 1988). *Collins et al.* (2000) used chemical measurements and assumptions about hygroscopic growth to average ambient size distributions from a DMA and OPC in their overlap range. The novelty of the approach described here is that in the reconciliation of overlap size regions between instruments, the particle refractive index and effective density are retrieved. Assuming the DMA size

distribution is the true distribution, the optical particle counter data should agree with the DMA when inverted with a refractive index that corresponds to the chemical composition of the measured particles. For an appropriate value of effective density, the APS distribution should also agree with both the OPC and the DMA distributions. Relative humidity effects on particle growth are avoided by performing the size distribution measurements dry.

4.1 PREVIOUS MEASUREMENTS OF REFRACTIVE INDEX AND DENSITY

Knowing refractive index is important for inverting optical particle counter data (see Chapter 3.3) but is also required for performing radiative calculations and to understand the radiative effects of aerosols. Few methods currently exist for retrieving time-resolved measurements of refractive index for atmospheric aerosols. *Stolzenburg et al.* (1998) used a differential mobility analyzer and finely size resolved optical particle size spectrometer (DMOPSS) to measure ambient size distributions at Meadview, Arizona. A high-flow DMA was used to provide an *in-situ* atmospheric calibration of an optical particle counter. The calibration was then used to invert ambient optical particle counter data. Refractive indices can be deduced from these measurements, as was also demonstrated with this method during the Southeastern Aerosol and Visibility Study (SEAVS) (*Kreisberg et al.*, 2001). *Dick* (1998a) used a DAWN-A optical particle counter to match azimuthal variabilities in light scattering with Mie theory to deduce complex refractive index. The same system also distinguishes between spherical and non-spherical particles (*Dick et al.*, 1998b). *Baumgardner et al.*, (1993, 1996) measured forward and backward scattered light by the multiangle aerosol spectrometer probe (MASP) and

applied Mie theory to infer refractive index. *Liu and Daum* (2000) estimated refractive index in closure experiments based on nephelometer measured light scattering coefficients and values derived from size distribution measurements. Refractive indices were inferred from a range of five values from m = 1.33 to m = 1.588. Calculations of refractive index based on volume weighted chemical composition or partial molar refraction are straightforward to perform (*Stelson*, 1990; *Hasan and Dzubay*, 1983; *Ouimette and Flagan*, 1982). However, the optical properties of aerosols can highly depend on the degree of mixing of particles and the physical position of aggregates of absorbing species with respect to host particles (*Fuller et al.*, 1999). Refractive indices derived from chemical measurements can be used to invert OPC data (*Ames et al.*, 2000), however, chemical data typically exist as integrated 24 hour samples and variability in OPC distributions is often observed on finer time resolutions. Applying one value of refractive index for all measured distributions during a 24-hour period may not be appropriate. The method developed here retrieves a value of real refractive index for each hourly averaged size distribution and demonstrates variability throughout the day (see Chapter 6).

Effective density, which includes the effects of both the particle density and dynamic shape factor (see Equation 2.1.4), is also retrieved by this alignment method. Particle density is needed to convert aerodynamic to geometric diameter. Several types of instruments sample aerosols based on aerodynamic diameter, and the data must be converted to a geometric diameter basis to relate these measurements to other types of data or to incorporate the data into radiative calculations. Density is also required to establish relationships between mass and volume concentrations. Density can be

estimated using a volume weighted calculation based on measured chemical compositions (*Hasan and Dzubay,* 1983) but uncertainties in compositions and thermodynamic properties of mixtures can lead to uncertainties in estimates of density (*McMurry,* 2000). Early attempts by *Hanel and Thudium* (1977) measured the mass of bulk samples and the volume of the sample to infer density. *Kelly and McMurry* (1992) review other early measurements as well as describe a technique based on selecting monodisperse laboratory aerosols with a DMA and classifying them with an impactor. *Stein et al.* (1994) measured densities of atmospheric particles in the size range of 0.06 – 0.18 μm using the DMA-impactor technique. Densities calculated from measured aerosol compositions were found to be approximately 20% lower than measured values for undetermined reasons. *McMurry et al.* (2000) have recently developed a new technique for measuring aerosol density by selecting particles of known mobility with a DMA and measuring their mass using an aerosol particle mass analyzer (APM; *Ehara et al.*, 1996). Recent results using this approach are very promising. The retrieval of effective density with the alignment method described in this dissertation relied on Equation 2.1.3 and the agreement between APS and DMA-aligned OPC size distributions for a dry aerosol sample.

4.2 TWOMEY INVERSION OF SIZE DISTRIBUTIONS

The size distribution measurements described in Chapter 1 produce histograms of data that provide the number concentration of particles measured in a given size range. These histograms do not include the known instrument response and do not allow for comparisons between different instruments because of their different size resolutions. To

account for these issues, an inversion or fitting of the measured data is desired to produce a finer resolved distribution that incorporates the instrument response. Data fitting can be performed by assuming a functional form of the size distribution, such as a lognormal (*Dzubay and Hasan,* 1990; *Hand et al.,* 2000); however if no functional form is desired, other types of inversion and/or fitting methods exist. *Crump and Seinfeld* (1982) review methods for inverting size distributions where no size distribution function is assumed. *Twomey* (1975) applied a nonlinear iterative method to relatively broad filter transmission functions. Twomey's inversion is frequently used to invert size distributions with a few modifications to account for sharper instrument efficiency functions than those in Twomey's original application. *Markowski* (1988) developed a smooth-Twomey algorithm that *Wang and John* (1988) applied to impactor derived size distributions. *Winklmayr et al.* (1990) further modified the Twomey inversion by investigating the effects of the initial guess distribution on the iterative method. They investigated how to treat endpoints of the distributions as well as how to treat impactor stages with zero mass due to low detection levels. The method of *Winklmayr et al.* (1990) was used to invert size distributions obtained in this study and will be reviewed in the subsequent section.

If a response y_i is detected on a sizing instrument such as an impactor or optical particle counter, recovering the actual size distribution ($f(D_p)$) requires solving the Fredholm equation of the first kind (Equation 4.2.1) for each channel or stage of the instrument. The size distribution could describe any type of data, such as number, volume, or mass concentrations. For this discussion $f(D_p)$ is assumed to be a number distribution. Equation 4.2.1 is the expression to be solved:

$$y_i = \int_{D_{p,\min}}^{D_{p,\max}} K_i(D_p) f(D_p) dD_p \qquad (4.2.1)$$

where the kernel function ($K_i(D_p)$) is the response function for a channel of the instrument and D_p is the particle diameter. The lower and upper size limits of the instrument are given by the $D_{p,min}$ and $D_{p,max}$. The initial guess distribution is given by $f_o(D_p)$ and is based on the measured data. Integrating Equation 4.2.1 with $f(D_p) = f_o(D_p)$ provides the number (y_{io}) that would result on channel i. In future iterations the guess distribution is modified by multiplying $f_j(D_p)$ by a ratio of actual number to calculated number on a channel multiplied by a weighting function $a_i(D_p)$. The subscript j refers to the iteration number.

The scheme can be approximated by replacing the integral in Equation 4.2.1 by a summation:

$$f_{j+1}(D_p) = f_j(D_p) \cdot [1 + \left(\frac{y_i}{y_{ij}} - 1 \right) a_i(D_p)] \tag{4.2.2}$$

where

$$y_{ij} = \sum_{p=1}^{m} K_i(D_p) f_j(D_p) d \log D_p \tag{4.2.3}$$

and

$$a_i(D_p) = K_i(D_p) \; i = 1,n \tag{4.2.4}$$

The number of channels is given by n, and m is the number of points where the size distribution is evaluated. In this application m = 100. The width of the size intervals where $f(D_p)$ is evaluated is given by $d\log D_p$ and is selected to be a constant value of 0.03.

In the original Twomey application, the weighting function and instrument kernel functions are identical (Equation 4.2.4). Twomey's application used much broader kernel functions; using narrower kernel functions that are typical of sizing instruments can introduce structures of the kernel functions into the resulting size distribution. To improve this effect, weighting functions broader than the kernel functions can be used

(*Gras,* 1983). An expression for these modified weighting functions is given by Equation 4.2.5:

$$a_i(D_p) = \left[\frac{K_i(D_p)}{\max[K_i(D_p)]} \right]^r \tag{4.2.5}$$

where r ranges from 0.3 - 0.7. A value of r = 0.3 was used for this study, however sensitivity to this parameter was investigated (see Chapter 5.3). The kernel functions used to invert optical particle counter and aerodynamic particle sizer data were described in Chapter 3.3 and Chapter 3.5. The DMA kernel functions were assumed to be perfect as these data were inverted with their appropriate transfer function before applying the Twomey inversion (see Chapter 4.3.1).

The first guess distribution uses a linear interpolation of the measured data in each channel. The data are the number concentrations in each channel divided by the area covered by the associated kernel function. A three term moving average (*Markowski,* 1983) was used to smooth the first guess and was applied five times before starting the inversion (see Equation 4.2.6 and 4.2.7).

$$f_o(D_p) = 0.25(D_{p-1}) + 0.5f_o(D_p) + 0.25f_o(D_{p+1}) \tag{4.2.6}$$

$$f_o(D_{p,1}) = 0.75f_o(D_{p,1}) + 0.25f_o(D_{p,2}) \tag{4.2.7}$$

Equation 4.2.7 was used at the small end of the distribution and an equivalent equation was used for the large end because three data points were not available for the moving average.

If the number concentration in a channel is zero or very small, the steep change in the distribution can result in artifacts because the overlapping kernel functions couple the data on adjacent channels. To correct for this, a maximum allowable ratio of data on

adjacent channels was applied by assuming a lognormal with a geometric standard deviation of 1.3. This ratio is on the order of 0.1, meaning that if a number concentration falls below 10% of an adjacent channel it is set to 10% of the higher concentration of the adjacent channels (*Winklmayr et al.*, 1990).

A lack of information at the endpoints of an instrument can result in problems with the inversion if peaks in the data occur near the small or large end of the instrument. To overcome this, the initial guess was extrapolated beyond the actual size limits of the instrument (*Winklmayr et al.*, 1990). Artificial channels were introduced on either end of the size distribution in this extrapolation. For this application, two channels on both the small and large ends were included. The data in these channels were taken to be linear interpolations of the size distributions on the measured channels. Size limits and kernels associated with the artificial channels were approximated by the values applied for the measured kernels for the real channels. The inverted size distribution does not include the data constructed for these artificial stages.

The stopping criterion used in the Twomey inversion is met when the inverted size distribution agrees with the measured data within the experimental uncertainties. Alternatively, the iteration is stopped when the improvement in the accuracy parameter (σ_a) is less than five percent. Equation 4.2.8 defines the accuracy parameter.

$$\sigma_a^{\,2} = \left(\frac{1}{n}\right)\sum_{j=1}^{m}\left[\frac{(y_i - y_{ij})}{\delta y_i}\right]^2 \qquad (4.2.8)$$

The uncertainty in the number concentration for a given channel is given by δy_i and described in Appendix A.

The Twomey inversion as described here is applied in the alignment method both to number and volume concentration data. It is applied to the DMA, OPC and APS data to provide smooth distributions for each instrument and produces size distributions that have the same diameter grid and channel spacing. Although these distributions are not continuous, as a function fit would be, they do provide much finer resolution than if no fitting was performed. Incorporation of the Twomey inversion into the alignment method is described in the following section.

4.3 RETRIEVING PARTICLE REFRACTIVE INDEX: ALIGNMENT METHOD PART 1

The first part of the alignment method reconciles the DMA and OPC distributions. The two instruments overlap in the size range from ~0.1 μm (lower size end of the OPC) to 0.87 μm (upper size end of the DMA). The alignment of the data in the overlap region is based on the calibration work of *Stolzenburg et al.* (1998) discussed earlier. Instead of using the DMA to produce a monodisperse aerosol for calibrating the OPC, we assume that while the two instruments are measuring the same aerosol sample, the true diameter measured by the DMA can be used to "calibrate" the OPC on a distribution by distribution basis. In effect this method calibrates several OPC channels with several DMA channels simultaneously. This method assumes an internal aerosol mixture over the sizes used in the reconciliation and that only one value of real refractive index is needed for the distributions to agree. The repercussions of this assumption will be discussed in Chapter 5.6.

Figure 4.3.1 presents the logic of the alignment method and will be discussed now. Because refractive index is not known *a priori*, a loop over refractive index is performed, ranging from $1.45 < m < 1.6$ ($\Delta m = 0.005$) because these values span the range of calibration species used (described in Chapter 3) and are expected to cover the range of refractive indices of atmospheric particles (*Stelson*, 1990). Included in this loop is the DMA data inversion for multiply charged particles, the OPC data inversion for refractive index, Twomey inversion of both OPC and DMA distributions, and a least squares fit to both data sets. The size distributions for which this method is applied are hourly averaged data with corrections applied for particle losses in the sampling tubes (see Appendix A). Each section of the method will be discussed separately.

4.3.1 INVERTING DMA DATA

In this section the DMA data inversion is described, which includes a multiply charged particle correction as well as corrections for particle losses in the sampling lines. This inversion was performed prior to the Twomey inversion of the DMA distribution data. As was discussed in Chapter 2, no impactor was used with the DMA in the experimental set-up because available impactors had D_{50} limits smaller than desired for this application. Not using an impactor does create a problem in that it is impossible to know from DMA data alone the maximum size of particles sampled and therefore to correct for the effects of multiply charged large particles. This effect was observed during the study due to the relatively high number of coarse particles measured at the study site. Unrealistic peaks in the DMA distributions were observed in the 0.6 – 1.0 diameter range and were believed to be due to multiply charged large particles that were not included in

the preliminary DMA inversion. To deal with this issue, OPC data for larger sizes were incorporated in the DMA inversion. Four artificial mobility channels were created for the DMA, corresponding to particle diameters larger than the maximum diameter sampled by the DMA. Because of the coarse resolution of the OPC, more resolution was required in order to incorporate the OPC data in the DMA artificial mobility channels. Before any charge corrections were applied to the DMA data, OPC data in bins 6 and 7 ($0.8 < D_p < 2.0$ μm) were smoothed using a Twomey inversion and then interpolated into the artificial DMA channels. The result was a raw DMA size distribution with an additional four bins extending to 2 μm. It was assumed that only singly charged particles were observed in the four artificial DMA channels. Although the DMA data do not depend on refractive index, this part of the inversion was included in the refractive index loop because the OPC data had to be converted to true size using the scaling polynomials described in Chapter 3.4 (see Figure 4.3.1). Incorporating the OPC data in the DMA inversion removed any unrealistic peaks in the DMA distribution that were occurring because of multiply charged particles.

The full DMA inversion is described by the following equations. The raw DMA concentrations, c, were related to the corrected concentrations, N, by matrix, **A** (Equation 4.3.1.1). The raw data were corrected for the DMA transfer function by multiplying the concentrations by a factor of two.

$$c = AN \tag{4.3.1.1}$$

In order to obtain the corrected concentration, the matrix **A** was inverted, as in Equation 4.3.1.2.

$$N = A^{-1}c \tag{4.3.1.2}$$

The matrix A included multiply-charged particle corrections for the original DMA channels (see Chapter 2.3) and the additional four artificial channels created by incorporating the OPC data into the distribution. An example of A can be found in Appendix C. Matrix A also included loss corrections as described by Equation 4.3.1.3, where f is a matrix consisting of charge corrections and η corresponds to values of loss corrections for the corresponding diameters (see Appendix A for discussion of loss calculations):

$$A = f\eta \tag{4.3.1.3}$$

As seen in Figure 4.3.1, the OPC data were inverted with the same refractive index as used to correct the DMA data. The next step in the method was to smooth the data to the same diameter grid and channel width using the Twomey inversion.

4.3.2. DATA SMOOTHING USING THE TWOMEY INVERSION

The Twomey inversion described earlier was applied to OPC and DMA number and volume distributions. Uncertainties in the number and volume concentrations for each channel were applied (see Appendix B) and experimental kernels derived for the OPC in Chapter 3.3 were included. Perfect kernels (100% collection for each channel) were assumed for the DMA because the DMA inversion described earlier included instrument response. All other parameters in the Twomey inversion were described in Chapter 4.2. Four artificial channels with concentrations and uncertainties initially forced to zero were included for the OPC (two channels on each end) according to *Winklmayr et al.* (1990) and were adjusted by the initial guess distribution. The four OPC-derived channels included for the large diameter end in the DMA distribution were included in

the Twomey inversion. Two artificial channels were also included, one at the small end and one at the large end. The concentration and uncertainty in the artificial channels were initially forced to zero.

4.3.3 DISTRIBUTION COMPARISON: LEAST-SQUARES FIT

The alignment method assumed that when the OPC data have been inverted with the appropriate refractive index, the DMA and OPC distributions should agree in each channel in their overlap region. Volume distributions were used for the comparison as they were more sensitive in the size region of interest. To compare the OPC and DMA Twomey inverted volume distributions an overlap size region was chosen based on instrument performance. All of the channels compared between instruments were Twomey inverted channels. The size limits of either instrument were avoided because of increased uncertainty in the size limits of the instruments, resulting in an 18 bin overlap evaluated between $0.2 < D_p < 0.7$ μm.

The reader can imagine constructing a scatter plot with values of the OPC volume distribution ($dV/d\log D_p$) in the overlapping range plotted on the abscissa axis and the corresponding values of the DMA volume distribution plotted on ordinate axis. The data should approach a line with slope = 1 and intercept of 0 when agreement has been reached. The intercept was forced to be zero to avoid a multiplicative offset between the data sets. A Fortran Numerical Recipes routine (*Press et al.*, 1992) was used to perform a least squares fit with uncertainties in both the DMA and OPC distributions on a per bin basis (see Appendix B). The Fortran routine returned the value of slope, uncertainty in slope, uncertainty in the zero intercept and a χ^2 goodness-of-fit to the slope as well as to a

1:1 line for each set of distributions compared. For each loop over refractive index, the DMA distribution was compared to the newly inverted OPC distribution and statistical information was saved for each pass through the loop. After the looping was complete, the aligned OPC data were chosen as the case when the value of χ^2 for a 1:1 line was a minimum; this case corresponded to the OPC volume distribution that best agreed with the DMA volume distribution. When this distribution had been determined, the value of refractive index used to invert that best-fit OPC distribution was retrieved. The aligned case was not chosen based on the value of slope closest to 1 because the existence of uncertainties in both data sets in the least squares fit may result in some bias of slope (*Johnston*, 1984). The aligned OPC volume distributions were limited to cases when the slope ranged between 0.8 and 1.2, although the average value of the slope uncertainty was $\delta b = 0.02$. Figure 4.3.3.1a shows a scatter plot of OPC and DMA data for aligned distributions for one hour on October 8 1999. The dashed line corresponds to the slope for the fit, and the 1:1 line is plotted as a solid line. The data tend to form an "S" shape because the overlap range between the instruments spanned the peak of the accumulation mode and therefore similar values of volume distributions are encountered on either side of the peak. Figure 4.3.3.1b shows a scatter plot for an unaligned case for the same distributions, using a refractive index of $m = 1.53$ to invert the OPC data. The data fall toward the OPC side of the scatter plot, demonstrating that the refractive index used to invert the OPC data was too low for this case. Figure 4.3.3.2 depicts the value of slope for each refractive index applied in the loop on the October 8 1999 data. A monotonic relationship between refractive index and slope was observed, with slope decreasing with increasing refractive index. Figure 4.3.3.3 demonstrates the behavior of χ^2 with refractive

index for the same day. A bow shaped curve was observed, with the minimum of the bow corresponding to the retrieved value of refractive index. The values of χ^2 were very large because of the "S" shaped nature of the compared data.

The effect of inverting the OPC with an inappropriate refractive index is shown in Figure 4.3.3.4. The OPC volume distribution from October 8 1999 was inverted with a refractive index corresponding to dry ammonium sulfate (m = 1.53). The differences between the DMA and OPC distributions are obvious with the OPC distribution overestimating volume with respect to the DMA. Figure 4.3.3.5 presents the same DMA volume distribution but now plotted with an OPC distribution inverted using m = 1.58 as determined from the alignment method. The data from each instrument are plotted as histograms with the smoothed Twomey inversion distribution overlying. These figures demonstrate the need for appropriate values of refractive index for inverting OPC data.

Although the discussion of this method has focused on aligning volume distributions, the Twomey inversion was used to align number distributions as well. Studies were performed to determine the sensitivity to different parameters in this method. Sensitivity to Twomey parameters, choice of kernels in the Twomey inversion, sizes compared in the overlap range and the effect of complex refractive index on this method were all investigated and will be discussed in Chapter 5.

4.4 RETRIEVING PARTICLE EFFECTIVE DENSITY: ALIGNMENT METHOD PART 2

The second part of this alignment method reconciles the APS data to the aligned OPC volume distribution in their overlap region. This part of the alignment method is

very similar to Part 1, but particle effective density is varied instead of refractive index (see Figure 4.3.1). A range of effective densities from ρ_e = 1.2 – 3 g cm^{-3} ($\Delta\rho_e$ = 0.05) was used. This step of the alignment method was inherently more uncertain because the shape of the volume distribution in the overlap region is fairly flat, with the overlap spanning the diameters where the accumulation mode typically ends and the coarse mode begins (see Figure 4.4.1). Figure 4.4.2a shows a scatter plot of aligned OPC and APS volume distributions for an hour on October 12 1999 for ρ_e = 1.6 g cm^{-3}. The effect of the flatness of the overlap region is depicted by the monotone values of data being compared. The dashed line corresponds to the slope returned by the fit; the solid line corresponds to a 1:1 line. Figure 4.4.2b shows a scatter plot for unaligned data for the same day but with ρ_e = 1.4 g cm^{-3}. Although the comparison between the OPC and APS is not inherently as good as the DMA and OPC, there does appear to be one value of density that optimizes agreement.

The Twomey inversion was applied to the APS data although the instrument was already finely resolved. This inversion included the instrument response and forced the data to the same diameter grid as the OPC and DMA. The same least squares fit subroutine was used to compare the OPC and APS distributions in the overlap region of 0.63 – 1.3 μm with 12 bins, again avoiding the diameter limits of either instrument. For each value of effective density over which the method looped, a χ^2 goodness of fit to a 1:1 line was calculated. Once the looping was complete, the distribution with the smallest χ^2 was chosen as the best fit case. Figure 4.4.3 shows the behavior of slope for each value of density applied in the looping procedure. In contrast to the behavior observed with refractive index, the slope increases with increased density. More structure is noticeable

between slope and density due to the difficulty in fitting a line to the scatter plot shown in Figure 4.4.2a. The erratic behavior hinted at in Figure 4.4.3 was pronounced in the comparison of χ^2 with density (Figure 4.4.4). The scalloped features suggested that the choice of range of densities that is looped over in the alignment method could affect the retrieval due to the presence of several minima. The slopes corresponding to the different minima may be close to one, as can be seen in Figure 4.4.3. The behavior is believed to be due to the flatness of the OPC and APS distributions in the overlap region (Figure 4.4.1). An effective density of 1.5 g cm^{-3} was chosen for the case shown in Figure 4.4.3 and Figure 4.4.4.

Weighted Average of Size Distributions

After the distributions from the three instruments were aligned, construction of a complete distribution from $0.03 < D_p < 20$ μm required averaging to be performed in the overlapped regions. A weighted average (x_{avg}) was used in order to include all available data (x_i) and their uncertainties (σ_i) (Equation 4.4.1). The uncertainty in the weighted average (σ^2_{avg}) was calculated by Equation 4.4.2 (*Bevington and Robinson*, 1992).

$$x_{avg} = \frac{\Sigma\left(x_i / \sigma_i^2\right)}{\Sigma\left(1 / \sigma_i^2\right)} \tag{4.4.1}$$

$$\sigma^2_{avg} = \frac{1}{\Sigma\left(1 / \sigma_i^2\right)} \tag{4.4.2}$$

From 0.03 – 0.37 μm only DMA data were used, however from 0.37- 0.65 μm a weighted average between DMA and OPC data was calculated. OPC data only were used

from 0.65 – 1.0 μm and a weighted average between OPC and APS data was used from 1.0 – 1.2 μm. APS data only were used from 1.2 – 21.4 μm. Overall the complete distribution resulted in 96 bins with a uniform logarithmic bin width of 0.03. Construction of both number and volume distributions was performed, and uncertainties were calculated on a per bin basis (See Appendix B). Figure 4.4.5 presents an example of a complete volume distribution constructed from aligned DMA, OPC and APS distributions for October 8 1999, with histograms representing the measured data and the smooth line showing the result of the alignment and the weighted averaging.

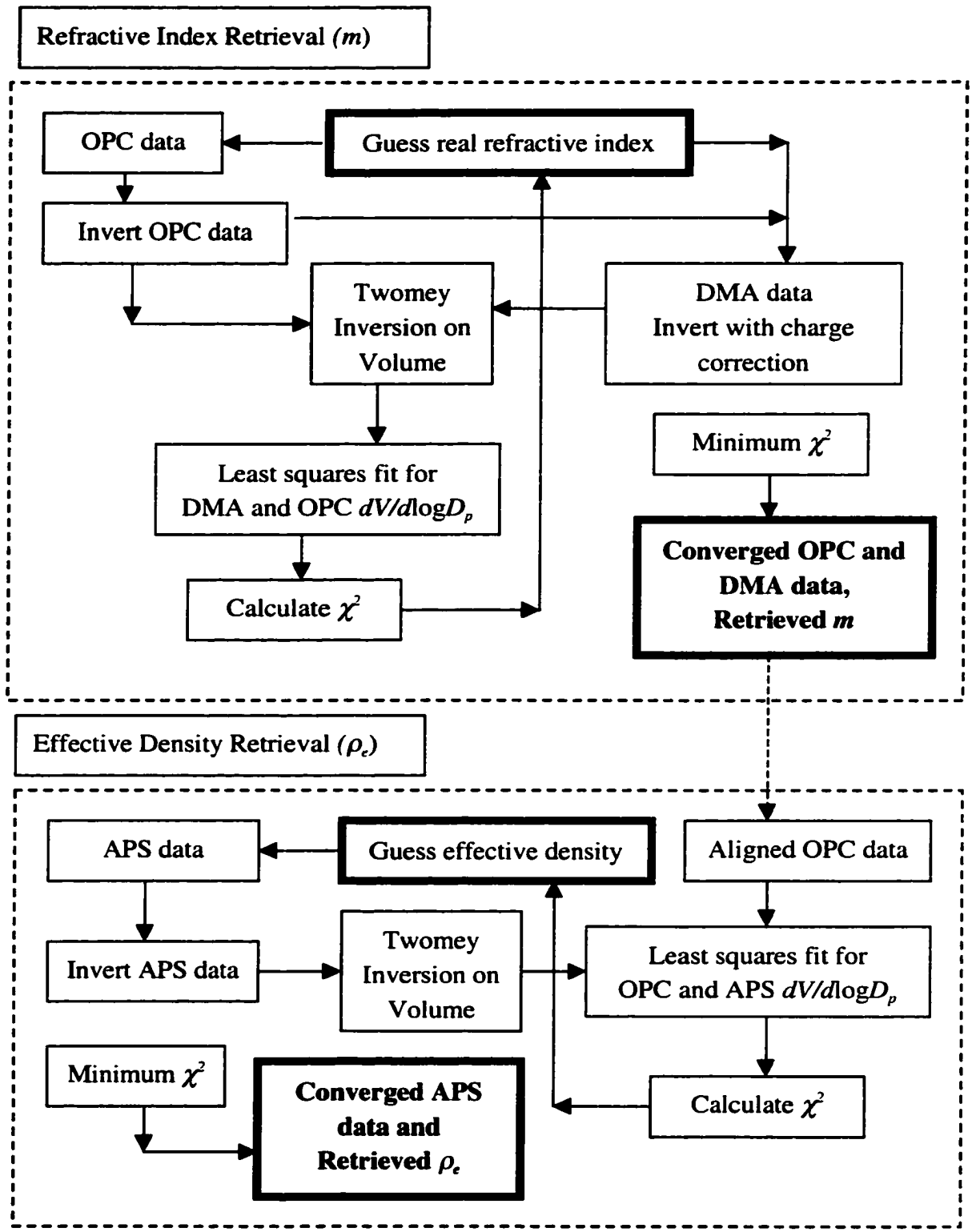

Figure 4.3.1 Flow chart of alignment method.

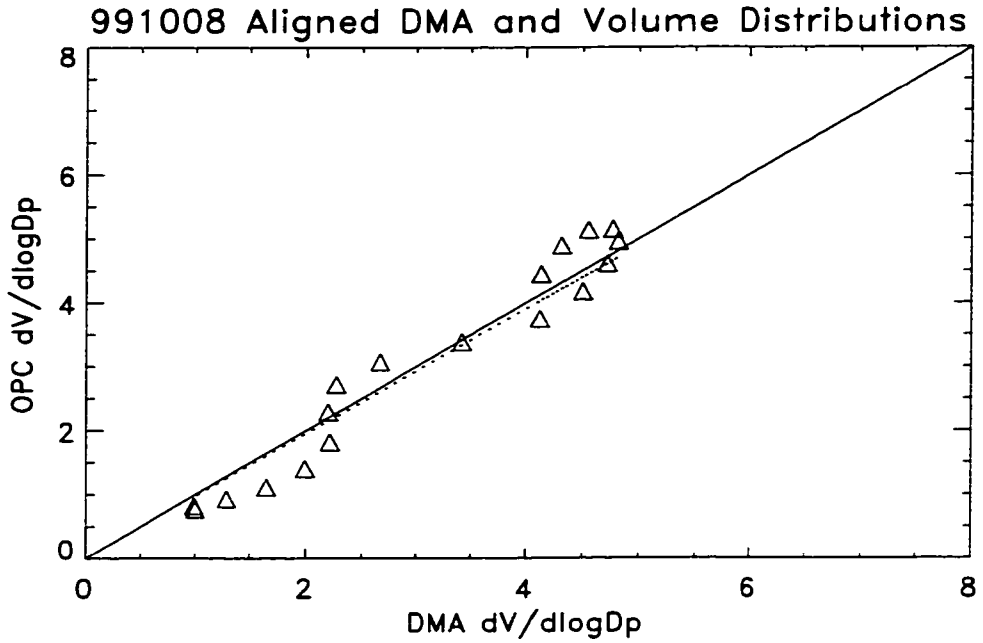

Figure 4.3.3.1a Scatter plot of aligned OPC and DMA volume distributions on October 8 1999. The dashed line corresponds to the slope fit to the data and the solid line corresponds to the 1:1 line. The retrieved refractive index was $m = 1.58$.

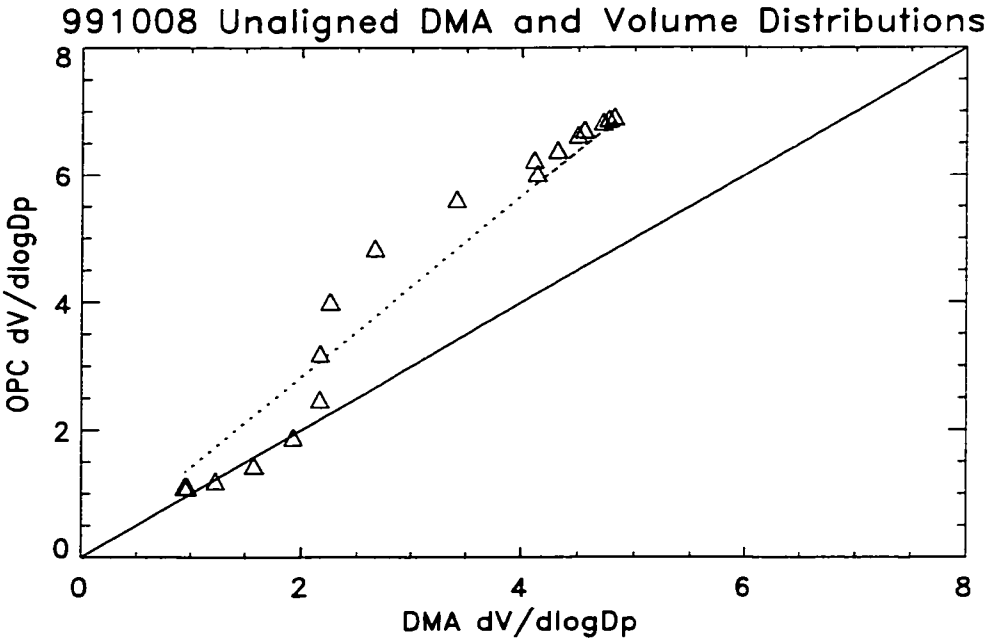

Figure 4.3.3.1b Scatter plot of unaligned OPC and DMA volume distributions on October 8 1999. The dashed line corresponds to the slope fit to the data and the solid line corresponds to the 1:1 line. The applied refractive index was $m = 1.53$.

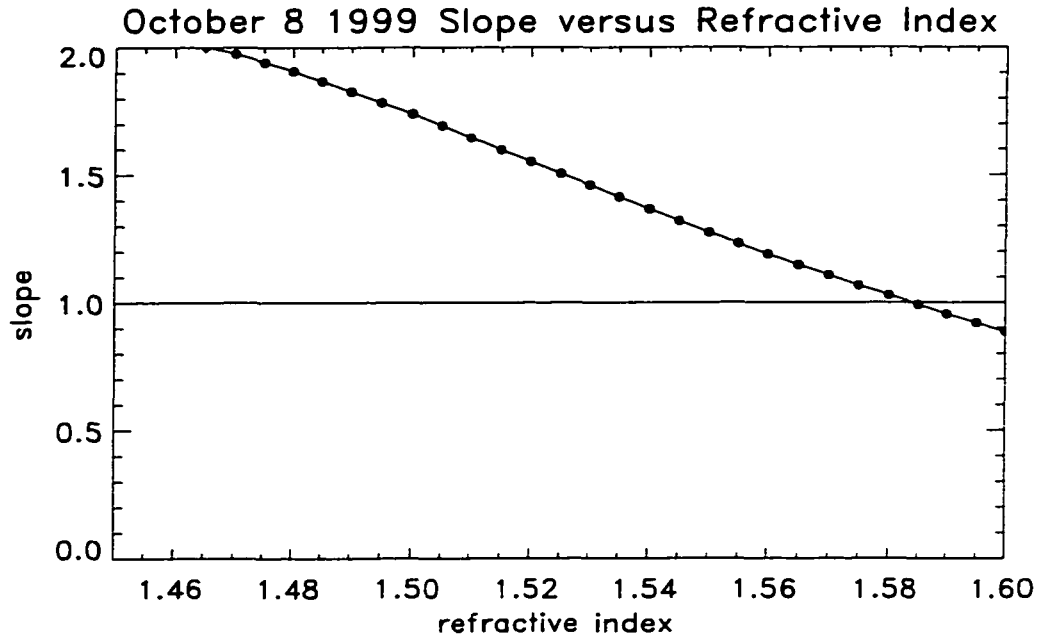

Figure 4.3.3.2 Slope versus applied refractive index for October 8 1999.

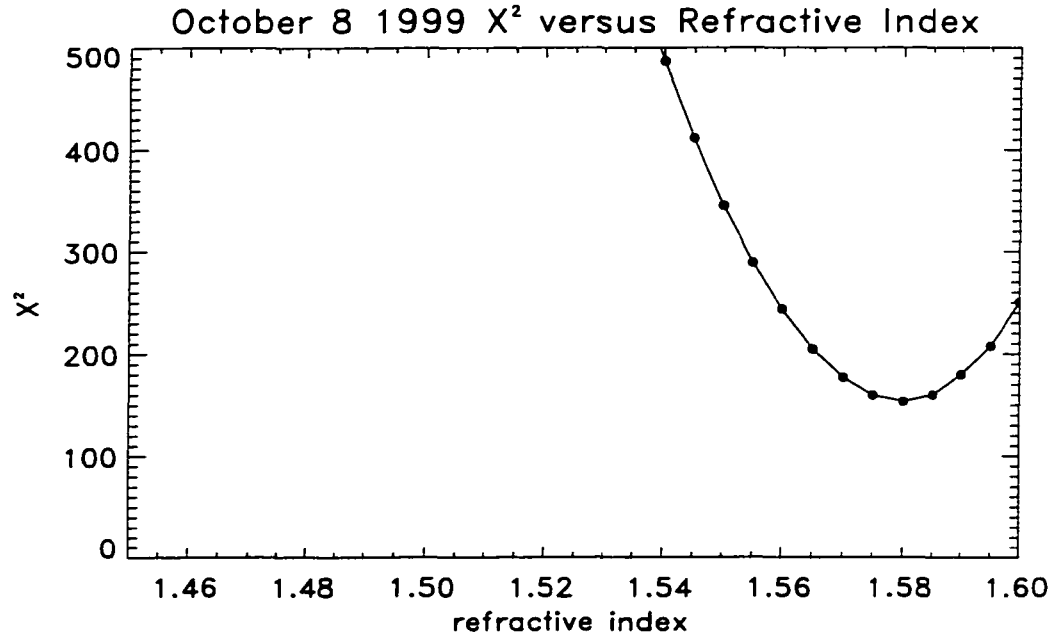

Figure 4.3.3.3 χ^2 versus retrieved refractive index for October 8 1999.

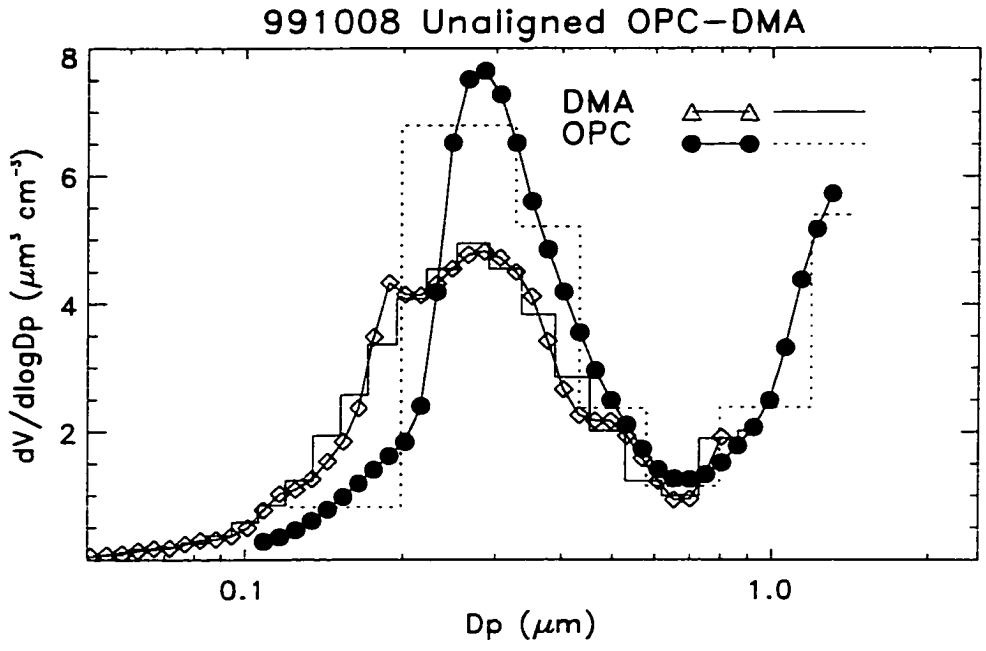

Figure 4.3.3.4 Unaligned OPC and DMA volume distributions on October 8 1999. A refractive index of $m = 1.53$ was used to invert OPC data.

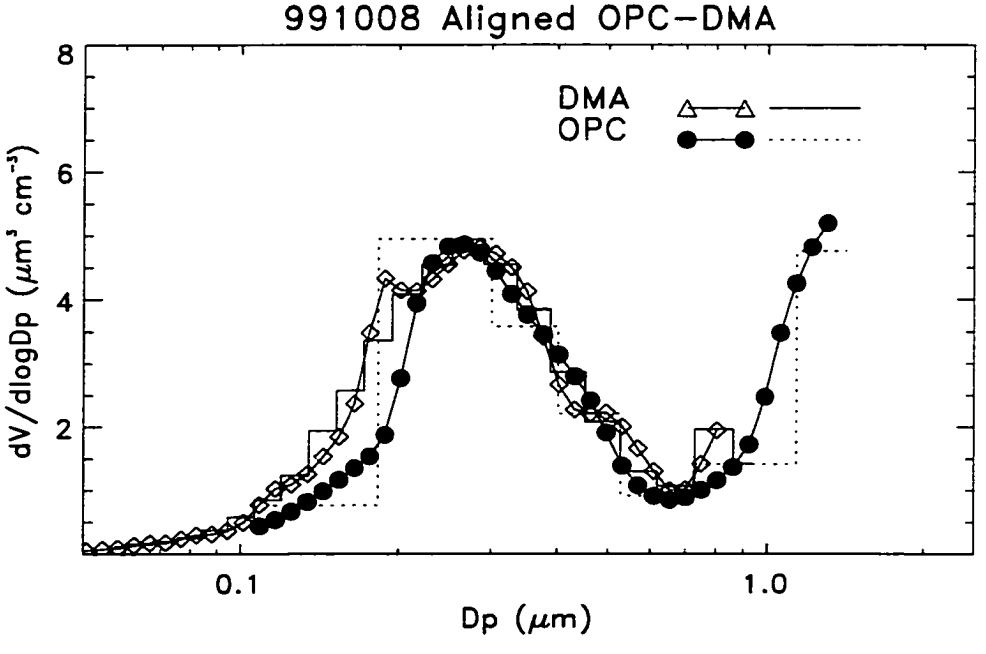

Figure 4.3.3.5 Aligned OPC and DMA volume distributions on October 8 1999. A refractive index of $m = 1.58$ was retrieved with the alignment method.

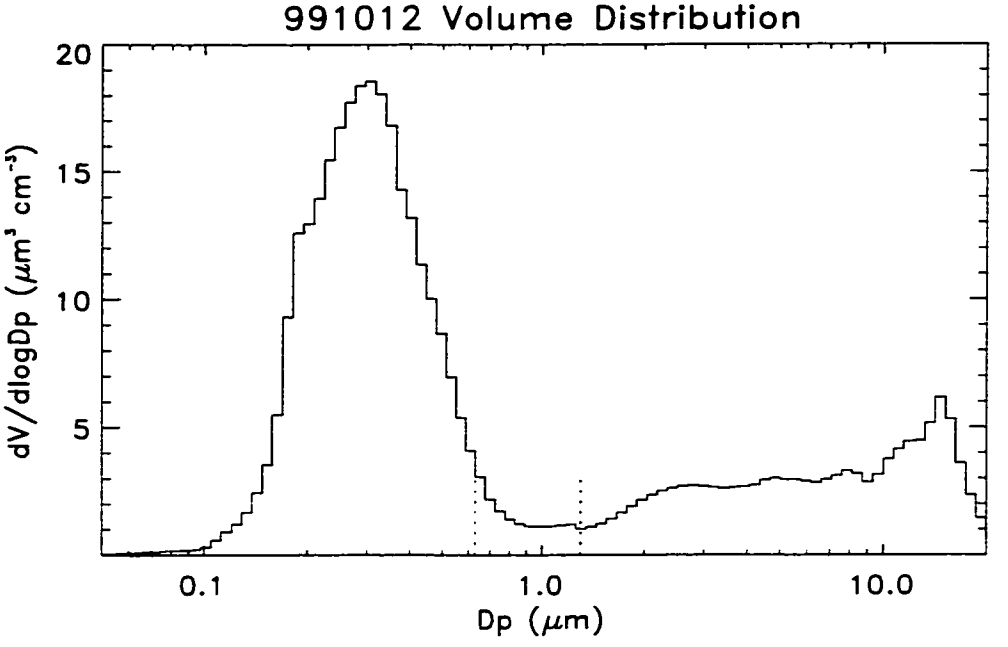

Figure 4.4.1 The APS-OPC overlap region for the fixed case on October 12, 1999 ranged from $0.63 < D_p < 1.3$ μm (dashed lines), typically where the accumulation mode ended and the coarse mode began.

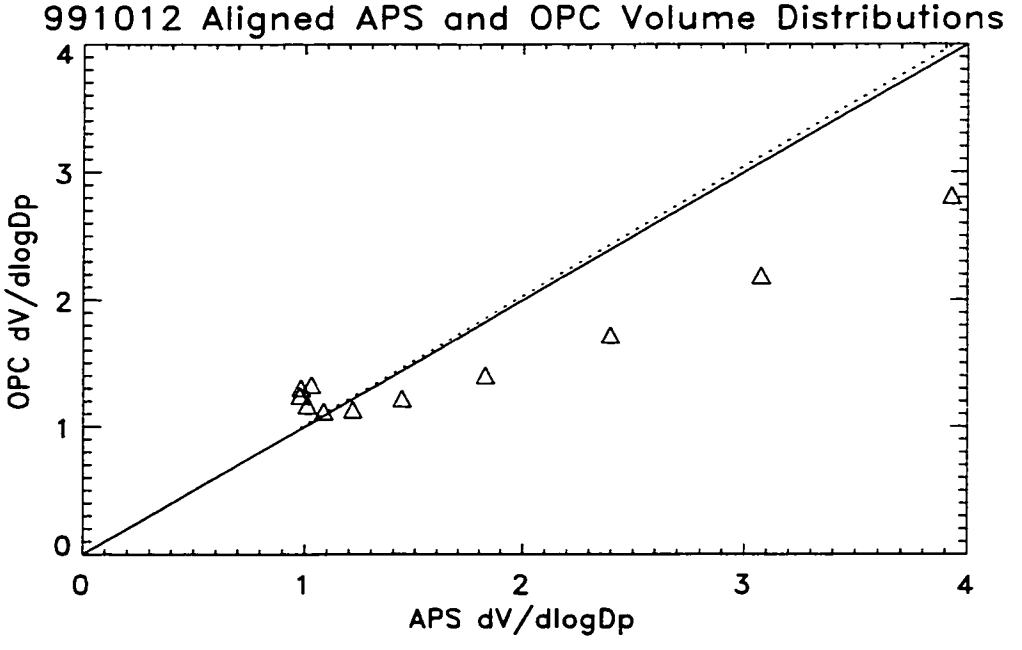

Figure 4.4.2a Aligned scatter plot of OPC and APS volume distributions on October 12, 1999. The dashed line corresponds to the slope fit to the data, and the solid line corresponds to the 1:1 line. The effective density for this case was $\rho_e = 1.6$ g cm^{-3}.

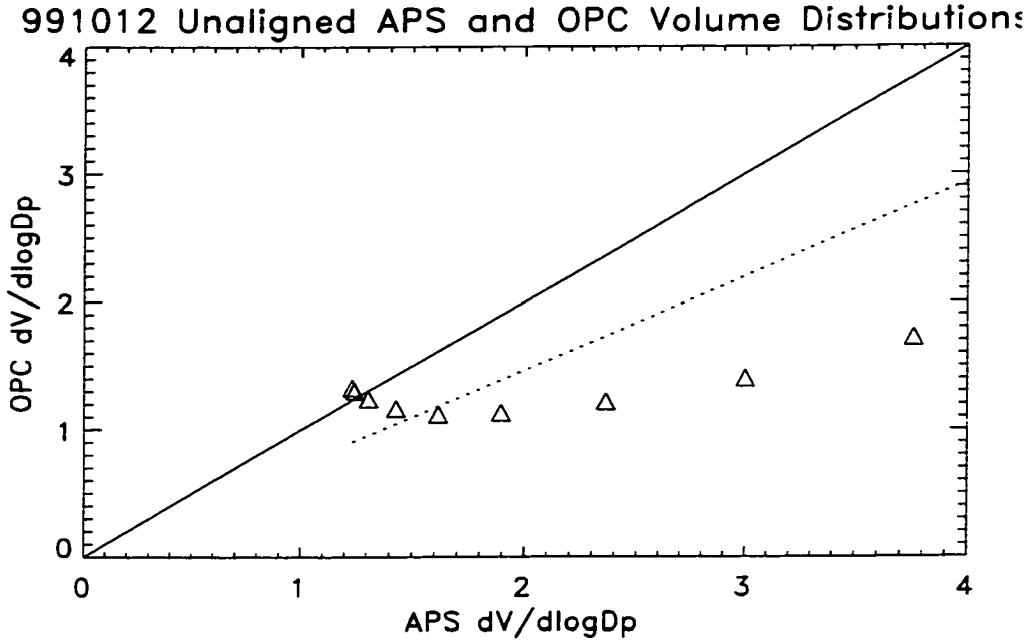

Figure 4.4.2b Unaligned scatter plot of OPC and APS volume distributions on October 12, 1999. The dashed line corresponds to the slope fit to the data, and the dark line corresponds to the 1:1 line. The effective density for this case was $\rho_e = 1.4$ g cm^{-3}.

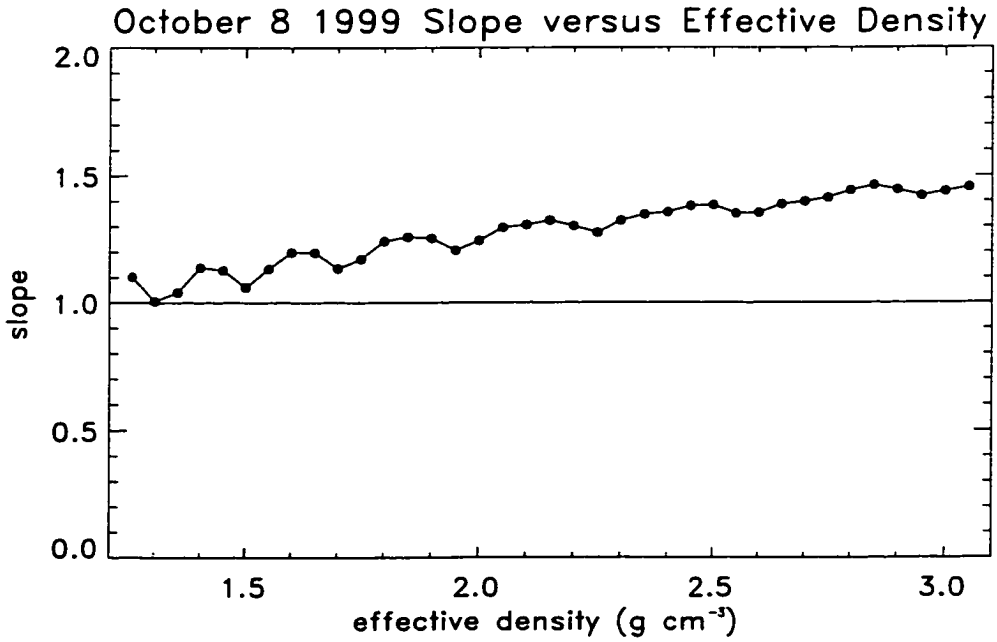

Figure 4.4.3 Slope versus effective density for October 8, 1999. A value of $\rho_e = 1.5$ gcm^{-3} was retrieved for this case.

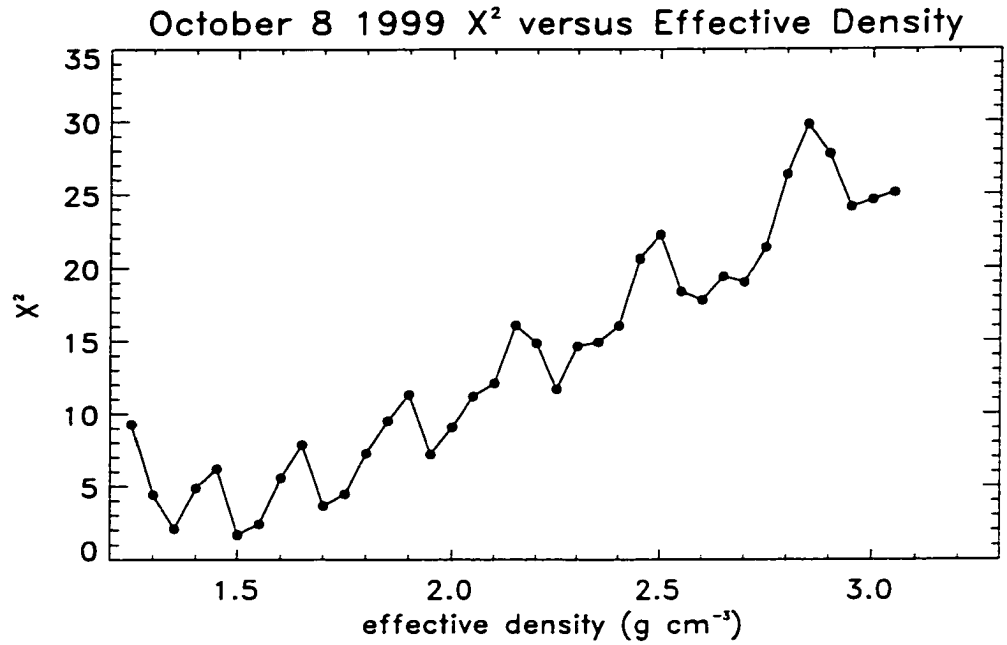

Figure 4.4.4 χ^2 versus effective density for October 8 1999. A value of $\rho_e = 1.5$ gcm^{-3} was retrieved for this case.

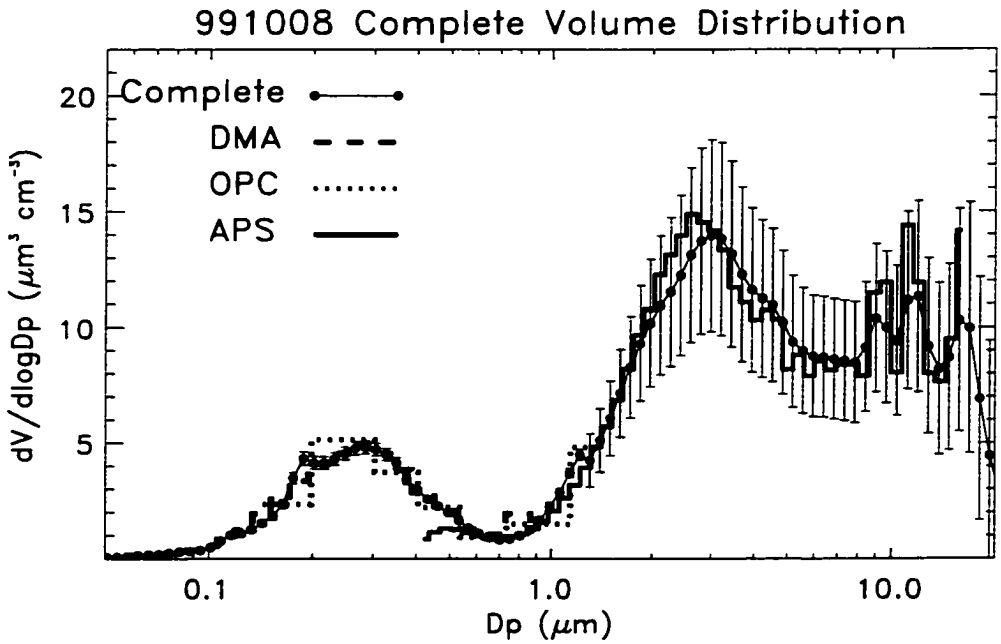

Figure 4.4.5 Complete size distribution from October 8 1999. The DMA, OPC and APS data are represented as histograms; the weighted average Twomey distribution is plotted on top. Uncertainties correspond to the Twomey curve.

CHAPTER 5. SENSITIVITY STUDIES FOR ALIGNMENT METHOD

Several sensitivity studies were performed to determine the parameters resulting in the largest uncertainties in refractive index and effective density retrieved from the alignment method. Each test will be compared to the "fixed" case with parameters believed to be the most reasonable. The sensitivity studies tested the effects of experimental versus perfect kernels applied in the Twomey inversion, kernel weighting parameters applied in the Twomey inversion, sensitivity to the DMA-OPC overlap region applied in the alignment method, sensitivity to the OPC-APS overlap region applied, and sensitivity to complex refractive index.

5.1 FIXED CASE: EXPERIMENTAL KERNELS

The set of parameters used in the "fixed" case will be described here. Experimental kernels derived for the OPC and APS (Chapter 3.3 and Chapter 3.5) were applied in the Twomey inversion. The kernel weight (Equation 4.2.5) used was $r = 0.3$, consistent with the range of values used in previous applications of the Twomey inversion to impactor data (*Lowenthal et al.*, 2000; *Winklmayr et al.* 1990). The overlap range between the DMA and OPC was chosen to be $0.2 < D_p < 0.7$ μm and the OPC-APS overlap range was chosen to be $0.63 < D_p < 1.3$ μm. Figure 5.1.1 presents the hourly retrieved refractive indices for July through October 1999. Variations in refractive index

were observed on short time scales. Recall that refractive index was allowed to vary by $\Delta m = 0.005$ in the alignment method; the effect of this imposed resolution is seen in the timelines. Several periods existed when the retrieved refractive index may have been larger than $m = 1.6$. Because the maximum refractive index of the calibration aerosol was $m = 1.588$ (PSL), the alignment method was not extended above this. Figure 5.1.1 suggested that the method should be extended to higher refractive indices. The timeline suggests that there were periods where retrieved refractive index may have been higher than $m = 1.6$; the retrieval was not extended above $m = 1.6$ because calibration data were not available for higher refractive indices. Figure 5.1.2 presents the slopes corresponding to the retrieved refractive indices. Values close to one were observed for most of the cases with uncertainties in slope on the order of $\delta b = 0.02$. Figure 5.1.3 shows the values of χ^2 corresponding to the minimum of all evaluated values. The reasons for these large values of χ^2 were discussed in Chapter 4.3.3. More discussion of retrieved values of refractive index and effective density can be found in Chapter 6 where comparisons with other estimates will be presented.

Figure 5.1.4 presents results of retrieved effective density. Recall that ρ_e includes the effects of particle shape factor that typically can range from 1.05 –2.0 for dust (*Willeke and Baron,* 1993). Values of effective density were allowed to vary by $\Delta\rho_e = 0.05$ in the alignment method. Slopes corresponding to retrieved density are presented in Figure 5.1.5. Slopes close to one were observed for most of these distributions with typical uncertainties of $\delta b = 0.09$. The minimum χ^2 is shown in Figure 5.1.6. Immediately noticeable are the smaller values of χ^2 compared to those obtained with the refractive index retrieval. These small values are a direct result in the lack of structure in

the volume distribution for the overlap region between the OPC and APS, as discussed in Chapter 4.4. Although the χ^2 associated with the APS alignment are smaller they do not reflect any greater certainty in the effective density retrieval as will be demonstrated later (see Chapter 5.5).

5.2 SENSITIVITY TO THE FORM OF KERNEL APPLIED IN THE TWOMEY INVERSION

The alignment method was performed with the same parameters described for the "fixed" case except perfect kernels instead of experimentally derived kernels were applied in the Twomey inversion for the OPC and APS. For this application perfect kernels are described as 100% sampling efficiency for a given channel such that each channel kernel can be represented as a step function. The comparisons can be found in Figure 5.2.1 and Figure 5.2.2 as percent differences in retrieved refractive index (Figure 5.2.1) and effective density (Figure 5.2.2) when compared to the "fixed" case. Percent difference between two variables (x,y) was calculated with Equation 5.2.1, therefore the sign of the difference was not observable in these timelines. The effect on refractive index is negligible; less than two percent difference was observed for all distributions aligned in the study period.

$$\%difference = 100\frac{|x-y|}{average(x,y)} \tag{5.2.1}$$

Larger percent differences were observed for retrieved effective density with the largest values ranging between 10% and 30%. Reasons for this difference can be demonstrated by investigating the resulting volume distributions. Figures 5.2.3 and 5.2.4 show the hourly averaged volume distribution for September 12 1999 inverted both ways.

Smoothed Twomey inverted distributions overlay histograms of the data from each instrument. The decreased counting efficiency for small particles is noticeable with the APS distribution falling off near 0.5 μm. The experimental kernels applied in the "fixed" case resulted in a retrieved density of ρ_e = 1.55 g cm^{-3} compared to ρ_e = 1.35 g cm^{-3} for the case when perfect kernels were applied. Applying an experimental kernel in the OPC Twomey inversion changed the endpoints of the smoothed OPC distributions (see Figures 5.2.3 and 5.2.4). These differences affected the alignment of the APS distributions because the position of the APS distribution depended on the behavior of the OPC data. The densities retrieved in this sensitivity study were not consistently higher or lower than those obtained with the "fixed" case. It is believed that experimental kernels should be applied in the Twomey inversion to include the effects of the instrument response on the smoothed distributions (see Chapter 3.3 and Chapter 3.5). However, this sensitivity points to the need for improved counting efficiencies at the small end of the APS. If these data were known with more certainty or if a correction could be applied, the alignment method would be less sensitive in this region.

5.3 SENSITIVITY TO KERNEL WEIGHTING IN TWOMEY INVERSION

Using sharp efficiencies in the Twomey inversion can introduce artifacts in the inverted size distribution (*Winklmayr et al.*, 1990). The recommended weighting factor r in Equation 4.2.5 ranges from $0.3 < r < 0.7$. A value of $r = 0.3$ was used in the "fixed" case and an upper limit of $r = 0.7$ was applied to test the effects of this parameter in the alignment method. The percent differences in the retrieved refractive indices and densities from the "fixed" case and this case can be found in Figures 5.3.1 and 5.3.2. The

effects on refractive index are negligible, typically 1% or less. The effects on effective density are larger, on the order of 3-15 %. Investigations of aligned size distributions did not reveal any systematic reasons for the differences observed between retrieved densities.

5.4 SENSITIVITY TO DMA-OPC OVERLAP REGION

A test was performed on the effects of the chosen range of diameters included in the overlap region between the DMA and OPC distributions. Ideally as many bins as possible were desired to improve the least squares fit, although the number was limited to avoid the size limits of the instruments. The "fixed" case used an overlap region ranging from $0.2 < D_p < 0.7$ μm with 18 channels derived from the Twomey inversion. This test was performed with a wider range from $0.1 < D_p < 0.75$ μm with 30 channels. The lowest size channel of the OPC is approximately 0.1 μm; this test therefore included some additional uncertainty based on the nearness of the overlap range to the OPC lower limit. Widening the overlap range to 0.1 μm allowed for the data from the lowest OPC instrument bin to be included in the Twomey channel comparison. Figure 5.4.1 presents the percent differences in retrieved refractive index. A larger effect was observed compared to other tests already discussed, however the effect is still small with a maximum on the order of 2-4%.

As will be seen in Chapter 6, the accumulation volume median diameters were almost always greater than 0.2 μm (average accumulation mode $D_{gv} = 0.26 \pm 0.04$ μm). The smallest diameter of the wider overlap range and the "fixed" case was smaller than the typical peak diameter of the accumulation mode. Including the typical diameters of

the peak of the accumulation mode in the overlap range provided the structure observed in the scatter plots (see Figure 4.3.3.1a and Figure 4.3.3.1b). It is believed that this structure reduced the uncertainty and the sensitivity in the retrieval of refractive index.

Figure 5.4.2 shows histograms of the DMA, OPC, and APS data with smoothed Twomey distributions overlying for the "fixed" case on October 12 1999. Agreement between the DMA and OPC data is observed on either side of the accumulation mode peak, with a retrieved refractive index of m = 1.55 for this case. Figure 5.4.3 depicts the same distributions aligned with a wider size range. The OPC distribution agrees with the DMA distribution only on the small diameter side of the accumulation mode, with a retrieved m= 1.6. Whether the alignment method was detecting a chemical composition difference between the small and large diameter range in the DMA distribution was impossible to conclude. A more reasonable conclusion was that the smaller diameter end of the wider overlap range was being weighted more heavily in the least squares fit because there were more channels in that size range for comparison than in the "fixed" case. Higher retrieved refractive indices were always observed for the wider overlap range case, which corresponded to a shift towards smaller diameters, consistent with more weight given to those channels.

Figure 5.4.4 presents the percent differences in retrieved density. Differences in density were expected because the alignment of the APS distribution depended on the position of the inverted OPC distribution. Differences of up to 25% were observed, in the same range as the other sensitivity tests discussed already. Investigating the volume distributions in Figures 5.4.2 and 5.4.3 revealed the reason for the differences. Figure 5.4.2 shows good agreement between all instruments for the "fixed" case in the diameter

range of ~0.5 – 1.0 μm, with retrieved density of ρ_e = 1.8 g cm^{-3}. In contrast, the wider overlapping range retrieved density was 2.3 g cm^{-3}. Examining Figure 5.4.3 shows the APS aligned with the OPC distribution for D_p < 1 μm, but neither were aligned with the DMA, which depicts the true diameter. The shift of the OPC distribution toward smaller diameters resulted in the APS also shifting to smaller diameters in the alignment, resulting in a larger retrieved density. The "fixed" case was believed to be a more realistic choice of overlap range because better agreement was observed between all three instruments in the larger diameter range (near 0.7 μm) and because of increased uncertainty in the lower diameter limit of the OPC size distribution.

5.5 SENSITIVITY TO OPC-APS OVERLAP RANGE

A similar sensitivity study was performed on the overlap range of the OPC and APS, changing the "fixed" case overlap range, 0.63 < D_p < 1.3 μm (12 Twomey inverted bins), to 1.0 < D_p < 1.3 μm (4 Twomey inverted bins). The lower limit of 1 μm avoided uncertainties that existed at the lower diameter limit of the APS due to decreased counting efficiencies observed during the instrument calibration. Differences of up to 30-40% were observed for retrieved effective density (Figure 5.5.1). The densities retrieved using a narrower overlap range were typically, although not always, lower than the "fixed" case. Figure 5.5.2 and Figure 5.5.3 show an hourly averaged distribution on October 12 1999 for both the "fixed" (Figure 5.5.2) and this test case (Figure 5.5.3). The APS distribution obviously did not agree with the DMA or OPC distributions in the 0.63 – 1.0 μm diameter range for this test case although the four overlapping bins (1.0 –1.3 μm) did appear to agree. The flatness of the volume distribution in this size range makes

it difficult to converge on a value of effective density. The scalloped behavior of χ^2 with ρ_e seen in Figure 4.4.4 demonstrates the lack of stability well. A value of ρ_e = 1.6 g cm^{-3} was retrieved for the "fixed" case compared to ρ_e = 1.35 g cm^{-3} for this test case. This difference in density is a very good example of why more structure in the size distribution was helpful in retrieving effective densities with this alignment method. Improved APS counting efficiencies at smaller diameters would therefore improve the retrieval, even over the "fixed" case used here.

5.6 SENSITIVITY TO COMPLEX REFRACTIVE INDEX

The calibration performed for the OPC included chemical species that were nonabsorbing at the wavelength of the instrument (632.8 nm). The scaling method derived in Chapter 3.4 was developed for real refractive indices only. If absorbing particles were sampled, the complex refractive index was not retrievable by this method as there was insufficient information to constrain both the real and imaginary parts of refractive index. A sensitivity study designed to test the effect of an absorbing particle on the alignment method and on retrieval of refractive index will be discussed now.

The geometry of the optics of an OPC is designed for a near monotonic relationship between the scattering response and particle diameter. The theoretical response (R) of the OPC was estimated by assuming a passive cavity with scattered light collected from 0-180 degrees (*Pinnick and Auvermann*, 1979) (Equation 5.6.1)

$$R = \frac{\pi}{k^2}\int_{\Omega}\left[\left|S_1(\theta)\right|^2 + \left|S_2(\theta)\right|^2\right]\sin\theta d\theta \qquad (5.6.1)$$

where $S_1(x,m,\theta)$ and $S_2(x,m,\theta)$ are the Mie scattering amplitude functions corresponding to perpendicular and parallel polarization. They depend on the size parameter $x=k_w r$

where k_w is the wave number and r is radius. Refractive index is designated m and θ is the scattering angle. The angular integration is performed over the solid angle Ω. Calculations of the response function were performed for calibration real-only refractive indices (m_r = 1.46, 1.53 and 1.588) as well as two complex values of refractive index (denoted as $m = m_r - ki$, where k is the imaginary component). Black carbon was used to demonstrate the response to a strongly absorbing particle ($m = 1.96 - 0.66i$) and a less absorbing particle was also assumed ($m = 1.58 - 0.1i$). Figure 5.6.1 demonstrates how an absorbing particle might be sized in the OPC. A line corresponding to a theoretical instrument response of $R = 1.0\times10^{-9}$ cm^2 particle^{-1} was drawn on the figure and intersects all of the curves plotted on Figure 5.6.1 at different diameters, demonstrating how different size particles with different refractive index could be sized similarly.

Further investigation of the response curves in Figure 5.6.1 is important for understanding how a particle with a complex refractive index is sized with an OPC. The real-only refractive index (m_r) curves in Figure 5.6.1 line up next to each other, with curves corresponding to lower refractive indices positioned at larger diameters. These curves do not intersect until approximately 1 μm. For a given R (for example, see Figure 5.6.1), this behavior results in increased size with decreased refractive index. In contrast, response curves for complex refractive indices are flatter and intersect the other curves at much smaller sizes, with flatter curves corresponding to a more absorbing particle. For example, the curve corresponding to black carbon ($m = 1.96 - 0.66i$) in Figure 5.6.1 intersects the other curves near 0.32 μm and is flatter than the curve corresponding to $m = 1.58 - 0.1i$. The effects on sizing are understood by noting the position of the flatter curve with respect to curves for real-only refractive indices. For a given response R, an

absorbing particle of a specific geometric size can either be undersized or oversized compared to a nonabsorbing particle, depending on the diameter where the curves intersect. *Covert et al.* (1990) observed this behavior with OPC measurements of laboratory-generated aerosols and atmospheric aerosols.

In the context of the alignment method, the DMA distribution defined the geometric diameter and the alignment method chose the response curve corresponding to a real refractive index at that geometric diameter. If curves for absorbing and nonabsorbing species intersected at the geometric diameter, the alignment method was unable to distinguish between them. As an example, two vertical lines are drawn on Figure 5.6.1, intersecting the line corresponding to $R = 1.0\times10^{-9}$ cm^2 particle^{-1} at the diameters where nonabsorbing and absorbing curves coincide. For a particle diameter of 0.32 μm, the black carbon curved intersects with the curve corresponding to PSL (m_r = 1.588). The alignment method would choose m_r = 1.588 as the retrieved refractive index, compared to a real part of refractive index m_r = 1.96 for the absorbing particle. Absorbing particles for this case would be oversized because a smaller real refractive index would be retrieved (recall a smaller real refractive index corresponds to a larger size). The opposite would be true for sizes when the absorbing curve bends lower than the nonabsorbing curves.

It would be impossible to distinguish between all combinations of real and complex refractive index with this alignment method without more information such as measured forward and backward scattering. However, this sensitivity study can be used to estimate the uncertainty resulting from the effects of complex refractive index. As will be demonstrated in Chapter 6, elemental carbon was a small fraction (~3 %) of the total

fine mass and the average fine imaginary component of refractive index was $k = 0.015 \pm 0.008i$; strongly absorbing particles were not expected. If an absorbing particle with a complex refractive index on the order of $m = 1.58 - 0.1i$ was sampled, a difference in the real parts of the refractive indices on the order of $\Delta m = 0.03$ was observed in the size region of interest (as demonstrated in Figure 5.6.1). This discrepancy corresponded to a percent difference on the order of 3% in refractive index, in the same range as the other studies described. This uncertainty was an upper limit because the imaginary component in the example was larger than observed during the study. The scaling procedure described in Chapter 3.4 was used to investigate the effect on derived OPC bin diameter for the case when $m = 1.58 - 0.1i$ was inverted with a nonabsorbing refractive index ($m_r = 1.53$). The magnitude of the difference in bin diameter varied because of the flatness of the complex refractive index response function, but typical percent differences of 10-20 % were observed.

5.7 DISCUSSION

The sensitivity studies discussed in this chapter point to the limitations of the alignment method. The most significant effects on retrieved refractive indices and effective densities were due to the choice of size range over which the data were reconciled. This range was limited by the instrument performance, e.g. the uncertainty in the diameter limits in the first and last channels and efficiency of the instrument performance in those channels. Specifically, the retrieved effective density was affected by the poor counting efficiencies of the APS at smaller sizes. An improvement in the

counting efficiency would provide more structure to the data reconciliation of the OPC-APS comparison, thereby improving the effective density retrieval.

Volume distributions were used in the alignment method because they were most sensitive to the presence of coarse particles from the APS measurement. This alignment method could be attempted with surface area distributions to optimize the position of the size distribution, however Figure 5.7.1 suggests that the sensitivity to the presence of coarse particles does not increase in the surface area distribution, and would not markedly improve the sensitivity in the APS-OPC overlap region.

The effects of absorbing aerosol may become significant in locations with strongly absorbing aerosols. This method currently is not able to distinguish between absorbing and nonabsorbing aerosols with out further information. *Covert et al.* (1990) showed that this issue arises with the use of an OPC regardless of its involvement in this method.

An important question is how do these uncertainties in retrieved refractive index and effective densities propagate to quantities derived from these measurements? For example, volume concentrations were computed for the "fixed" case and for the cases when the DMA-OPC and OPC-APS overlap regions were adjusted. A 2 % difference in accumulation mode volume concentrations between the "fixed" and DMA-OPC overlap case was observed. The APS-OPC overlap region had no effect on the derived accumulation mode, as expected. The percent difference in coarse mode volume concentration between the "fixed" case and the DMA-OPC overlap case was 13 ± 12% and the difference with the APS-OPC overlap case was 18 ± 14 %. The percent difference in total volume between the "fixed" case and the DMA-OPC overlap case was

7 ± 7% and the difference with the APS-OPC case was 11 ± 8 %. These differences were on the order of the derived experimental uncertainties (see Chapter 6). Percent differences in accumulation mode volume mean diameters between the "fixed" case and the DMA-OPC overlap case were less than 2 %. The differences in coarse mode volume mean diameters between the "fixed" case and the two overlap cases were both less than 10 %, on the order of the experimental uncertainties. The effect of these sensitivities on derived optical properties (see Chapter 7) was not significant. The percent difference in total light scattering coefficient was less than 2 % between the DMA-OPC and APS-OPC overlap cases and the "fixed" case. For light scattering coefficients derived for the accumulation mode only, the percent difference between the "fixed" case and the DMA-OPC case was 3 ± 2 %. The percent difference in light scattering coefficients due to the coarse particle mode for both cases was on the order of 10 %, reflecting the increased sensitivity in coarse parameters as already demonstrated. Overall it appeared that these sensitivities were not significant in terms of derived quantities.

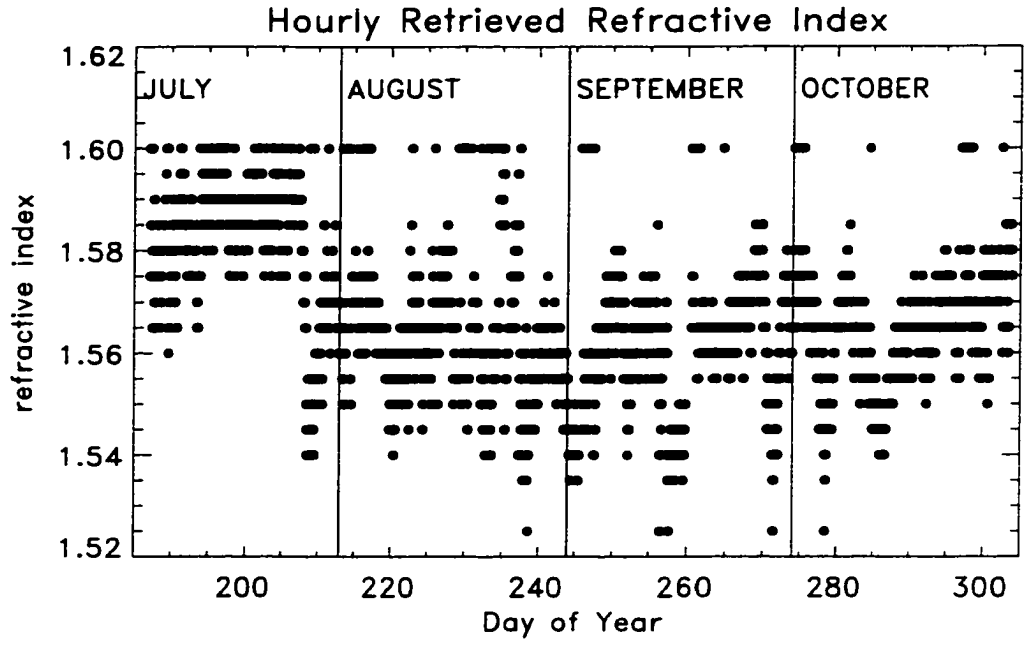

Figure 5.1.1 Retrieved hourly refractive index for the "fixed" case.

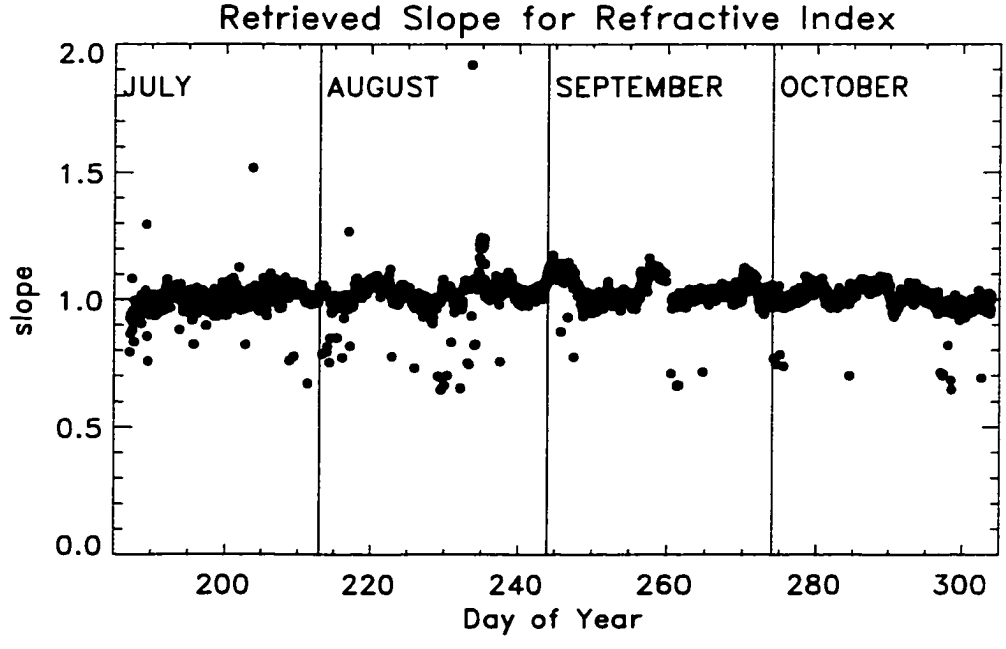

Figure 5.1.2 Slopes corresponding to retrieved refractive indices for the "fixed" case.

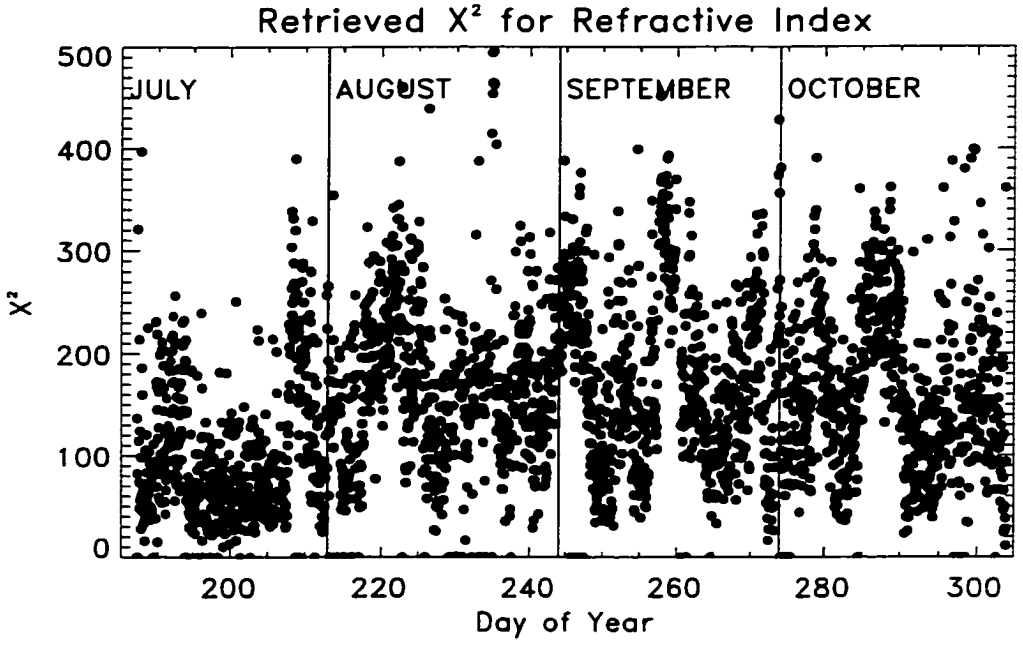

Figure 5.1.3 χ^2 corresponding to retrieved refractive indices for the "fixed" case.

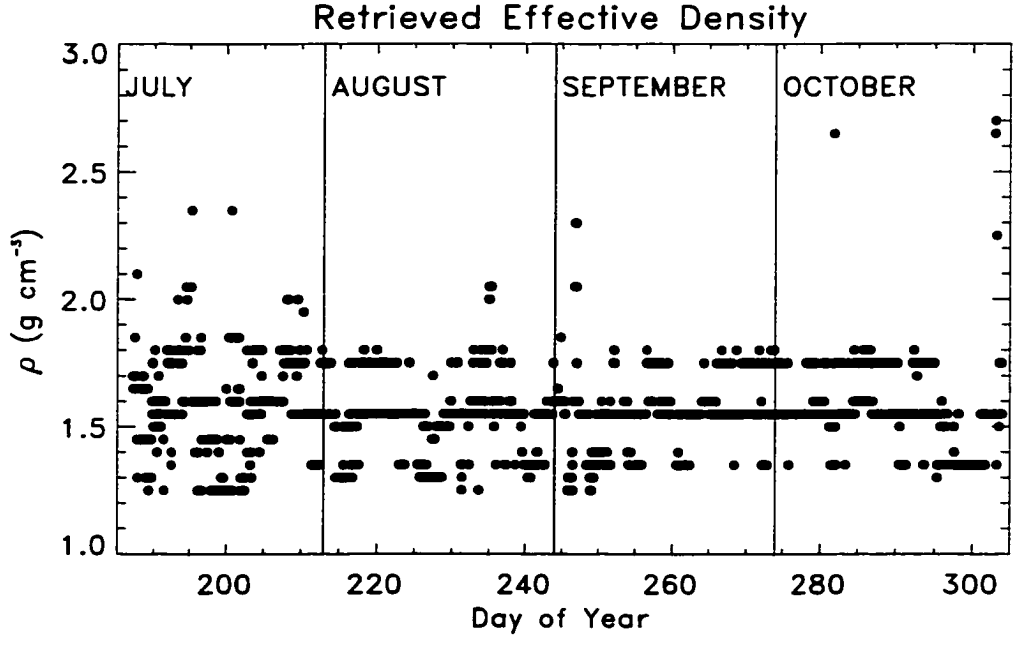

Figure 5.1.4 Retrieved hourly effective density for the "fixed" case.

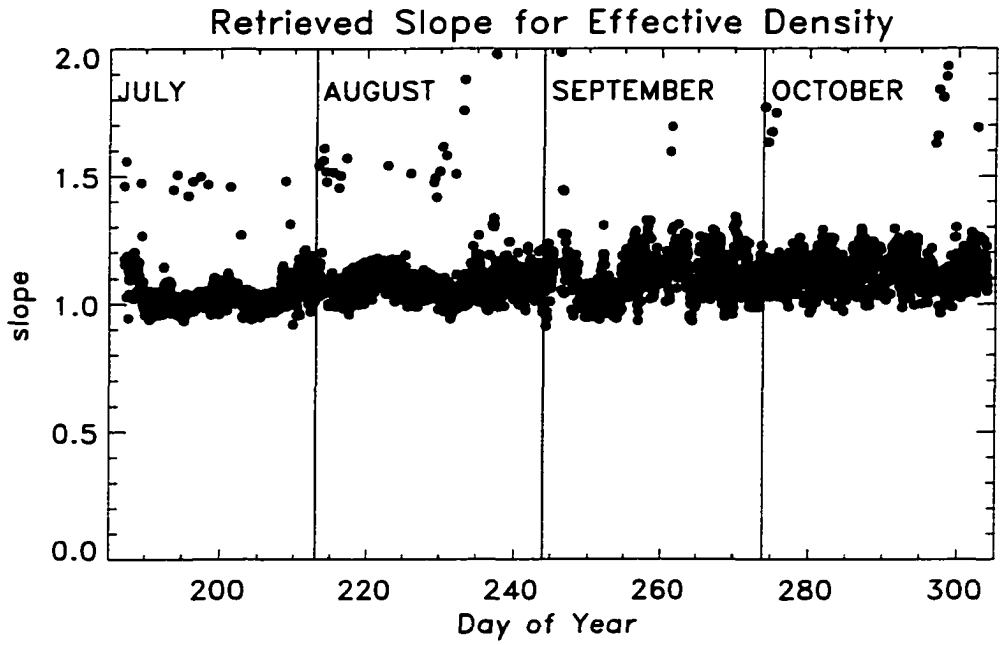

Figure 5.1.5 Slopes corresponding to retrieved effective densities for the "fixed" case.

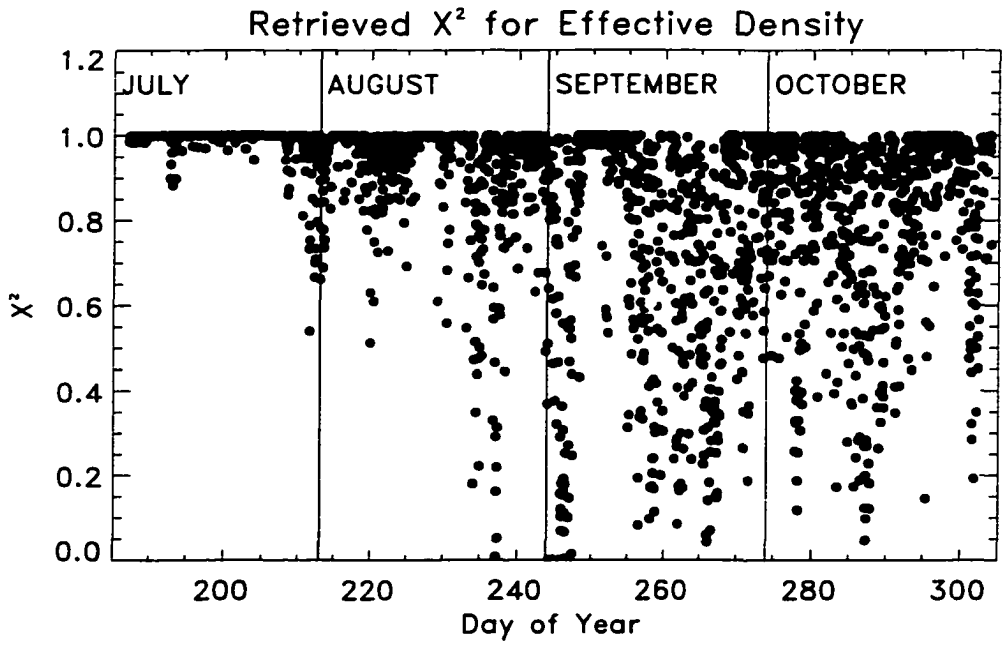

Figure 5.1.6 χ^2 corresponding to retrieved effective densities for the "fixed" case.

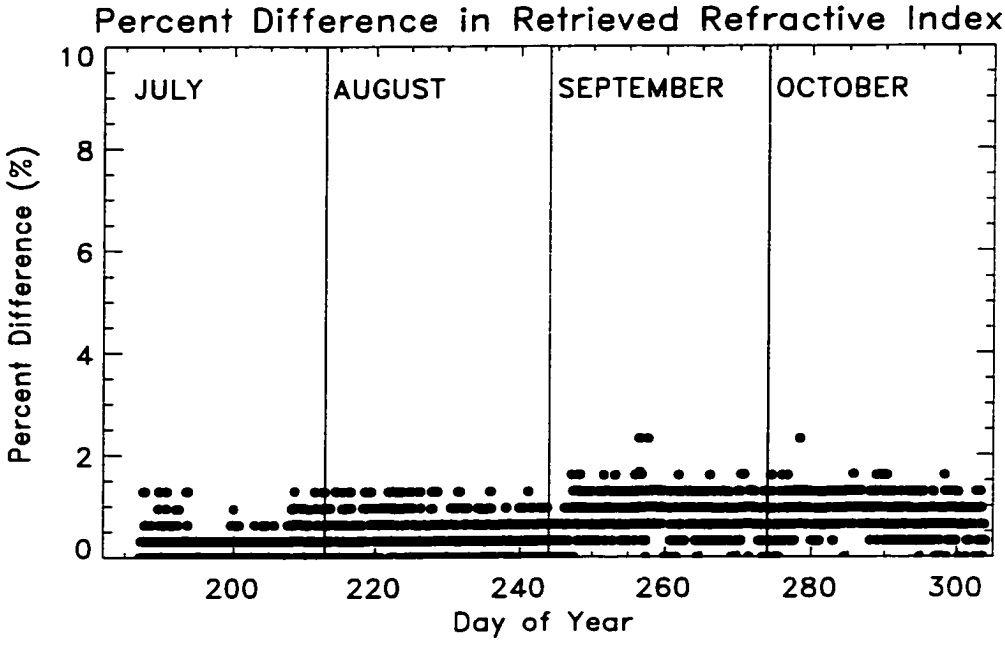

Figure 5.2.1 Percent difference in refractive index between the "fixed" case and the perfect kernel case.

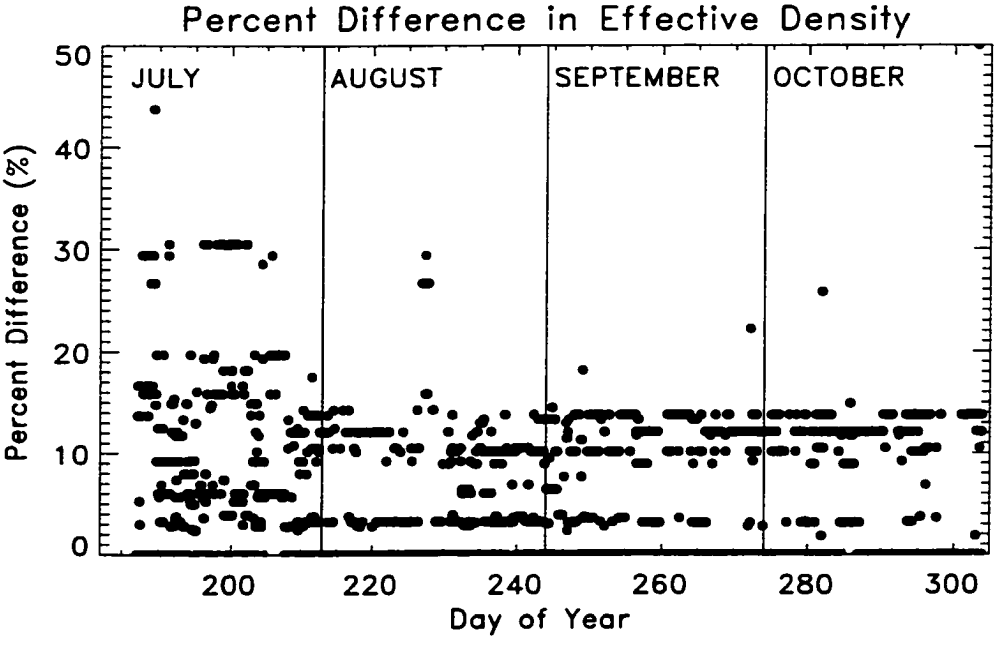

Figure 5.2.2 Percent difference in effective density between the "fixed" case and the perfect kernel case.

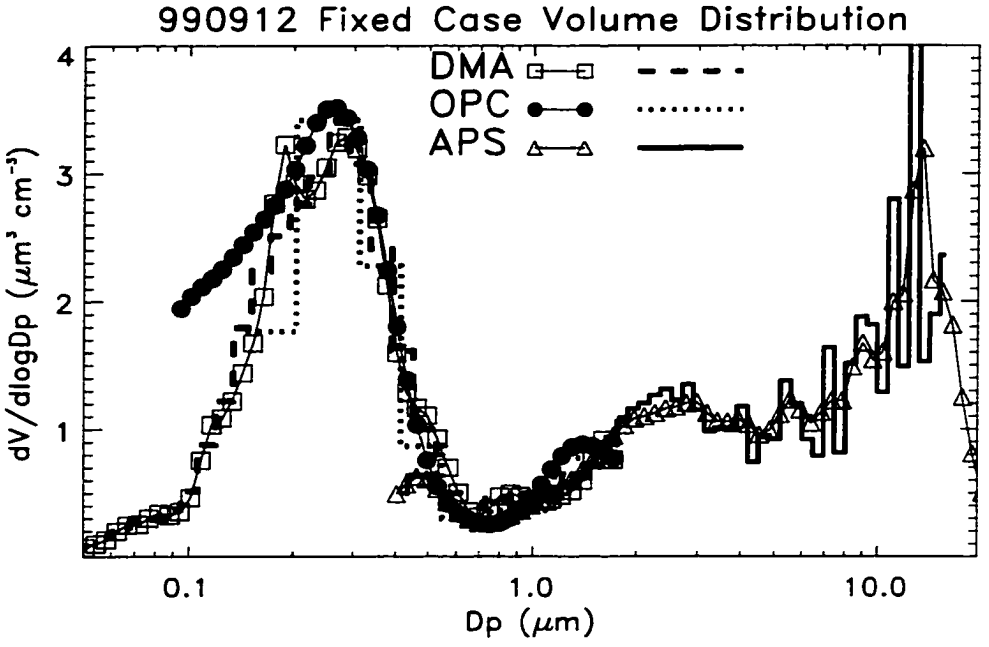

Figure 5.2.3 Aligned volume distributions for the "fixed" case on September 12 1999. Symbols with lines correspond to the smoothed Twomey distributions and the histograms show the original data.

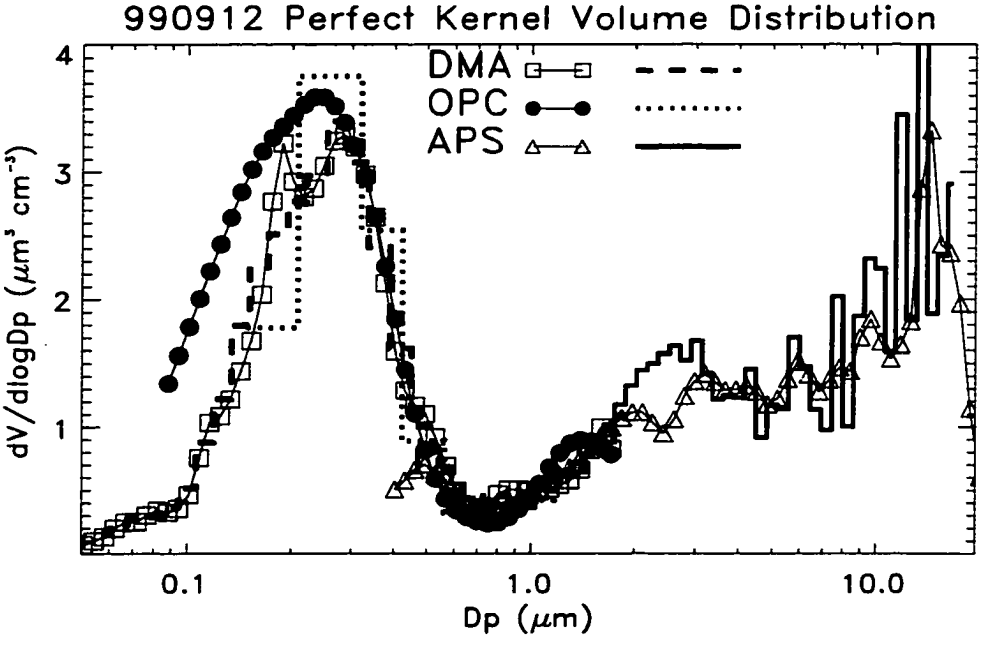

Figure 5.2.4 Aligned volume distributions for the perfect kernel case on September 12 1999. Symbols with lines correspond to the smoothed Twomey distributions and the histograms show the original data.

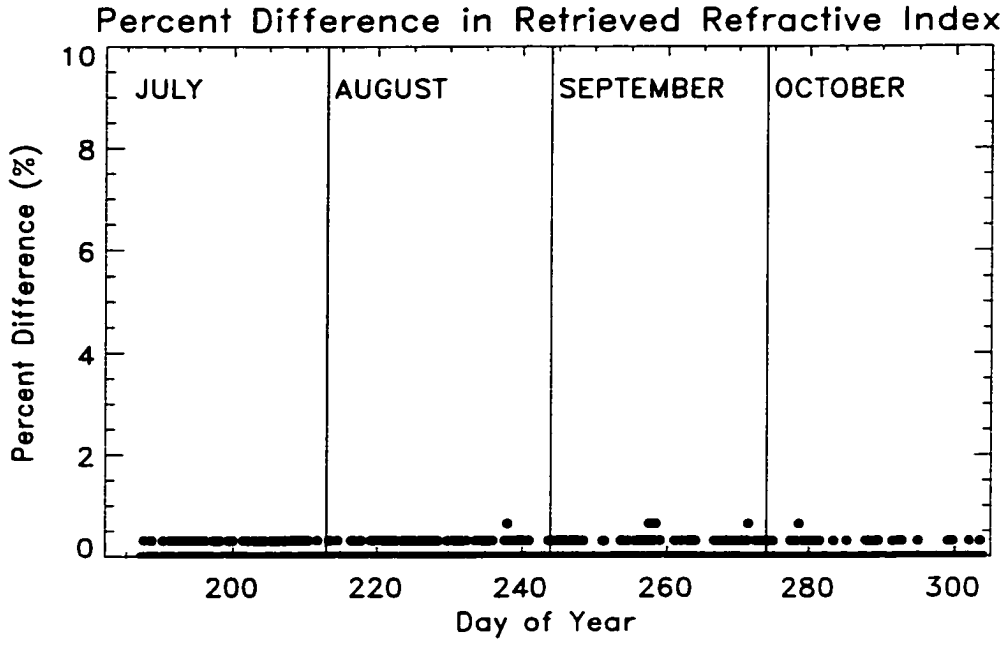

Figure 5.3.1 Percent difference in refractive index between the "fixed" case and the Twomey weight parameter case.

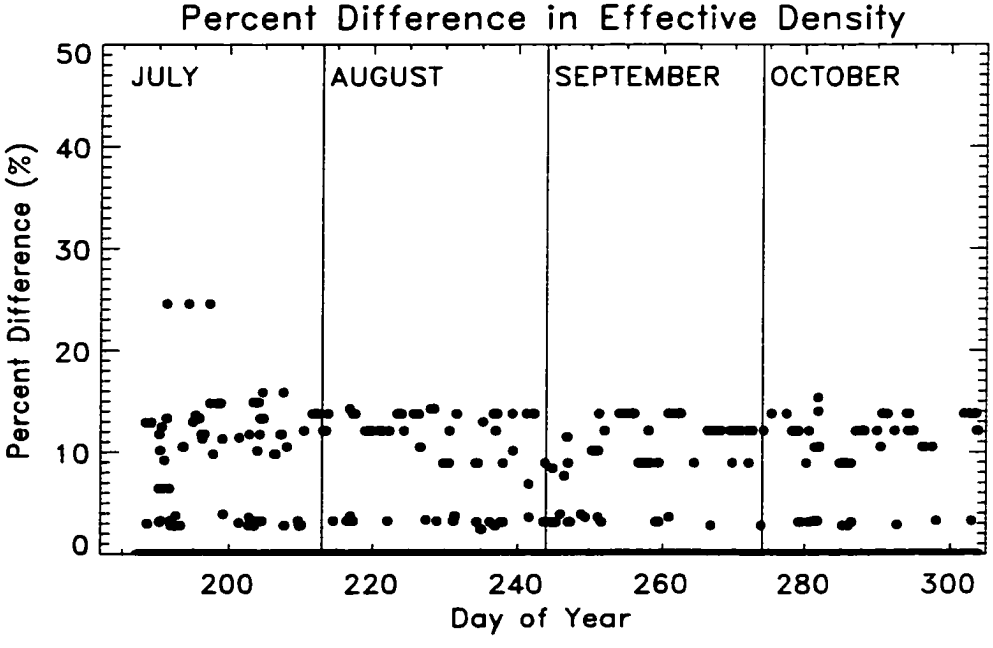

Figure 5.3.2. Percent difference in effective density between the "fixed" case and the Twomey weight parameter case.

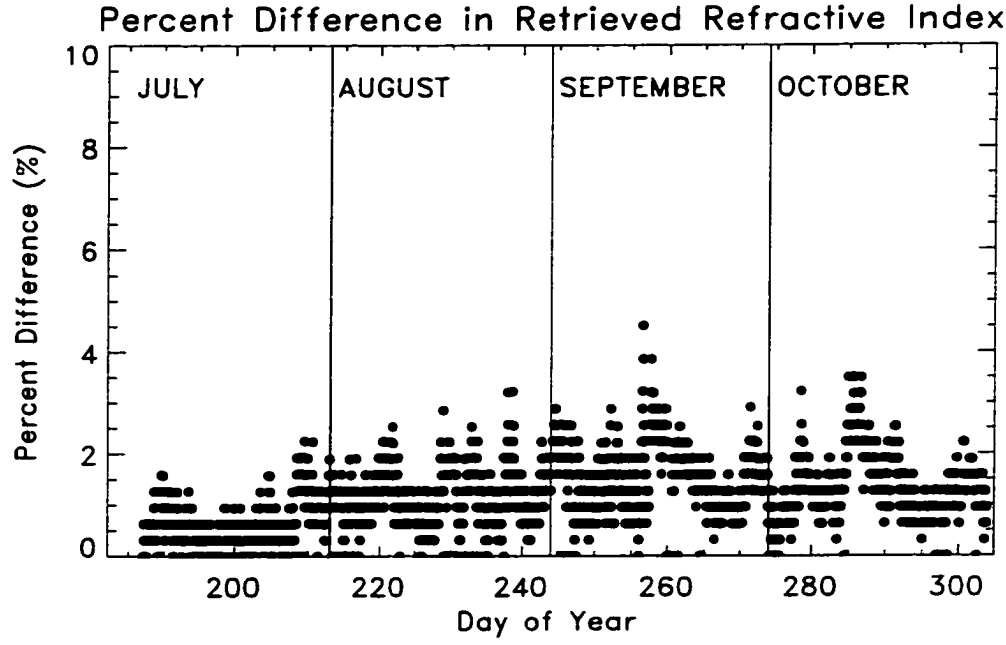

Figure 5.4.1 Percent difference in refractive index between the "fixed" case and the wider DMA-OPC overlap case.

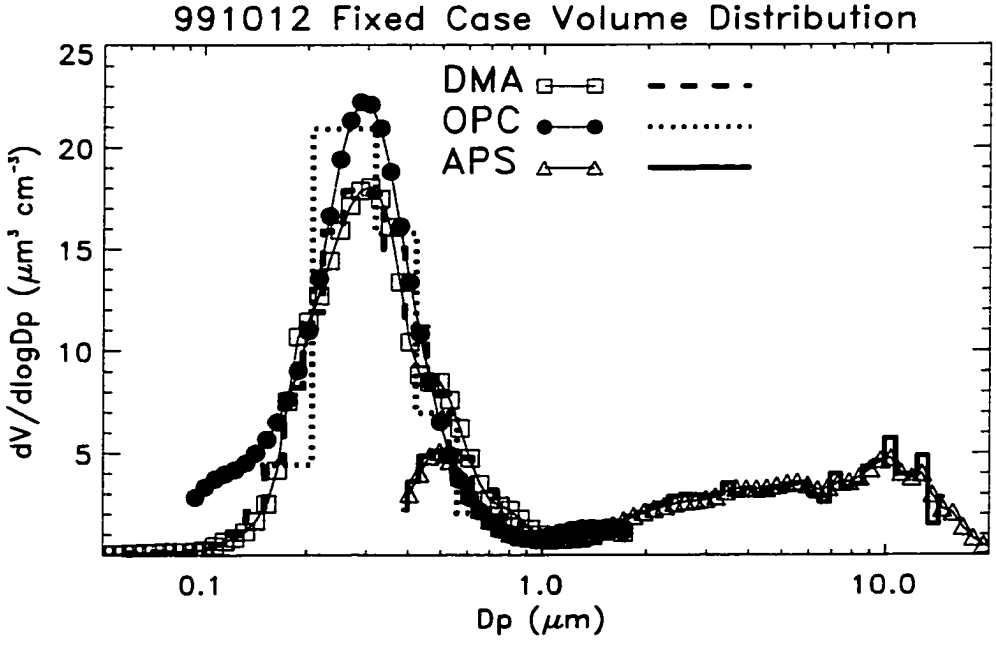

Figure 5.4.2 Aligned volume distributions for the "fixed" case from one hour on October 12 1999 (DOY 285). The lines with symbols correspond to the smoothed Twomey distributions and the original data are given as histograms.

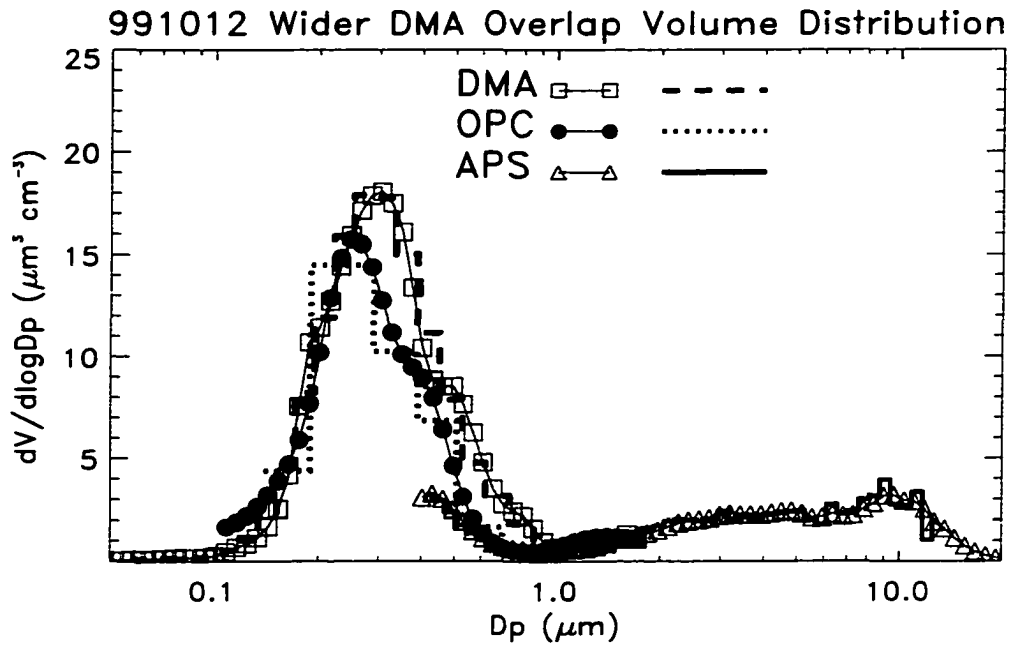

Figure 5.4.3 Aligned volume distributions for the wider DMA-OCP overlap case from one hour on October 12 1999(DOY 285). Symbols with lines correspond to smoothed Twomey distributions and the original data are shown as histograms.

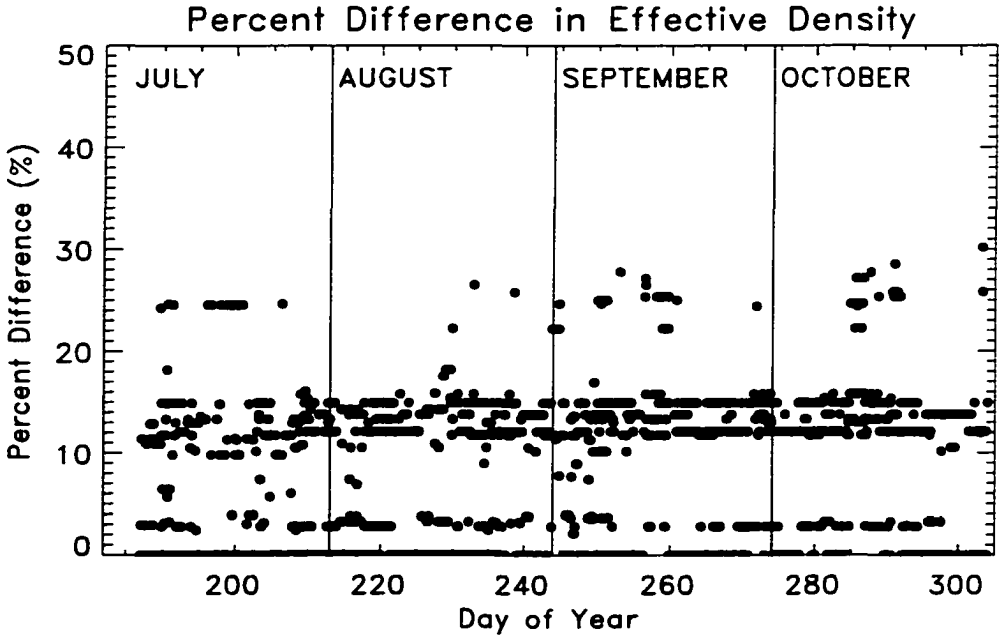

Figure 5.4.4 Percent difference in effective density between the "fixed" case and the wider DMA-OPC overlap case.

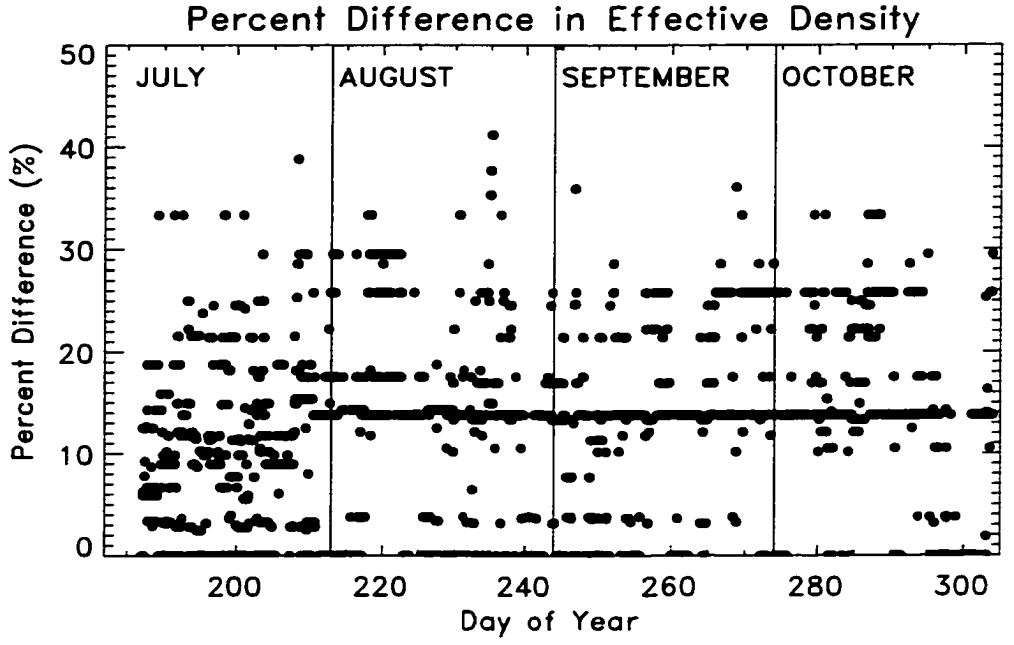

Figure 5.5.1 Percent difference in effective density between the "fixed" case and the narrower APS-OPC overlap case.

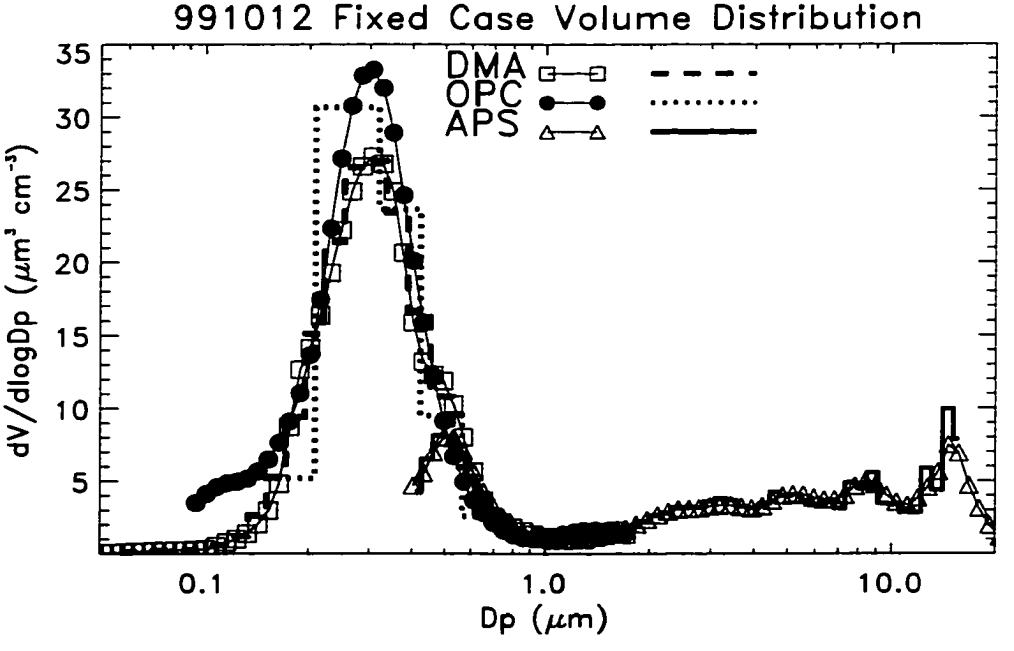

Figure 5.5.2 Aligned volume distributions for the "fixed" case for one hour on October 12 1999 (DOY 285). Symbols with lines are the smoothed Twomey distributions and the original data are shown as histograms.

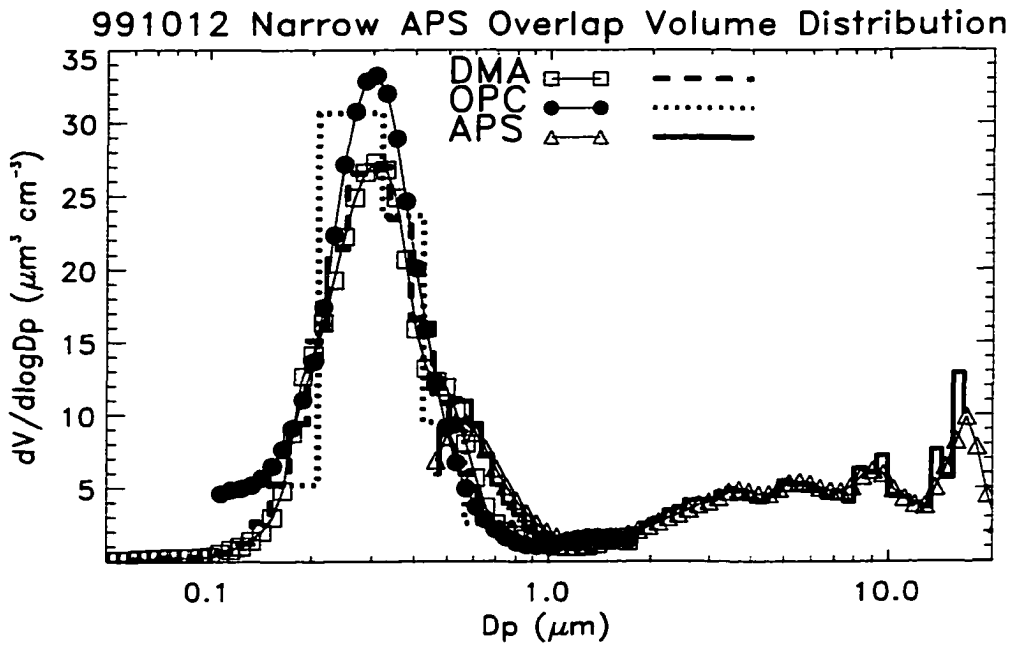

Figure 5.5.3 Aligned volume distributions for the narrow APS-OPC overlap case for one hour on October 12 1999 (DOY 285). Symbols with lines are the smoothed Twomey distributions and original data are shown as histograms.

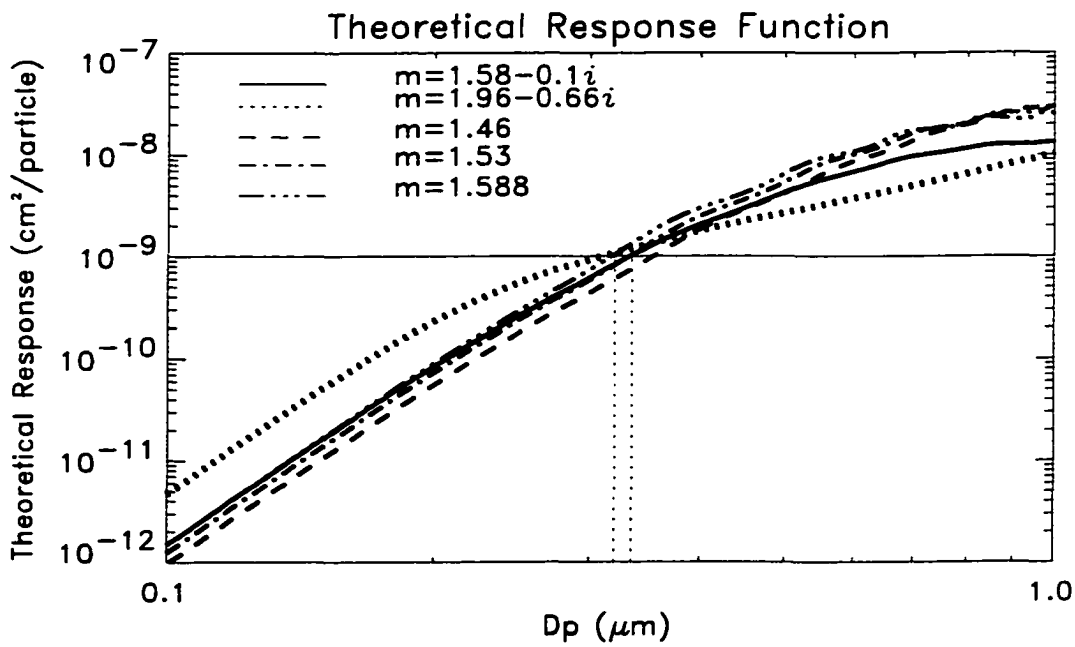

Figure 5.6.1 Theoretical response function for calibration species and two absorbing species.

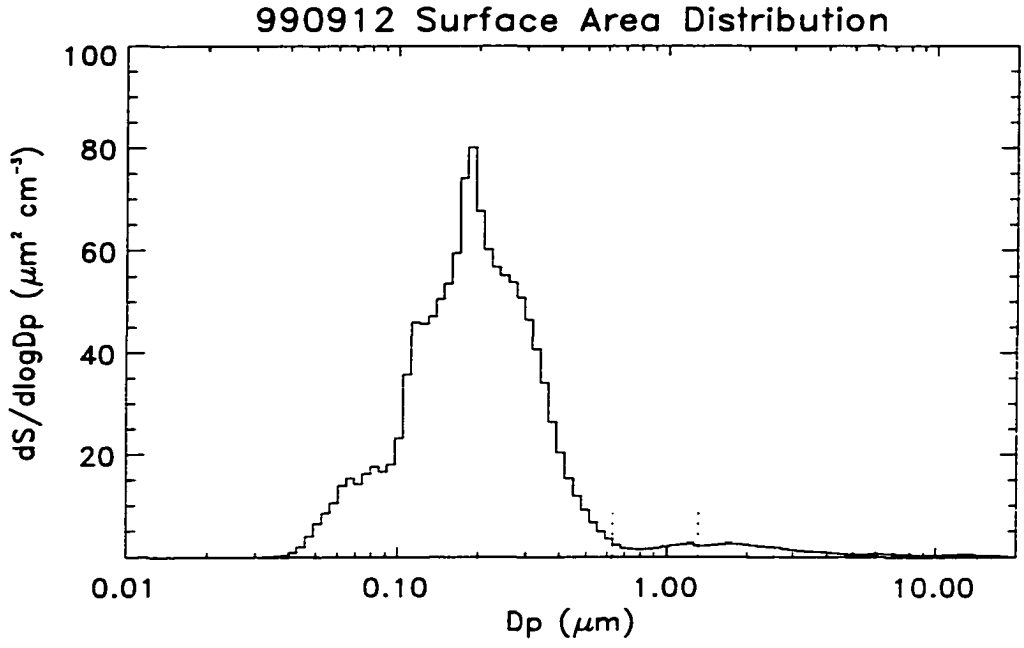

Figure 5.7.1 Surface area distribution for September 12 1999 (DOY 255). The overlap region of the APS and OPC is noted with dashed lines.

CHAPTER 6. AEROSOL PHYSICAL AND CHEMICAL PROPERTIES

One purpose of this chapter is to present a composite of the physical and chemical aerosol properties measured during the BRAVO study and to relate these properties to observed meteorology. The other purpose is to demonstrate the consistencies between the derived physical and chemical properties and to validate the new inversion method presented in Chapter 4. Chapters 7 and 8 focus on observed aerosol optical properties; investigating aerosol physical and chemical properties is important for placing the visibility observations in perspective.

Results derived from the size distribution measurements are presented in Section 6.1. Size parameters were calculated for the accumulation and coarse modes, and aerosol properties were observed to vary with meteorological periods. Periods with enhanced coarse mode volume concentrations and periods with dominant accumulation mode volume concentrations were observed and corresponded to different transport patterns. Uncertainties were calculated for each parameter, but error bars were not included on timelines for easier viewing. A full description of uncertainty calculations is provided in Appendix B.

Results of chemical analyses by Colorado State University (CSU) and University of California, Davis (UCD) will be presented in Section 6.2. On average the fine aerosol was acidic with sulfate and ammonium as dominant species. Episodes did exist when soil

and organic carbon were major contributors to fine mass concentrations. Coarse chemical speciation suggested soil and organic carbon were the major contributors to coarse mass. Discussions of chemical composition size distributions obtained with a MOUDI impactor will be presented in the context of major fine and coarse species distributions.

Computations of refractive index and density from chemical compositions will be compared to retrieved values in Section 6.3. These comparisons demonstrated excellent agreement in refractive index, with trends and magnitudes agreeing within experimental uncertainties. Comparisons of density were more difficult to perform as they required estimates of dynamic shape factor.

Comparisons between mass concentrations derived from size distribution measurements and chemistry data will be presented in Section 6.4. Reconstructed PM_{10} mass concentrations from UCD and computed total mass concentrations from integrated total volume and retrieved densities compared within experimental uncertainties. MOUDI mass distributions and mass distributions computed from volume size distributions agreed in the position of the modes. Although the MOUDI distributions represented major ions only, the comparisons suggested that the alignment method produced realistic estimates of aerosol size distributions.

Meteorological Conditions during BRAVO

Before discussing the physical and chemical properties measured during BRAVO, a brief background of the observed meteorological periods is provided. NOAA Hysplit back-trajectories were obtained daily and demonstrated that the transport patterns during BRAVO were similar to the historical record (*Sherman et al.*, 2000, *Gebhart et al.*, 2000)

with the dominant transport pathway from the southeast during summer and shifting toward the east-southeast during early autumn. Flow from the southeast could have arrived either from Mexico only or along the border of Mexico and Texas after having passed over east Texas, complicating the relationships between source regions and particle properties. Several patterns did emerge, however (*Sherman, et al.*, 2000).

In July and early August, the flow arriving at the park was dominated by transport from Mexico only, from the direction of the Gulf of Mexico. Several of these days were associated with high fine soil compositions and coarse mode volume concentrations and were suspected to be Saharan Dust episodes (Day of Year, DOY 182-184, 186-187, 190, 194-196, 200-201, 203-206, 223 and 227). Summertime transport of dust from North Africa westward across the Atlantic Ocean is a well-known phenomenon *(Perry et al.*, 1997) and Saharan dust has been observed at Big Bend in July in the historical record (*Gebhart et al.*, 2000; *Perry et al.*, 1997). TOMS imagery suggested that such transport occurred during the BRAVO study, and synoptic maps also confirmed that several of these transport patterns occurred during the early part of the study (*Sherman et al.*, 2000). Beginning in September, flow originating from eastern Texas and the eastern United States was observed. Some days were associated with flow from the southwestern U. S. and the California Baja (DOY 255, 261-263, 266, 268-269, 283 and 291). Mid October was associated with flow primarily from eastern Texas (DOY 282, 284-289) after which flow from north Texas was dominant (DOY 290, 293-295). These different meteorological periods corresponded to trends seen in the aerosol physical, chemical and optical properties, as will be demonstrated in the following sections.

To understand the relationships between aerosol composition and transport patterns, back-trajectories for the 10 days with highest and lowest mass concentrations of CSU $PM_{2.5}$ SO_4^{-2}, NO_3^-, Na^+ and NH_4^+ were investigated (*Sherman et al.*, 2000). Highest sulfate days corresponded to flow from industrial regions and the "lignite" belt in eastern Texas and along the Mexico border near the location of the Carbon I/II power plants. Lowest sulfate concentrations were associated with flow from Mexico only. High and low nitrate concentrations were strongly differentiated, with low concentrations associated with flow from the north. High nitrate concentrations corresponded to days with flow from the southern and southeastern Gulf region, suggesting association of NO_3^- with sea salt or dust particles. High sodium concentrations were observed for similar transport patterns associated with high nitrate concentrations, suggesting flow from the Gulf of Mexico and the presence of sea salt particles. Low sodium was associated with transport primarily from the north and west and occasionally from the east.

6.1 AEROSOL SIZE DISTRIBUTION STATISTICS

The procedure described by *Knutson and Lioy* (1989) was used to calculate size statistics for the size distributions described in Chapter 4. Statistics were calculated for hourly averaged volume distributions because volume was more sensitive to the presence of coarse particles. Statistics were determined for accumulation and coarse modes, where modes were defined by the minimum in the volume distribution between the modes. A giant mode was often observed earlier in the study; in those cases the coarse mode was further defined by the minimum that occurred between the coarse and giant modes. The

total integrated volume is the sum of the accumulation, coarse and giant mode volume concentrations.

The geometric mean diameter (D_{gv}) was calculated for each mode using Equation 6.1.1:

$$D_{gv} = anti\log\left[\frac{\sum_{D_{p,min}}^{D_{p,max}} \log_{10} D_{p,m} \frac{dV}{d\log D_p} d\log D_p}{V_{mode}}\right] \quad (6.1.1)$$

where $D_{p,min}$ and $D_{p,max}$ mark the lower and upper diameter limits of the mode and $D_{p,m}$ is the midpoint diameter of the channel. The integrated volume in the mode of interest is given by V_{mode} and was summed over all channels from $D_{p,min}$ to $D_{p,max}$. The accumulation mode $D_{p,min}$ remained unchanged at 0.03 μm, but the diameter limits for the other modes varied throughout the study. The $D_{p,min}$ between the accumulation and coarse modes varied between 0.5 and 1.0 μm and the $D_{p,min}$ between the coarse and giant modes varied from 5 to 10 μm. The geometric standard deviation (σ_g) was calculated with Equation 6.1.2.

$$\sigma_g = anti\log\left[\left[\frac{\sum_{D_{p,min}}^{D_{p,max}} (\log_{10} D_{p,m})^2 \frac{dV}{d\log D_p} d\log D_p}{V_{mode}} - \left[\log D_{gv}\right]^2\right]^{1/2}\right] \quad (6.1.2)$$

Figure 6.1.1 presents hourly averaged integrated dry particle number concentrations from $0.03 < D_p < 21$ μm. Hourly averaged ambient total number concentrations measured with a TSI 3010 Condensation Particle Counter (CPC) ($D_p > 15$ nm) were plotted for comparison to demonstrate the presence of particles in the size range of $15 < D_p < 30$ nm. Experimental uncertainty in integrated total number

concentrations was on the order of 1 %. Although difficult to discern in Figure 6.1.1, diurnal patterns in the 3010 total number concentrations were sometimes observed with peaks occurring near midnight, suggesting possible mixing and entrainment of free tropospheric aerosols or new particle production; the data are not yet available to investigate this further. The total number concentration was dominated by accumulation mode particles, with highest values observed in October and smallest average values observed in July, as summarized in Table 6.1.1. The overall average and standard deviation of dry total integrated total number concentration ($0.03 < D_p < 21$ μm) was 1000 ± 400 cm^{-3}.

Timelines of integrated volume concentrations from the accumulation and coarse particle modes are shown in Figure 6.1.2. Uncertainties in accumulation and coarse mode volume concentrations were on the order of 2 % and 10 %, respectively. Immediately noticeable was the dominance of coarse volume concentrations in July and early August. Many of these days were believed to be associated with Saharan Dust transport to the park. For the later part of the study, accumulation mode volume concentrations dominated coarse volume with the exception of occasional days in late September and October that were associated with flow from north Texas. Figure 6.1.3 presents the fractional contribution of accumulation and coarse mode volume to integrated total volume, where total volume included accumulation, coarse and giant modes. Giant volume modes were observable during the early part of the study and correspond to periods when the fractional contribution from accumulation and coarse modes do not sum to one. The periods with dominant coarse volume are obvious from this figure. Periods with dominant accumulation mode volume were associated with flow from east Texas

and along the border with Mexico. The overall average and standard deviation in accumulation mode volume concentration was 3 ± 2 μm^3 cm^{-3} with highest average values observed in August and September and lowest average values in July (see Table 6.1.1). The overall average and standard deviation in coarse mode volume concentration was 4 ± 4 μm^3 cm^{-3} with the highest values in July and early August and the lowest values in September (see Table 6.1.2).

Hourly averaged dry accumulation mode volume mean diameters are presented in Figure 6.1.4. Uncertainties were on the order of 2 %. Values of D_{gv} track well with accumulation mode volume concentrations with higher accumulation mode periods corresponding to larger mean diameters. Figure 6.1.5 shows a scatter plot of accumulation mode D_{gv} and volume concentrations. The average accumulation mode D_{gv} was 0.26 ± 0.04 μm with smallest average values observed in July and October and largest average values in August and September (see Table 6.1.1).

Coarse mode volume geometric mean diameters are shown in Figure 6.1.6 with uncertainties on the order of 20 %. Coarse mode D_{gv} increased during the study period with an overall average of 3.4 ± 0.8 μm (see Table 6.1.2). In July and August small diameters were observed during suspected Saharan Dust episodes when coarse mode volume was the major contributor to total integrated volume (e.g. DOY 205, 215, 227) and enhanced fine soil mass compositions were observed (see Section 6.2). Figure 6.1.7 shows a scatter plot of coarse mode D_{gv} and volume concentrations.

Accumulation mode geometric standard deviations are shown in Figure 6.1.8; uncertainties are on the order of 10 %. The overall average (see Table 6.1.1) was 1.58 ± 0.08 with largest average values observed in July and early August and smallest average

values observed in September. Periods with the lowest σ_g corresponded to larger accumulation mode D_{gv} and volumes (see Figure 6.1.9). Coarse mode σ_g are shown in Figure 6.1.10 with uncertainties on the order of 10 %; the overall average was 1.82 ± 0.14. Larger average values were observed in October compared to July (see Table 6.1.2). Smaller average values were observed at the beginning of September when coarse volume concentrations were very stable and coarse mean diameters increased.

Figure 6.1.11 presents a contour plot of volume distributions for the entire study. The volume distributions are viewed from above with diameter on the abscissa and day of year on the ordinate. The previous discussions of size parameters are represented well in this figure. Immediately noticeable was the dominance of coarse and giant modes in early July and August (DOY 182-227), after which the giant mode essentially disappeared. The coarse mode shifted toward larger size and width as the study progressed, both evidenced in the size parameter results. Accumulation mode volume peaked in September and October and the mean D_{gv} increased from July to September and decreased toward October. The minimum in the volume distribution between the accumulation and coarse modes shifted during the study but typically was less than 1 μm. An apparent periodicity in time was observed with accumulation mode volume, however the cause has yet to be determined, such as reasons for shifts in observed meteorology.

6.2 AEROSOL COMPOSITION

Aerosol composition was measured by collecting 24-hour integrated filter samples. Data from CSU and UCD were used in this work. CSU sampled with a $PM_{2.5}$ inlet and analyzed for major ions with analytical equipment located on site. UCD

operated standard IMPROVE samplers (see *Malm et al.*, 1994) with both $PM_{2.5}$ and PM_{10} inlets. UCD filters from the $PM_{2.5}$ and PM_{10} samplers were analyzed post study for major ions as well as organic carbon (OC), elemental carbon (EC) and soil elements. CSU performed size resolved sampling using a MOUDI impactor on a daily basis, however, analyses were performed for major ions on a subset of impaction substrates representing about 40 days. These UCD and CSU samplers were located at the Kbar Ranch site next to the other aerosol instrumentation, except for a period in July (DOY 182 – 203) when the UCD $PM_{2.5}$ sampler was located approximately 2 miles away. It should be noted that the definitions of fine and coarse modes differ between the size and chemistry data; the modes were determined based on the true minimum between the distributions with the size data. The chemistry data were obtained with the same size cut regardless of the aerosol distribution, and this size cut was based on aerodynamic diameter. This section focuses on the results from these measurements; for details about the measurements and analyses, see *Lee et al.* (2000) and *Malm et al.* (1994).

Comparisons between redundant measurements by CSU and UCD demonstrated some discrepancies. Adjustments were made to the UCD data based on the CSU data because the CSU data were analyzed on site and believed to have fewer artifacts due to storage (*Collett*, personal communication). Differences between CSU and UCD 24-hr $PM_{2.5}$ sulfate were observed and because CSU sulfate was corroborated by other sulfate measurements (*Malm*, personal communication), a scaling factor was derived based on the differences in sulfate. The factor was applied to the entire UCD $PM_{2.5}$ data because the discrepancies were believed to exist in all of the species, possibly due to sampling volume issues (*Malm, Ashbaugh*, personal communication). The final data set used in this

dissertation included CSU sulfate, ammonium, sodium and nitrate with UCD scaled OC, EC and soil components.

The fine aerosol were acidic with an ammonium to sulfate molar ratio average and standard deviation of 1.53 ± 0.3 (see Figure 6.2.1). MOUDI results suggested sulfate and ammonium existed primarily in the fine mode, whereas nitrate was measured primarily in the coarse mode (*Lee et al.*, 2000). Nitrate measured in $PM_{2.5}$ samples was believed to be the tail of the coarse nitrate mode and differences observed between UCD and CSU fine nitrate were believed to be due to different cyclone collection efficiencies in the two inlets. Because of the acidic nature of $PM_{2.5}$ aerosols, MOUDI evidence of sodium and nitrate associated together in coarse particles, and the patterns observed in the meteorology, nitrate was assumed to exist as $NaNO_3$.

Timelines of $PM_{2.5}$ composition are shown in Figure 6.2.2. Ammoniated sulfate mass concentrations were calculated by including sulfate, ammonium and hydrogen ion concentrations as a function of degree of neutrality. The assumed ammoniated sulfate species varied between $(NH_4)_2SO_4$, NH_4HSO_4, $(NH_4)_3H(SO_4)$ and H_2SO_4 depending on the value of molar ratio. Organic and elemental carbon concentrations were obtained from thermal optical reflectance (TOR) combustion (*Chow et al.*, 1993) where organic carbon was computed as the sum of low and high temperature carbon. Organic carbon was adjusted for carbon and hydrogen weights by multiplying by a mass correction factor of 1.4 (*Malm et al.*, 1994). Elemental carbon (also referred to as light absorbing carbon, LAC) was computed from the sum of low and high temperature elemental carbon from TOR. Soil composition was computed from Equation 6.2.1, the IMPROVE soil formula that includes mass conversion factors and UCD elemental mass concentrations.

Comparisons of local resuspended soils and ambient aerosols in the western United States confirmed these components (*Cahill et al.*, 1981; *Pitchford et al.*, 1981).

$$[Soil] = 2.20[Al] + 2.49[Si] + 1.63[Ca] + 2.42[Fe] + 1.94[Ti] \qquad (6.2.1)$$

Ammoniated sulfate was typically the dominant $PM_{2.5}$ species although periods with high soil mass fractions in July and early August were observed. These periods corresponded to high coarse volume concentrations (see Figure 6.1.2) observed in size distribution data and were associated with suspected Saharan dust events. The largest peaks in ammoniated sulfate occurred in September and October, consistent with high accumulation mode volume concentrations seen in Figure 6.1.2 and flow from east Texas. Figure 6.2.3 presents fine mass fractions showing ammoniated sulfate to be the dominant species, but episodes with significant OC and soil mass fractions occurred. Elemental carbon and $NaNO_3$ were minor contributors to $PM_{2.5}$ mass. The monthly averaged fine mass fractions are listed in Table 6.2.1. On average sulfate was 51 ± 18 % of fine mass, with organic carbon as 22 ± 9%, soil as 20 ± 16%, elemental carbon as 2.6 ± 1.5 % and sodium nitrate as 4 ± 3 %.

Fine soil composition is shown in Figure 6.2.4. The major species contributing to soil was SiO_2, consistent with other data in the southwest United States (*Pitchford et al.*, 1981). Al_2O_3 and Fe_2O_3 were the next highest contributors to soil composition. Computed mineral ratios (Figure 6.2.5) (Al/Ca and Si/Al) suggested different sources of soil during the study. Aluminum to calcium ratios greater than 3.8 have been suggested to be indicative of North African dust (*Perry et al.*, 1997). Higher Al/Ca ratios were observed in July and early August on days of suspected Saharan dust. *Sokolik and Toon* (1999) discussed ratios of Si/Al for different locations around the globe with higher values

corresponding to dust in Arizona (Si/Al = 4.02). *Perry et al.* (1997) observed Si/Al values close to 2 during Saharan dust events in the eastern United States. The magnitude of Si/Al started increasing about the time that Al/Ca decreased (DOY ~ 235), suggesting changing soil sources.

Coarse composition data are shown in Figure 6.2.6. These data begin on DOY 232 (August 20) and were obtained by differencing the PM_{10} and $PM_{2.5}$ data. Figure 6.2.7 presents coarse species mass fractions and demonstrates that on average OC and soil contributed more than sulfate to the coarse mode (see Table 6.2.2). Other species assumed were $NaNO_3$ (on the order of 7%) and elemental carbon (2%). Coarse soil compositions are shown in Figure 6.2.8. SiO_2 and Al_2O_3 were the major contributors to coarse soil, although TiO_2 was higher in the coarse mode than in the fine.

6.3 RETRIEVED REFRACTIVE INDEX AND EFFECTIVE DENSITY

The refractive indices and effective densities retrieved with the alignment method were presented in Chapter 5 in the context of sensitivity studies performed to test the method for varying assumptions. In this section comparisons will be made to estimates from other methods. Refractive index estimates computed using a volume weighted mixing method and measured chemical compositions agreed with retrieved values within experimental uncertainties. Comparisons of computed density to retrieved effective density relied on estimates of dynamic shape factor and therefore were inherently more difficult to perform.

Density was computed following *Hasan and Dzubay* (1983) using Equation 6.3.1:

$$\overline{\rho}^{-1} = \sum_i \frac{X_i}{\rho_i} \qquad (6.3.1)$$

where X_i is the mass fraction for species i and ρ_i is the individual species density (g cm^{-3}). Aerosol composition was assumed to be ammoniated sulfate, organic carbon, elemental carbon, sodium nitrate and soil components (see Section 6.2).

Refractive index can be computed by different mixing rules, two of which are partial molar refraction (*Stelson,* 1990) and volume weighted method (*Hasan and Dzubay,* 1983; *Ouimette and Flagan*, 1982). *Hand* (1997) showed these methods produced the same mean refractive index, therefore the volume weighted method was used (Equation 6.3.2) to calculate mean refractive index ($m = m_r - ki$).

$$\overline{m} = \overline{\rho}\sum_i \frac{X_i m_{r,i}}{\rho_i} - \overline{\rho}\sum_i \frac{X_i k_i}{\rho_i} i \qquad (6.3.2)$$

where $m_{r,i}$ is the real part of a complex refractive index for species i and k_i is the imaginary part. Table 6.3.1 provides dry species refractive indices and densities used in these calculations. Refractive indices of dry ammoniated sulfate were computed based on measured degrees of neutrality. Refractive indices and densities were known for certain degrees of neutralization but for compounds with molar ratios in between these known values a linear interpolation was performed. The fine and coarse average ammoniated sulfate refractive indices were $m_r = 1.52 \pm 0.02$ and $m_r = 1.48 \pm 0.05$, respectively. The only absorbing species included was elemental carbon. Dust was assumed to have negligible absorption based on the work of *Sokolik and Toon* (1999). They demonstrated that for soil components expected at Big Bend (both local and Saharan), the imaginary part of refractive index is on the order of $0.0001 < k < 0.001$ at $\lambda = 530$ nm. The major absorbing dust species (Fe_2O_3) ($k \sim 0.1 - 0.5$ at $\lambda = 530$ nm) was typically less than 10-15 % of the total soil component both in the fine and coarse modes.

Figure 6.3.1 presents timelines of daily averaged retrieved dry refractive indices and computed fine and coarse refractive indices. Retrieved refractive indices correspond to the DMA-OPC overlap range from 0.2 – 0.7 μm. Excellent agreement was observed between retrieved and fine m_r, within the experimental uncertainties of the retrieved values (2-3 %). Lower values estimated by both methods corresponded to aerosols dominated by sulfate (see Figure 6.2.4). Both methods produced higher estimates in July and early August, consistent with higher fine soil mass fractions associated with suspected Saharan dust episodes. The agreement between the two estimates was very encouraging considering the very different methods used. The average retrieved refractive index was $m_r = 1.566 \pm 0.012$ and the average computed fine refractive index was $m_r = 1.56 \pm 0.02$. The computed coarse refractive indices were higher than for the fine mode (average value of $m_r = 1.58 \pm 0.02$). The overall values were lower than expected for a coarse mode typically assumed to be dominated by wind blown soil. The presence of coarse organic carbon lowered the computed values by weighting the mean with a lower refractive index and offsetting the contributions from soil. Figure 6.3.2 presents estimates of the absorbing part of refractive index based on elemental carbon concentrations. Although elemental carbon had an overall average contribution on the order of 3 % in the fine and coarse modes, the average imaginary part of refractive index was $k = 0.015 \pm 0.008$ in the fine mode and $k = 0.013 \pm 0.012$ in the coarse mode. Refractive indices computed for soil only are shown in Figure 6.3.3 for the fine and coarse modes. Higher concentrations of SiO_2 ($m_r = 1.486$) in the coarse mode resulted in smaller computed coarse soil refractive indices than observed in the fine mode. The

average fine and coarse soil refractive indices were $m_r = 1.69 \pm 0.03$ and $m_r = 1.65 \pm 0.05$, respectively.

Density comparisons are shown in Figure 6.3.4. In order to compare retrieved effective density to densities computed from fine and coarse chemical components, a dynamic shape factor (χ) was required to convert effective density to a bulk density (recall Equation 2.1.4). Spheres have shape factors of 1 while more extreme shapes such as fibers or aggregates have much larger values, up to 2 or greater. *Willeke and Baron* (1993) list several shape factors for different types of particles, with dusts ranging from $\chi = 1.05 - 2$. Shape factors have been measured by settling irregularly shaped particles in liquids (*Willeke and Baron*, 1993) and recent work by *Kalashnilova and Sokolik* (2001) described obtaining shapes of dust using automated scanning electron microscopy and transmission electron microscopy on individual particle data. Estimating the effects of irregularly shaped particles on aerosol optical and physical properties is a very active area of research (e.g. *Kalashnilova and Sokolik*, 2001) and beyond the scope of this work. The value of χ assumed obviously dictated the magnitudes of densities obtained from the retrieval method. Using a constant value of $\chi = 1.2$ retrieved densities that agreed with computed values within experimental uncertainties. Estimates of χ were obtained by ratioing the computed fine density to the retrieved effective density and are shown in Figure 6.3.5. Recall that effective density was retrieved in the size range from $0.6 < D_p < 1.3$ μm, well within the $PM_{2.5}$ mass concentration size cut, therefore comparisons with computed fine density were appropriate. Larger values of χ were observed during periods associated with higher fine soil mass fractions (see DOY 198, 215, 227 and 300 in Figure 6.2.4), consistent with the possibility of irregularly shaped particles. Periods associated

with high sulfate mass fractions corresponded to lower derived shape factors, consistent with particles that may be less affected by the presence of dust. The overall value of χ determined from this method was 1.19 ± 0.14, consistent with the value assumed in Figure 6.3.4 and with values listed in *Willeke and Baron* (1993). The average value of computed fine density was 1.85 ± 0.14 g cm^{-3} and coarse density was 1.97 ± 0.15 g cm^{-3}. The average value of retrieved effective density was 1.56 ± 0.12 g cm^{-3}; applying χ = 1.2 resulted in an average retrieved density of 1.87 ± 0.13 g cm^{-3}.

Sensitivities of computed refractive indices and densities to assumed chemical components were investigated by performing calculations with varying realistic choices of different species. The "accepted" values for computed fine and coarse refractive index and density were based on ammoniated sulfate, organic carbon, elemental carbon, and the IMPROVE soil formula (see Section 6.2). All of the values computed with the sensitivity studies agreed with the retrieved values within experimental uncertainty, but the "accepted" values were believed to be the most representative of the measured aerosols. A different soil formula and the effects of including elemental carbon on the mean refractive index and density were investigated. A soil formula based on *Hand* (1997) was used that included MgO instead of TiO_2 and slightly different mass conversion factors. Overall the effect on refractive index was small (on the order of 0.5 %), however days with high soil mass fractions were more affected, with the adjusted soil formula producing smaller estimates of mean refractive index (see Figure 6.3.6). Sensitivity to absorbing species is also shown in Figure 6.3.6. The effect of an absorbing species was small (on the order of 0.6%), consistent with EC being a small percentage of fine mass. Both effects were well within the experimental uncertainty in retrieved refractive index (2

- 3 %). The effect of these different assumptions on computed density is shown in Figure 6.3.7. For density the assumed soil formula had the largest effect (on the order of 2 %) compared to the effect of absorbing species (0.25 %). The periods most affected were days corresponding to high soil mass fractions. These uncertainties were within the experimental uncertainty of retrieved densities (on the order of 20 %).

Similar trends were observed for sensitivity tests performed for coarse refractive index and density. Using a different soil formula resulted in a 0.6 % difference in coarse refractive index and a 4 % difference in coarse density. Removing elemental carbon from the calculation resulted in a 0.6 % difference in coarse refractive index and a 0.2 % difference in coarse density. These differences due to soil were more pronounced for days with higher soil mass fractions.

Total Mass Concentrations and MOUDI Distributions

Two final comparisons between chemical and physical measurements were performed. Total mass concentrations were calculated based on integrated accumulation and coarse mode volumes and retrieved densities. Derived shape factors shown in Figure 6.3.5 were used to convert effective density to bulk density, essentially reflecting the values of computed density from aerosol compositions. PM_{10} gravimetric mass and reconstructed PM_{10} mass concentrations based on assumed species are plotted on Figure 6.3.8 for comparison with the daily averaged retrieved total mass from size distribution estimates. Size distributions suggested no significant volume beyond $D_p \sim 10\mu m$ during the days compared, therefore the sizes over which the PM_{10} mass and computed mass were compared were reasonable. Excellent agreement was observed in both trends and

magnitudes between the three estimates. The agreement between the estimates suggested that the size distribution results were realistically representing the measured aerosol. Closure between reconstructed and gravimetric PM_{10} mass concentrations suggested that assumed species represented the mean aerosol composition.

MOUDI mass distributions of major ions were compared to the volume distributions shown in Figure 6.1.8 (see *Lee et al.*, 2000 for a full discussion of MOUDI measurements). Some of the issues involved in comparing these data sets were that volume distributions measured the total aerosol while MOUDI filters were analyzed for major ions only (SO_4^{-2}, NO_3-, Cl^-, NH_4^+, Ca^{+2}, K^+, Na^+, and Mg^{+2}). Organic carbon, elemental carbon and soil elements were not included in the MOUDI distributions. The MOUDI measurements were performed on aerodynamic diameters and volume distributions are presented on a true diameter basis. Comparisons required some estimate of effective density to convert true diameter to an aerodynamic diameter because the full chemistry speciation was not available for the MOUDI distributions. MOUDI measurements were obtained for 24-hour integrated samples while 15-minute volume distributions had to be averaged to 24-hours. The MOUDI sampled over 8 size stages so the Twomey inversion (see Chapter 4) was used to produce a smoothed, resolved MOUDI distribution for each ion that included the effects of collection kernels for each stage of the impactor.

Two days were chosen for example purposes: DOY 227 (August 15, 1999) was associated with high fine soil mass fractions and coarse volume concentrations and day 257 (September 14, 1999) was associated with a sulfate dominated accumulation mode aerosol. The purpose of this comparison was to test whether the two methods agreed in

the position of the aerosol modes. Differences were possible because the MOUDI was not analyzed for all the species that the volume distributions included. The average retrieved effective densities used to convert true diameter to aerodynamic diameter were 1.358 g cm^{-3} for DOY 227 and 1.694 g cm^{-3} for DOY 257. An average value of shape factor χ = 1.2 was to convert effective density to a bulk density and compute mass distributions from volume distributions. Figure 6.3.9a presents results for DOY 227 with the MOUDI distribution summed over all major ions. Fairly good agreement existed between the two methods with reasonable positions in the modes. The differences between the two methods were likely associated with soil or organic carbon given that the fine mass was dominated by soil and OC on DOY 227 and the MOUDI measurements do not include either. In contrast, Figure 6.3.9b shows the results for DOY 257 with a dominant accumulation mode sulfate distribution. The position and magnitude of the accumulation mode was well represented by both methods and the good agreement is striking given the completely different methods. Although only two examples were shown here, the agreement was typical for all the MOUDI distributions analyzed. This agreement suggested that the size distributions obtained with the new inversion method described in Chapter 4 were producing realistic distributions as well as retrieved effective densities.

The results presented in this chapter demonstrated the variability in aerosol properties observed during the study with enhanced fine soil in July and early August compared to a mostly sulfate dominated aerosol in September and October when flow was associated with east Texas. Size distribution data were consistent with these observations. Organic carbon was present in the fine mode, and was a major contributor to coarse mode mass. Because composition data in the coarse mode were not available in

July, temporal variations between coarse aerosol in July compared to September were not observable.

The good agreement between the variety of parameters derived from size distributions and those obtained from chemical measurements validated the alignment method developed in Chapter 4 as well as demonstrated the method's sensitivity to changing aerosol properties. Although the comparisons were made on a daily basis, the method demonstrated aerosol variations on much finer time scales. The next two chapters will present aerosol optical properties derived from these parameters and comparisons with other measurements.

Table 6.1.1 Average accumulation mode size parameters for each month during the study and overall. One standard deviation is provided.

Month	Number (cm^{-3})	Volume ($\mu m^3\ cm^{-3}$)	D_{gv} (μm)	σ_g
July	800 ± 300	2.1 ± 1.1	0.25 ± 0.03	1.59 ± 0.08
August	1000 ± 400	4 ± 2	0.28 ± 0.03	1.58 ± 0.08
September	900 ± 300	4 ± 3	0.28 ± 0.05	1.56 ± 0.07
October	1100 ± 400	3 ± 2	0.25 ± 0.04	1.58 ± 0.08
Overall	1000 ± 400	3 ± 2	0.26 ± 0.04	1.58 ± 0.08

Table 6.1.2 Average coarse mode size parameter for each month during the study and overall. Averages in total volume and number concentrations are also listed. One standard deviation is provided. Total volume concentrations include the contributions from accumulation, coarse and giant particle modes.

Month	Number (cm^{-3})	Volume ($\mu m^3\ cm^{-3}$)	D_{gv} (μm)	σ_g	Total Number	Total Volume
July	3 ± 3	6 ± 4	2.6 ± 0.4	1.78 ± 0.10	800 ± 300	11 ± 7
August	2 ± 2	5 ± 4	3.2 ± 0.6	1.8 ± 0.13	1000 ± 400	10 ± 6
September	0.4 ± 0.2	2.1 ± 1.1	3.7 ± 0.6	1.82 ± 0.17	900 ± 300	7 ± 4
October	0.5 ± 0.5	3 ± 3	4.0 ± 0.6	1.85 ± 0.12	1100 ± 400	7 ± 4
Overall	2 ± 2	4 ± 4	3.4 ± 0.8	1.82 ± 0.14	1000 ±400	9 ± 5

Table 6.2.1 Average fine ($PM_{2.5}$) chemistry mass fractions for each month and overall. Soil was computed using the IMPROVE formula. Ammoniated sulfate concentrations varied as a function of neutralization. One standard deviation is provided.

Month	Ammoniated Sulfate	Soil	Organic Carbon	Elemental Carbon	$NaNO_3$
July	0.34 ± 0.19	0.32 ± 0.18	0.26 ± 0.14	0.02 ± 0.02	0.07 ± 0.05
August	0.52 ± 0.14	0.22 ± 0.17	0.19 ± 0.07	0.03 ±0.02	0.041 ± 0.018
September	0.61 ± 0.14	0.10± 0.09	0.22 ± 0.08	0.027 ± 0.011	0.04 ± 0.03
October	0.53 ± 0.14	0.18 ± 0.12	0.23 ± 0.05	0.029 ± 0.008	0.034 ± 0.019
Overall	0.51 ± 0.18	0.20 ± 0.16	0.22 ± 0.09	0.026 ± 0.015	0.04 ± 0.03

Table 6.2.2 Average coarse (PM_{10} - $PM_{2.5}$) chemistry mass fractions for each month and overall. Soil was computed using the IMPROVE formula. Ammoniated sulfate concentrations varied as a function of neutralization. One standard deviation is provided.

Month	Ammoniated Sulfate	Soil	Organic Carbon	Elemental Carbon	$NaNO_3$
August 20-31	0.3 ± 0.3	0.3 ± 0.2	0.3 ± 0.2	0.017 ±0.013	0.07 ± 0.05
September	0.2 ± 0.3	0.4 ± 0.2	0.4 ± 0.2	0.03 ± 0.03	0.06 ± 0.05
October	0.09 ± 0.07	0.5 ± 0.2	0.30 ± 0.10	0.02 ± 0.02	0.08 ± 0.05
Overall	0.2 ± 0.2	0.4 ± 0.2	0.3 ± 0.2	0.02 ± 0.03	0.07 ± 0.05

Table 6.3.1 Physical constants of species used in refractive index and density calculations.

Species	Density ($g\ cm^{-3}$)	Refractive Index	Source
H_2SO_4	1.8	1.408	S*
NH_4HSO_4	1.78	1.479	S*
$(NH_4)_3H(SO_4)_2$	1.83	1.527	S*
$(NH_4)_2SO_4$	1.76	1.531	T
Organic Carbon	1.4	1.55	S*,D
Elemental Carbon	2.0	1.96-0.66*i*	S,OF
$NaNO_3$	2.261	1.587	T
SiO_2	2.32	1.486	CRC,S,S*
Al_2O_3	3.97	1.765	CRC,S,S*
Fe_2O_3	5.24	3.011	CRC,S,S*
CaO	3.3	1.833	CRC,S,S*
MgO	2.58	1.735	CRC,S,S*
TiO_2	4.23	2.58	CRC,S,S*

S refers to values directly from *Stelson* (1990)
*S** refers to values derived from *Stelson* (1990)
T refers to values directly from *Tang* (1996)
CRC refers to the Handbook of Chemistry and Physics, 61st Edition (1980-1981)
OF refers to *Ouimette and Flagan* (1982)
D refers to *Dick et al.*, (2000)

Table 6.3.2 Monthly averaged dry retrieved refractive indices and effective densities ($g\ cm^{-3}$) from the alignment method. One standard deviation is provided.

Month	Refractive Index	Effective Density ($g\ cm^{-3}$)
July	1.582 ± 0.011	1.60 ± 0.13
August	1.562 ± 0.007	1.53 ± 0.11
September	1.560 ± 0.010	1.57 ± 0.10
October	1.564 ± 0.008	1.56 ± 0.12
Overall	1.566 ± 0.012	1.56 ± 0.12

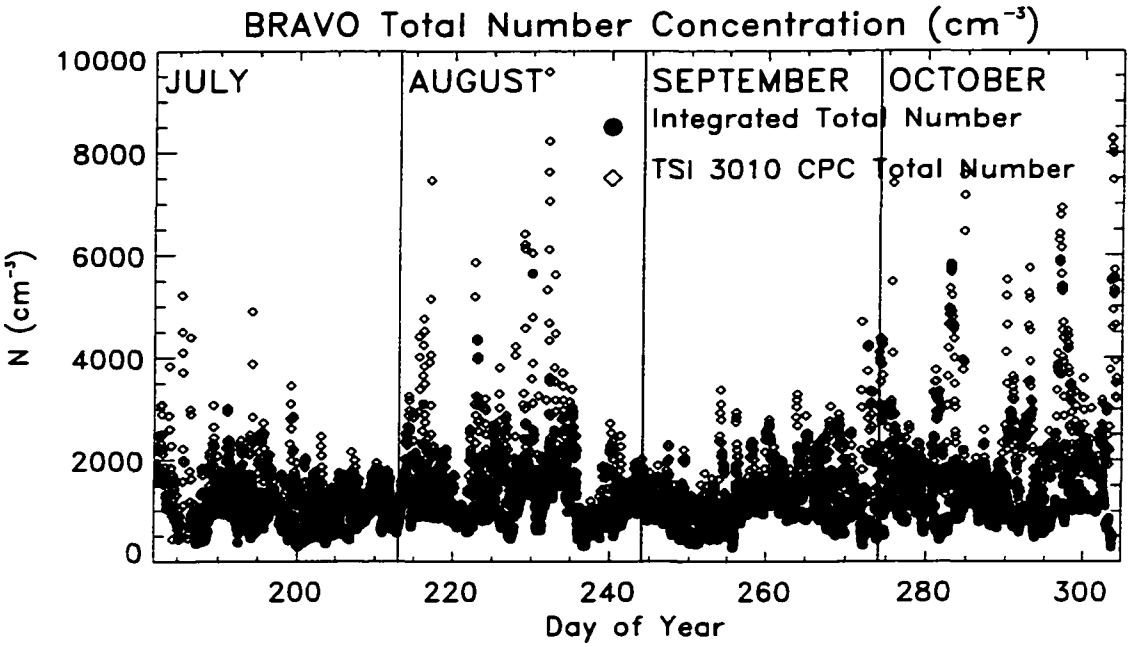

Figure 6.1.1 Dry integrated total number concentrations (cm^{-3}) from size distributions ($0.03 < D_p < 21$ μm) and TSI 3010 CPC ($D_p > 15$ nm).

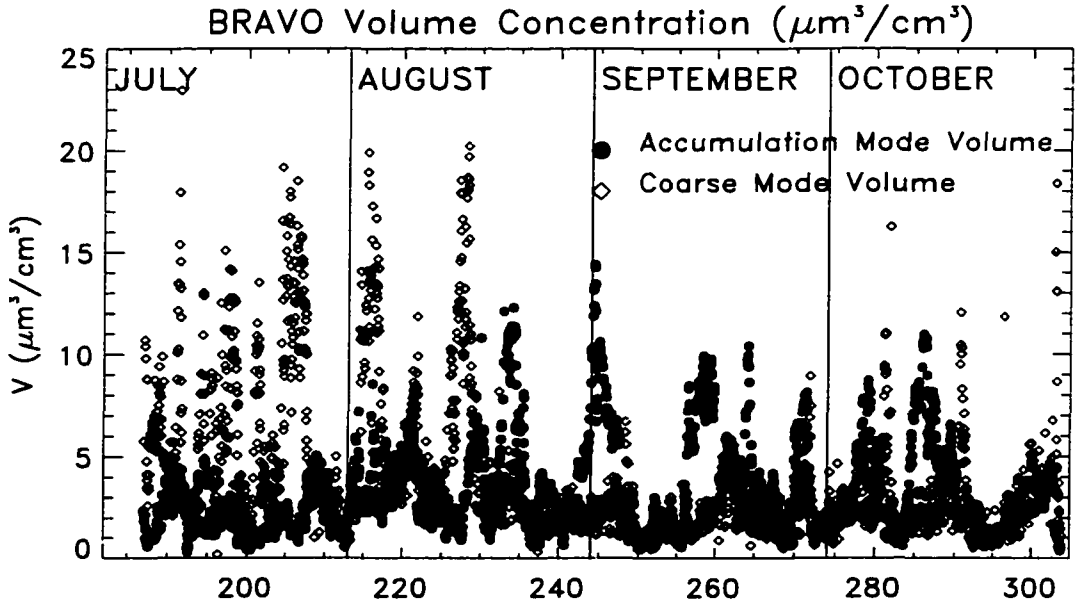

Figure 6.1.2 Dry integrated accumulation mode and coarse mode volume concentrations (μm^3 cm^{-3}) from size distributions.

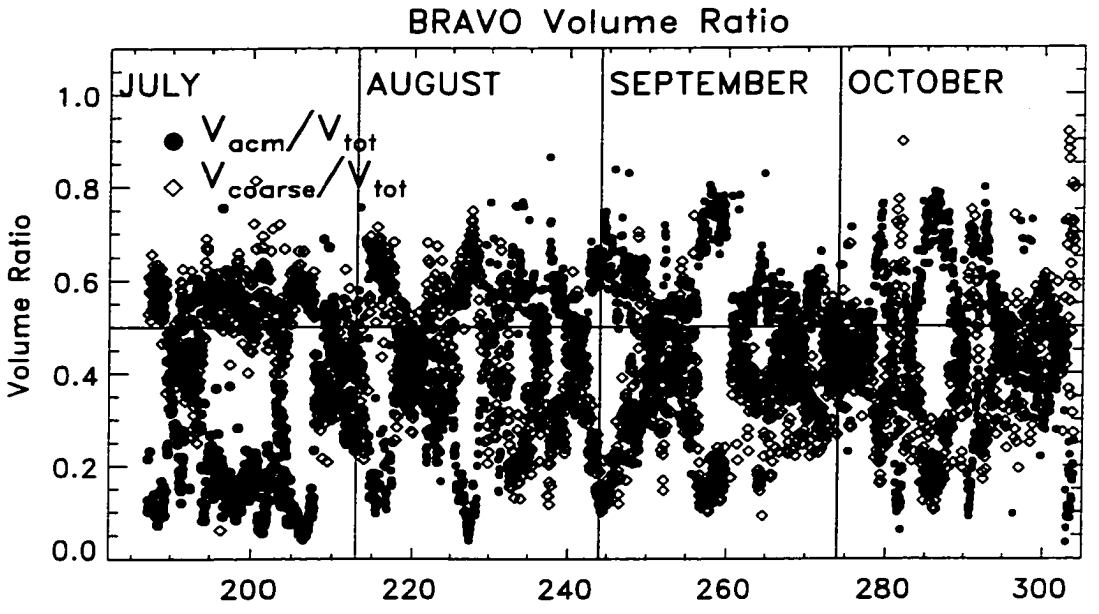

Figure 6.1.3 Fractional contributions of accumulation and coarse mode volume concentrations to total volume concentrations derived from size distribution measurements. The line drawn at 0.5 demonstrates 50% contribution. Total volume includes contributions from accumulation, coarse and giant modes.

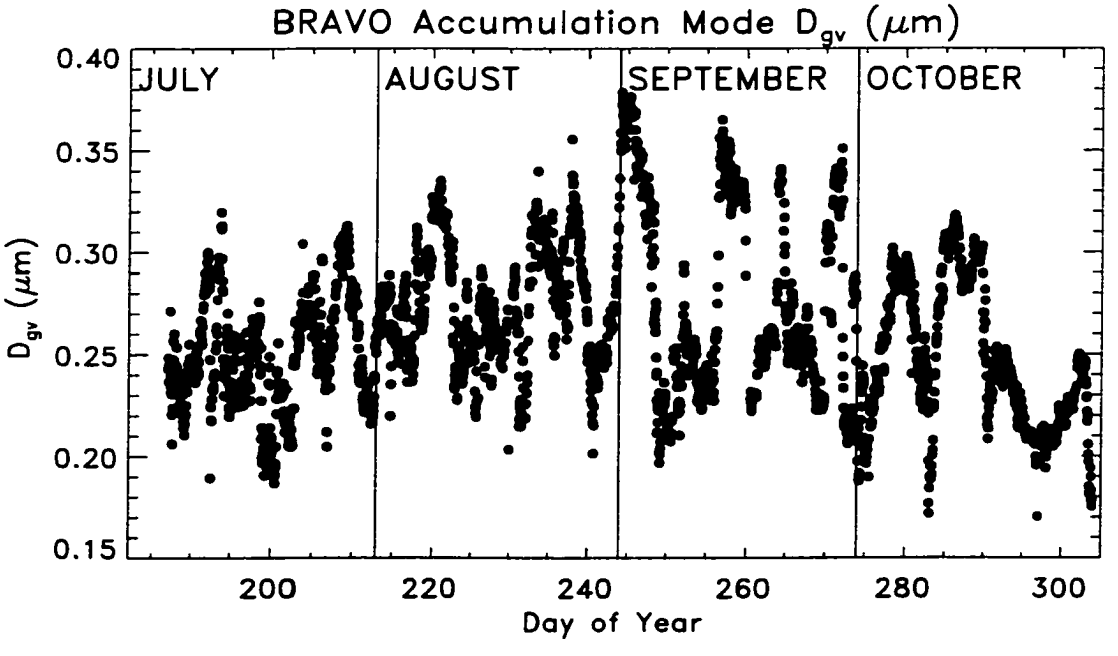

Figure 6.1.4 Dry accumulation mode volume geometric mean diameter (D_{gv}) (μm).

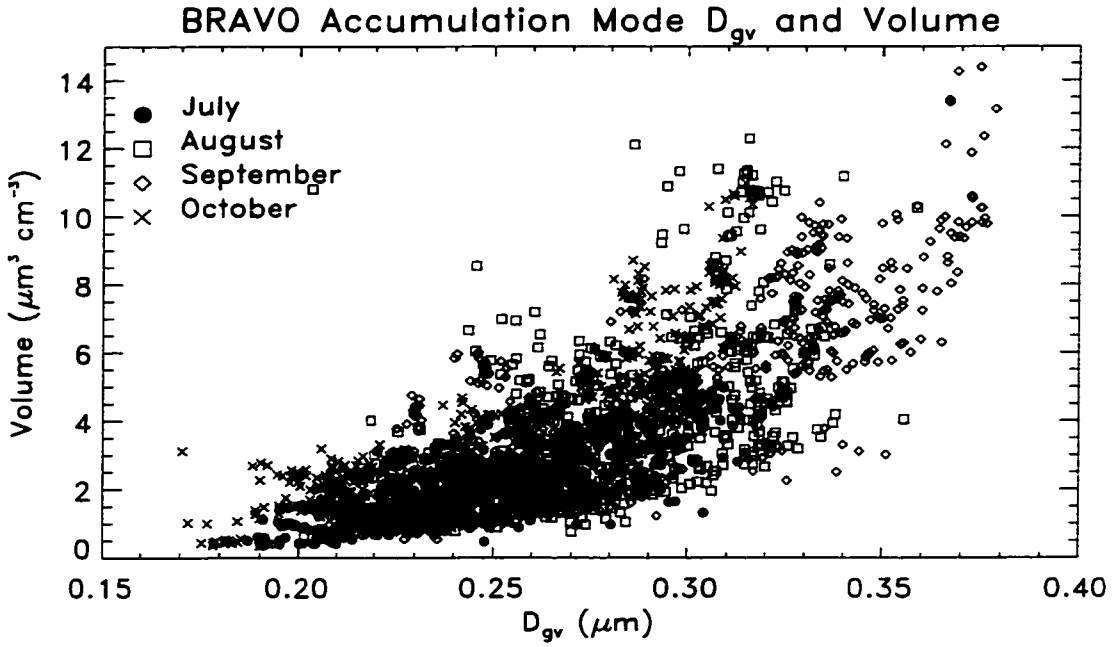

Figure 6.1.5 Scatter plot of accumulation mode volume geometric mean diameter (μm) and accumulation mode volume concentration (μm^3 cm^{-3}).

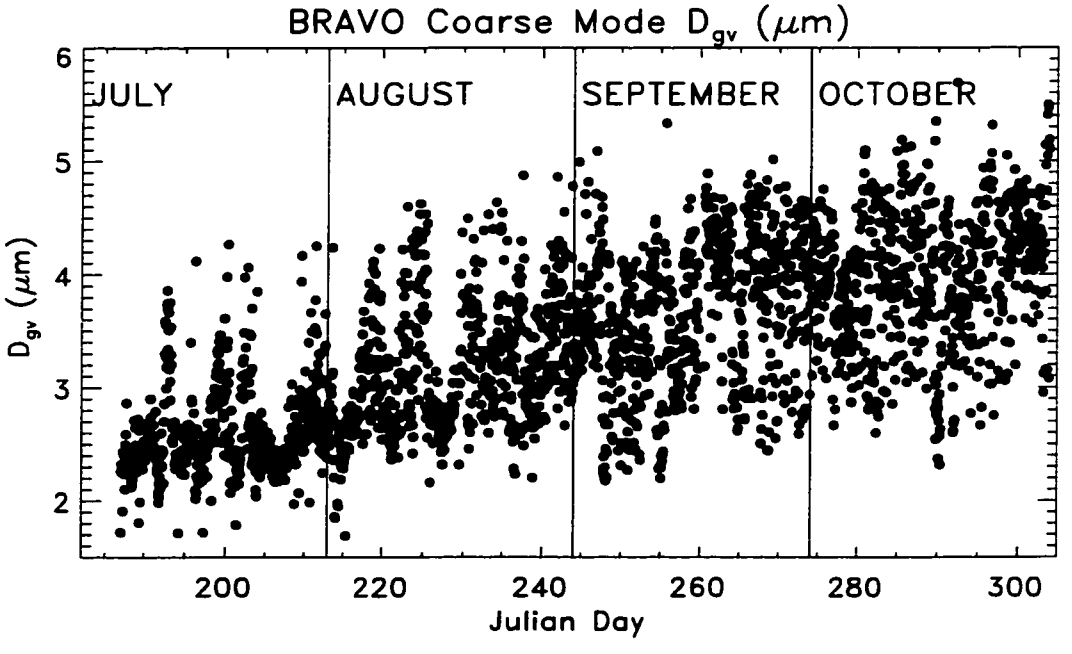

Figure 6.1.6 Dry coarse mode volume mean geometric diameter (D_{gv}) (μm).

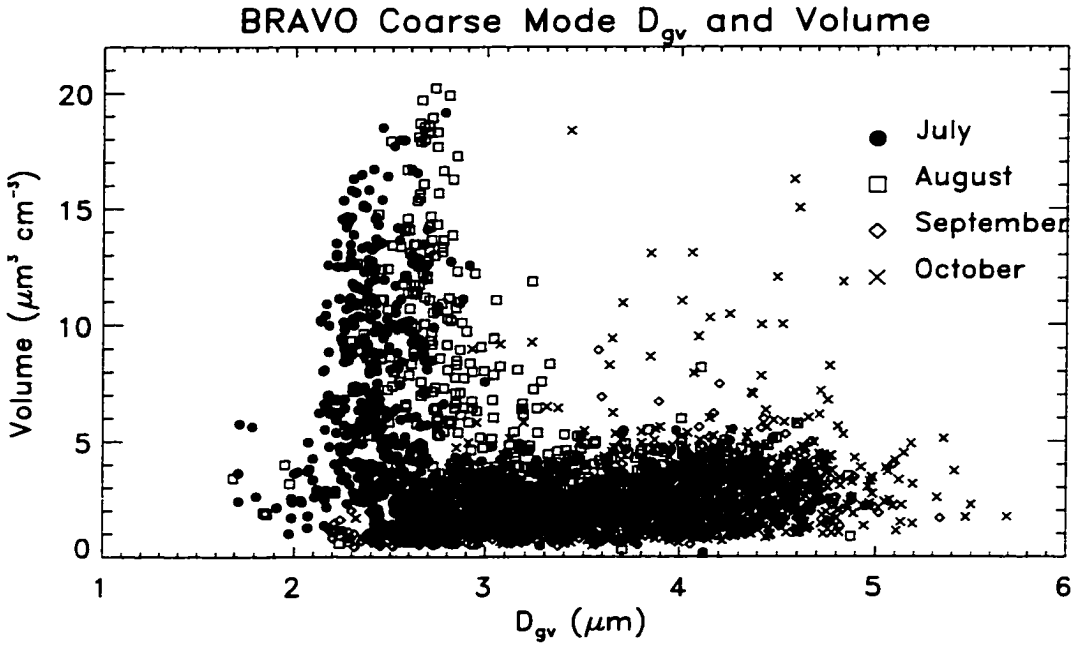

Figure 6.1.7 Scatter plot of coarse mode volume geometric mean diameter (μm) and coarse mode volume concentration (μm^3 cm^{-3}).

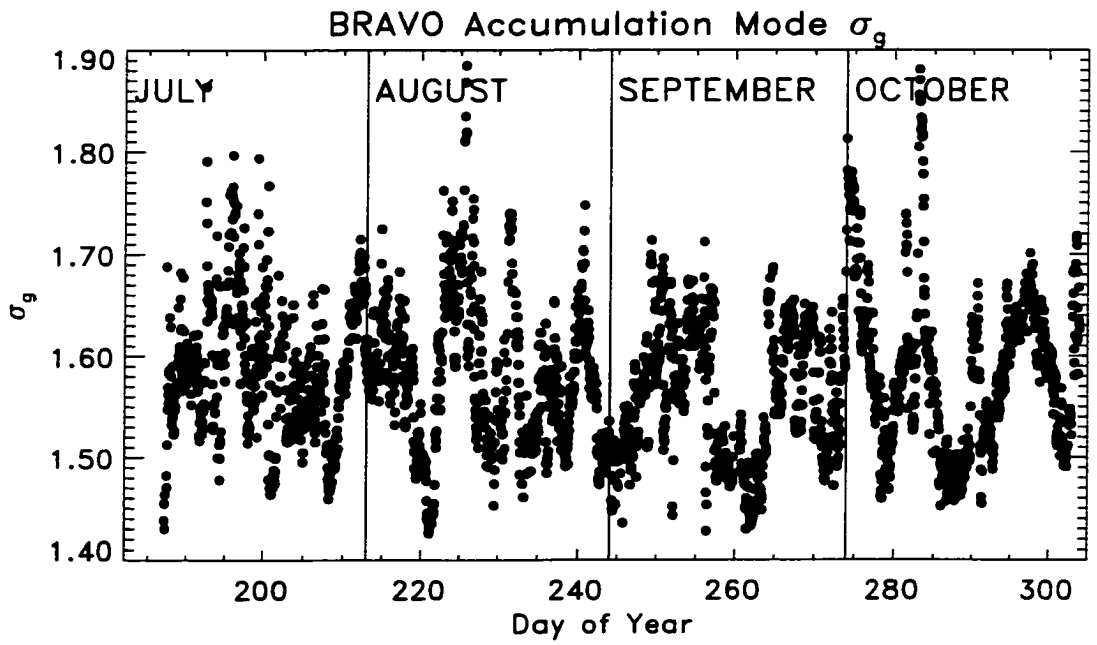

Figure 6.1.8 Accumulation mode volume geometric standard deviation (σ_g).

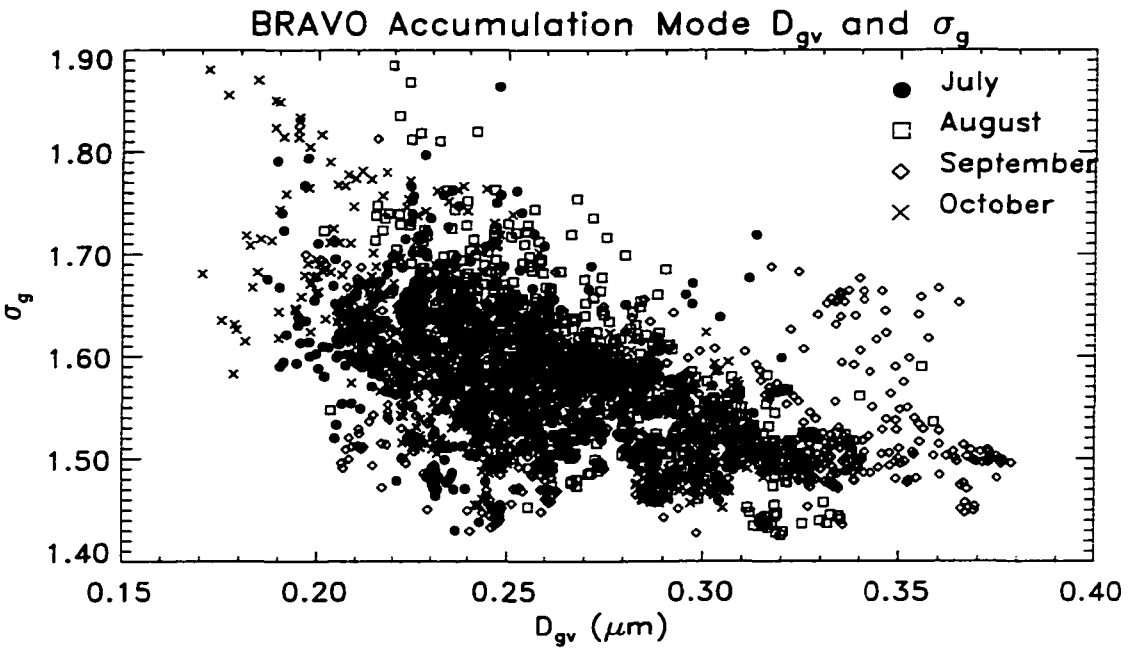

Figure 6.1.9 Scatter plot of accumulation mode volume geometric mean diameter (μm) and geometric standard deviation (σ_g).

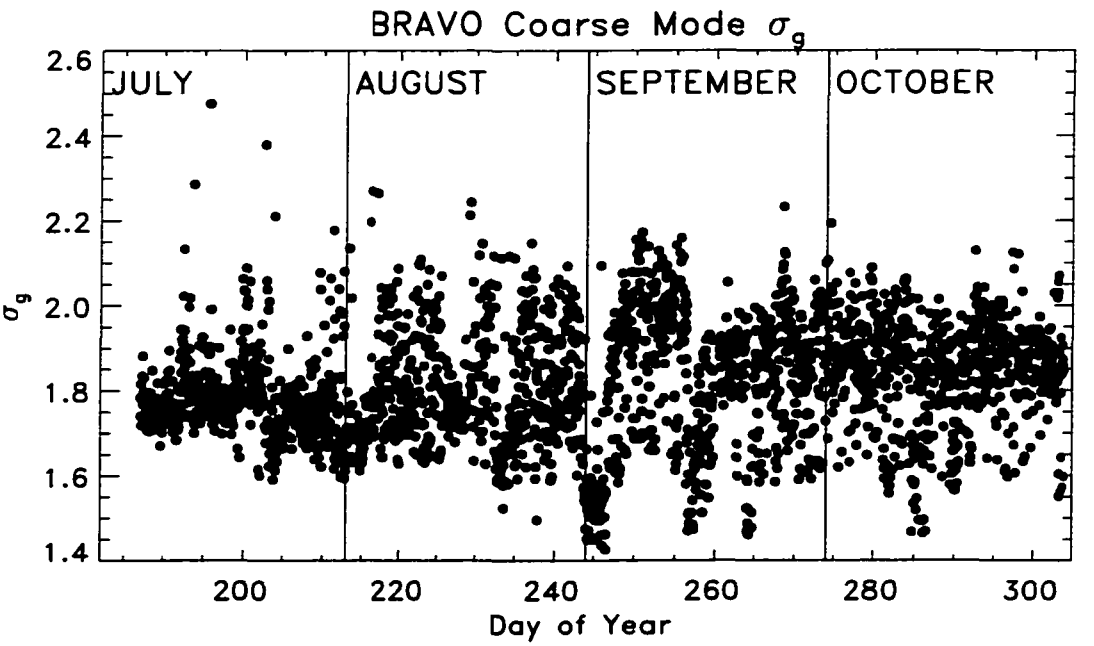

Figure 6.1.10 Coarse mode volume geometric standard deviation (σ_g).

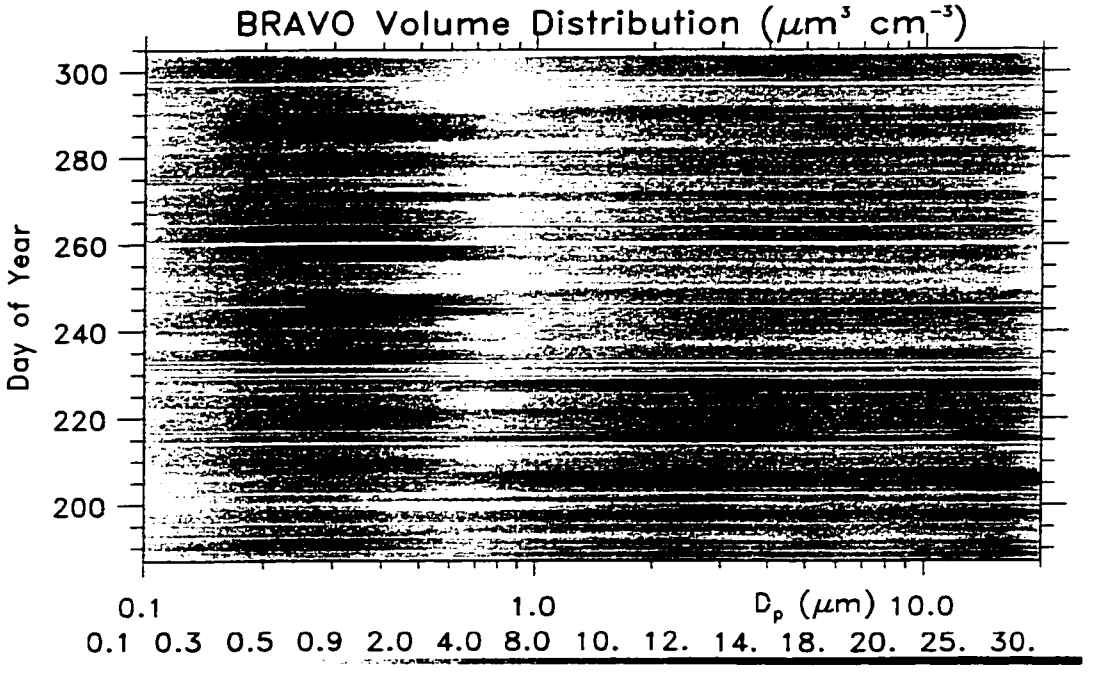

Figure 6.1.11 Contour plot of dry volume distributions (μm^3 cm^{-3}) for the entire study.

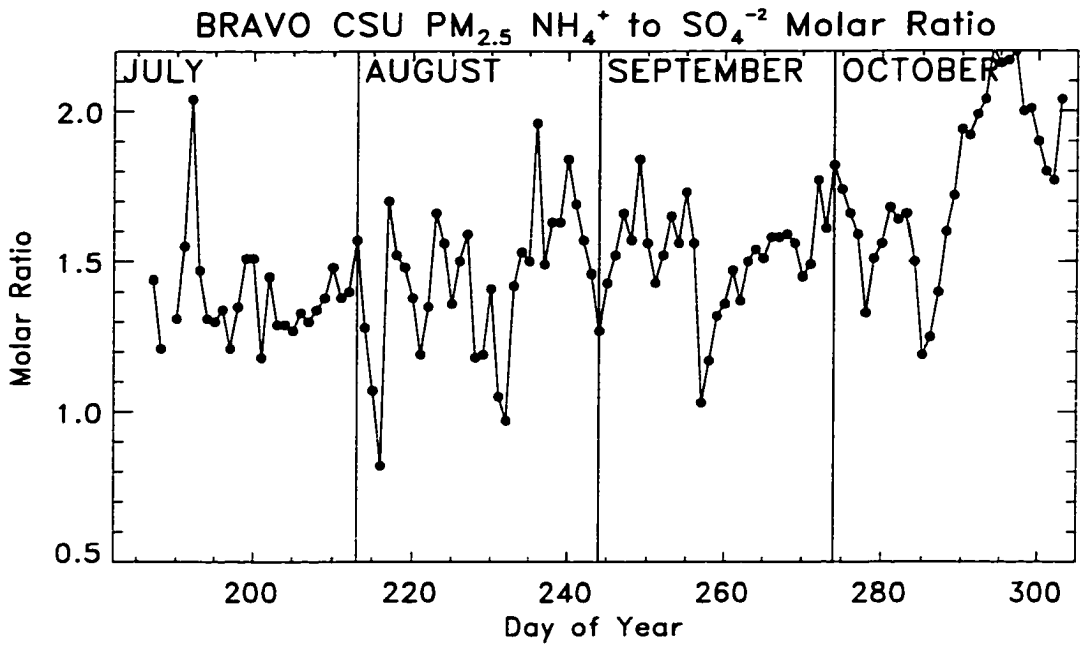

Figure 6.2.1 Ammonium to sulfate molar ratios computed from CSU $PM_{2.5}$ data.

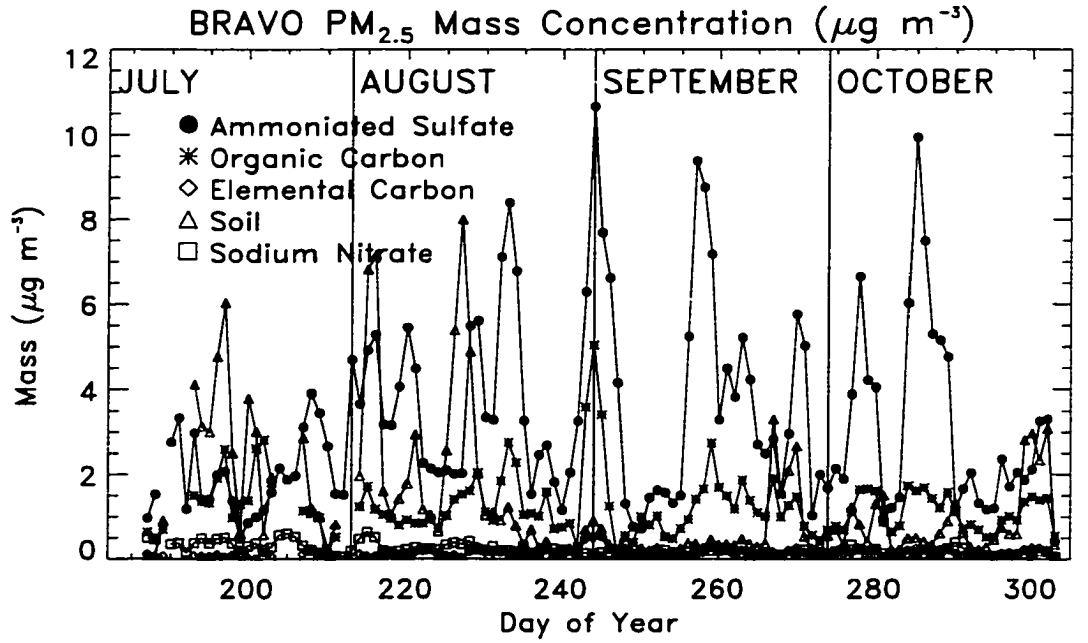

Figure 6.2.2 Fine ($PM_{2.5}$) chemical composition in $\mu g\ m^{-3}$.

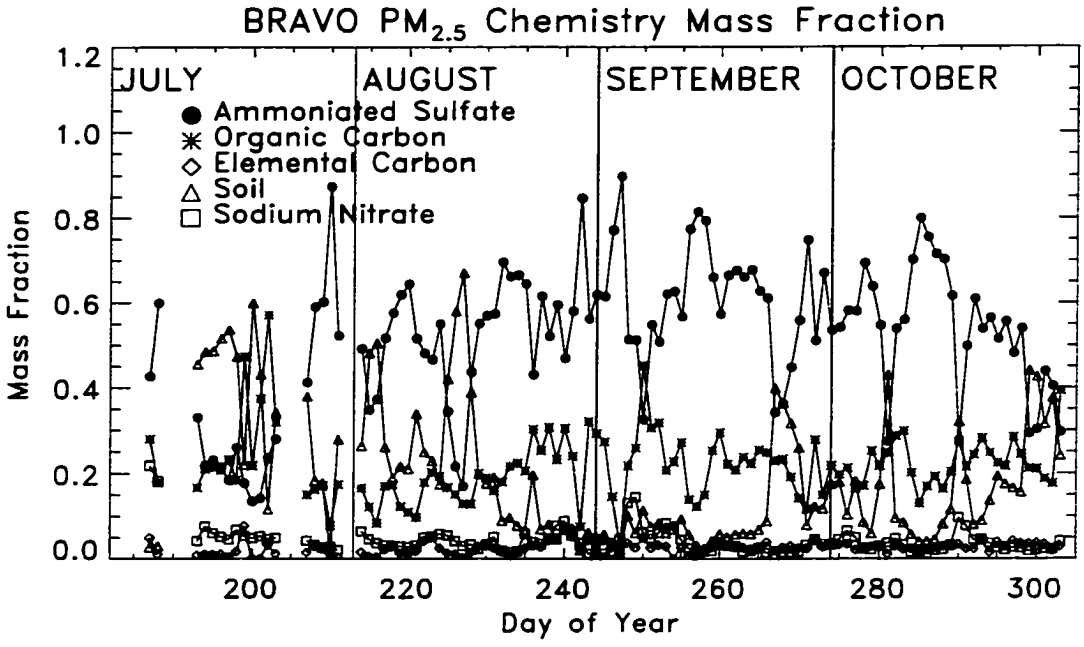

Figure 6.2.3 Fine ($PM_{2.5}$) chemistry mass fractions.

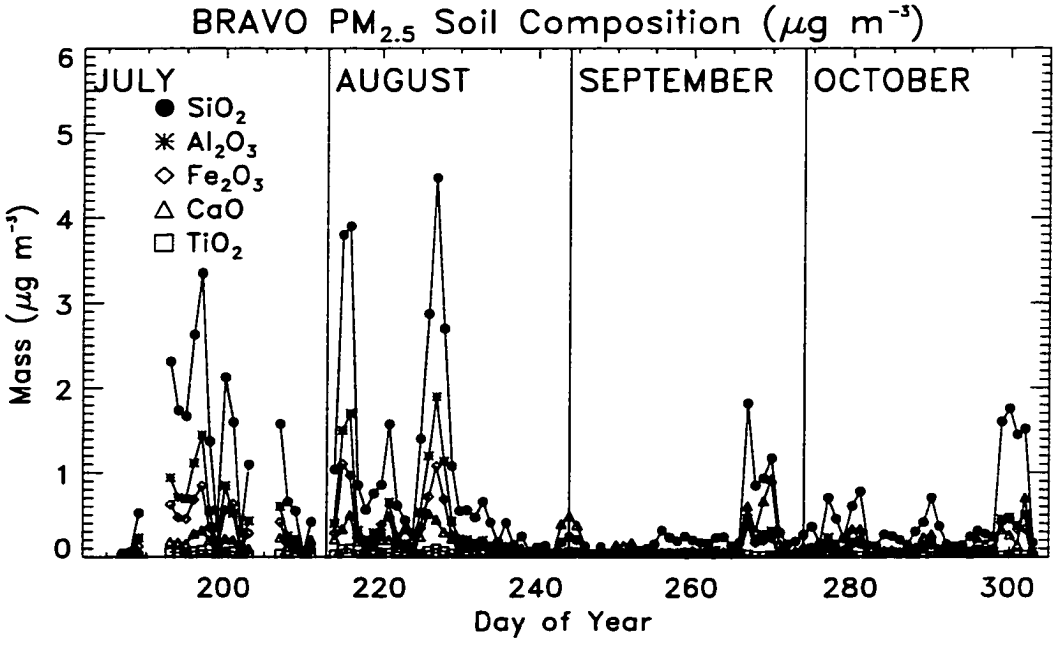

Figure 6.2.4 Fine ($PM_{2.5}$) soil species assumed in the IMPROVE soil formula.

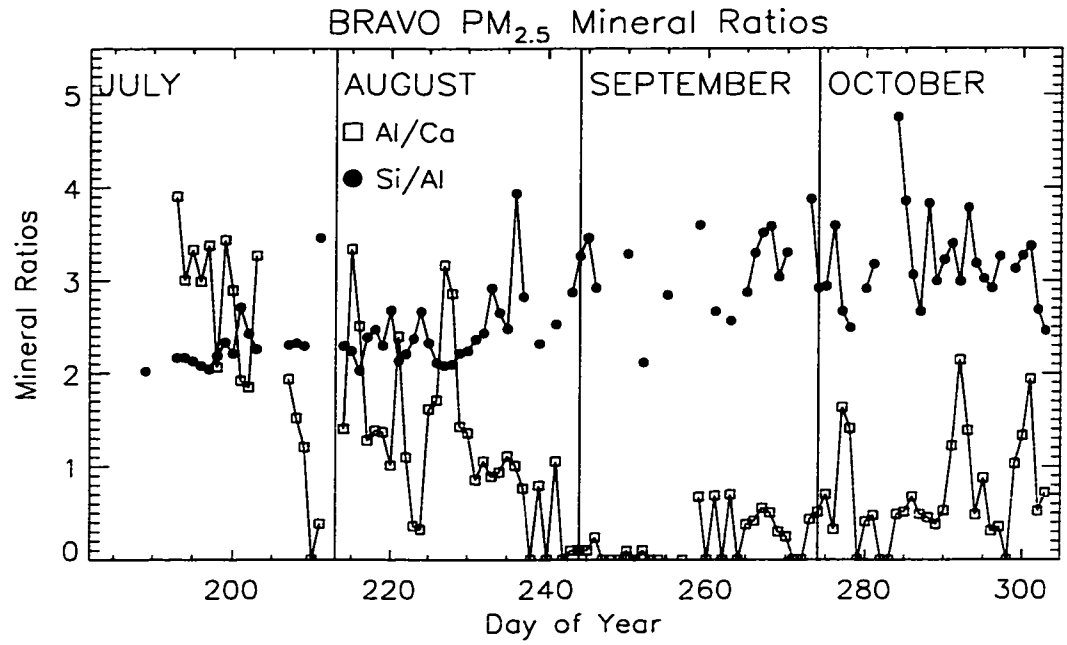

Figure 6.2.5 Fine ($PM_{2.5}$) mineral ratios of Al/Ca and Si/Al.

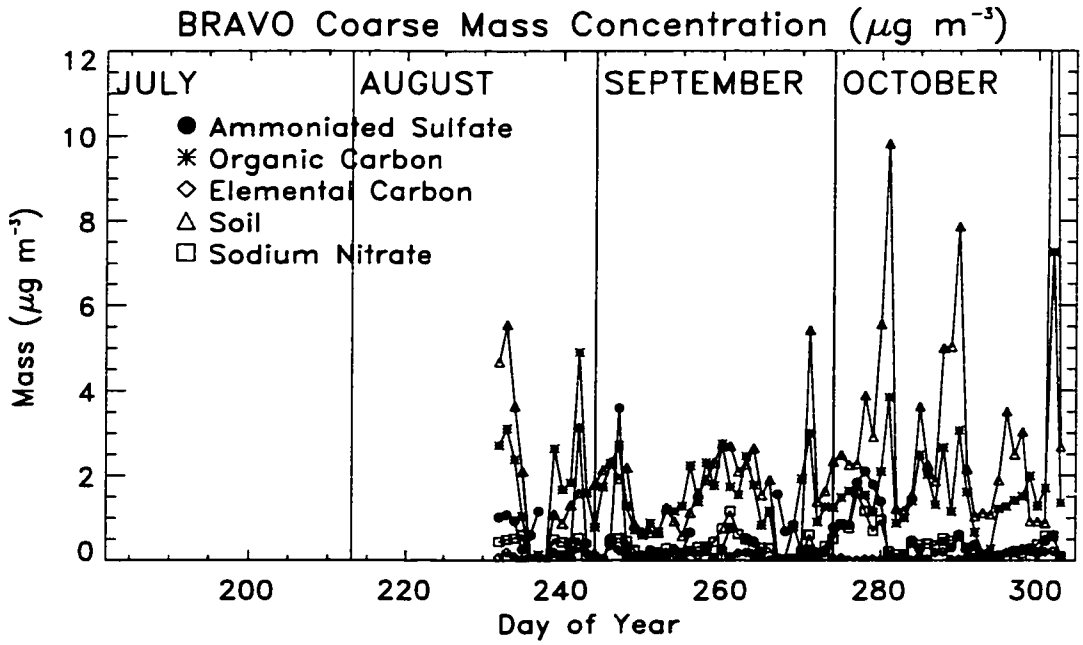

Figure 6.2.6 Coarse ($PM_{10} - PM_{2.5}$) chemical composition in $\mu g\ m^{-3}$.

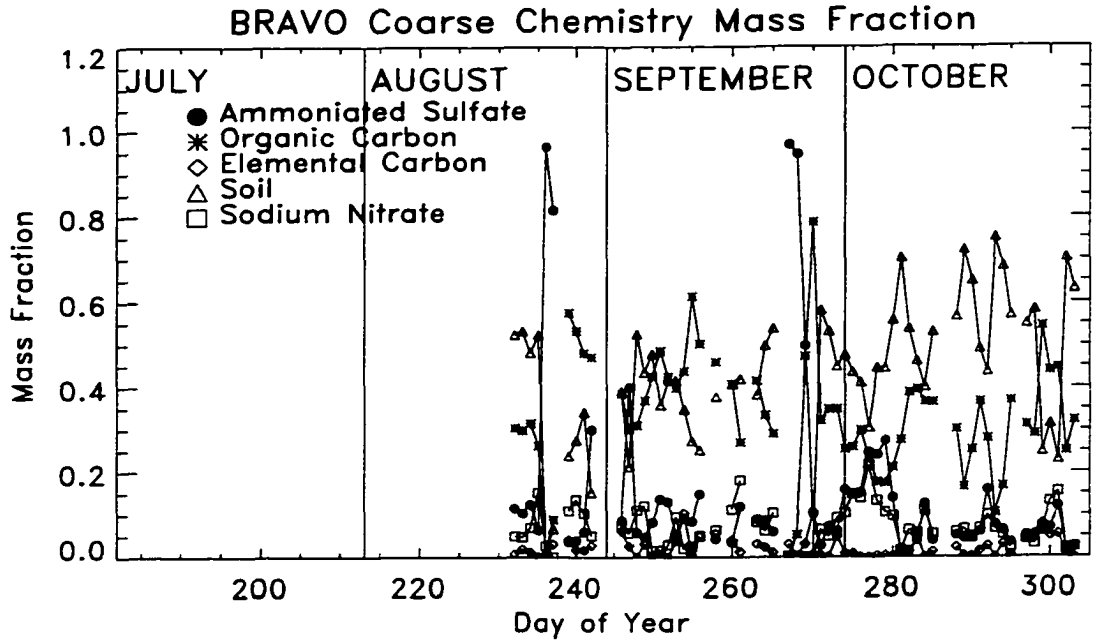

Figure 6.2.7 Coarse (PM_{10} - $PM_{2.5}$) chemistry mass fractions.

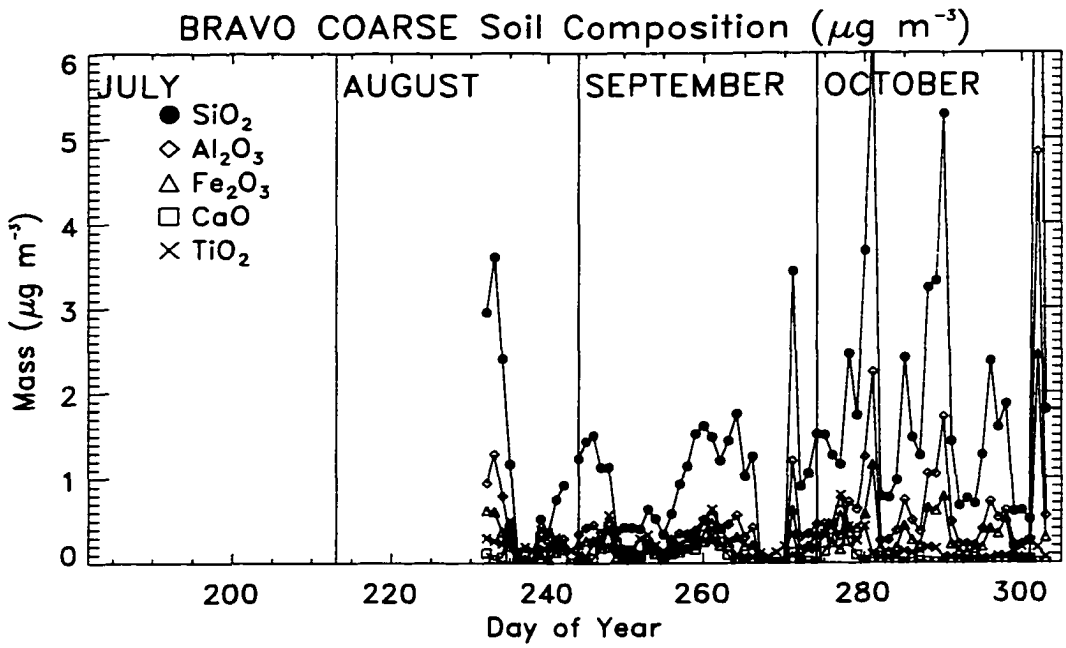

Figure 6.2.8 Coarse (PM_{10} - $PM_{2.5}$) soil species assumed in the IMPROVE soil formula.

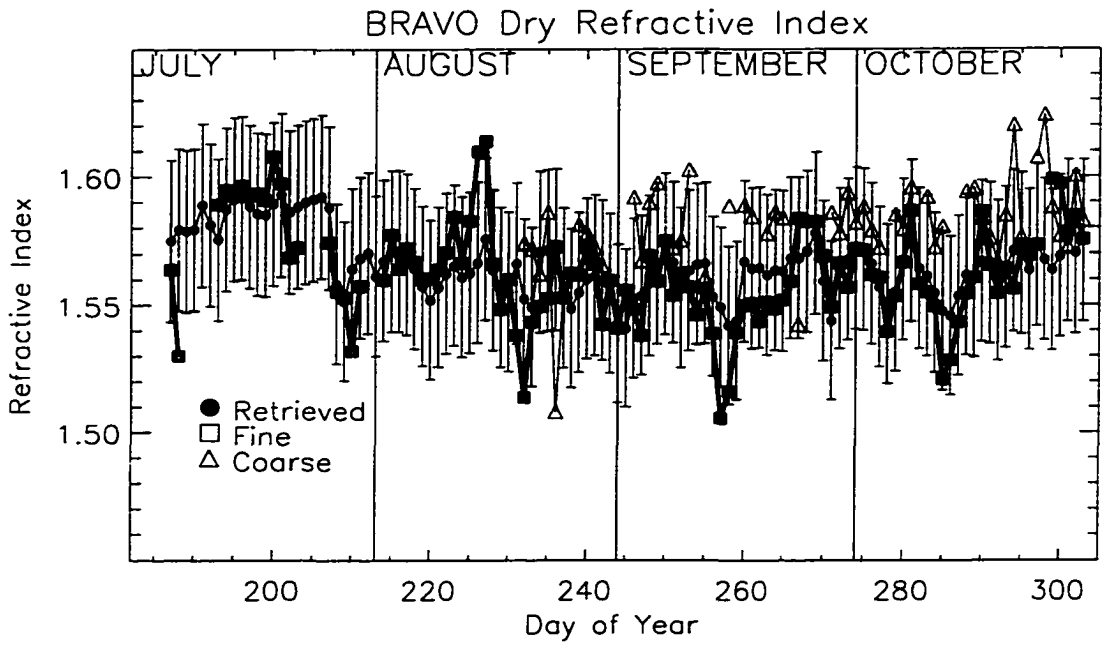

Figure 6.3.1 Daily averaged retrieved dry refractive indices with computed fine and coarse estimates using chemical compositions. Error bars represent a 2 % uncertainty in retrieved refractive index.

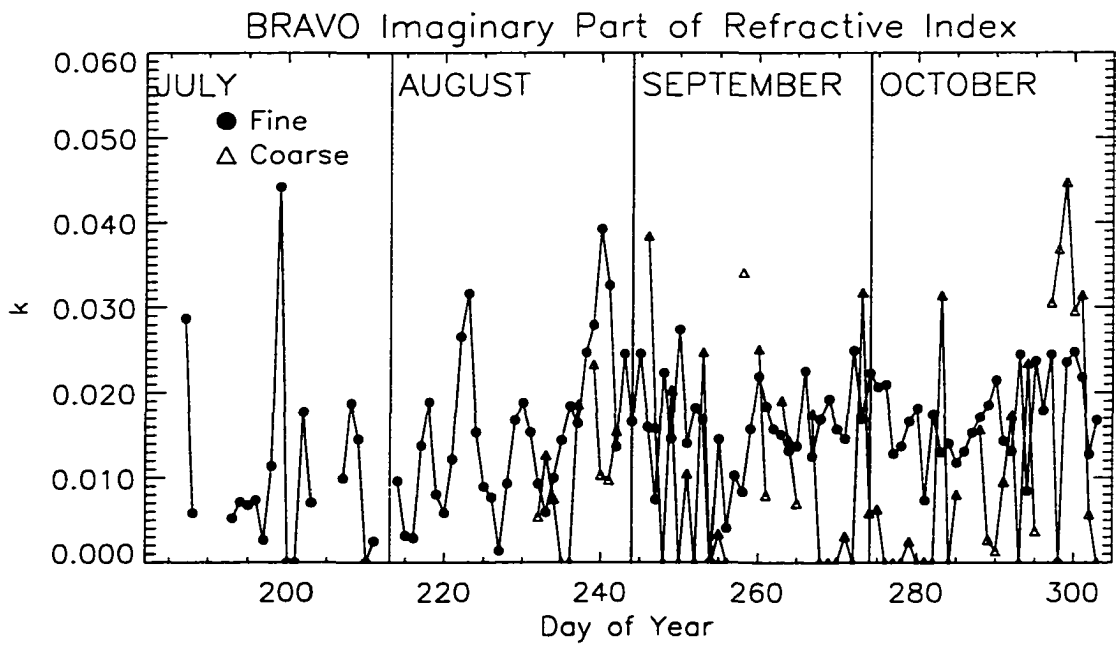

Figure 6.3.2 Fine and coarse imaginary part of refractive index assuming only elemental carbon was absorbing.

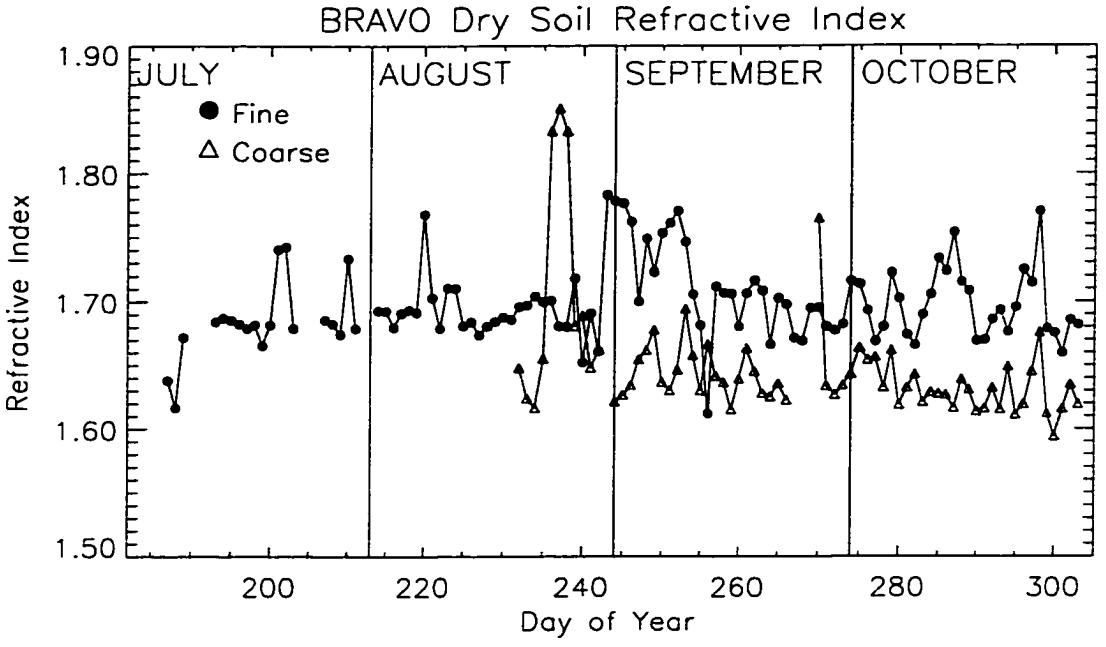

Figure 6.3.3 Fine and coarse dry soil refractive indices computed with soil compositions based on the IMPROVE soil formula.

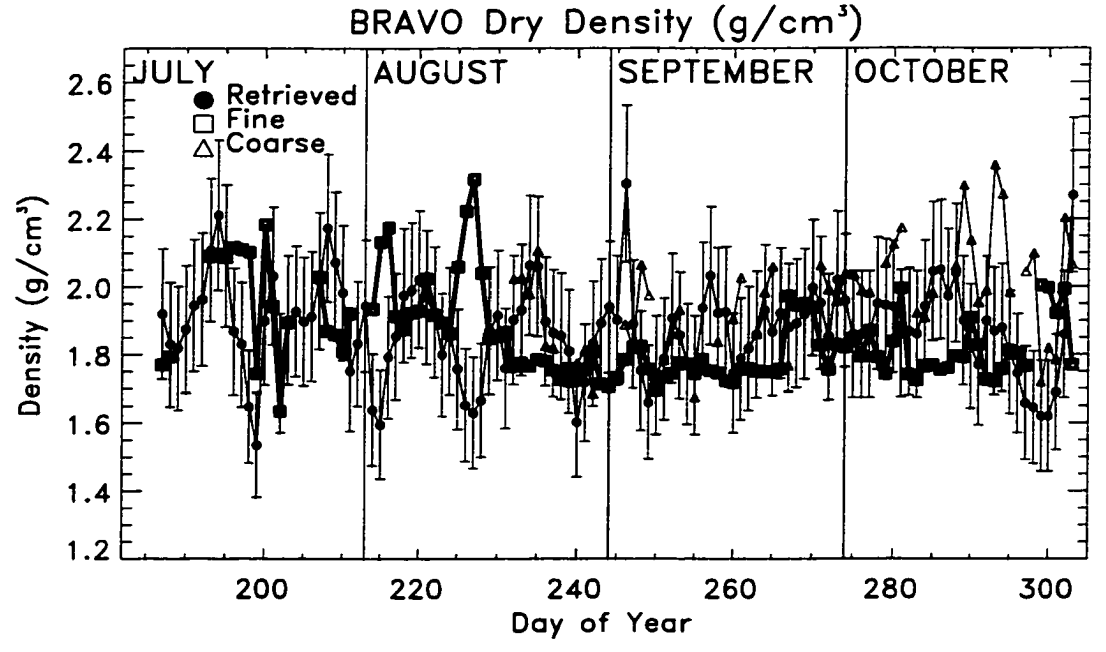

Figure 6.3.4 Daily averaged retrieved dry densities (g cm^{-3}) assuming $\chi = 1.2$ with computed values from fine and coarse chemical components. Error bars represent a 20 % uncertainty in retrieved density.

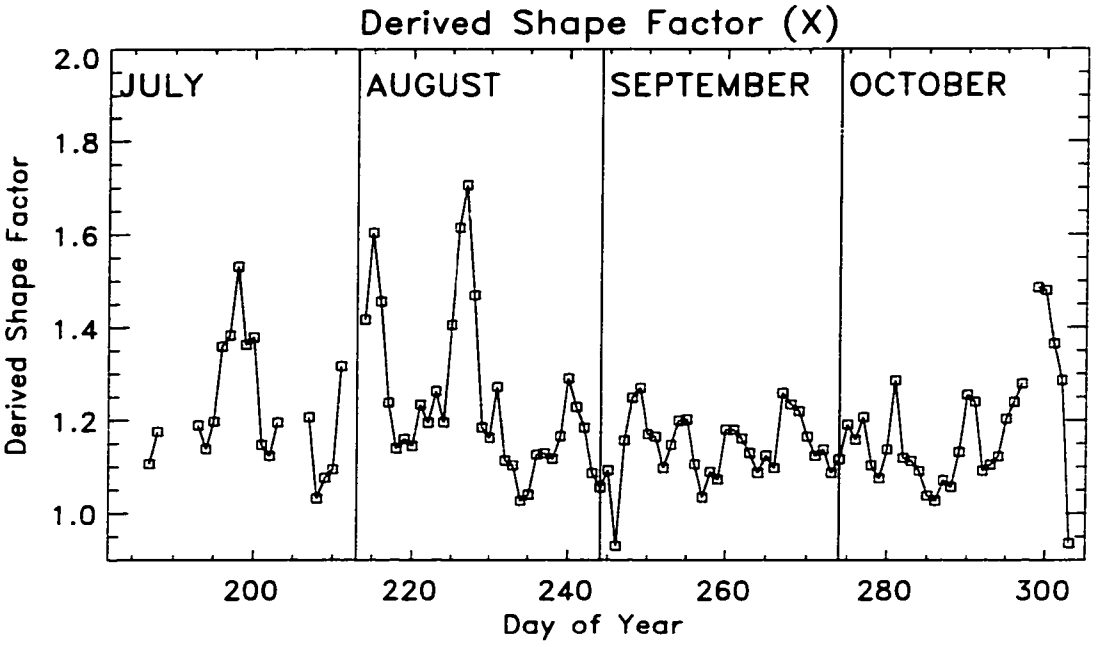

Figure 6.3.5 Derived dynamic shape factors (χ) from computed densities and retrieved effective densities.

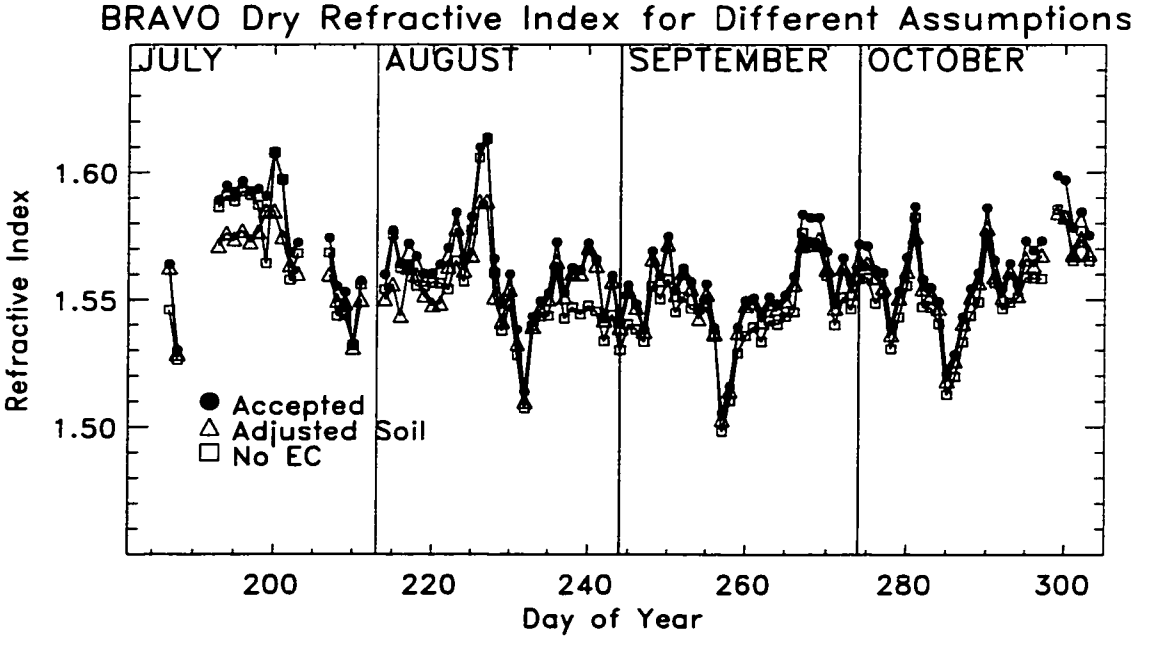

Figure 6.3.6 Computed fine refractive indices for different assumptions of chemical components (see text).

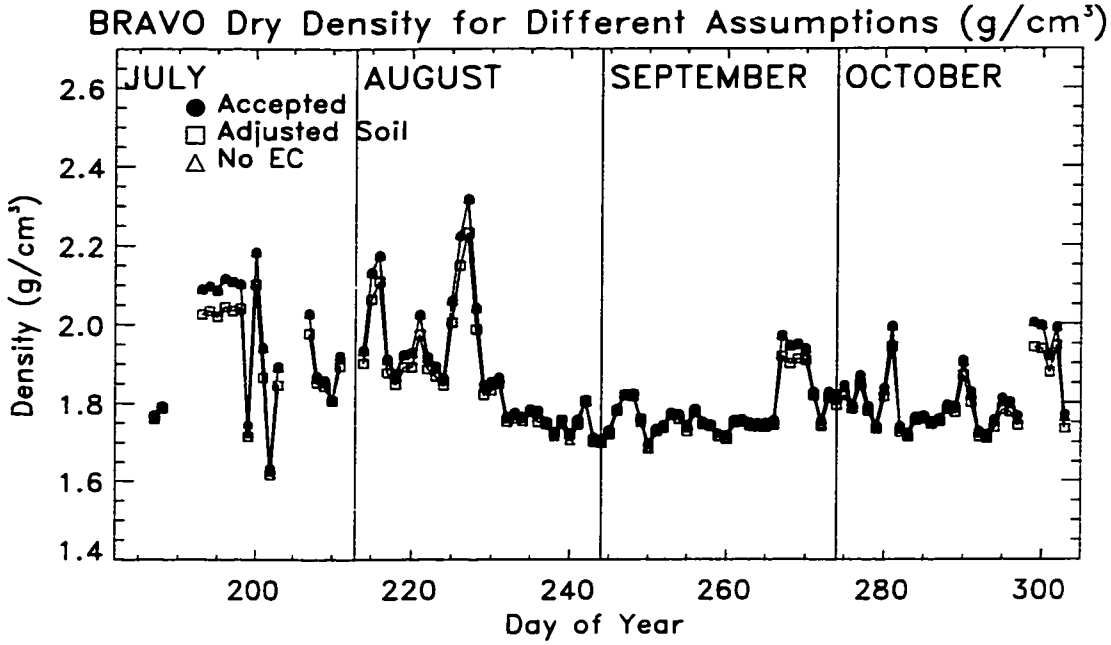

Figure 6.3.7 Computed densities (g cm^{-3}) for different assumptions of chemical components (see text).

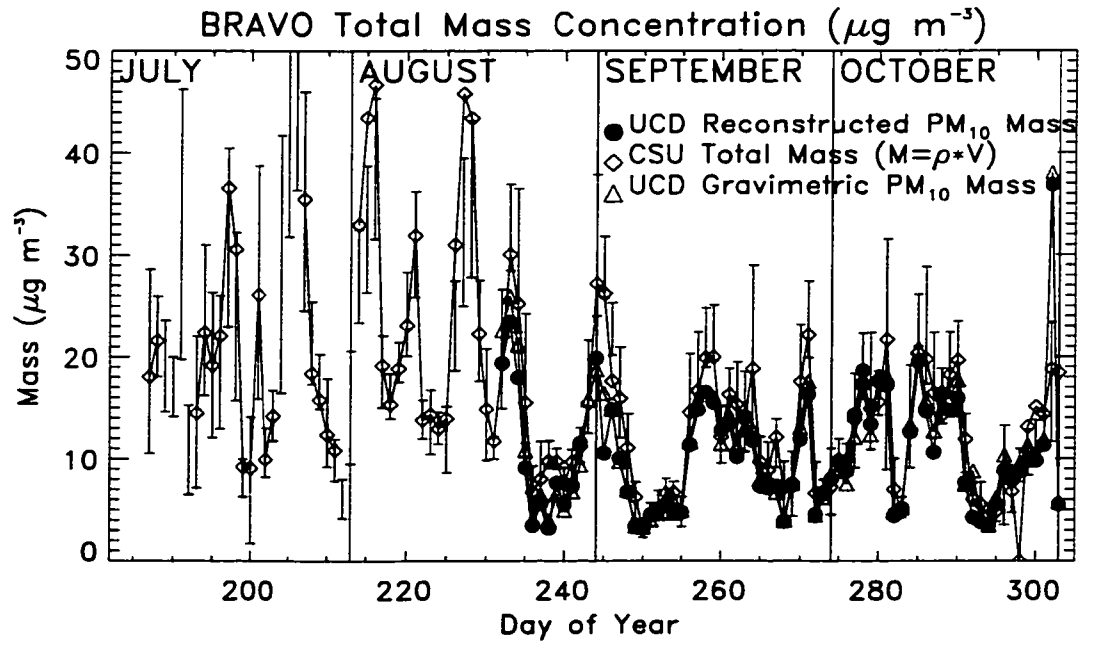

Figure 6.3.8 Total mass concentrations ($\mu g\ m^{-3}$) from UCD PM_{10} gravimetric mass, reconstructed mass and values derived from size distributions and densities determined with shape factors presented in Figure 6.3.5.

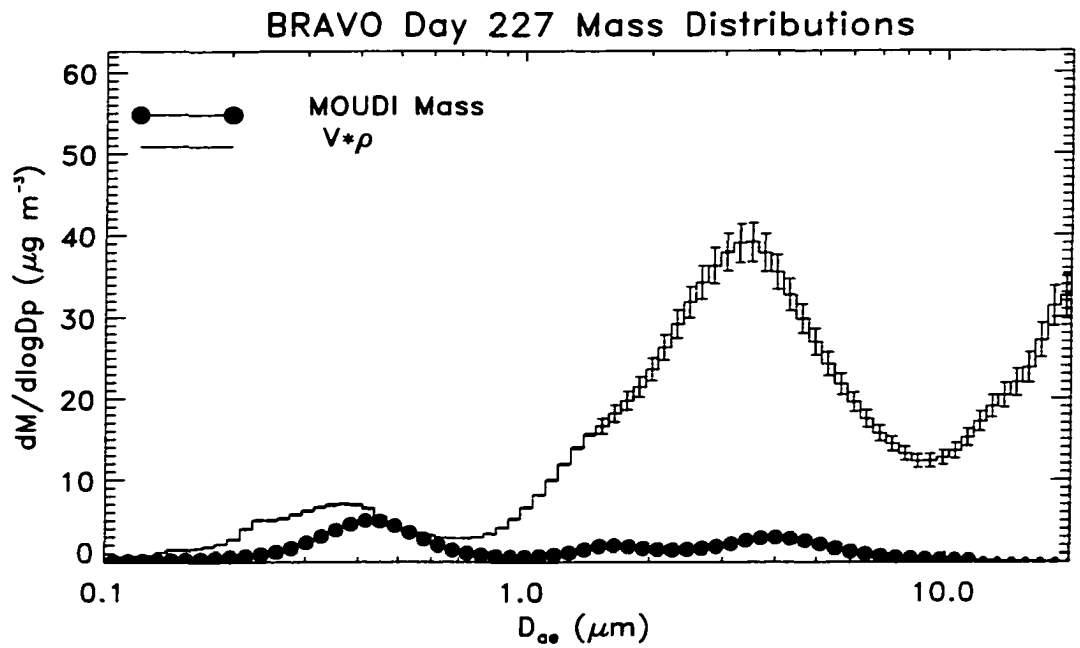

Figure 6.3.9a MOUDI mass distributions for DOY 227 (August 15, 1999). Also plotted is a daily averaged mass distribution derived from volume distributions and effective densities.

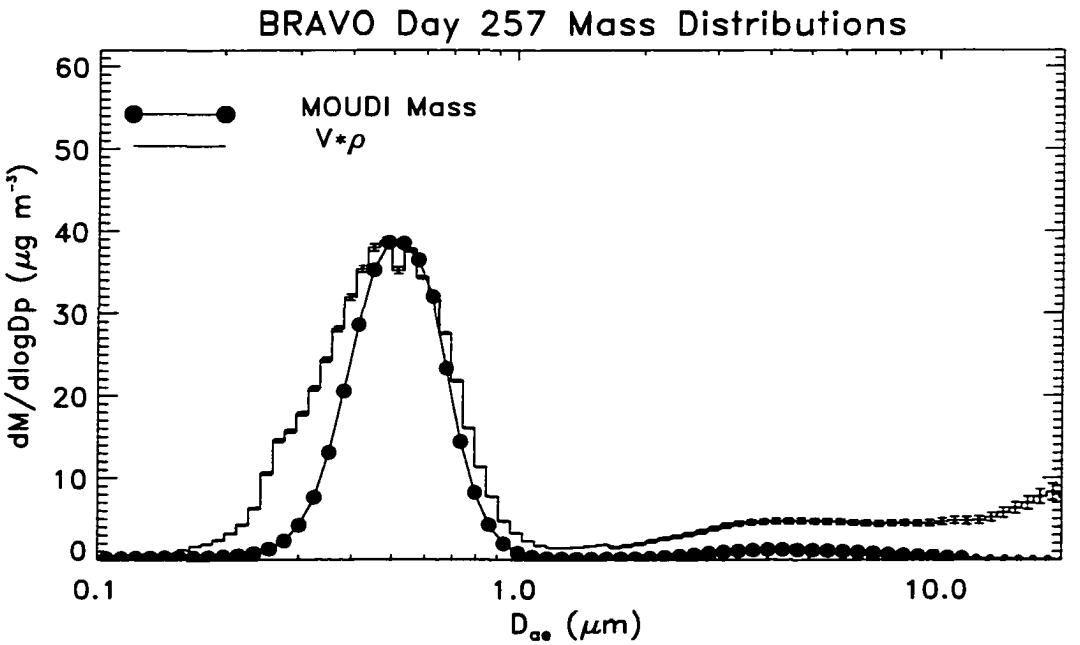

Figure 6.3.9b MOUDI mass distributions for DOY 257 (September 14, 1999). Also plotted is a daily averaged mass distribution derived from volume distributions and effective densities.

CHAPTER 7. DERIVED AEROSOL OPTICAL PROPERTIES AND VISIBILITY ESTIMATES

The scientific definition of visibility can vary depending on the context in which it is used. In this work visibility will be described as the interaction of particles with incident radiation and the dependence of the interaction on particle composition and size. Visibility includes the ability of particles to both scatter and absorb light and the combined effect is referred to as extinction. Visibility is routinely monitored by the IMPROVE network using a variety of techniques, and results from this monitoring network have shown that contributions to extinction vary spatially (*Malm et al.*, 1994). Sulfates are responsible for up to 60-70 % of total light extinction in the eastern U. S. and only about 30 % in the inner mountain west. In the inner mountain west carbonaceous aerosols account for 35 % of total light extinction and coarse mass scattering accounts for about 15 – 25 % (*Malm and Day*, 2000).

Estimates of total light extinction coefficients (b_{ext}) are made by a number of different methods. The IMPROVE network measures visibility with transmissometers (total extinction) and nephelometers (scattering); however, these methods do not provide information about the size or chemical composition of particles responsible for visibility degradation. Impactor measurements of particle mass size distributions can be used to investigate the size and composition dependence of light extinction (*Lowenthal et al.*,

2000); however, this method is analytically intensive and still may not provide the complete chemical composition. Aerosol number and volume distributions can be used to compute visibility but some estimate of refractive index is required to perform the calculations using Mie theory. Reconstructed scattering and extinction estimates are made by applying mass efficiencies to chemical composition measurements; however, efficiencies can vary based on the chemical components and the degree and type of mixing of particles (*Ouimette and Flagan,* 1982). Comparisons of reconstructed and measured scattering coefficients typically agree well in regions dominated by sulfate aerosols where the scattering properties are well understood (*Sisler,* 1996).

A recent study in Grand Canyon National Park (*Malm and Day,* 2000) was motivated by the inability to apportion 50 % of the extinction budget. This discrepancy may be due to inaccurate predictions of the contributions of coarse particles to scattering or of particle absorption, both of which are not well understood. Many of the measurements performed during BRAVO were designed to investigate the optical properties of coarse particles. Coarse particle chemical speciation and coarse aerosol size data provided information that had not been available in earlier NPS special studies. These data were used to investigate the contributions of coarse particles to total scattering and the conditions under which scattering by coarse particles was a significant contribution to total extinction. The 1996 Big Bend National Park Scoping Study suggested that reconstructed extinction in the park was 94 % scattering and 6 % absorption, with 17 % of the scattering due to coarse mass. The correlation between measured and reconstructed extinction was 0.804 (*Gebhart et al.,* 2000).

The calculations presented in this chapter were designed to investigate many of the issues mentioned above. Section 7.1 provides estimates of calculated light scattering coefficients using measured size distributions. The contributions from accumulation and coarse particle modes to total light scattering were determined and episodes with significant scattering due to coarse particles were identified; these occurred mostly in July and early August. Comparisons to $PM_{2.5}$ nephelometer dry scattering coefficient measurements demonstrated agreement with calculated values, although were lower by a 35 % offset. Section 7.2 focuses on derived mass scattering efficiencies and their applicability to reconstructed scattering coefficients. Section 7.3 presents estimates of extinction and absorption coefficients and their variation with size. Single-scattering albedo estimates will also be discussed.

7.1 CALCULATIONS OF OPTICAL PROPERTIES

The efforts to carefully measure aerosol size distributions over the full aerosol spectrum culminated in calculations of derived aerosol optical properties. These wavelength dependent properties are expressed as extinction, scattering and absorption coefficients, and are related by Equation 7.1.1:

$$b_{ext} = b_{sp} + b_{ap} + b_{sg} + b_{ag} \qquad (7.1.1)$$

where *s, a, p,* and *g* refer to scattering, absorption, particles and gases, respectively. Scattering by gas molecules (b_{sg}) is referred to as Rayleigh scattering and is pressure dependent (*van de Hulst*, 1981). Absorption by gases (b_{ag}) at visible wavelengths is due primarily to NO_2 and is negligible at most remote sites like Big Bend National Park (*Malm et al.*, 1994). Extinction coefficients were assumed to have contributions from

particle scattering and absorption only. Many previous studies have demonstrated that particle scattering and absorption are size and composition dependent by using impactor-derived particle mass size distributions to estimate light scattering coefficients (*Lowenthal et al.*, 2000; *Malm et al.*, 2000; *Quinn et al.*, 1998; *Quinn et al.*, 1995; *Zhang et al.*, 1994). This method is useful in that it demonstrates size-resolved compositions and subsequent effects on visibility. However, analysis of impactor filters is time-consuming and typically the filters are analyzed for major ions only, providing no information about elemental carbon and organic carbon or soil elements which can be 25 – 40 % and 5-20 % of fine mass in the U. S., respectively (*Sisler*, 1996). Impactors segregate particles based on aerodynamic size that must be converted to geometric size with particle density before calculations of optical properties are made.

Another approach to estimating size-resolved optical properties is the method applied here using measured volume distributions and retrieved refractive indices (Equation 7.1.2):

$$b_{sp} = \int \frac{3}{2} \frac{Q_{sp}}{D_p} \frac{dV}{d\log D_p} d\log D_p \qquad (7.1.2)$$

where the Mie scattering efficiency (Q_{sp}) is a function of particle diameter (D_p), refractive index and wavelength (λ = 530 nm) and was calculated using Mie theory assuming spherical particles (*Mie*, 1908; *Bohren and Huffman*, 1983). The volume distribution is $dV/d\log D_p$ and the integral was performed over the size range of interest. An advantage to this method over the direct measurement of scattering coefficients was the ability to estimate b_{sp} over any size range of interest within the limits of the distribution. Contributions to total b_{sp} from the accumulation and coarse particle volume modes as derived in Chapter 6 were investigated. A constant value of retrieved refractive index was

applied across the total size distribution. The magnitudes of computed fine and coarse refractive indices derived from measured compositions were within experimental uncertainties (see Section 6.3); therefore, applying a constant refractive index over the full size range was assumed reasonable. Extinction coefficients (b_{ext}) were calculated by replacing the scattering efficiency with the extinction efficiency and applying retrieved real refractive indices and imaginary components computed in Chapter 6 from elemental carbon concentrations. Absorption coefficients (b_{ap}) were computed by taking the difference in extinction and scattering coefficients ($b_{ap} = b_{ext} - b_{sp}$).

Figure 7.1.1 presents timelines of computed b_{sp} from Equation 7.1.2. Overall the average total dry b_{sp} was (average plus one standard deviation) 0.026 ± 0.016 km^{-1}, with the highest values observed in August and September and lowest in July and October. Statistics for each month are summarized in Table 7.1.1. Experimental uncertainties in calculated scattering coefficients were on the order of 15 % due to uncertainties in particle losses in the sampling lines. These uncertainties were greater than those derived from sensitivity studies in the alignment method (see Chapter 5). Several relatively high total b_{sp} episodes were observed in August, September and October (e.g. DOY 232, 244, and 285). All of these periods were associated with high sulfate mass concentrations, high accumulation mode volume concentrations, and flow from east Texas.

The contributions to total scattering from the accumulation and coarse modes are shown on Figure 7.1.1, but were more visible in a fractional form where the b_{sp} from each mode was ratioed to the total b_{sp}, as shown in Figure 7.1.2. Scattering due to coarse particles was a major contributor to total b_{sp} for days in July and early August, corresponding to suspected Saharan dust episodes discussed in Chapter 6. Three periods

in October also demonstrated high coarse mode scattering coefficients, consistent with observations that suggested a significant coarse volume mode during these periods (see Chapter 6). DOY 283 and DOY 291 were associated with flow from southwest U.S. and the California Baja. DOY 303 was associated with flow from north Texas. The overall average ratio of coarse mode b_{sp} to total b_{sp} was 0.20 ± 0.18, with largest values in July and smallest values in September (see Table 7.1.1). Total b_{sp} was dominated by accumulation mode scattering from late August through October, consistent with sulfate dominated accumulation mode aerosols that were efficient at light scattering. The overall accumulation mode b_{sp} fractional contribution was 0.79 ± 0.18, with highest values in September and lowest values in July.

Figure 7.1.3 compares ratios of accumulation mode volume to total volume concentration (V_{acm}/V_{tot}) from Chapter 6 and ratios of accumulation mode b_{sp} to total b_{sp} ($b_{sp,acm}/b_{sp,tot}$). Volume ratios greater than 0.5 (50 % of total volume due to the accumulation mode) corresponded to dominant accumulation mode scattering ($b_{sp,acm}/b_{sp,tot}$ > 90 %). Less significant accumulation mode b_{sp} ($b_{sp,acm}/b_{sp,tot}$ < 50 %) corresponded to accumulation mode volume contributing less than 20 % to total volume. In general accumulation mode b_{sp} ratios increased with accumulation mode volume ratios, showing that particles with size distributions dominated by accumulation mode volume were also dominated by accumulation mode light scattering.

In contrast, significant coarse mode volume did not always correspond to high contributions from coarse mode scattering. Figure 7.1.4 shows a comparison of the fractional contribution of coarse mode volume and the fractional contribution of coarse mode light scattering. Coarse mode volume ratios greater than 50 % corresponded to

coarse mode b_{sp} ratios ranging from 10 – 80 % of total scattering. Coarse mode volume ratios less than 50 % corresponded to coarse mode b_{sp} ratios also less than 50 %. Figure 7.1.5 shows the variation of accumulation mode b_{sp} with accumulation mode volume concentration. Despite variations in fine mass composition from month to month as discussed in Chapter 6, Figure 7.1.5 shows a similar relationship for all months, with b_{sp} increasing approximately linearly with accumulation mode volume concentration. In contrast for the coarse mode, Figure 7.1.6 demonstrates that differences in this relationship were observed month to month, suggesting that the variations in composition and particle mean size played a larger role in the variations in coarse scattering coefficient.

Scattering distributions ($db_{sp}/dlogD_p$) were used to investigate the relationships between particle size and visibility degradation. Figure 7.1.7 shows a b_{sp} distribution for a suspected Saharan dust day on July 6 1999 (DOY 187) with two distinct scattering modes. Scattering due to coarse particles was 53 % of the total b_{sp} on this day. The peak of the accumulation b_{sp} mode occurred near 0.3 μm, and the peak of the coarse b_{sp} mode occurred around 2.0 μm. In contrast, Figure 7.1.8 shows a b_{sp} distribution on October 12 1999 (DOY 285), a day with high sulfate mass concentrations and high accumulation mode b_{sp} (96 % of total). Scattering due to coarse mode particles was negligible and the peak of the accumulation b_{sp} mode occurred near 0.35 μm. Because differences were observed in the sizes corresponding to the peaks in the scattering distributions on these days, the geometric mean diameters for both b_{sp} modes were calculated following Equation 6.1.1 and are summarized in Table 7.1.2. Figure 7.1.9 presents a timeline of accumulation mode b_{sp} geometric mean diameter (D_{gb}) plotted with the accumulation

mode volume geometric mean diameter (D_{gv}). The variations in D_{gb} tracked well with variations in D_{gv}, although D_{gb} was consistently larger. The overall average value of D_{gb} was 0.33 ± 0.04 μm (see Table 7.1.2). The large values of D_{gb} observed in July corresponded to oddly shaped distributions (e.g. see Figure 7.1.10). In general D_{gb} increased with increasing D_{gv}, suggesting larger accumulation mode particles were more efficient for light scattering for the conditions at Big Bend (Figure 7.1.11). Figure 7.1.12 shows the timeline of coarse mode geometric mean diameters for the b_{sp} and volume distributions. Coarse mode D_{gb} increased as the study progressed with an overall average D_{gb} of 2.1 ± 0.6 μm. Coarse mode D_{gb} were smaller than the volume mode D_{gv}, suggesting sizes smaller than the coarse mode geometric mean volume diameters were more efficient for light scattering. Figure 7.1.13 showed that in general D_{gb} increased with increasing D_{gv}.

Comparing D_{gb} to the integrated mode b_{sp} demonstrated the sizes most responsible for light scattering for a given mode. Figure 7.1.14 shows this relationship for the accumulation mode. Larger accumulation mode D_{gb} corresponded to larger b_{sp}, consistent with the relationship observed between D_{gb} and D_{gv}. Figure 7.1.15 presents a different picture for the coarse mode, with smaller coarse mode D_{gb} associated with larger coarse mode scattering coefficients. Highest coarse mode scattering coefficients were observed for suspected Saharan dust events in July and early August and corresponded to coarse particles with D_{gb} less than 2.0 μm. All of these trends can be observed in Figure 7.1.16 where b_{sp} distributions for the entire study are plotted as contours. The significant coarse mode b_{sp} during the first part of the study essentially disappeared after mid-August, except for three coarse mode scattering events in October.

Sensitivity to Refractive Index in Calculations

One of the advantages of the alignment method was the retrieval of refractive index on the same temporal resolution as the size distributions, and the application of these to estimates of optical properties. If these retrieved refractive indices were not available, b_{sp} would be computed with refractive indices determined from measured compositions. To test the sensitivity of computed b_{sp} to the applied refractive index, the calculations were re-performed with the $PM_{2.5}$ "accepted" 24-hour UCD composition-derived refractive indices (see Section 6.3). The contributions from each mode to total scattering coefficients were determined by applying these daily refractive indices to hourly averaged total volume distributions with Equation 7.1.2. The fine mode refractive indices were used because these data were available for the entire study and the magnitudes of fine and coarse mode refractive indices were within experimental uncertainty. On average a 3 ± 3 % difference in total b_{sp}, 4 ± 4 % difference in accumulation mode b_{sp} and a 0.4 ± 0.6 % difference in coarse mode b_{sp} were observed with neither estimate consistently higher or lower. Although computed b_{sp} does depend on refractive index, these results suggested that b_{sp} was not significantly sensitive to these choices of applied refractive index, most likely because of the good agreement between retrieved and computed refractive index demonstrated in Section 6.3.

Nephelometer Measurements of Dry b_{sp}

Comparisons to direct measurements were performed to validate calculated estimates of b_{sp} and the methods used to obtain them. Dry b_{sp} was measured by the NPS

using a Radiance Research Integrating nephelometer and a $PM_{2.5}$ size cut (see *Malm and Day*, 2000 for a detailed description of the particle drying system). Nephelometer measurements are routinely performed and many researchers (e.g. *Hasan and Lewis*, 1983; *Sloane et al.*, 1990) have estimated nephelometers measure about half of the scattering from representative coarse particle distributions because of large angle truncation errors and stronger angle-dependent scattering for large particles.

All of the data in this work have been corrected for theoretical size-dependent particle losses in the sampling lines (see Appendix A). These losses were computed for each size distribution and on average increased the derived quantities (such as volume concentrations) by 10 – 15 %. The losses in the nephelometer measurements were determined in the following way. At low ambient relative humidities (less than 30 – 35 %) the nephelometer was disconnected from the drying inlet and the particles were sampled directly through a portion of the hose. The nephelometer was then reconnected to the inlet and particles were sampled through the inlet. The differences between the two measurements were assumed to be caused by particle losses in the sampling lines and on average were 10 – 15 % of the signal (*Day*, personal communication). These losses were determined and applied nearly every day and were not applied as a function of size although variations in aerosol properties were observed on much finer time scales. Figure 7.1.17 presents a timeline of dry hourly averaged calculated accumulation mode b_{sp} and $PM_{2.5}$ dry b_{sp} measured with the nephelometer, demonstrating remarkable agreement in trends (R^2 correlation of 0.974). A scatter plot of the two estimates (shown in Figure 7.1.18) demonstrated higher calculated b_{sp} compared to measured values. The overall average percent difference was 33 ± 18 %. Calculating b_{sp} beyond the

accumulation mode to D_{ae} = 2.5 μm made very little difference in the comparison (see Figure 7.1.19). The correlation was 0.979 and the overall percent difference was 33 ± 17 %.

One possible reason for the discrepancy between measured and calculated b_{sp} is the difference in the losses applied to the data. If the theoretically predicted losses were too large, the calculated b_{sp} could decrease by 10 – 15 %, bringing the two estimates into better agreement. The almost constant offset suggested a multiplicative factor, such as a loss correction, could be the cause. No other reasons for the offset have been identified and this offset was not observed in any of the other closure experiments performed in Chapter 6.

7.2 MASS SCATTERING EFFICIENCIES

A mass extinction efficiency can be assigned to any particle that scatters or absorbs light along a sight path. The formulation in the previous section to calculate b_{sp} can be used to compute the mass scattering and absorption efficiencies. If Equation 7.1.2 is written in terms of a particle mass distribution, a mass scattering efficiency (e_{sp}) can be related to the Mie scattering efficiency, Q_{sp}, by Equation 7.2.1:

$$e_{sp} = \frac{3}{2}\frac{Q_{sp}}{D_p \rho_p} \qquad (7.2.1)$$

where the particle density (ρ_p) is now included. The scattering efficiency for a particular species for use in a linearized model is often computed by assuming a lognormal distribution, mass mean diameter and geometric standard deviation that represents measured species mass distributions. In general, however, total light scattering

coefficients cannot be represented by the sum of multiplied species mass concentrations (M_i) and scattering efficiencies (e_i) ($b_{sp} \neq \Sigma M_i e_i$) in an internally mixed aerosol model due to non-linearities in efficiency with size and composition (*Ouimette and Flagan*, 1982). However, other researchers have shown that assumptions of internally mixed aerosols produced results that were only 5-10% different from the assumptions of externally mixed aerosols and $b_{sp} = \Sigma e_i M_i$ (*Malm et al.*, 2000; *Malm*, 1998; *Sloan*, 1986; *Ouimette and Flagan*, 1982). *Hasan and Dzubay* (1983) showed that the presence of an absorbing species reduced scattering but enhanced absorption when aerosols were assumed to be internally versus externally mixed, however the overall extinction was unchanged.

It should be pointed out that the effect of particle hygroscopicity on derived scattering coefficients is very important because the uptake of water alters the particle optical properties as well as particle size. Estimates of humidity dependent scattering coefficients are measurable and derivable by assuming models of aerosol hygroscopicity, however this work focuses on accurate estimations of dry scattering coefficients. If the dry aerosol scattering properties are not well understood, neither will be the effects of humidity on those properties.

Reconstructed scattering was calculated by following IMPROVE methods and applying typical estimates of dry mass scattering efficiencies (*Malm et al.*, 1994). Equation 7.2.2 provides the relationship between reconstructed total b_{sp} and species mass concentrations (given in brackets):

$$b_{sp} = (3\ m^2\ g^{-1})[SO_4^{-2}] + (3\ m^2\ g^{-1})[NO_3^-] + (3\ m^2\ g^{-1})[OC] + (1\ m^2\ g^{-1})[Soil] + 0.6[\text{Coarse Mass}] \quad (7.2.2)$$

The dry scattering efficiency for sulfate, nitrate and organic carbon is assumed to be 3 m^2 g^{-1},for fine soil 1.0 m^2 g^{-1}, and for coarse mass 0.6 m^2 g^{-1}. The nominal scattering efficiency of 3 m^2 g^{-1} is based on a literature review by *Trijonis et al.* (1988, 1990). A 3 m^2 g^{-1} efficiency was used for nitrate and OC because no additional information was available due to a lack of measured nitrate and OC size distributions. Sulfate mass size distributions measured in the Grand Canyon region suggested values of 2.2 m^2 g^{-1} (*Malm and Pitchford*, 1997), whereas a value of 3.8 ± 0.6 m^2 g^{-1} was determined in the Great Smoky Mountains National Park (*Ames et al.*, 2000). An efficiency of 3 m^2 g^{-1} corresponds to a lognormal aerosol distribution with a mass mean diameter of 0.4 μm and geometric standard deviation of 2.0.

Malm and Day (2000) discussed observed discrepancies of 50 % or more in the western U. S. between measured extinction by transmissometry and reconstructed extinction. As mentioned, one reason could be the assumed value of coarse mass scattering efficiency. Although many studies have been performed to investigate the fine mode optical properties, less effort has been invested into understanding optical properties of coarse particles. Typically it is assumed that coarse mass composition is dominated by wind blown soil with corresponding mass scattering efficiencies of 0.4 – 0.6 m^2 g^{-1}. *Malm and Day* (2000) found higher values in the Grand Canyon with episodes having values near 1 m^2 g^{-1}. These issues were investigated during BRAVO using detailed measurements of accumulation and coarse mode particle size, b_{sp} and composition.

Estimates of mass scattering efficiencies for accumulation and coarse modes were made using size distribution information and calculated light scattering coefficients (Equation 7.3.1).

$$e_{mode} = \frac{b_{sp,mode}}{M_{mode}} = \frac{b_{sp,mode}}{V_{mode}\rho_p} \quad (7.3.1)$$

Mass concentrations were computed by multiplying the mode integrated volume concentrations (V_{mode}) (Chapter 6) by the retrieved effective densities converted to density using daily varying shape factors. The efficiencies computed from Equation 7.3.1 represented all species present in the accumulation or coarse modes. Figure 7.2.1 presents a timeline of hourly averaged dry accumulation mode mass scattering efficiencies (e_{acm}) demonstrating the variations during the study. The overall average was 3.4 ± 0.5 m^2 g^{-1} with lowest values in July (see Table 7.2.1), similar to the nominal value of 3 m^2 g^{-1} applied in the IMPROVE formula for fine non-soil species. The relationship between e_{acm} and derived accumulation mode mass concentrations is shown in Figure 7.2.2. A weak relationship was observed with increasing mass concentration corresponding to increasing efficiency. The relationship between e_{acm} and accumulation mode geometric volume mean diameter (D_{gv}) is shown in Figure 7.2.3. A similar relationship was observed for all months except for some periods in July and demonstrated a strong relationship of increasing e_{acm} with D_{gv}.

Coarse mode mass scattering efficiencies (e_{cm}) were calculated using Equation 7.2.2 and a timeline is presented in Figure 7.2.4. Higher values of e_{cm} were observed in July with an overall study average of 0.6 ± 0.2 m^2 g^{-1} (see Table 7.2.1), consistent with assumed values in the IMPROVE reconstructed scattering formula. Higher values of e_{cm} corresponded to lower coarse mass concentrations especially during September and

October as shown in Figure 7.2.5. Less dependence of e_{cm} on coarse mass concentrations was observed for July with overall higher e_{cm} than in the other months. *Malm and Day* (2000) observed similar trends in Grand Canyon National Park as those seen in September and October. They surmised that values as high as 1 m^2 g^{-1} were possible if coarse soil mass distributions shifted near the cyclone cut point (D_{ae} = 2.5 μm), or if coarse particles consisted of lower density species that scatter more light on a per mass basis. Coarse mass composition for BRAVO was not available in July and early August when the highest values of e_{cm} were observed but on average OC was 30 % of the coarse mass concentration during the rest of the study. Highest values of e_{cm} corresponded to volume geometric mean diameters near 2 μm (Figure 7.2.6), consistent with theoretical calculations performed by *Malm and Day* (2000) that suggested that higher efficiencies occurred for mass mean diameters near the 2.5 μm aerodynamic cyclone cut.

Reconstructed scattering calculations were made following the IMPROVE formula (Equation 7.2.2) as well as applying the efficiencies derived from size distribution data (see Equation 7.2.3).

$$b_{sp,rec} = e_{acm}[\text{fine}] + e_{cm}[\text{coarse}] \qquad (7.2.3)$$

where [fine] and [coarse] refer to the UCD fine and coarse mode mass concentrations, respectively, and included ammoniated sulfate, sodium nitrate, OC and soil. Reconstructed scattering estimates ($b_{sp,rec}$) were compared to calculated and direct nephelometer measurements of b_{sp}. Fine mode comparisons between calculated and reconstructed b_{sp} were made for the entire study but comparisons with nephelometer measurements could be made only after mid August. Calculated and reconstructed coarse

mode and total b_{sp} comparisons were made from late August through October when the coarse mode chemical composition was available.

Figures 7.2.7, 7.2.8, and 7.2.9 are scatter plots of calculated and reconstructed b_{sp} for the fine mode, coarse mode, and total distributions, respectively. Percent differences between calculated and reconstructed estimates were on the order of 35 % or less for both cases of reconstructed scattering coefficients. Correlations (R^2) were observed between calculated and reconstructed b_{sp} using IMPROVE efficiencies for fine (R^2= 0.864), coarse (R^2 = 0.583) and total b_{sp} (R^2 = 0.887). Reconstructed scattering coefficients computed with Equation 7.2.3 were correlated to calculated b_{sp} with R^2 = 0.788 for the fine mode, R^2 = 0.657 for the coarse mode and R^2 = 0.928 for total scattering coefficients. The fine mode correlation worsened when applying the computed efficiencies shown in Figure 7.2.1, however applying the computed coarse efficiencies resulted in a better correlation in total scattering coefficient. A correlation between calculated and reconstructed scattering using computed efficiencies was expected because both b_{sp} and mass scattering efficiencies were derived from the same size distributions, and closure between UCD mass concentrations and computed mass concentrations from size distributions was observed (see Chapter 6).

Fine ($PM_{2.5}$) nephelometer b_{sp} and both estimates of reconstructed b_{sp} were compared and demonstrated that estimates of efficiencies did not strongly affect the correlations, with R^2 = 0.880 for IMPROVE efficiencies and R^2 = 0.873 for derived efficiencies. Figure 7.2.10 is a scatter plot between $PM_{2.5}$ nephelometer b_{sp} and both cases of fine reconstructed b_{sp}; the overall percent difference was less than 30 % for both cases.

7.3 ESTIMATES OF PARTICLE EXTINCTION AND ABSORPTION

Estimates of absorption coefficients (b_{ap}) are often made by assigning an absorption efficiency to elemental carbon mass concentration measurements or by direct estimates of light attenuation through a filter membrane on which aerosols are deposited, such as a laser integrated plate method (LIPM) or an aethalometer. *Horvath* (1993) reviewed several filter based absorption measurements and discovered that depending on the method, filter measurements could be too high by 20 – 80 % because of filter albedo and loading. These results were confirmed by *Hitzenberger et al.* (1999) who showed that although different absorption measurements were correlated, estimates varied by more than factors of two. *Arnott et al.* (1999, 2000) have recently employed a new method to detect particle absorption by a photoacoustic technique that is very promising. Comparisons of data from this new instrument with aethalometer data during BRAVO resulted in a derived absorption efficiency of 6.5 m^2 g^{-1} (*Arnott et al.*, 2000). Mass absorption efficiencies have been reported in the literature to range from 5 to 20 m^2 g^{-1} (*Horvath*, 1993) with a value near 10 m^2 g^{-1} typically assumed. *Fuller et al.* (1999) were unable to justify values this high based on theoretical studies and concluded that efficiencies ranging from 5 –8 m^2 g^{-1} were more appropriate.

Obviously there is no well agreed upon method for measuring particle absorption, yet estimates are important because of their implications not only to visibility, but to climate forcing effects of aerosols. Direct forcing estimates can range from +0.16 to +0.42 W m^{-2} for black carbon aerosol (*Myhre et al.*, 1998). The sign of this forcing (heating or cooling) is governed by the particle single-scattering albedo (ω) which is a measure of the particle scattering versus extinction properties. Lower values of ω

correspond to a more absorbing aerosol. The single-scattering albedo is a function of the aerosol size distribution and chemical composition. Estimates of ω during BRAVO will be presented later in this section.

Light absorption and extinction distributions ($db_{ap}/dlogD_p$, $db_{ext}/dlogD_p$) were calculated similarly to the scattering distributions shown in Figure 7.1.7 and Figure 7.1.8, but using complex refractive indices with the imaginary part computed from UCD fine EC compositions (see Chapter 6). The extinction, scattering and absorption distributions are shown in Figure 7.3.1 for a Saharan dust day on July 6 1999 (DOY 187). The presence of significant coarse particle extinction and absorption is demonstrated well on this day, in contrast to Figure 7.3.2 that shows a strong accumulation mode contribution to extinction and negligible coarse mode contributions to extinction on October 12 1999 (DOY 285). October 12 was associated with high sulfate mass concentrations.

The presence of significant coarse particle absorption on DOY 187 was very interesting and can be explained by investigating the behavior of the Mie extinction efficiencies (Q_{ext}) at larger sizes. Particles with diameters near 0.7 – 1.0 μm become less efficient at scattering and more efficient at total extinction, relative to smaller particles, so the difference between them, the Mie absorption efficiency ($Q_{ap} = Q_{ext} - Q_{sp}$), increases. To illustrate this, Figure 7.3.3 presents the extinction, scattering and absorption efficiencies as functions of particle diameter for two complex refractive indices ($m = 1.57 - 0.005i$, $m = 1.57 - 0.1i$). The increase in Q_{ap} and decrease in Q_{sp} occurred near the same diameter (~ 0.7 μm) and varied in magnitude depending on the value of the absorbing part of refractive index. Figure 7.3.4 demonstrates this behavior more clearly by showing Q_{ap}/Q_{ext} and its increase for $D_p > 0.7$ μm. Significant coarse mode contributions to

particle absorption occur because the importance of small concentrations of EC is magnified when there are significant mass concentrations in particles larger than 1 μm. The accumulation and coarse mode dry b_{ap} and b_{ext} were computed for each sample by integrating the distributions over each mode. The overall average total, accumulation mode and coarse mode extinction coefficients were 0.029 ± 0.017 km^{-1}, 0.023 ± 0.016 km^{-1} 0.006 ± 0.005 km^{-1}, respectively (see Table 7.3.1). The overall average absorption coefficients were 0.0026 ± 0.0016 km^{-1}, 0.0015 ± 0.0012 km^{-1}, and 0.0009 ± 0.0007 km^{-1}, respectively (Table 7.3.2). Figure 7.3.5 shows the variation of total, accumulation mode and coarse mode b_{ap} during the study.

A McGee Scientific aethalometer was operated in two modes during BRAVO to investigate the extent of coarse mode b_{ap} contributions to the total absorption coefficient. The aethalometer inlet switched between a PM_1 URG cyclone and a total aerosol inlet every hour to measure black carbon concentrations, [BC], (*Brown et al.*, 2000) that can be converted to an absorption coefficient by applying an absorption efficiency. In general, only minor contributions from coarse [BC] were observed, although periods did occur when ambient [BC] were larger than PM_1 [BC]. Figure 7.3.6 shows a timeline of daily averaged ambient and PM_1 black carbon concentrations (courtesy *S. Brown*) and many days with larger ambient [BC] are noticeable. However, it was believed that internal particle losses in the aethalometer could have removed a significant number of coarse particles from the sample flow before the aerosols were deposited on the filter. These losses have not been characterized.

Dry single-scattering albedo (ω) for the total distribution, accumulation and coarse modes were calculated with Equation 7.3.1.

$$\omega_{mode} = \frac{b_{sp,mode}}{b_{ap,mode} + b_{sp,mode}} \quad (7.3.1)$$

Daily averaged values of dry ω are shown in a timeline in Figure 7.3.7. The overall average total ω was 0.88 ± 0.05 with highest values observed in August and September (Table 7.3.3), suggesting particles during this period were more efficient at scattering, rather than absorbing light. The overall accumulation mode average ω was 0.92 ± 0.04, reflecting the higher scattering compared to absorption observed in the b_{ext} distributions. The overall coarse mode average ω was 0.75 ± 0.08, consistent with the higher relative absorption observed in the coarse mode distributions.

7.4 SUMMARY AND DISCUSSION

Estimates of dry light scattering coefficients were computed by applying Mie theory and measured dry aerosol size distributions. This method allowed for insight into the size distribution and composition of particles responsible for reduced visibility. Periods were observed when scattering by coarse mode particles contributed significantly to total light scattering coefficients. It was shown that scattering due to coarse mode particles by sizes near 2.0 μm was higher than scattering due to particles that were larger in size, suggesting smaller coarse mode particles were more efficient at light scattering. These periods occurred in July and early August and were linked to transport of Saharan dust into the park and to elevated fine soil mass concentrations. Although significant scattering due to coarse mode particles was observed during these periods, the highest overall light scattering coefficients measured during the study occurred under different conditions.

Accumulation mode particles were found to be the major contributor to total b_{sp}, with ~ 80 % of total b_{sp} due to scattering by accumulation mode particles. These events corresponded to peaks in fine mass concentration and transport to the park from east Texas and the Texas-Mexico border. The overall strong relationship between increased scattering due to accumulation mode particles and increased accumulation mode volume concentrations suggested that variations in composition and size of fine particles did not play as large a role in variations of b_{sp} as was seen for variations in b_{sp} due to coarse mode particles.

Comparisons of calculated and directly-measured dry b_{sp} by nephelometry were highly correlated although calculated values were larger by an offset of approximately 35 %. The differences were most likely due to the manner in which particle losses were treated for the different experimental methods.

The results presented in this chapter provided a thorough evaluation of the optical properties measured at the surface-based Kbar site. In the following chapter these investigations will be extended to comparisons with remotely-sensed aerosol optical properties.

Table 7.1.1 Estimates of dry light scattering coefficients (b_{sp}) using volume size distributions for the total, accumulation and coarse modes. Fractional contributions from the accumulation mode (R_{acm}) and coarse mode (R_{coarse}) are listed. Results are given as the average plus one standard deviation.

Month	Total b_{sp} (km^{-1})	Accumulation Mode b_{sp} (km^{-1})	Coarse Mode b_{sp} (km^{-1})	R_{acm}	R_{coarse}
July	0.024 ± 0.010	0.014 ± 0.007	0.010 ± 0.007	0.59 ± 0.19	0.40 ± 0.19
August	0.030 ± 0.015	0.024 ± 0.014	0.006 ± 0.005	0.80 ± 0.16	0.20 ± 0.16
September	0.03 ± 0.02	0.03 ± 0.02	0.0019 ± 0.0009	0.90 ± 0.07	0.10 ± 0.07
October	0.022 ± 0.014	0.020 ± 0.014	0.0023 ± 0.0017	0.86 ± 0.11	0.14 ± 0.10
Overall	0.026 ± 0.016	0.021 ± 0.015	0.005 ± 0.005	0.79 ± 0.18	0.20 ± 0.18

Table 7.1.2 Size parameters derived from dry light scattering distributions ($db_{sp}/dlogD_p$) for the accumulation and coarse modes. Results are given as the average plus one standard deviation.

Month	Accumulation Mode D_{gb} (μm)	Coarse Mode D_{gb} (μm)
July	0.34 ± 0.07	1.6 ± 0.4
August	0.34 ± 0.02	2.1 ± 0.5
September	0.33 ± 0.04	2.2 ± 0.6
October	0.31 ± 0.02	2.3 ± 0.3
Overall	0.33 ± 0.04	2.1 ± 0.6

Table 7.2.1 Accumulation and coarse mode dry mass scattering efficiencies ($m^2\ g^{-1}$) derived from volume size distributions and light scattering coefficients. Results are given as the average plus one standard deviation.

Month	Accumulation Mode e_{acm} ($m^2\ g^{-1}$)	Coarse Mode e_{coarse} ($m^2\ g^{-1}$)
July	3.3 ± 0.5	0.8 ± 0.2
August	3.4 ± 0.4	0.58 ± 0.12
September	3.4 ± 0.5	0.6 ± 0.2
October	3.4 ± 0.4	0.59 ± 0.11
Overall	3.4 ± 0.5	0.6 ± 0.2

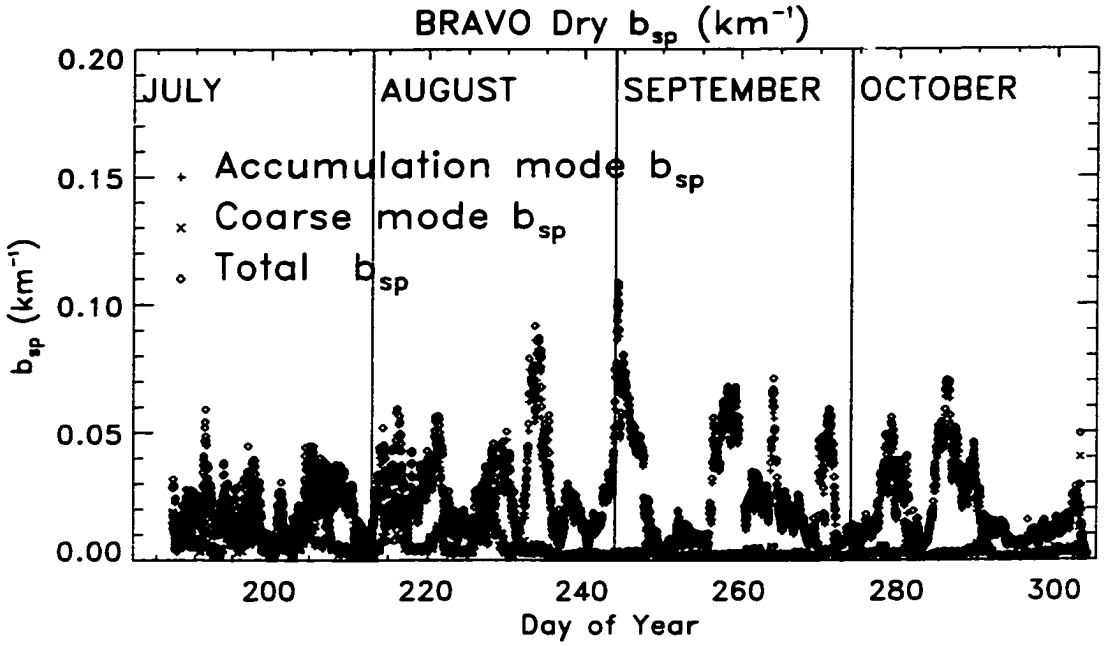

Figure 7.1.1 Hourly averaged dry calculated total b_{sp} (km^{-1}) from volume size distributions and retrieved refractive indices. Estimates for the accumulation and coarse modes are also shown.

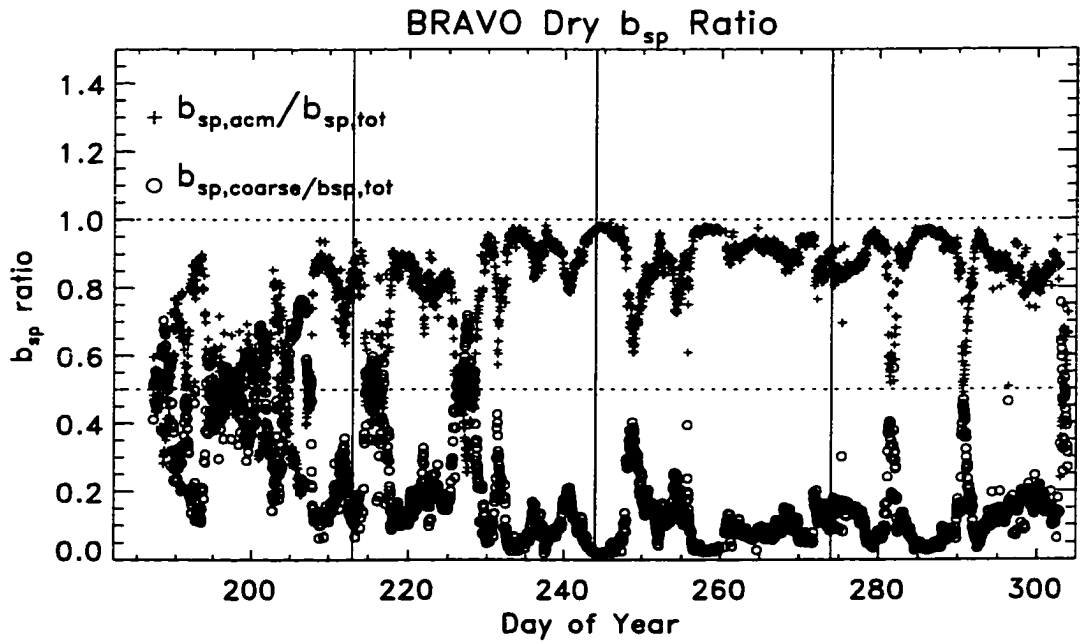

Figure 7.1.2 Fractional contribution of accumulation mode b_{sp} and coarse mode b_{sp} to total b_{sp}. Total b_{sp} included accumulation, coarse and giant particle modes.

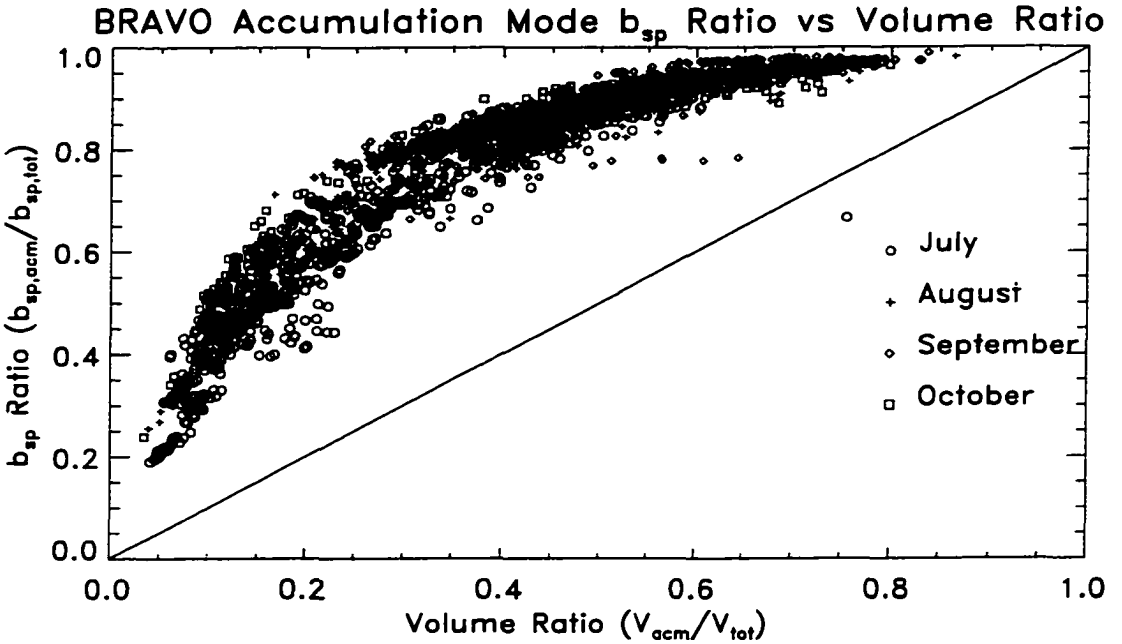

Figure 7.1.3 Accumulation mode volume ratios plotted with accumulation mode b_{sp} ratios.

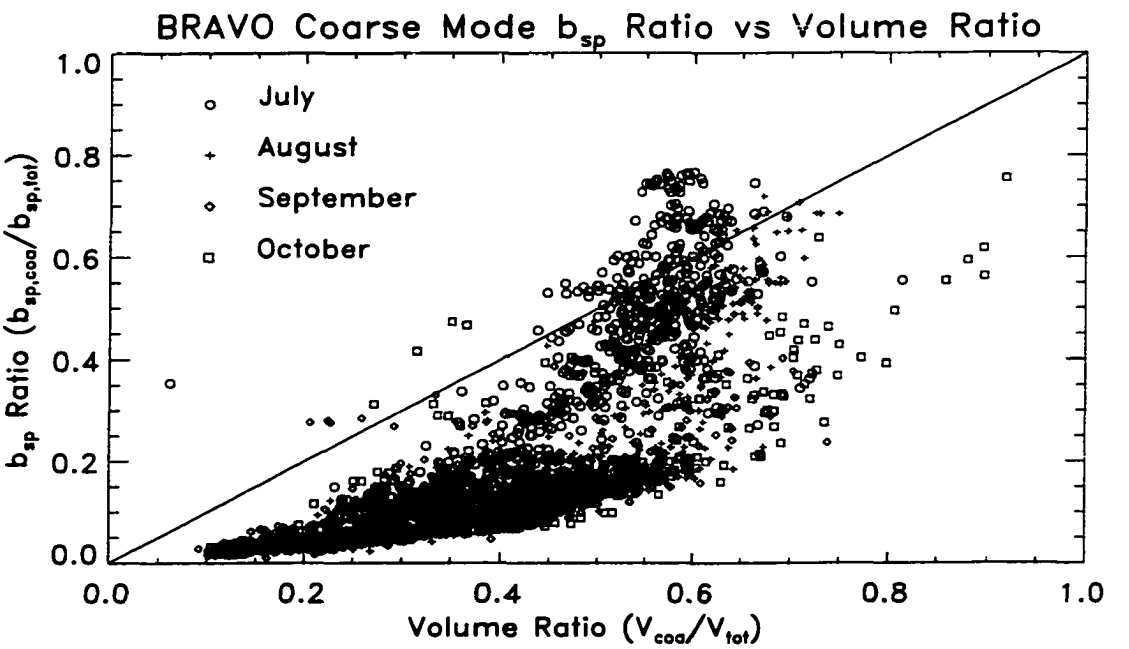

Figure 7.1.4 Coarse mode volume ratios plotted with coarse mode b_{sp} ratios.

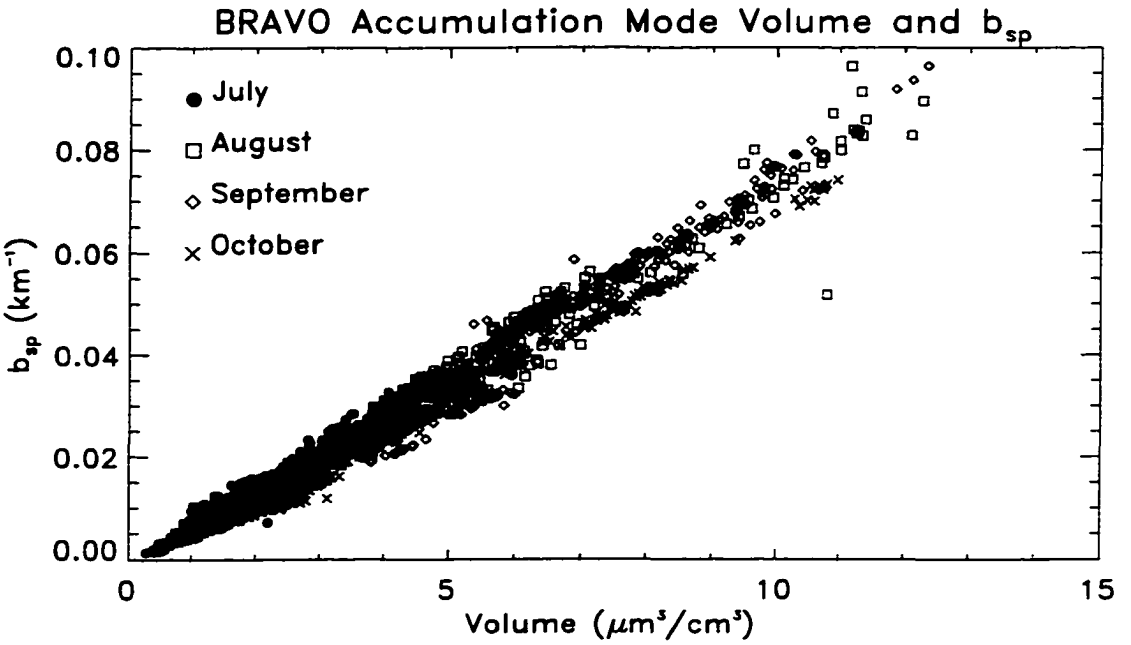

Figure 7.1.5 Accumulation mode b_{sp} (km^{-1}) versus accumulation mode volume concentrations (μm^3 cm^{-3}).

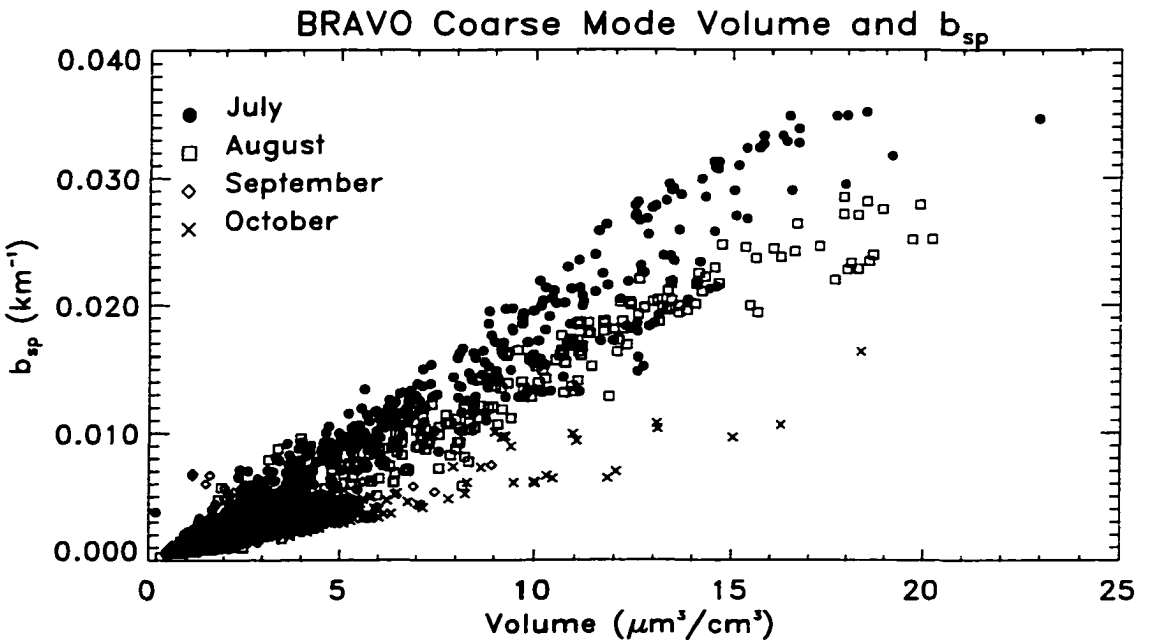

Figure 7.1.6 Coarse mode b_{sp} (km^{-1}) versus coarse mode volume concentrations (μm^{3}cm^{-3})

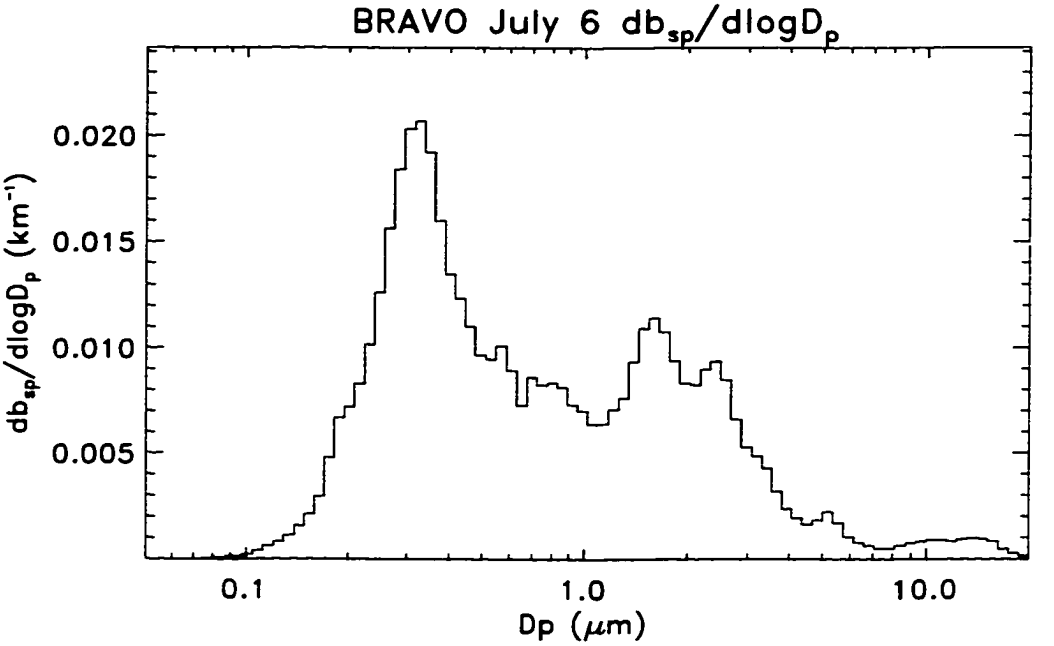

Figure 7.1.7 Light scattering distribution ($db_{sp}/dlogD_p$) on July 6 1999 (DOY 187).

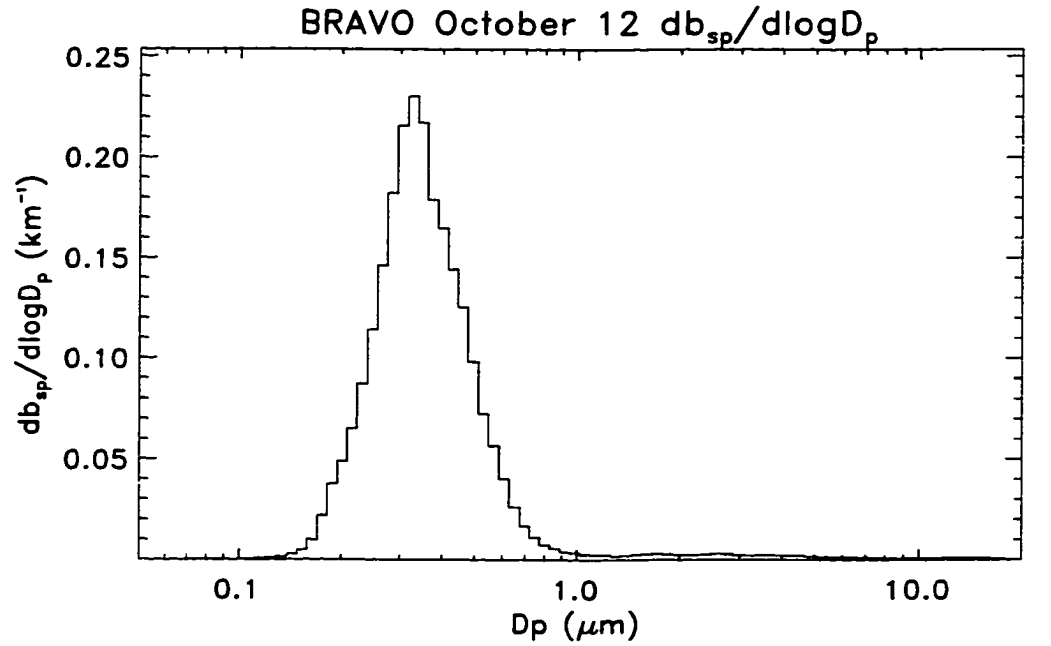

Figure 7.1.8 Light scattering distribution ($db_{sp}/dlogD_p$) on October 12 1999 (DOY 285).

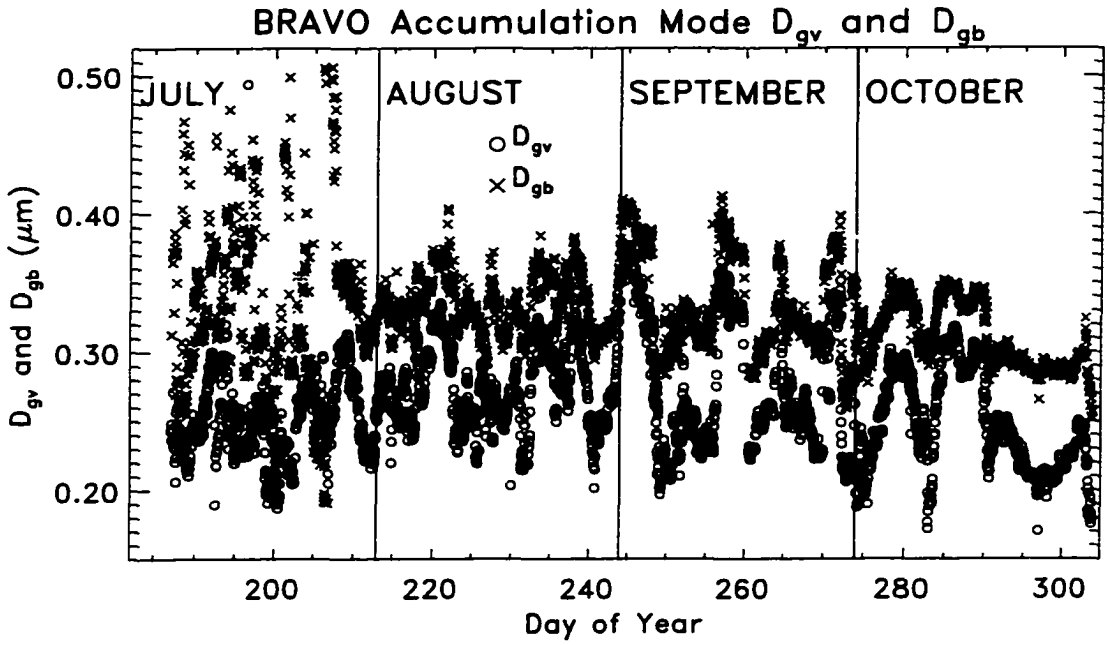

Figure 7.1.9 Timeline of dry hourly averaged accumulation mode volume geometric mean diameter (D_{gv}) and light scattering geometric mean diameter (D_{gb}) in micrometers.

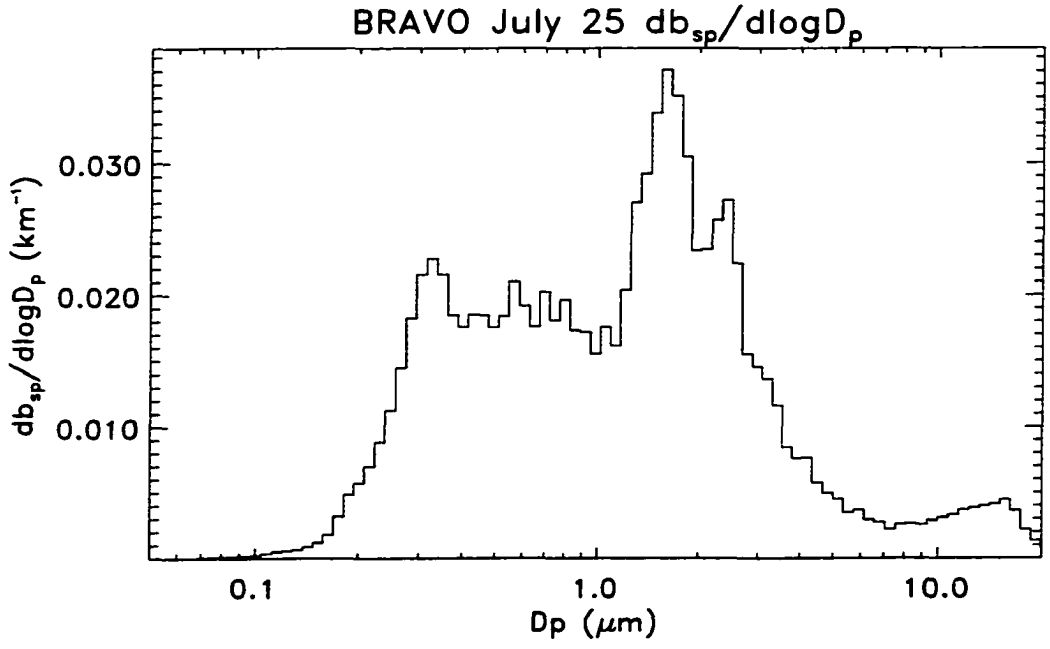

Figure 7.1.10 Light scattering distribution ($db_{sp}/dlogD_p$) on July 25 1999. The odd shape of the accumulation mode demonstrates the reason for large accumulation mode D_{gb}.

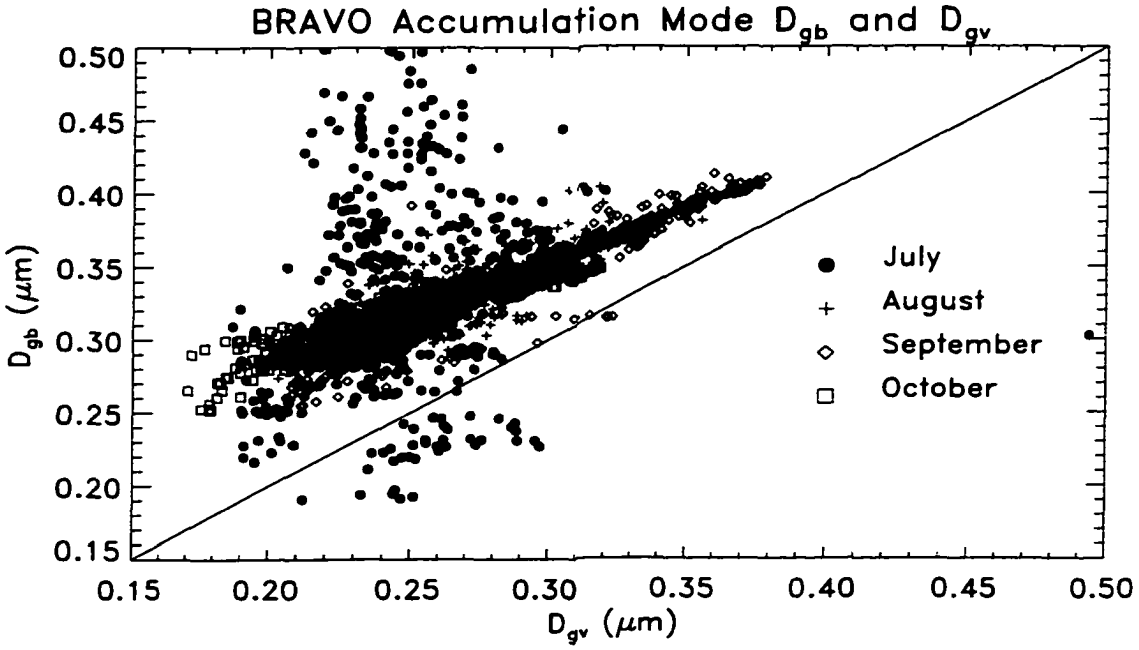

Figure 7.1.11 Accumulation mode volume mean geometric diameter (D_{gv}) versus light scattering geometric mean diameter (D_{gb}) in micrometers.

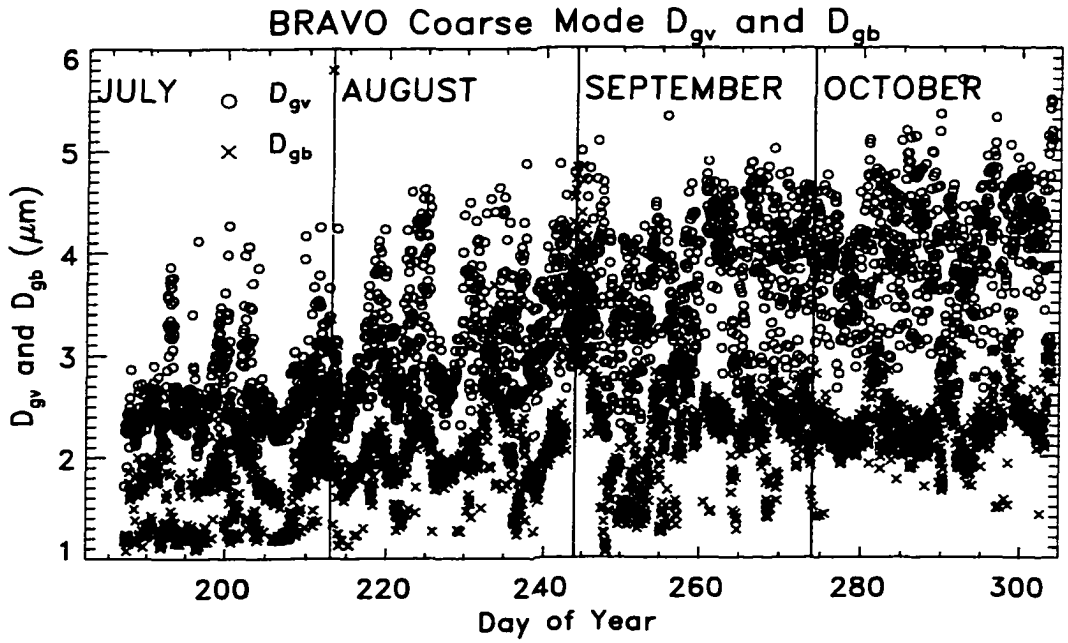

Figure 7.1.12 Timeline of hourly averaged dry coarse volume geometric mean diameter (D_{gv}) and light scattering geometric mean diameter (D_{gb}) in micrometers.

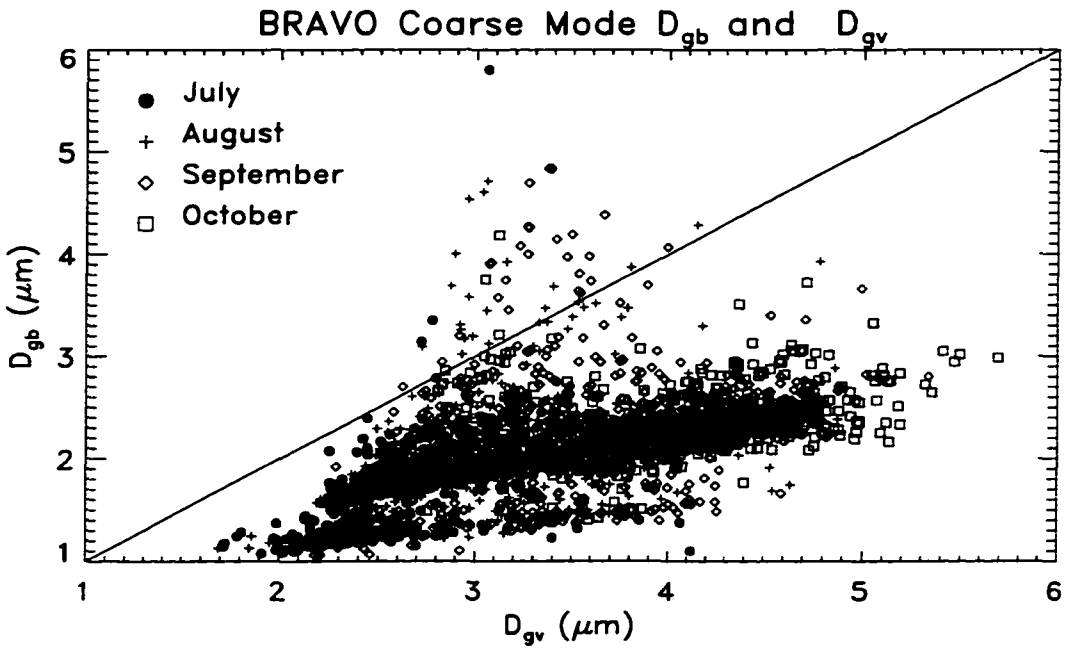

Figure 7.1.13 Coarse mode volume geometric mean diameter (D_{gv}) versus coarse mode light scattering geometric mean diameter (D_{gb}).

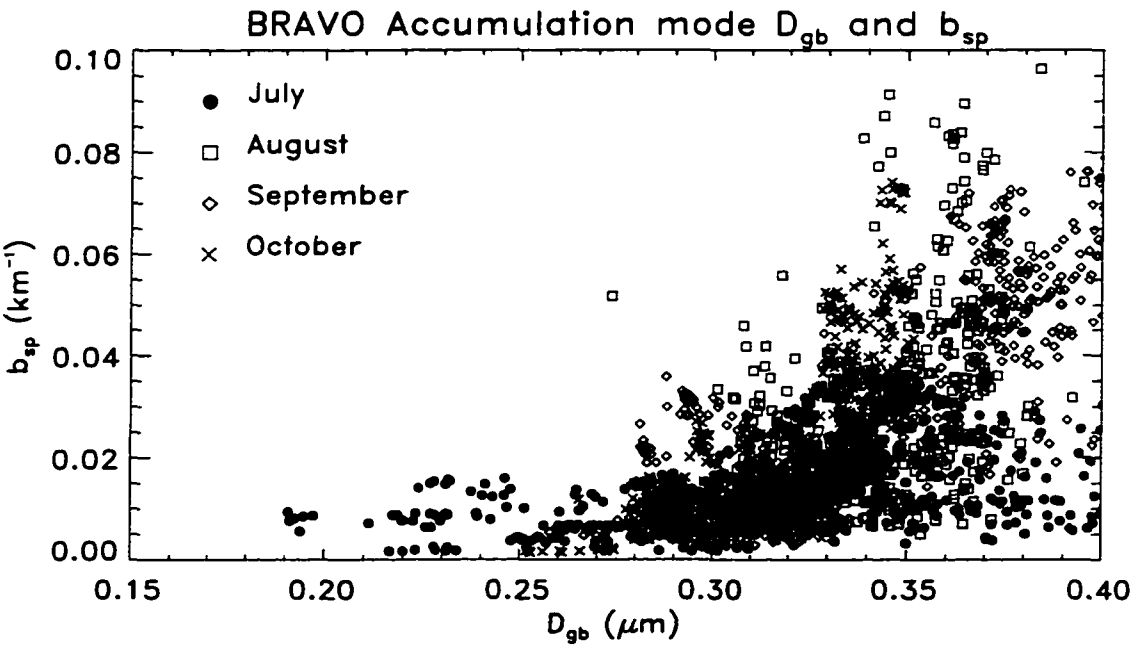

Figure 7.1.14 Accumulation mode b_{sp} versus light scattering geometric mean diameter (D_{gb}).

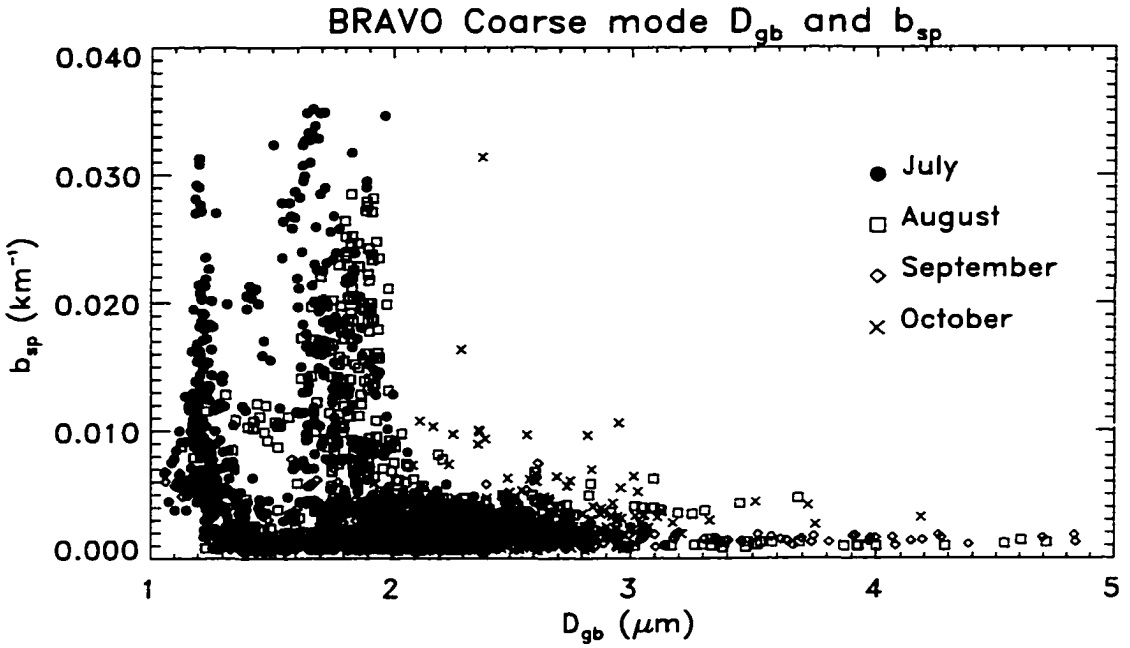

Figure 7.1.15 Coarse mode b_{sp} versus light scattering geometric mean diameter (D_{gb}).

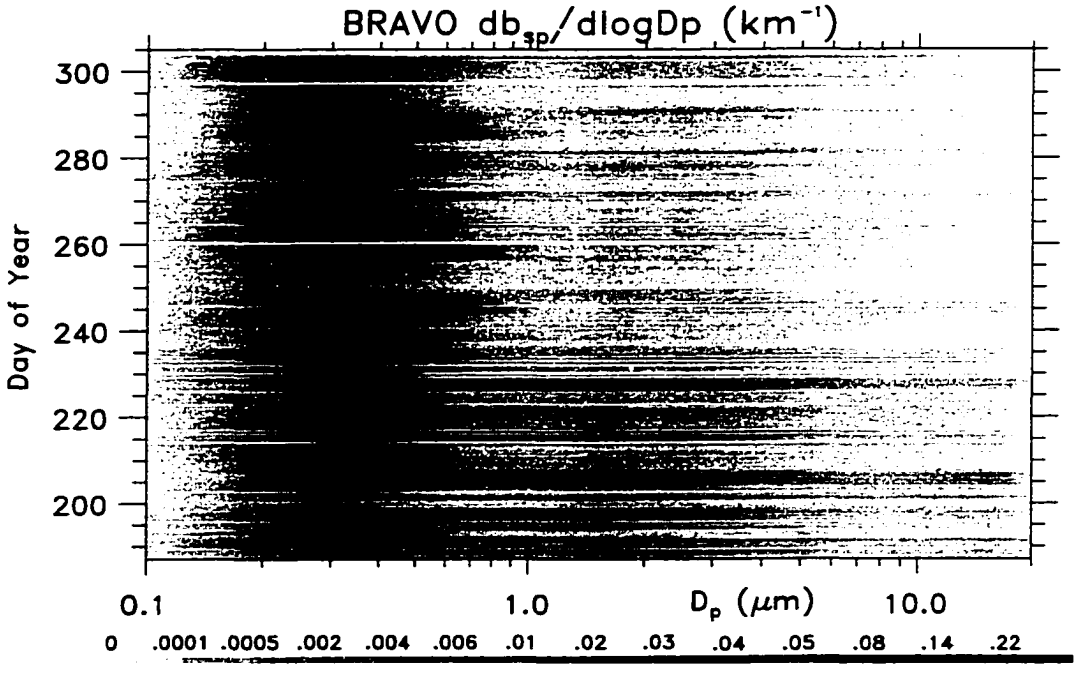

Figure 7.1.16 Contours of light scattering coefficient distributions (km^{-1}).

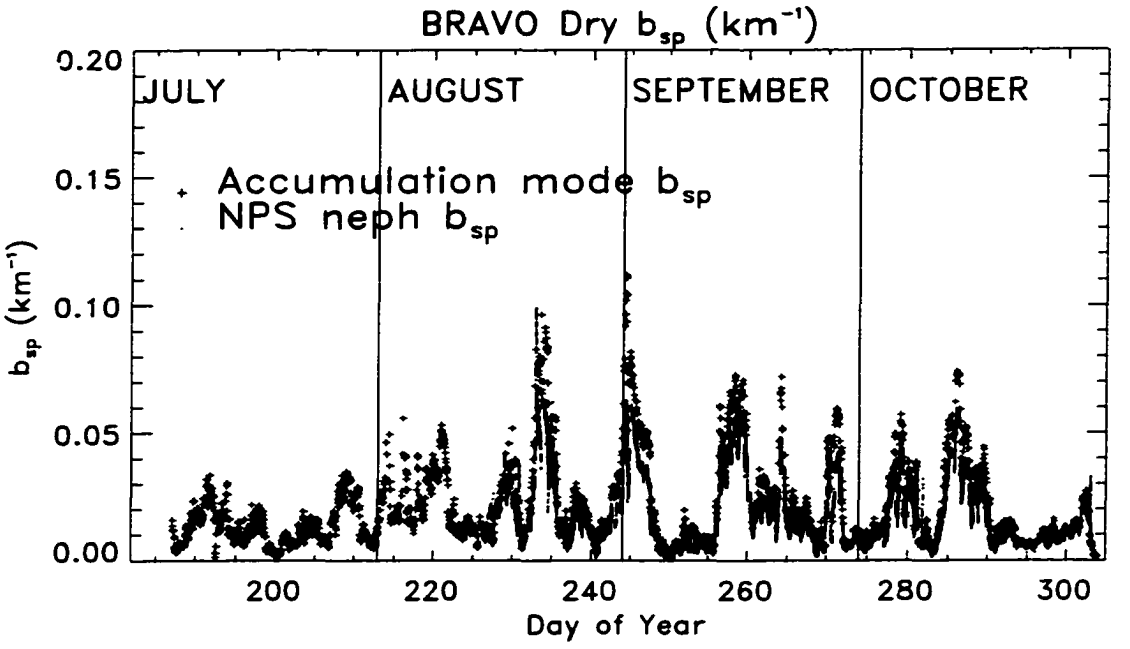

Figure 7.1.17 Timeline of hourly averaged dry NPS nephelometer $PM_{2.5}$ b_{sp} with calculated accumulation mode b_{sp} (km^{-1}).

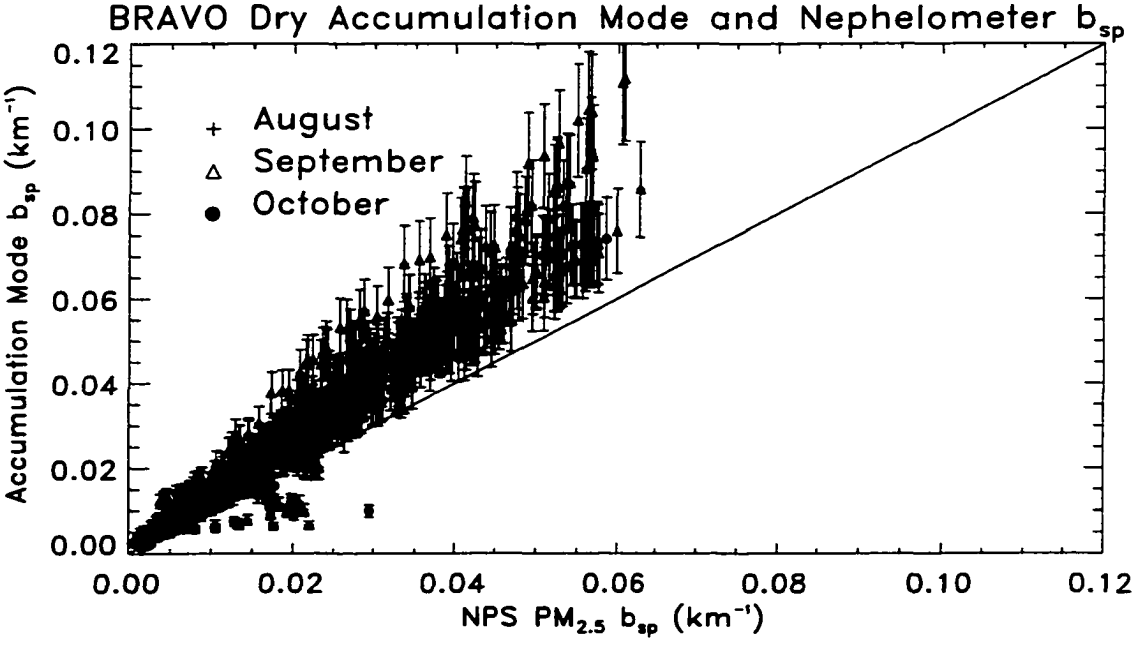

Figure 7.1.18 Calculated hourly averaged dry accumulation mode b_{sp} versus NPS nephelometer $PM_{2.5}$ b_{sp}.

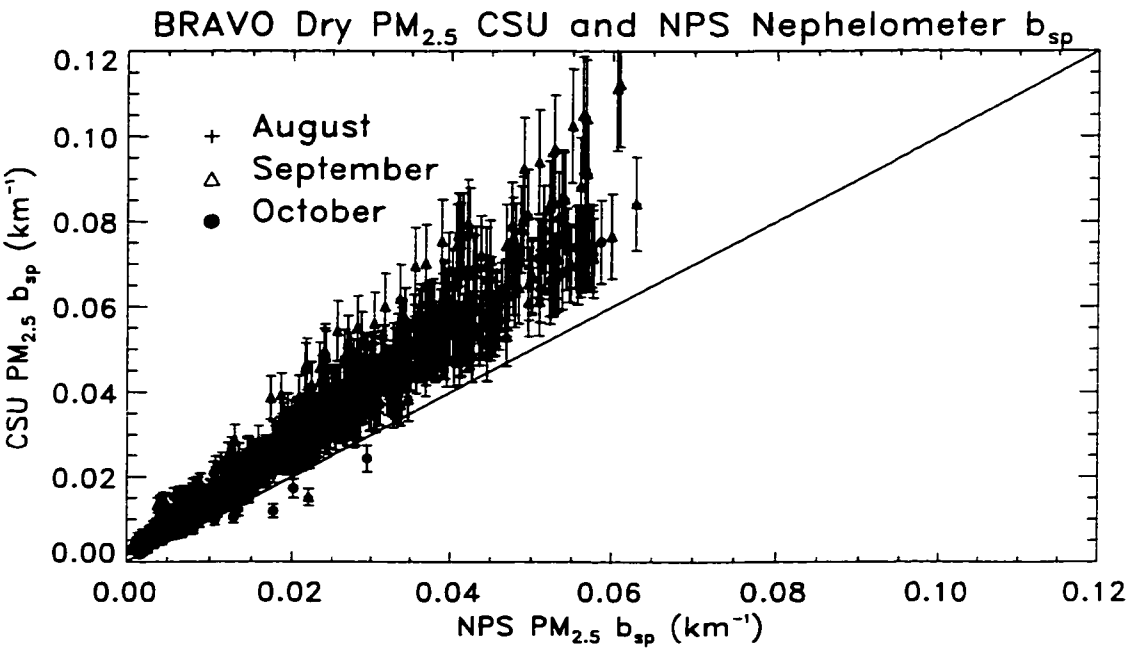

Figure 7.1.19 Calculated hourly averaged dry $PM_{2.5}$ b_{sp} by CSU versus NPS nephelometer $PM_{2.5}$ b_{sp} (km^{-1}).

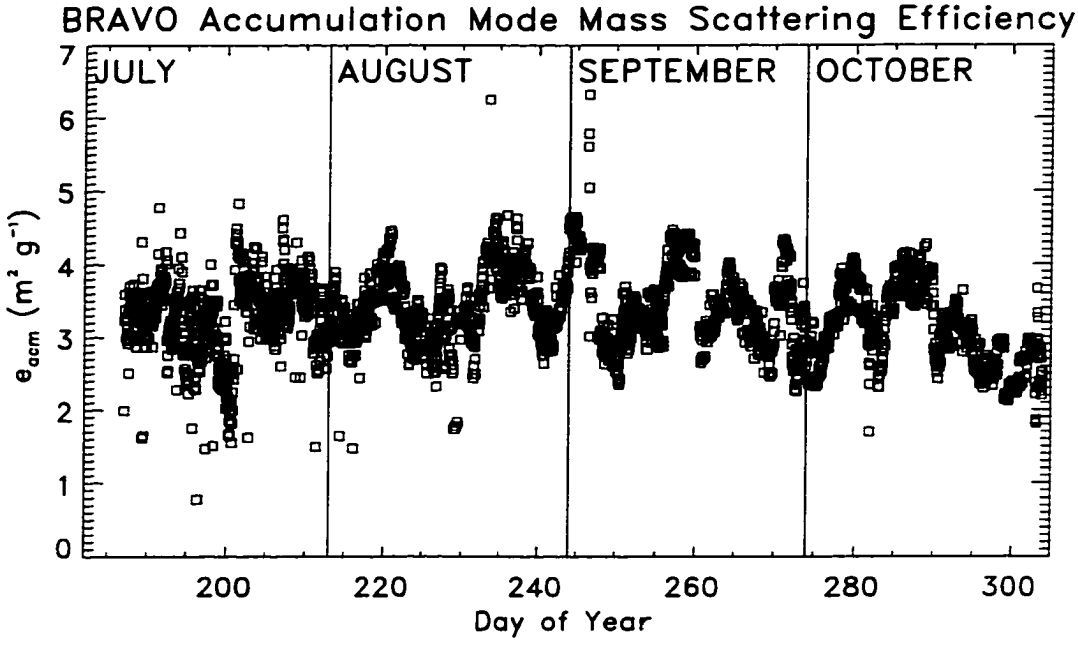

Figure 7.2.1 Timeline of hourly averaged dry accumulation mode mass scattering efficiencies (m^2 g^{-1}) calculated from volume distributions and retrieved densities.

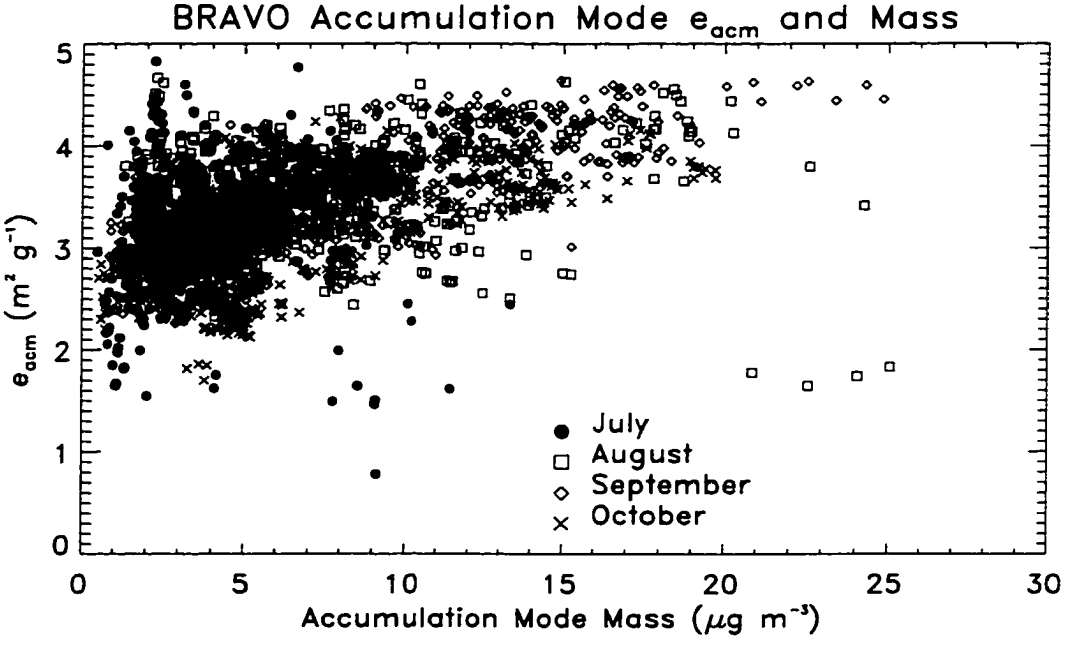

Figure 7.2.2 Dry accumulation mode mass scattering efficiencies (m^2 g^{-1}) versus derived accumulation mode mass concentration (μg m^{-3}).

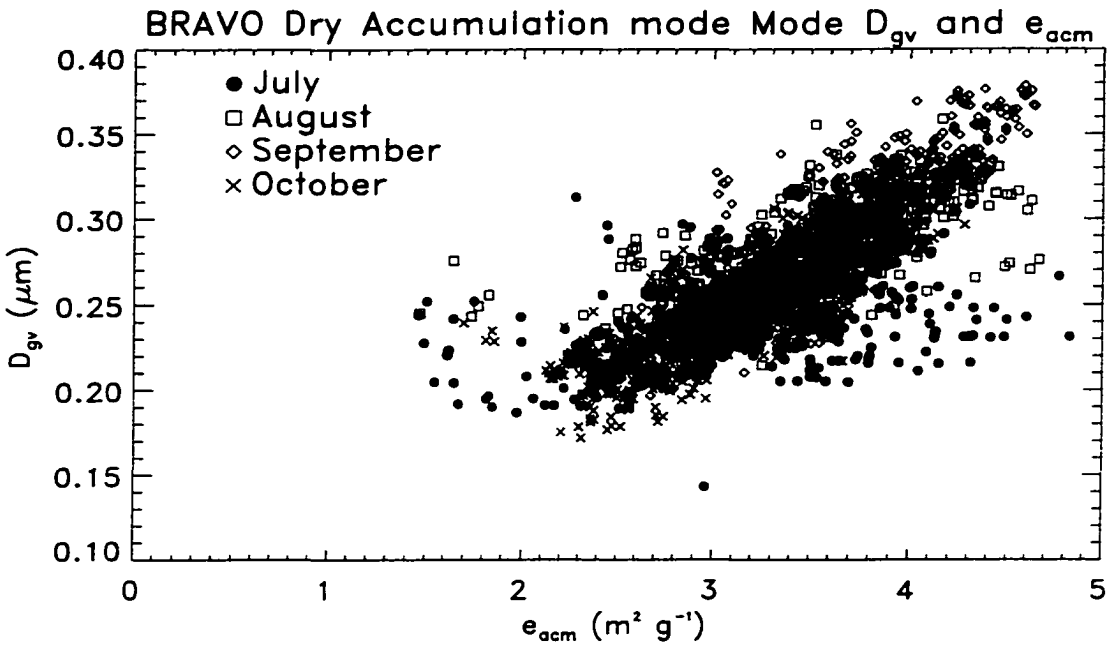

Figure 7.2.3 Dry accumulation mode mass scattering efficiencies (m^2 g^{-1}) versus accumulation mode volume geometric mean diameter (μm).

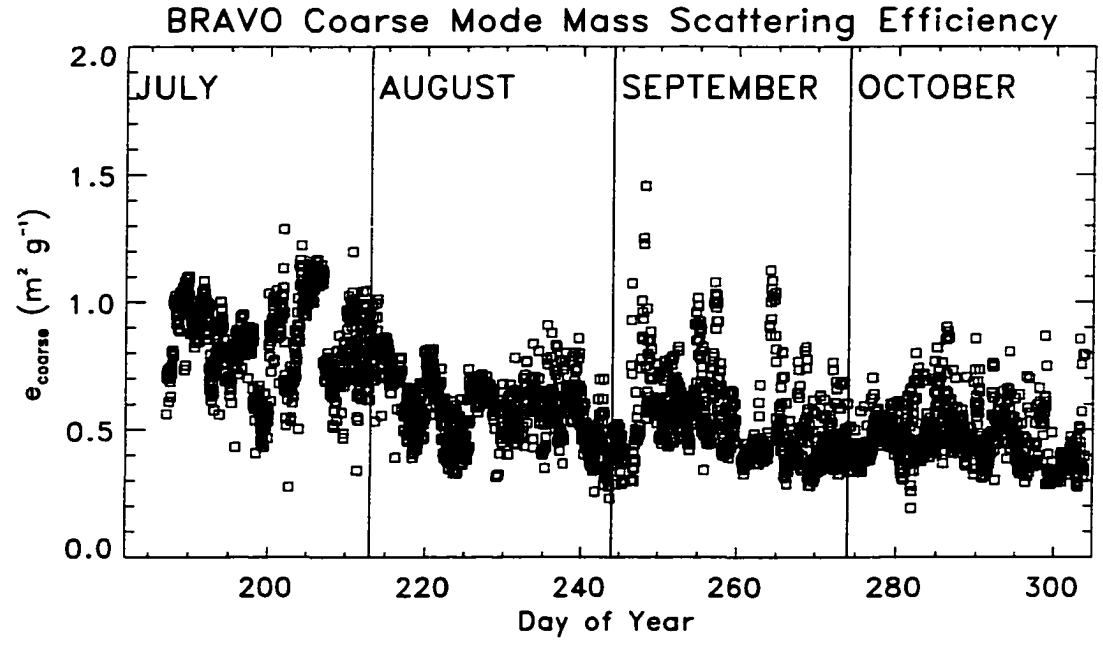

Figure 7.2.4 Timeline of hourly averaged dry coarse mass scattering efficiencies (m^2 g^{-1}) derived from size distributions and retrieved densities.

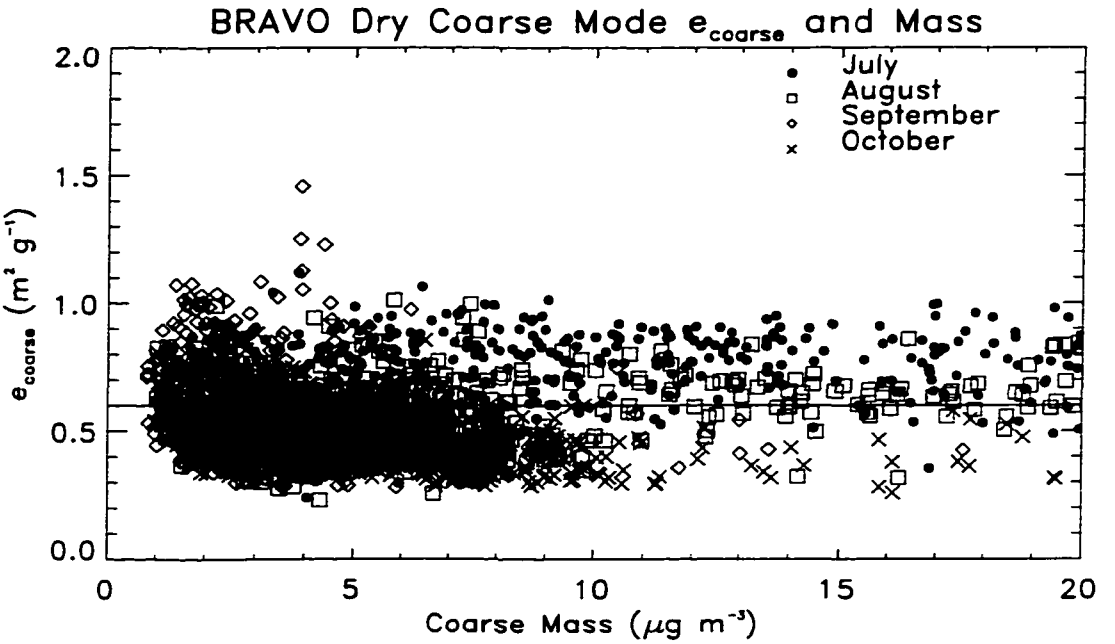

Figure 7.2.5 Dry coarse mode scattering efficiencies (m^2 g^{-1}) versus derived coarse mass concentration (μg m^{-3}). The line corresponding to 0.6 m^2 g^{-1} represents a wind-blown soil composition.

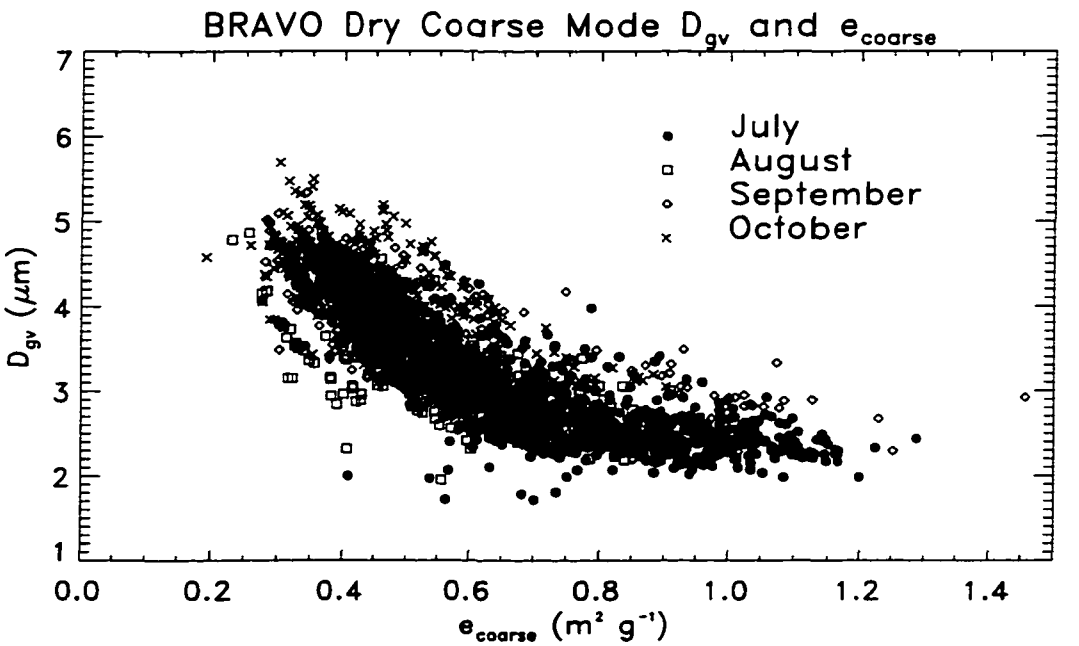

Figure 7.2.6 Dry coarse mode mass scattering efficiencies (m^2 g^{-1}) versus coarse mode volume geometric mean diameter (μm).

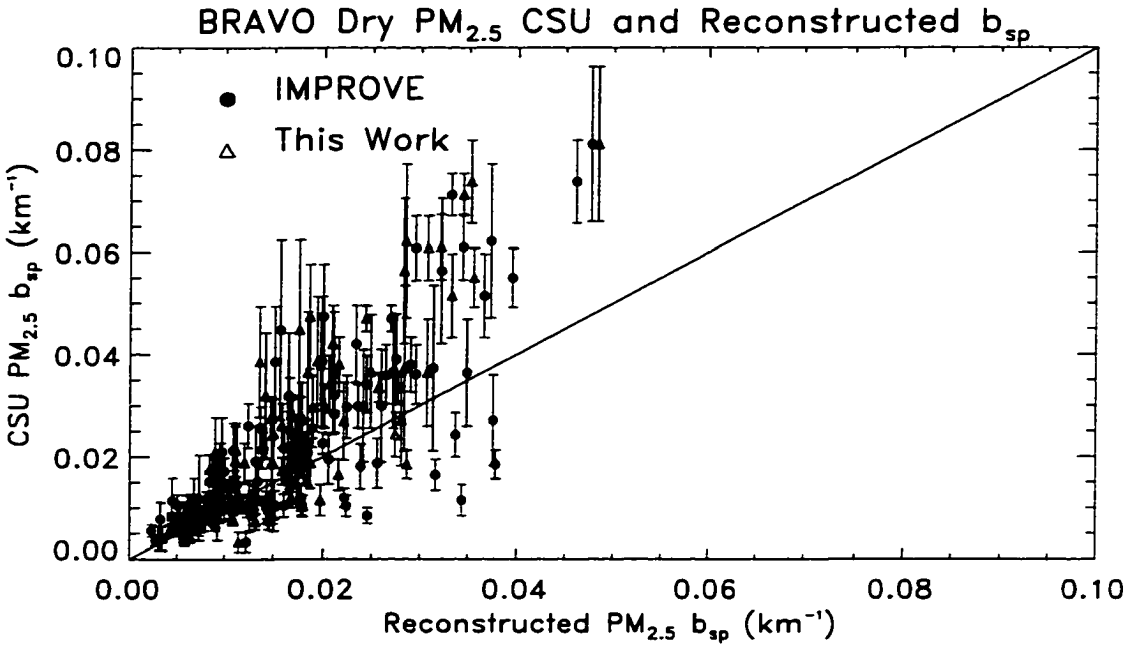

Figure 7.2.7 Dry reconstructed fine b_{sp} calculated with IMPROVE mass scattering efficiencies and those derived in this work, versus calculated daily averaged dry accumulation mode b_{sp}.

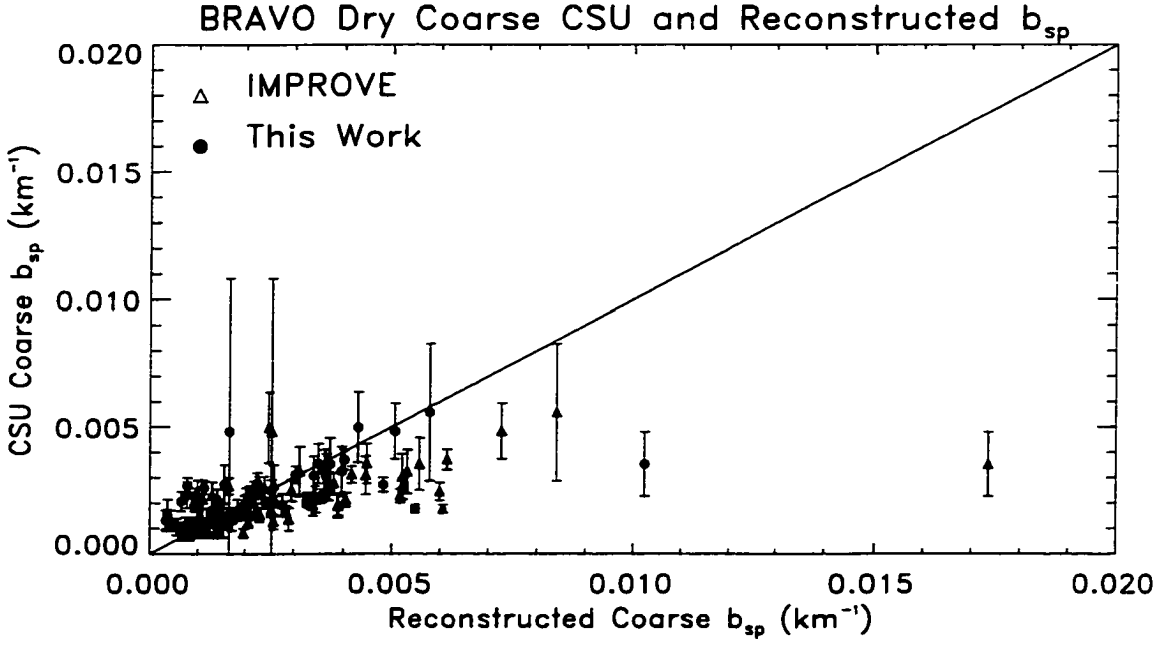

Figure 7.2.8 Dry reconstructed coarse b_{sp} calculated with IMPROVE mass scattering efficiencies and those derived in this work, versus calculated daily averaged dry coarse mode b_{sp}.

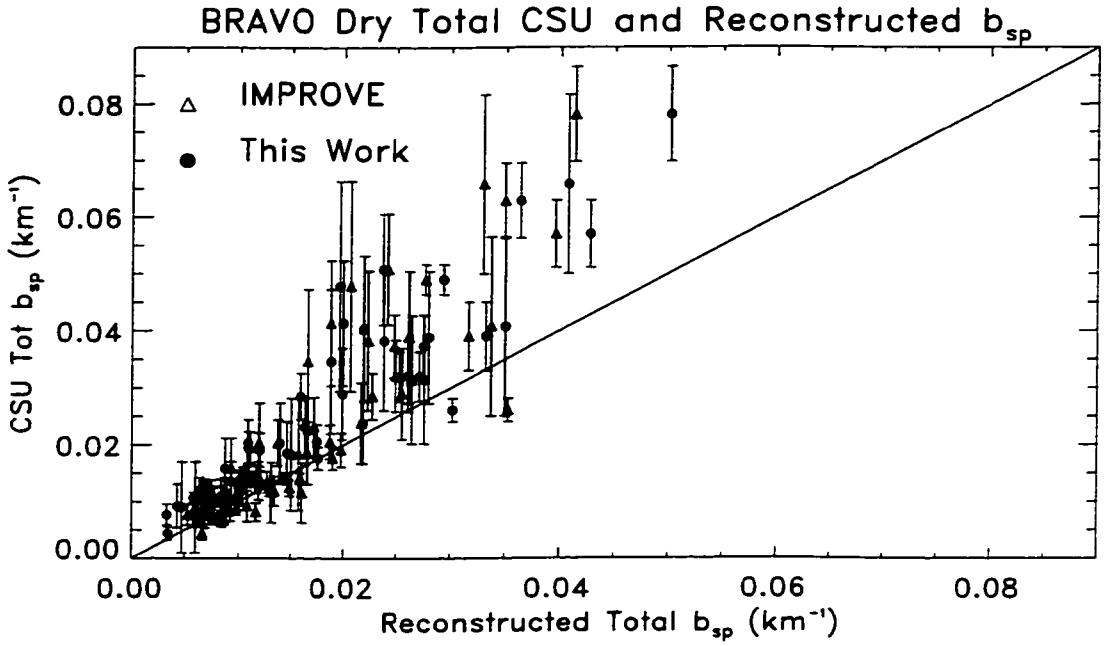

Figure 7.2.9 Dry reconstructed total b_{sp} calculated with IMPROVE mass scattering efficiencies and those derived in this work, versus calculated daily averaged dry total b_{sp}.

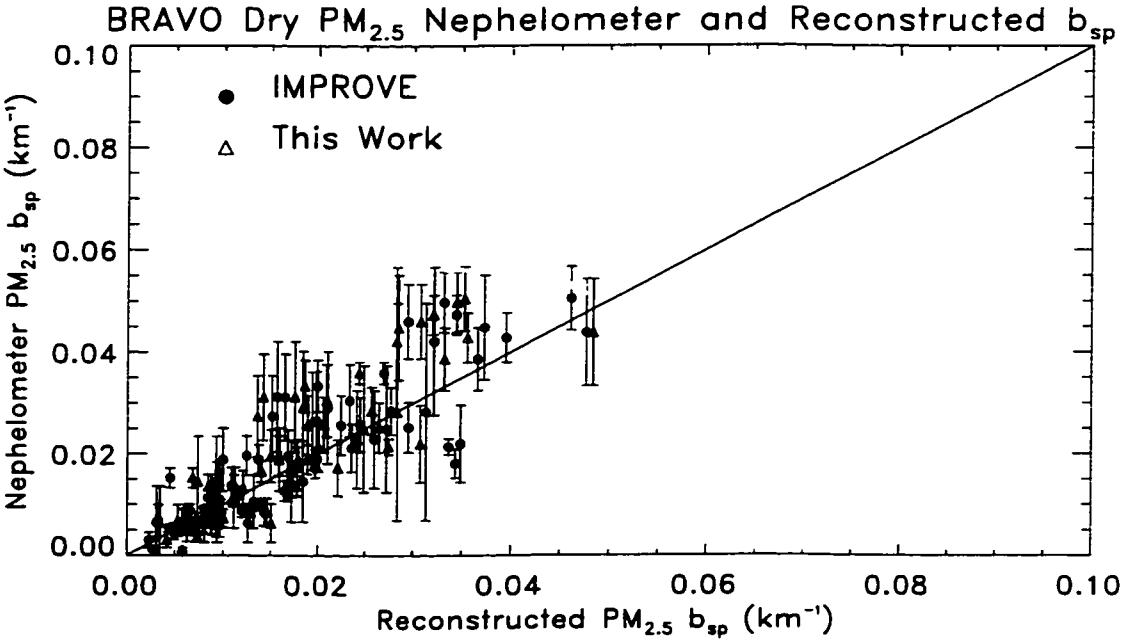

Figure 7.2.10 Dry reconstructed fine b_{sp} calculated with IMPROVE mass scattering efficiencies and those derived in this work, versus nephelometer measured dry $PM_{2.5}$ b_{sp}.

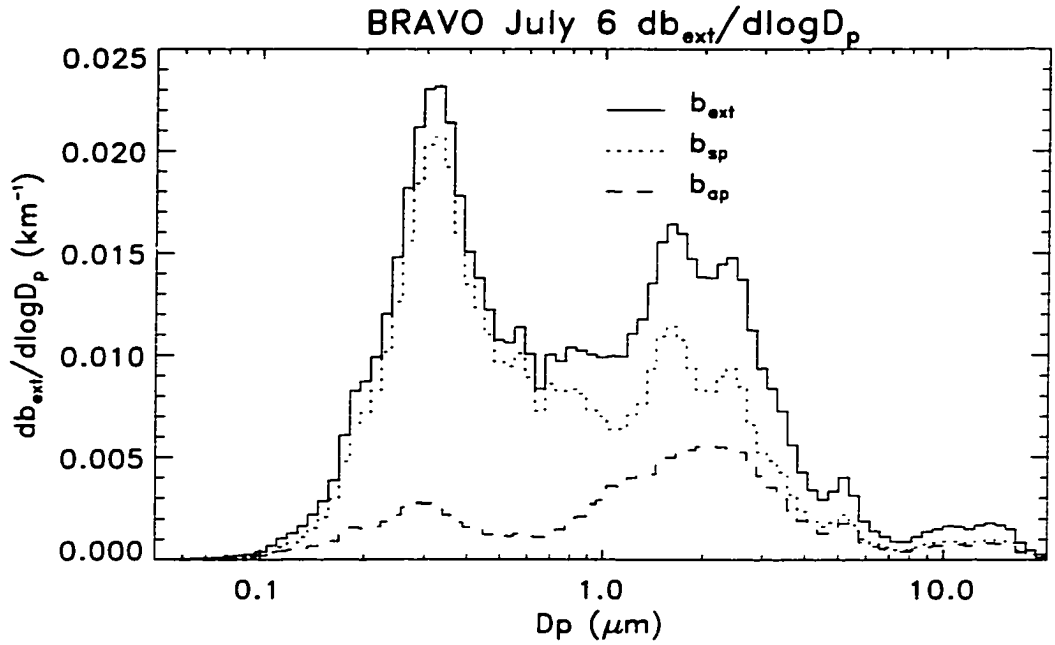

Figure 7.3.1 Light extinction, scattering, and absorption distributions for July 6 1999 (DOY 187).

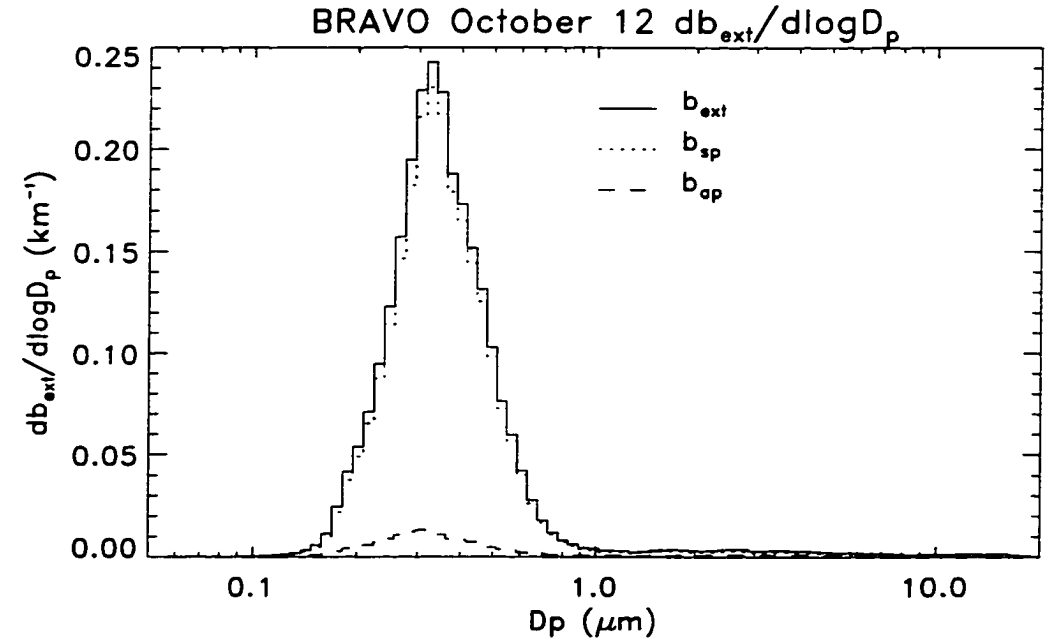

Figure 7.3.2. Light extinction, scattering, and absorption distributions for October 12 1999 (DOY 285). Notice the change in scale from Figure 7.3.1.

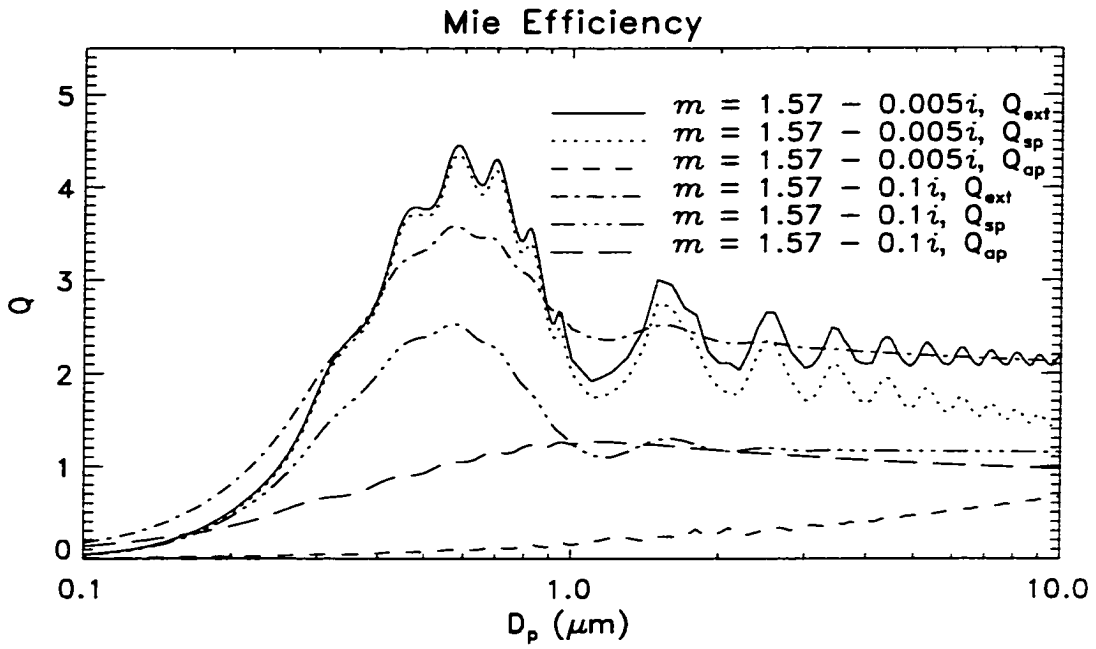

Figure 7.3.3 Mie scattering (Q_{sp}), extinction (Q_{ext}) and absorption (Q_{ap}) efficiencies for m = 1.57 –0.005i, and m = 1.57 –0.1i.

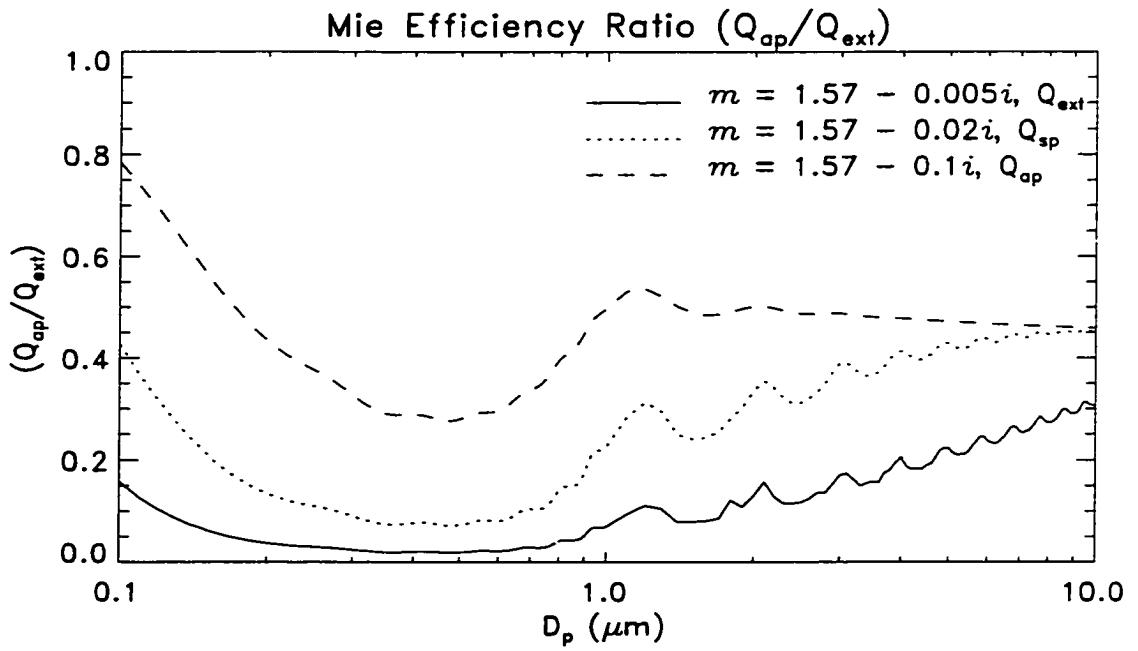

Figure 7.3.4 Ratio of Mie absorption to Mie extinction efficiencies (Q_{ap}/Q_{ext}) for m = 1.57 – 0.02i, m = 1.57 – 0.005i and m = 1.57 –0.1i.

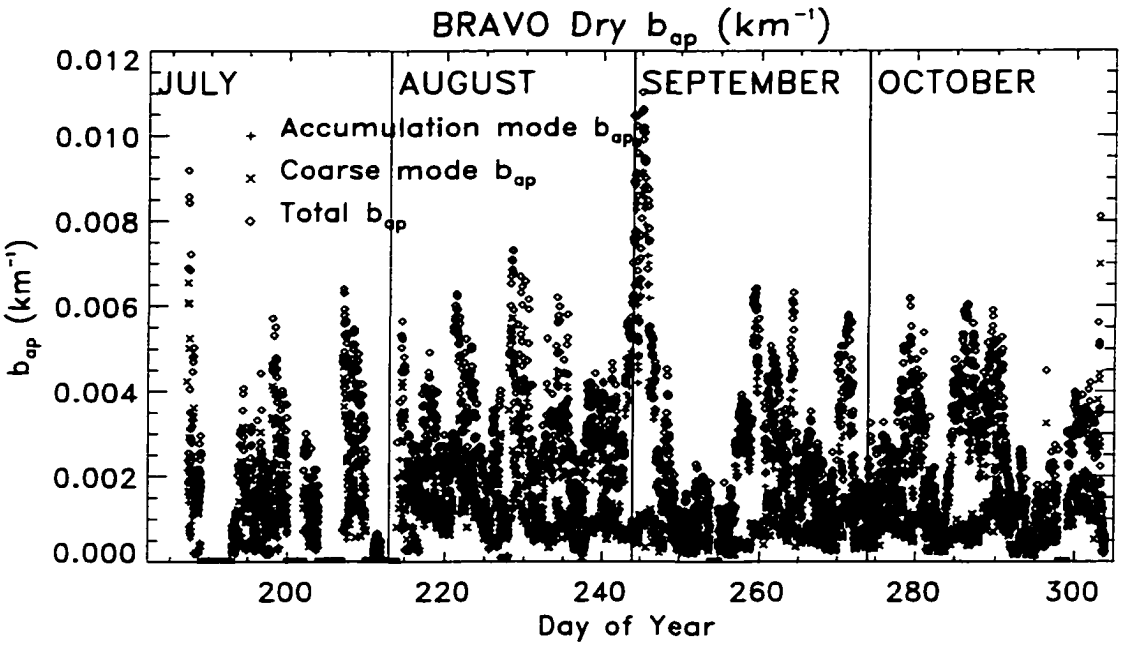

Figure 7.3.5 Timeline of dry hourly averaged total, accumulation mode and coarse mode light absorption coefficients (b_{ap}) derived from size distributions.

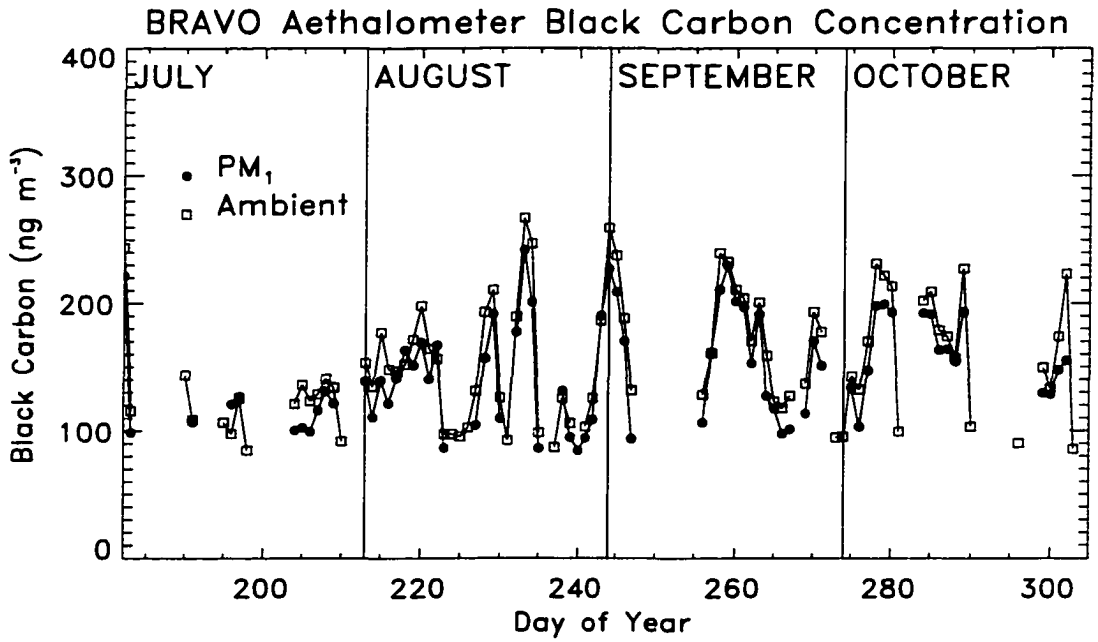

Figure 7.3.6 Timeline of ambient black carbon concentrations (ng m^{-3}) and PM_1 black carbon concentrations measured using an aethalometer. The minimum detection limit was 84 ng m^{-3}.

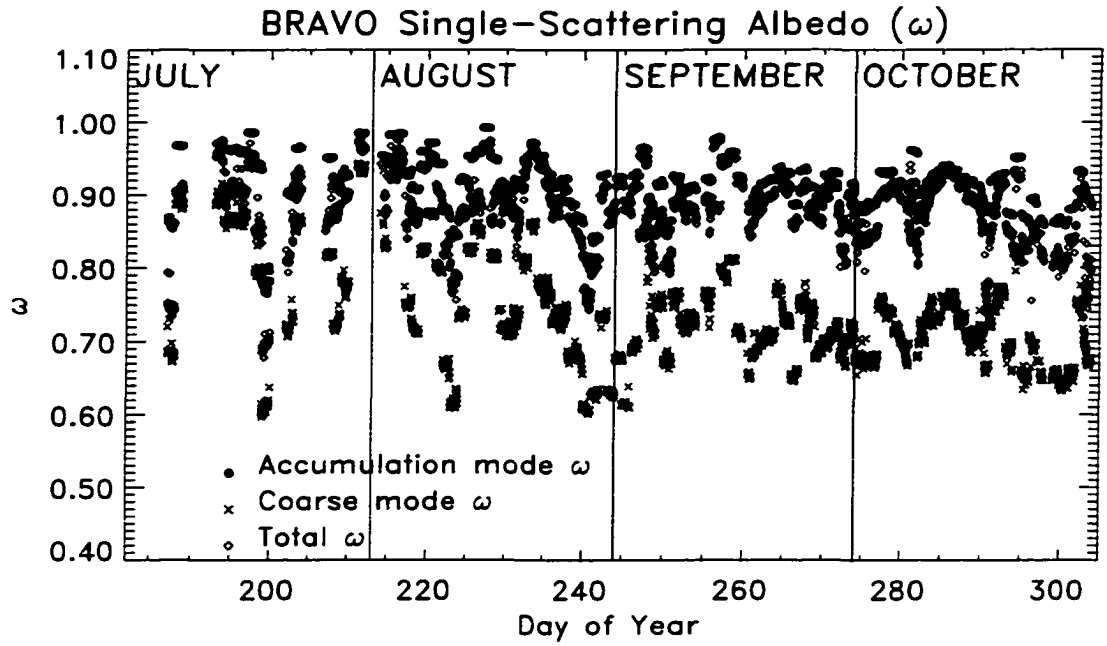

Figure 7.3.7 Timeline of dry hourly averaged single-scattering albedo for total, accumulation and coarse particle modes, derived from size distribution measurements and estimates of light extinction and absorption coefficients.

CHAPTER 8. AEROSOL OPTICAL PROPERTIES FROM GROUND-BASED REMOTE SENSING

The previous chapter presented derived aerosol optical properties in the context of visibility. In this chapter these properties will be considered in terms of their direct and indirect climate forcing effects. Only direct effects will be discussed here and include the ability of a particle to absorb and scatter short wave and thermal infrared radiation. As stated by *Haywood and Boucher* (2000), the effects of aerosols represent one of the largest uncertainties in predicted climate change. Current direct forcing estimates due to aerosols range from: -0.26 to –0.82 W m^{-2} for sulfate aerosols (*Haywood and Ramaswamy,* 1998), +0.16 to +0.42 W m^{-2} for black carbon aerosols (*Myhre et al.*, 1998), and –0.46 W m^{-2} (*Sokolik and Toon,* 1996) to + 0.09 W m^{-2} (*Tegen et al.*, 1996) for mineral dust. The current estimate for well-mixed greenhouse gases is +2.45 W m^{-2} (*IPCC*, 1996). Clearly the aerosol effect is important for understanding current and future climate, and knowledge of the aerosol chemical composition is obviously a very important component to the problem. Although estimates of aerosol radiative forcing will not be made in this chapter, investigations into the optical properties important to aerosol radiative forcing will be discussed.

One of the aerosol properties that govern direct forcing is aerosol optical depth (τ_{aer}), which is a measure of the aerosol loading and is characterized by the vertical

integration of the extinction coefficient (b_{ext}). Single-scattering albedo (ω) is also a pertinent property and was discussed in Section 7.3. Other important properties are the aerosol phase function (a function of the aerosol size distribution) and the spectral dependence of aerosol optical depth, or Ångstrom wavelength exponent (α), which is related to variations in the aerosol size distribution.

Estimates of direct forcing have relied on surface measurements of aerosol radiative properties with the assumption that the properties at the surface represent those of a well-mixed column (*Charlson et al.*, 1992; *IPCC*, 1995). Whether this assumption is appropriate in general has yet to be shown systematically. One method used by other researchers to test this assumption is to perform closure experiments by comparing aerosol optical depths from surface-based remote sensing with vertically integrated b_{ext} measured at the surface. *Bergin et al.* (2000) reviewed several such experiments and noted that some of the inherent difficulties included differences in relative humidity effects on aerosol optical properties measured with a nephelometer at the surface compared to the column-based ambient optical properties. Discrepancies due to aerosol horizontal spatial variability were seen by *Clarke et al.* (1996) in aircraft measurements over the Atlantic Ocean. *Hoppel et al.* (1990) observed correlations between estimated and measured aerosol optical depths in the marine boundary layer, however estimated τ_{aer} were a factor of 2 to 4 lower and the lack of vertical information about the aerosol extinction was assumed to be the reason. *Bergin et al.* (2000) required estimates of the vertical profile of aerosol extinction from lidar measurements to obtain estimates of τ_{aer} that were within 30 % of measured values at the Southern Great Plains (SGP) Atmospheric Radiation Measurement (ARM) site.

A similar closure experiment was performed during the BRAVO study by comparing surface-based estimates of τ_{aer} and Ångstrom wavelength exponents from the Kbar Ranch site with column-based values derived from ground-based remote sensing at a site approximately 30 miles from the Kbar Ranch site. The assumption of a well-mixed boundary layer was applied because no vertical profile of aerosol extinction existed. Section 8.1 describes the ground-based remote sensing measurements and the methods used to obtain aerosol optical properties. The second section describes the removal of cloud-contaminated data based on the work of *Smirnov et al.* (2000). The final section (Section 8.3) focuses on comparisons between surface- and column-based measurements of aerosol optical properties.

8.1. GROUND-BASED REMOTE SENSING OF AEROSOL OPTICAL PROPERTIES

In 1992 the United States Department of Agriculture (USDA) established an Ultraviolet Radiation Monitoring Program to monitor the changing levels of UV irradiance and the impact on agricultural production in the U. S. There are now 28 sites chosen for an approximate equal-area representation of the contiguous U. S., near areas of agricultural, biological, or ongoing UV research (*Bigelow et al.*, 1998). A fully instrumented site includes: a Yankee Environmental Systems (YES) UV Multi-Filter Rotating Shadowband Radiometer (UV-MFRSR), YES visible MFRSR (VIS-MFRSR), YES UVB-1 broadband meter (λ = 280 – 360 nm), Vaisala relative humidity and temperature probe, and downward looking Li-Cor photometer to detect snow cover (see *Harrison et al.*, 1994 for a full description of instrument operation). Measurements are made every 15 seconds (except for 20-second measurements for the UV-MFRSR) and

averaged to 3 minutes. The results presented in this chapter include data from the visible instrument only. The VIS-MFRSR has six wavelength channels (λ = 415, 500, 610, 665, 860 and 940 nm) and measures total horizontal, diffuse and direct normal irradiance.

As for any instrument, the accuracy of the calibration is imperative to obtaining meaningful measurements. The Langely method was used for calibration purposes and will be described only briefly here. *Slusser et al.* (2000) and *Harrison and Michalsky* (1994) provide an in depth discussion of this method. The Beer-Lambert law is applied in this calibration (see Equation 8.1.1).

$$I_\lambda = I_{o,\lambda} \exp[-\Sigma \tau_{\lambda,i} m_{air}] \tag{8.1.1}$$

The wavelength dependent direct irradiance at the ground is given by I_λ and the extra-terrestrial irradiance at the top of atmosphere (TOA) is given by $I_{o,\lambda}$. The optical depth of the i^{th} absorber is given by $\tau_{\lambda,i}$ and the air mass, or slant path, is given by m_{air}. Taking the natural log of Equation 8.1.1 and substituting uncalibrated channel voltages gives Equation 8.1.2:

$$\ln V_\lambda = \ln V_{o,\lambda} - m_{air}\tau \tag{8.1.2}$$

where V_λ is the measured voltage for a given channel and $V_{o,\lambda}$ is the extrapolated voltage for zero air mass. Plotting $\ln V_\lambda$ versus air mass gives a line with a slope corresponding to the atmosphere optical depth (τ), and the intercept is the voltage if the detector was pointed at the sun at TOA ($V_{o,\lambda}$) (*Bigelow et al.*, 1998). Equation 8.1.3 is used to retrieve I_λ at the ground, where c is a calibration factor and is the integral multiplication of the solar irradiance $I_{o,\lambda}$ and the filter response, or filter function (F_λ).

$$I_\lambda = V_\lambda c = V_\lambda \frac{\int I_{o,\lambda} F_\lambda d\lambda}{V_{o,\lambda} \int F_\lambda d\lambda} \tag{8.1.3}$$

The precision of the calibration is determined by the variance of $V_{o,\lambda}$.

The optical depth of the atmosphere was divided into its wavelength dependent constituents (Equation 8.1.4)

$$\tau = \tau_{ray} + \tau_{O3} + \tau_{aer} \tag{8.1.4}$$

where τ_{ray} is the optical depth due to Rayleigh scattering by molecules, τ_{O3} is the optical depth due to gaseous absorption by ozone and τ_{aer} is the aerosol optical depth due to both absorption and scattering by aerosols. In order to obtain τ_{aer}, both τ_{ray} and τ_{O3} were removed from τ obtained from Equation 8.1.2. Rayleigh optical depth is wavelength and pressure dependent and was computed following *Hansen and Travis* (1974) by Equation 8.1.5.

$$\tau_{ray} = 0.008569\lambda^{-4}(1 + 0.0113\lambda^{-2} + 0.00013\lambda^{-4})\frac{P}{P_o} \tag{8.1.5}$$

Wavelength (λ) is in micrometers, and τ_{ray} was corrected to the average site pressure (P) relative to sea level pressure (P_o). The ozone optical depth (τ_{O3}) was computed by Equation 8.1.6:

$$\tau_{O3} = \overline{\sigma}[X] \tag{8.1.6}$$

The column ozone is given by $[X]$ and the weighted ozone cross section ($\overline{\sigma}$) is a function of wavelength and was computed with Equation 8.1.7:

$$\overline{\sigma} = \frac{\int \sigma_\lambda I_\lambda F_\lambda d\lambda}{\int I_\lambda F_\lambda d\lambda} \tag{8.1.7}$$

where the solar irradiance is given by I_λ, channel filter functions are given by F_λ, and the ozone cross section is denoted by σ. MODTRAN (*Abreu and Anderson*, 1996) solar irradiances were used and are shown in Figure 8.1.1 for the wavelengths of interest.

Chappius band ozone cross sections were used for the visible wavelengths (*Shettle and Anderson*, 1994) and are plotted in Figure 8.1.2. The visible channel filter functions are plotted as a function of wavelength in Figure 8.1.3 (*Slusser, personal communication*). Figure 8.1.4 shows the resulting τ_{ray} and τ_{O3} for the wavelengths corresponding to the visible channels. Values of τ_{ray} were computed for P = 890 mbar and P = 910 mbar to demonstrate the negligible differences in τ_{ray} for the ranges of pressure observed during the study. Rayleigh optical depths corresponding to P = 890 mbar were removed from total optical depth. Column ozone of 300 Dobson Units (DU) was used to compute the values of τ_{O3} shown in Figure 8.1.4, however monthly values obtained from the TOMS website (*toms.gsfc.nasa.gov*) at latitude 28.5° N and longitude 103.125° S were applied in Equation 8.1.6 to obtain monthly corrections for τ_{aer}. Column ozone values in July and August were [X] = 297 DU, in September [X] = 281 DU and in October [X] = 276 DU.

The spectral dependence of τ_{aer} is important for modeling the radiative effects of aerosols on the earth/atmosphere system and is related to the aerosol size distribution. Obtaining accurate estimates of aerosol size distributions is important for many applications, specifically because variations in size distributions influence radiative properties of aerosols through the spectral dependence on τ_{aer}. To quantify the spectral dependence of τ_{aer}, *Ångstrom's* (1929) empirical equation was used (Equation 8.1.8).

$$\tau_{aer} = \beta\lambda^{-\alpha} \tag{8.1.8}$$

The Ångstrom turbidity coefficient is denoted β, the wavelength (λ) is in micrometers and α is the Ångstrom wavelength exponent. Ratioing Equation 8.1.8 at two wavelengths and taking the logarithm gives Equation 8.1.9:

$$\alpha = -\frac{\ln(\frac{\tau_{aer,2}}{\tau_{aer,1}})}{\ln(\frac{\lambda_2}{\lambda_1})} = -\frac{d\ln(\tau_{aer})}{d\ln(\lambda)} \qquad (8.1.9)$$

The Ångstrom wavelength exponent was computed as the negative of the slope of $\ln(\tau_{aer})$ versus $\ln(\lambda)$. Higher values ($\alpha > 2.0$) are typically observed for accumulation mode particles (*Reid et al.*, 1999; *Eck et al.*, 1999; *Nakajima and Higurashi*, 1998) and lower values (α near 0) have been observed for Saharan dust episodes (*Eck et al.*, 1999; *Smirnov et al.*, 1998) and coarse mode particles.

The Junge power law distribution (*Junge*, 1955) is related to α with Equation 8.1.10:

$$\frac{dN}{d\ln r} = cr^{v} \qquad (8.1.10)$$

where $v = \alpha - 2$ and c are fitting parameters and the number distribution is given by $\frac{dN}{d\ln r}$ in terms of particle radius. Because aerosol size distributions are not typically well-represented by the Junge power law, curvature may result between $\ln(\tau_{aer})$ versus $\ln(\lambda)$ (*Eck et al.*, 1999). The value of α obtained from Equation 8.1.9 also depends on the range of wavelengths over which it is computed (*Kaufman*, 1993). In this work, α was computed by a linear fit over the full range of visible wavelengths from the radiometer measurements ($415 < \lambda < 860$ nm), excluding data for $\lambda = 940$ nm because they were not available during the study period. Results of derived aerosol optical depths and Ångstrom wavelength exponents from the UVB measurements are presented in Section 8.3. However, before these data can be evaluated, any contamination by clouds must be removed. The next section describes the cloud removal method.

8.2 CLOUD-CONTAMINATION REMOVAL

The UVB aerosol optical depths computed in the previous section do not have any cloud-contamination removed. The cloud-screening method applied here followed the work of *Smirnov et al.* (2000) for the AERONET database. Although the method was developed specifically for the Sun photometers in the AERONET network (*Holben et al.*, 1998), aspects of the method were applied successfully to the data retrieved from the UVB Sun photometers.

The majority of the screening occurred by applying a smoothness criterion used by *Smirnov et al.* (2000). This criterion limited the root mean square of the second derivative in aerosol optical depth with time (t). The second derivative is a measure of how rapidly the rate of change in τ_{aer} occurred in time with the assumption that it is sensitive to oscillations in τ_{aer} by clouds. *Smirnov et al.* (2000) adopted a threshold for the smoothness criterion as described by Equation 8.2.1.

$$(D_2)^2 = \int_{t_1}^{t_2} \left(\frac{\partial^2 \tau(t)}{\partial t^2} \right)^2 dt \leq D_{crit}^2 \qquad (8.2.1)$$

In this application, τ included both the contributions of clouds and aerosols, but Rayleigh, ozone and optical depths corresponding to high sun angles (greater than 65 degrees) were removed. The threshold D^2_{crit} was defined *a priori* and corresponded to the maximum expected variability in τ. A logarithmic derivative was used because an absolute derivative removed any large changes in τ between clear and hazy conditions. *Smirnov et al.* (2000) defined a first derivative index, D, similar to Equation 8.2.1 for operational purposes (Equation 8.2.2). The number of discrete measurements is given by n.

$$D = \sqrt{\frac{1}{(n-2)} \sum \left[\frac{\ln \tau_i - \ln \tau_{i+1}}{t_i - t_{i+1}} - \frac{\ln \tau_{i+1} - \ln \tau_{i+2}}{t_{i+1} - t_{i+2}} \right]^2} \leq 16 \qquad (8.2.2)$$

Smirnov et al. (2000) defined the threshold ($D \leq 16$) based on experimental data obtained in a variety of optical conditions including biomass burning aerosols, urban aerosols, clean maritime aerosols and background continental aerosols. For $D > 16$, the term with the maximum input to D was determined and the optical depth associated with it was removed. The value of D applied in this smoothness criterion was tested in the cloud-screening of the UVB data and did not make a noticeable difference in the data removed.

Once only data corresponding to $D < 16$ remained, both the optical depths and the Ångstrom exponents were required to pass a three standard deviation (3σ) criterion (*Smirnov et al.*, 2000). If any of the measurements of τ at $\lambda = 500$ nm (τ_{500}) fell outside of the 3σ range about the mean of τ_{500} during a 24-hour period, the data for all wavelengths were eliminated. This criterion was also applied to Ångstrom exponents. These cloud-screening criteria successfully removed optically thick clouds but optically thin cirrus clouds (*Kinne et al.*, 1997) with low Ångstrom exponents (near zero or negative) were not removed. No criterion was placed on the lowest allowable Ångstrom exponent because several dust episodes were observed and low Ångstrom exponents were expected (*Smirnov et al.* 1998). To remove cirrus clouds, any decrease in Ångstrom exponents that corresponded to increased optical depths were removed.

8.3 COMPARISONS OF SURFACE- AND COLUMN-BASED AEROSOL OPTICAL PROPERTIES

Surface-based aerosol optical depths were computed following the method of *Bergin et al.* (2000) using surface-based extinction coefficient measurements (b_{ext}). It was assumed that the aerosols were entirely within a well-mixed boundary layer because no vertical profile of extinction was available. Estimates of the boundary layer height (H_B) were estimated from the ATAD transport model (*Gebhart*, personal communication, *Heffter*, 1980) that provided six-hour transport layer depths from August through October. A linear interpolation was performed to obtain hourly values of H_B. The ATAD model had minimum and maximum heights of 0.3 km and 3 km, respectively. Equation 8.3.1 was used to compute aerosol optical depth with ambient extinction coefficients ($b_{ext,amb}$):

$$\tau_{aer} = b_{ext,amb} H_B \tag{8.3.1}$$

Using Equation 8.3.1 required a correction for relative humidity (RH) effects on aerosol extinction because b_{ext} was computed from dry size distributions (see Chapter 7). An extensive RH correction would include daily variations in aerosol acidity, vertical profiles of RH, variations in refractive index due to the addition of water, increased aerosol mass with added water, and changing aerosol size distributions due to particle growth. Including all of these effects was beyond the scope of this work, therefore a rough correction was applied based on a constant average value of surface relative humidity, a constant average observed aerosol acidity, and the corresponding changes in aerosol size distributions and aerosol mass. The surface relative humidities observed during BRAVO were fairly low with an average RH measured at the Kbar site of 46 ± 18

%. The average aerosol ammonium to sulfate molar ratio (as measured by CSU) was 1.53 ± 0.3, suggesting an acidic aerosol corresponding to letovicite. *Tang's* (1996) estimates of aerosol hygroscopicity were used to compute the particle growth for letovicite at RH = 60 %, a reasonable guess of RH based on the average plus one standard deviation. Equation 8.3.2 was used to compute a corrected ambient light extinction coefficient ($b_{ext,amb}$) from dry values of volume distributions and diameters:

$$b_{ext,amb} = \int \frac{3}{2} \frac{Q_{ext,amb}}{D_{p,dry}} [f(RH)]^2 \frac{dV_{dry}}{d\log D_p} d\log D_p \qquad (8.3.2)$$

where $f(RH)$ is the diameter growth factor for letovicite at RH = 60 % ($f(RH)$ = 1.25), and $Q_{ext,amb}$ is the Mie extinction efficiency computed at ambient diameters ($D_{p,amb}$ = $f(RH)D_{p,dry}$) with complex refractive indices that included estimates of UCD EC concentrations (see Chapters 6 and 7). Refractive index was not adjusted for increased aerosol water content, therefore ($b_{ext,amb}$) is an overestimation because the addition of water would decrease derived refractive indices and would result in lower estimates of extinction coefficients. The effect of ignoring aerosol water content is discussed in Section 8.5. Estimates of $b_{ext,amb}$ were computed for the visible wavelengths corresponding to the VIS-MFRSR.

Figure 8.3.1 presents a timeline of ambient aerosol optical depth from CSU surface-based estimates (denoted τ_{csu}) and UVB column-based estimates (denoted τ_{uvb}) at λ = 500 nm. No values were plotted for July and early August because no height information was available during those periods. Uncertainties in τ_{csu} at λ = 500 nm were on the order of ± 0.02 due to uncertainties in b_{ext}. The uncertainties in τ_{uvb} were ± 0.01 at λ = 500 nm, and the minimum detection limit at this wavelength was τ_{uvb} = 0.02 (*Slusser,*

personal communication). The overall average in τ_{csu} was 0.12 ± 0.12 and in τ_{uvb} was 0.14 ± 0.06 (see Table 8.3.1). The two estimates trend well although τ_{csu} was much larger during certain periods (e.g. DOY 232-233, 244, 257 and 285). It is interesting to note that these days corresponded to the lowest molar ratios (and most acidic aerosol) observed (molar ratio ≤ 1.2, see Chapter 6). It is possible that not correcting refractive indices for aerosol water content on these more acidic days resulted in overestimated light extinction coefficients. The ambient aerosols would have taken up water and the addition of water would lower their refractive indices, thereby producing lower estimates of τ_{uvb}. The overall correlation between τ_{csu} and τ_{uvb} was $R^2 = 0.691$ and was highest in October (R^2 = 0.822) (see Table 8.3.2). The overall percent difference was 43 ± 28 % with the largest differences observed in September and the smallest in August (see Table 8.3.3).

Figure 8.3.2 shows a scatter plot of the two estimates of aerosol optical depth, with surface-based values being higher at larger τ_{aer}. One possible reason for the discrepancy between the estimates was the boundary layer height applied in Equation 8.3.1. Comparing $b_{ext,amb}$ to τ_{uvb} resulted in a higher overall correlation ($R^2 = 0.770$) than between the estimates of optical depth (see Table 8.3.2). Figure 8.3.3 shows a scatter plot of $b_{ext,amb}$ to τ_{uvb} for the study. This comparison suggested that more realistic estimates of boundary layer height were required for computing aerosol optical depths. *Bergin et al.* (2000) demonstrated that better agreement between measured and computed aerosol optical depths was observed at the SGP site when information on the vertical profile of extinction was included than when the aerosols were assumed to be well-mixed in the boundary layer.

Timelines of Ångstrom wavelength exponents (α) derived from both methods are shown in Figure 8.3.4. Values of surface-based estimates (labeled CSU) were computed by substituting $b_{ext,amb}$ for τ_{aer} in Equation 8.1.9. The two methods demonstrated remarkable agreement and reflected changes observed in the measured aerosol size distributions. The overall average value of the Ångstrom wavelength exponent from the CSU surface-based measurements was $\alpha_{csu} = 1.4 \pm 0.4$ and from the UVB column-based measurement was $\alpha_{uvb} = 1.1 \pm 0.5$ (see Table 8.3.1). Modest correlations between the two estimates were observed for each month except September (see Table 8.3.2) and the overall correlation was $R^2 = 0.755$. A scatter plot of the two estimates is shown in Figure 8.3.5. Discrepancies observed in September may have been due to uncertainties in low values of τ_{uvb} (DOY 250 – 255 were very clean). The overall percent difference between the two estimates was 28 ± 25 % and was surprisingly small given the different methods. Most importantly, the sites were approximately 30 miles apart and separated by the Chisos Mountains.

Variations in the Ångstrom exponent coincided with changes in meteorological periods and aerosol properties already discussed in Chapter 6 and Chapter 7. For example, both α_{csu} and α_{uvb} decreased around DOY 207, 215-216 and 227. These days were associated with suspected transport of Saharan Dust to the park and corresponded to larger contributions of coarse particles and higher fine soil chemical compositions. The average value of the Ångstrom exponent was lowest in July, with $\alpha_{csu} = 1.0 \pm 0.4$ and $\alpha_{uvb} = 0.7 \pm 0.3$. Low values of the Ångstrom exponent in October (DOY 281, 290 and 303) also corresponded to periods with increased coarse particle mass and transport from the north. The periods associated with dominant accumulation mode sulfate particles

(mostly September and October) corresponded to higher Ångstrom exponents, typical of higher loadings of small particles.

To test whether the variations in Ångstrom exponents were related to particle size, a scatter plot of the fractional contribution of accumulation mode volume concentrations to total volume concentrations (V_{acm}/V_{tot}) and α_{csu} is shown in Figure 8.3.6. In general α_{csu} increased with increasing V_{acm}/V_{tot}, consistent with higher values of Ångstrom exponents associated with aerosols dominated by accumulation mode particles. Comparisons between V_{acm}/V_{tot} and radiometer derived α_{uvb} are shown in Figure 8.3.7 and demonstrate a similar relationship. Comparisons between coarse mode volume ratios (V_{coarse}/V_{tot}) and both estimates of Ångstrom exponents are shown in Figure 8.3.8 (α_{csu}) and Figure 8.3.9 (α_{uvb}). For both estimates Ångstrom exponents decreased with increasing (V_{coarse}/V_{tot}), consistent with the presence of significant concentrations of coarse particles.

Comparisons between volume geometric mean diameters (D_{gv}) and Ångstrom exponents did not result in a clear relationship. Figure 8.3.10 and Figure 8.3.11 are scatter plots of accumulation mode mean diameters with α_{csu} and α_{uvb}, respectively. A weak relationship between D_{gv} and α_{uvb} was observed (Figure 8.3.11), but was less obvious in the comparison between D_{gv} and α_{csu}. Figure 8.3.12 and Figure 8.3.13 show similar comparisons of coarse mode mean diameters with α_{csu} and α_{uvb}, respectively. In general it appeared that lower values of Ångstrom exponents corresponded to lower values of coarse volume mean diameter. *Reid et al.* (1999) demonstrated that the correlations between Ångstrom exponents and size parameters were very sensitive to the wavelength range used to compute Ångstrom exponents, with a decreased correlation expected when

longer wavelengths (λ > 870 nm) were included. Higher correlations between size parameters and Ångstrom exponents were observed when shorter wavelengths were used. *Eck et al.* (1999) showed that Ångstrom exponents for biomass burning aerosols measured in Bolivia varied from 0.46 to 2 depending on the adjacent pairs of wavelengths used to compute them. They found a linear fit over all wavelengths (340 < λ < 870 nm) yielded an Ångstrom exponent of 1.75. Performing calculations of Ångstrom exponents over different wavelength regimes may result in higher correlations with aerosol mean size.

8.4 EFFECTS OF RELATIVE HUMIDITY CORRECTION ON AEROSOL OPTICAL DEPTH AND ÅNGSTROM WAVELENGTH EXPONENT

The effect of a relative humidity correction on τ_{aer} was investigated by computing τ_{aer} with dry b_{ext}. Estimates of dry τ_{csu} were made using Equation 8.3.1 and the dry estimates of b_{ext} presented in Chapter 7. The overall percent difference between dry τ_{csu} and ambient τ_{uvb} increased to 87 ± 40 % (see Table 8.3.6) compared to 43 ± 28 % when both estimates were ambient. The overall average dry τ_{csu} was half the estimated ambient τ_{csu} (Table 8.3.4), suggesting that relative humidity effects were very important even in the relatively dry conditions at Big Bend (see Figure 8.3.15). The overall correlation between dry surface-based aerosol optical depths and column-based ambient optical depths did not change significantly (dry R^2 = 0.690 compare to ambient R^2 = 0.691) (Table 8.3.5) and the same increased correlation between $b_{ext,dry}$ and τ_{uvb} was observed as for the ambient comparison. *Bergin et al.* (2000) experienced the same level of improvement when the effects of relative humidity on aerosol optical depth were

included at the SGP site. They found that using dry extinction coefficient measurements underestimated τ_{aer} by as much as 70 % and improved to 40 % when the effects of aerosol hygroscopicity were included.

Although the overall average Ångstrom exponent computed with dry b_{ext} was not greatly affected (α_{dry} = 1.5 ± 0.4, see Table 8.3.4), the overall correlation between dry α_{csu} and α_{uvb} actually increased (R^2 = 0.832 compared to R^2 = 0.755, see Table 8.3.5). The increased correlation was due to better agreement during September around DOY 245 (see Figure 8.3.14). The value of relative humidity applied in the ambient estimate during this period was too high; the average RH on DOY 245 was 44 ± 9 %. In any case this difference appeared to be related to a relative humidity effect because of the differences observed between dry and ambient Ångstrom exponents on this day. Overall the percent difference between Ångstrom exponent increased from 28 ± 25 % for the ambient estimates to 31 ± 25 % for the dry estimates. Figure 8.3.16 shows a scatter plot of dry and ambient surface-based Ångstrom exponents demonstrating higher dry values in September.

8.5 SUMMARY AND DISCUSSION

Some of the possible reasons for discrepancies observed between the surface- and column-based aerosol optical properties could be due to the mixing heights applied in the calculation. Higher correlations were observed when surface-based light extinction coefficients were compared to column-based aerosol optical depth than for surface-based estimates of aerosol optical depths. The assumption of a well-mixed boundary layer may not apply, and the calculated boundary layer depths may be wrong, but data describing

the vertical profile of aerosol extinction were not available to test the assumption. Variations in aerosol size and composition could vary with height but no information describing these changes was available. As was shown, relative humidity effects were very important and were applied in a general manner to the entire study. Further, variations in aerosol acidity were not accounted for, nor were varying relative humidities measured at the surface or vertical profiles of RH with height. Future work should include a more representative variation of these properties. Local effects on aerosol properties due to the different site locations could also have affected the comparisons in the two methods. Even with all of these uncertainties, the comparisons suggested that surface-based estimates of ambient extinction coefficients can be used to estimate column-based aerosol optical depth to within roughly 40 % at Big Bend National Park during the study. These results also suggested that the column-based aerosol optical depths were good indicators of visibility because of the correlation observed between b_{ext} and τ_{aer}. Finally, estimates of Ångstrom exponents from the UVB column-based measurements were representative of particle size and were consistent with measured size distributions and computed estimates of Ångstrom exponents from light extinction coefficients.

Table 8.3.1. Average values and one standard deviation of computed ambient (RH = 60 %) aerosol optical depths from CSU estimates (τ_{csu}) and the UVB network (τ_{uvb}) at λ = 500 nm, and computed Ångstrom wavelength exponents for CSU and UVB (α_{csu} and α_{uvb}) over the wavelength range of $\lambda = 415 - 860$ nm.

Month	τ_{csu}	τ_{uvb}	α_{csu}	α_{uvb}
July	NA	0.13 ± 0.04	1.0 ± 0.4	0.7 ± 0.3
August	0.17 ± 0.16	0.15 ± 0.05	1.3 ± 0.3	1.1 ± 0.4
September	0.12 ± 0.12	0.15 ± 0.08	1.5 ± 0.2	1.4 ± 0.3
October	0.1 ± 0.1	0.11 ± 0.06	1.6 ± 0.2	1.5 ± 0.3
Overall	0.12 ± 0.12	0.14 ± 0.06	1.4 ± 0.4	1.1 ± 0.5

Table 8.3.2 Correlations (R^2) between surface-based (CSU) and column-based (UVB) ambient properties. Optical depths correspond to λ = 500 nm.

Month	τ_{csu} vs τ_{uvb}	b_{ext} vs τ_{uvb}	α_{csu} vs α_{uvb}
July	NA	0.649	0.734
August	0.604	0.765	0.807
September	0.677	0.824	0.05
October	0.822	0.888	0.493
Overall	0.691	0.770	0.755

Table 8.3.3 Percent differences between ambient surface-based optical properties and column-based optical properties (optical depths correspond to λ = 500 nm).

Month	τ_{csu} vs τ_{uvb} (%)	α_{csu} vs α_{uvb} (%)
July	NA	46 ± 33
August	36 ± 22	24 ± 20
September	49 ± 31	23 ± 21
October	39 ± 23	18 ± 14
Overall	43 ± 28	28 ± 25

Table 8.3.4 Average values and one standard deviation of computed dry aerosol optical depths from CSU estimates (τ_{csu}) at λ = 500 nm, and computed Ångstrom wavelength exponents for CSU (α_{csu}) over the wavelength range of λ = 415 – 860 nm.

Month	τ_{csu}	α_{csu}
July	NA	1.0 ± 0.4
August	0.07 ± 0.06	1.4 ± 0.4
September	0.06 ± 0.06	1.7 ± 0.2
October	0.05 ±0 .04	1.7 ± 0.2
Overall	0.06 ± 0.05	1.5 ± 0.4

Table 8.3.5 Correlations (R^2) between surface-based (CSU) and column-based (UVB) dry properties. Optical depths correspond to λ = 500 nm.

Month	τ_{csu} vs τ_{uvb}	b_{ext} vs τ_{uvb}	α_{csu} vs α_{uvb}
July	NA	0.579	0.795
August	0.604	0.751	0.838
September	0.676	0.828	0.447
October	0.825	0.894	0.647
Overall	0.690	0.778	0.832

Table 8.3.6 Table 8.3.3 Percent differences between dry surface-based optical properties and column-based optical properties (optical depths correspond to λ = 500 nm).

Month	τ_{csu} vs τ_{uvb} (%)	α_{csu} vs α_{uvb} (%)
July	NA	43 ± 30
August	79 ± 36	32 ± 20
September	97 ± 42	28 ± 23
October	79 ± 37	18 ± 17
Overall	87 ± 40	31 ± 25

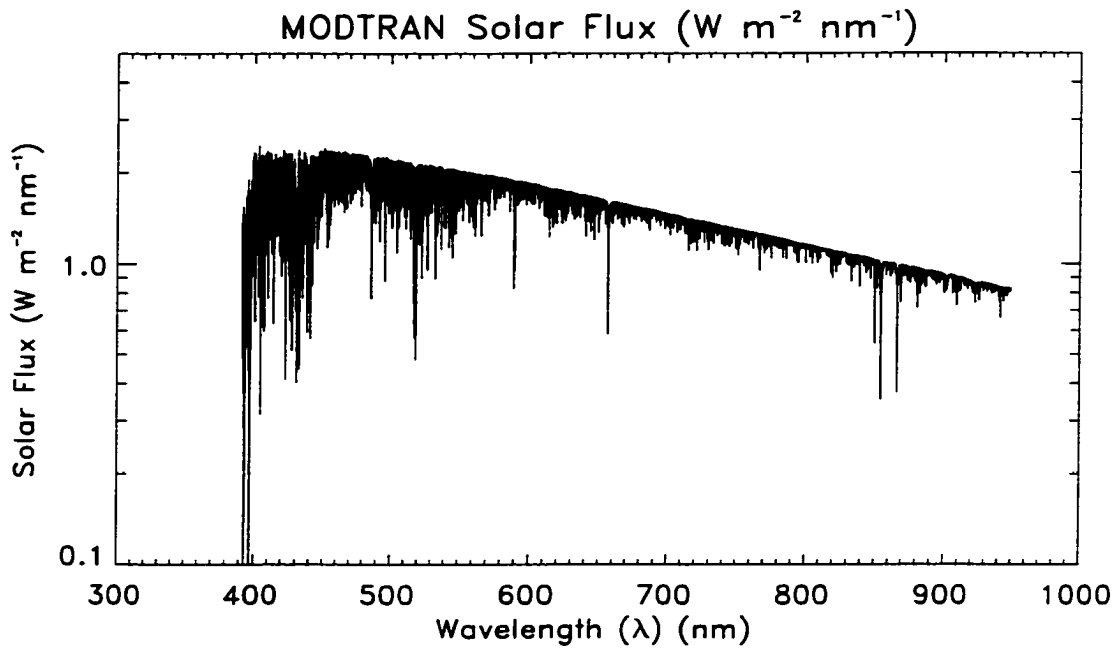

Figure 8.1.1 Solar irradiance from MODTRAN used to computed weighted ozone cross sections (W m^{-2} nm^{-1}).

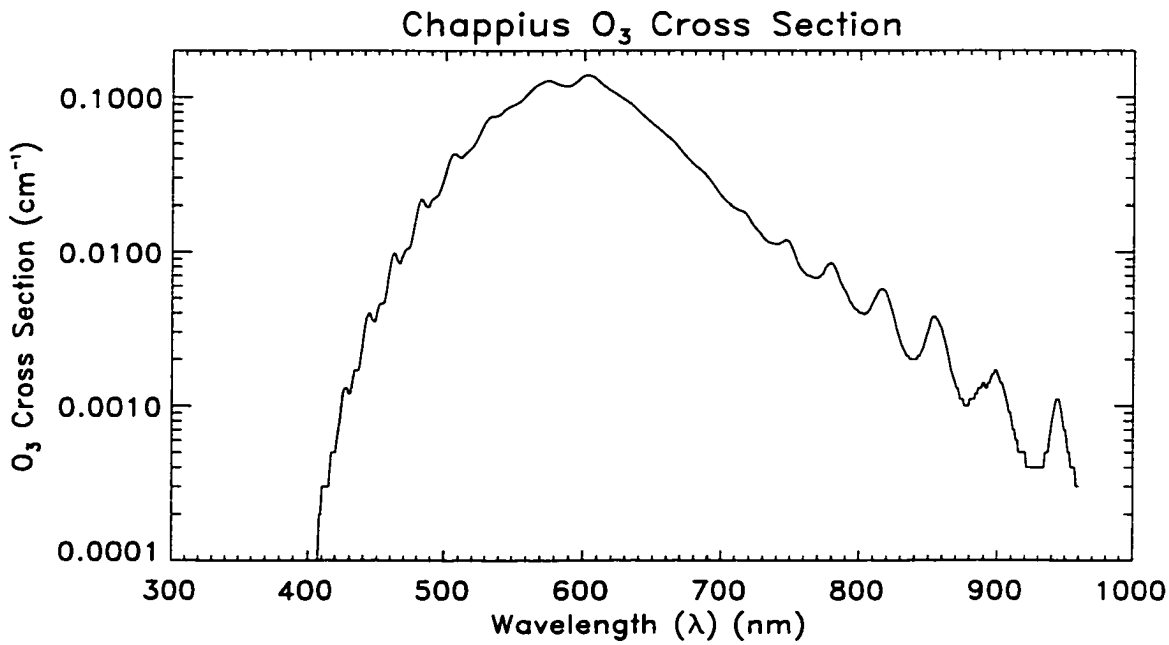

Figure 8.1.2 Chappius band ozone cross sections (cm^{-1}).

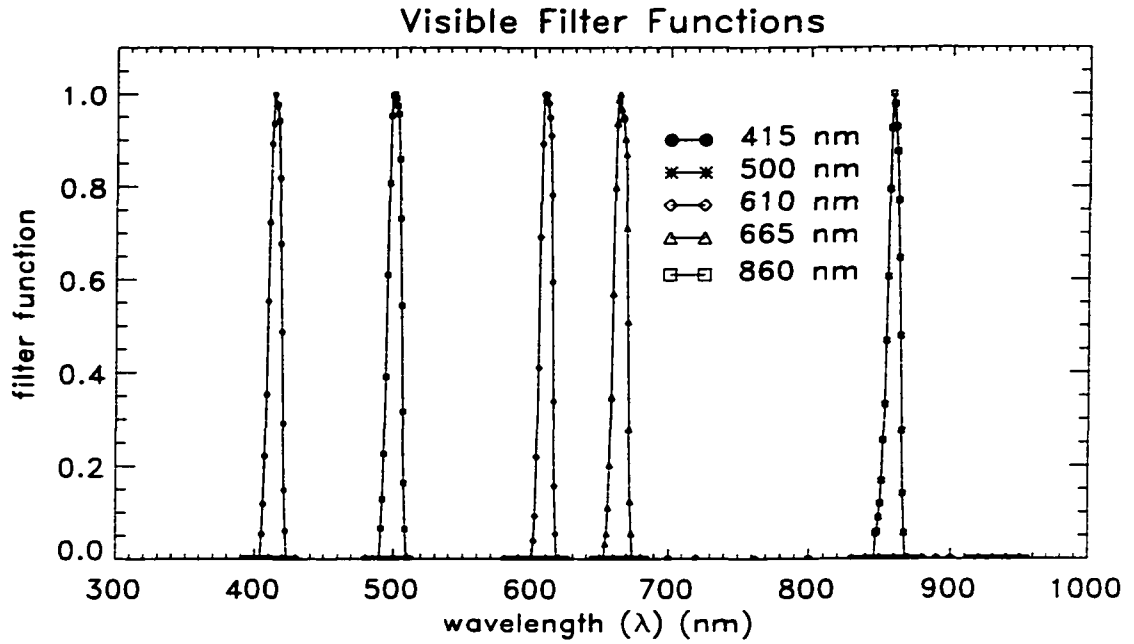

Figure 8.1.3 Filter functions for the visible wavelength channels of the VIS-MFRSR.

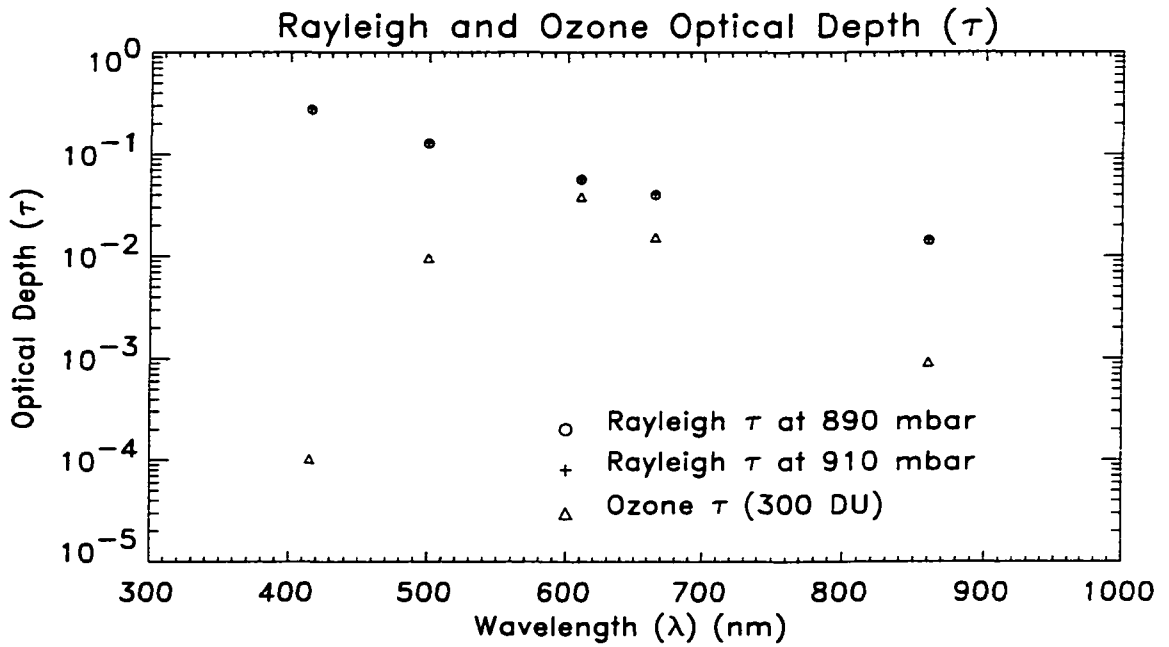

Figure 8.1.4 Rayleigh and ozone optical depths computed at the wavelengths of the VIS-MFRSR channels. Aerosol optical depth was obtained by removing the contributions of Rayleigh and ozone from total optical depths. Raleigh optical depths computed at two pressures are shown for comparison.

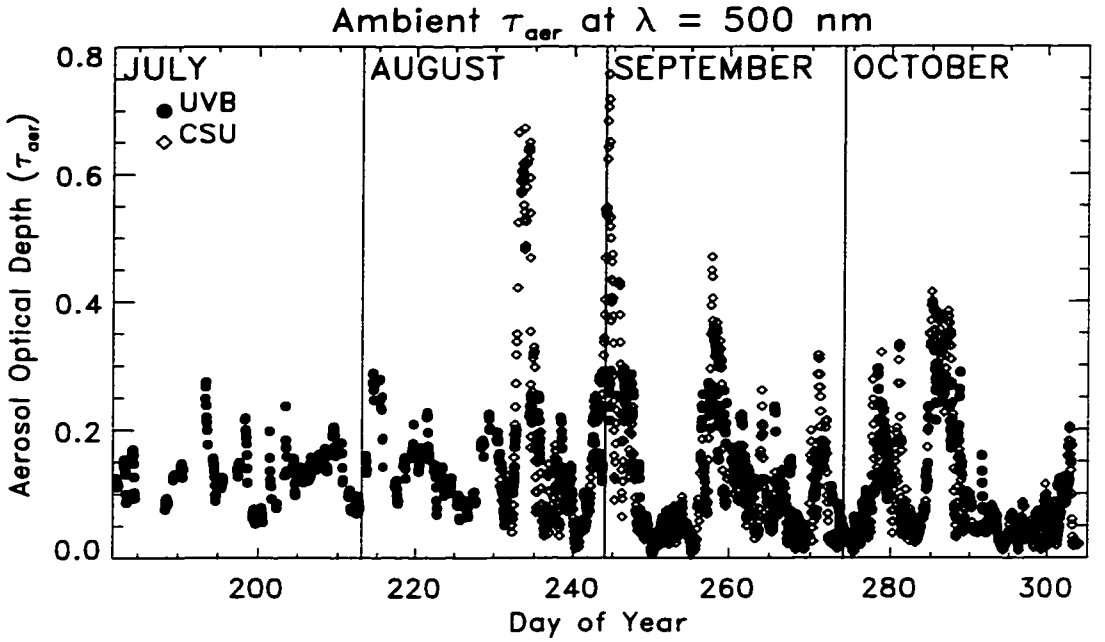

Figure 8.3.1 Timeline of surface- and column-based ambient aerosol optical depths (τ_{aer}). The surface-based measurements were corrected for 60 % relative humidity.

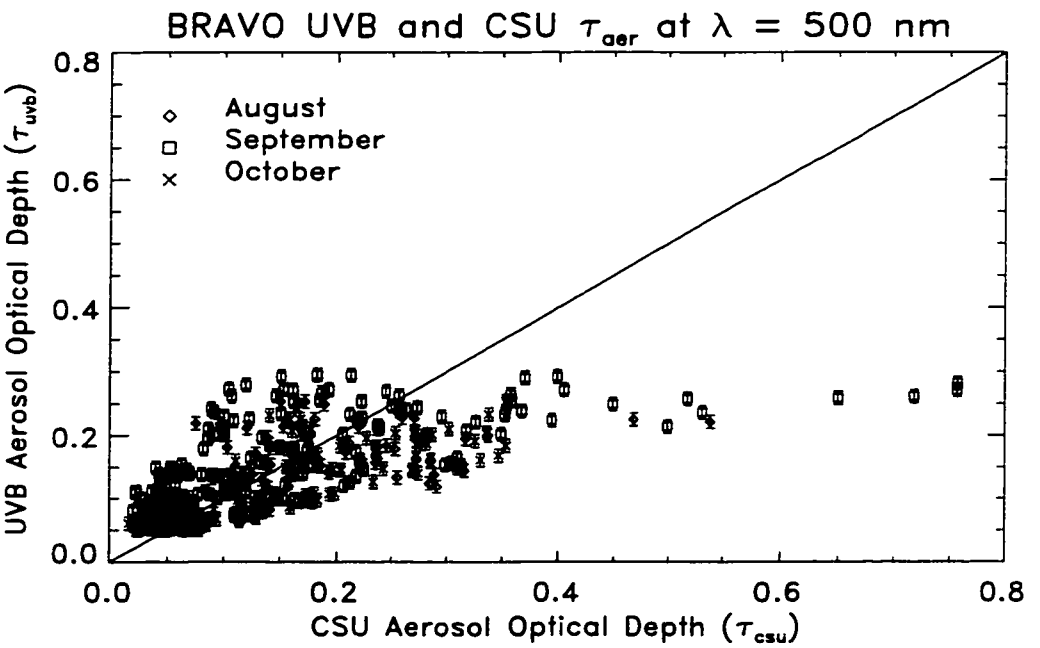

Figure 8.3.2 Comparison of surface-based (CSU) and column-based (UVB) estimates of ambient aerosol optical depth. The uncertainties in surface-based optical depths are ± 0.02 and ± 0.01 for column-based optical depths.

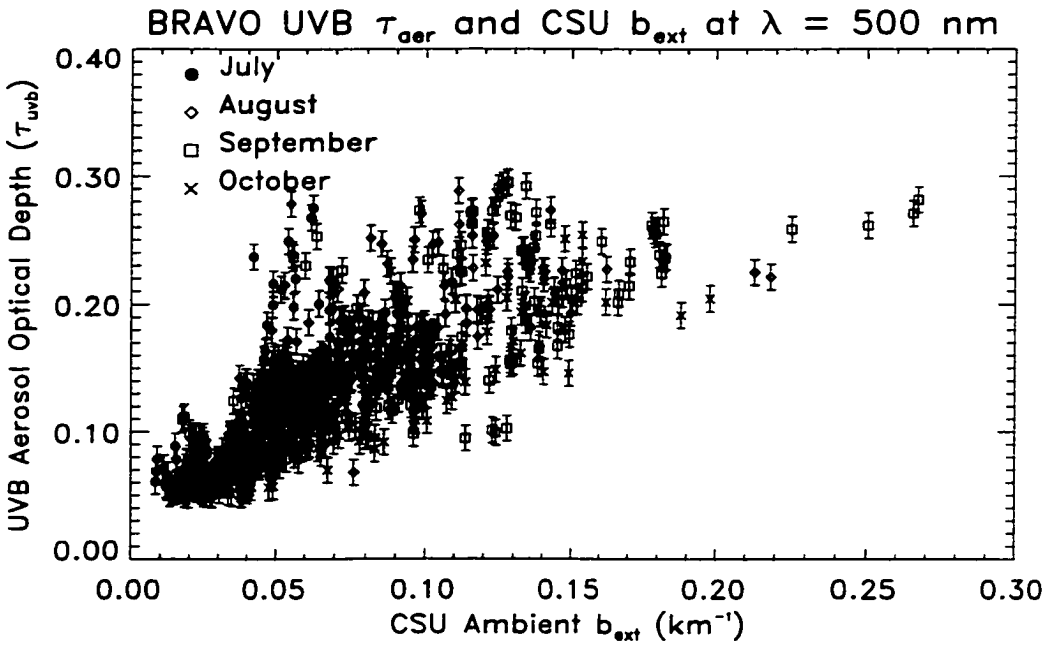

Figure 8.3.3 Comparisons of ambient b_{ext} and column-based (UVB) aerosol optical depth.

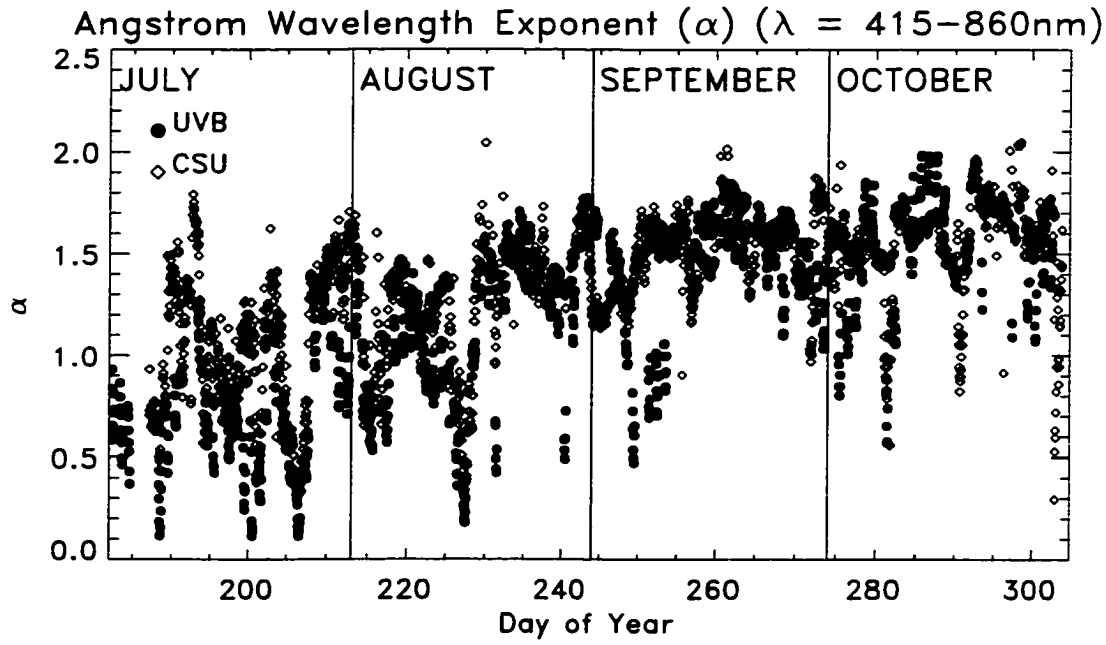

Figure 8.3.4 Timeline of surface- and column-based ambient Ångstrom wavelength exponents (α). The surface-based measurements were corrected for 60 % relative humidity.

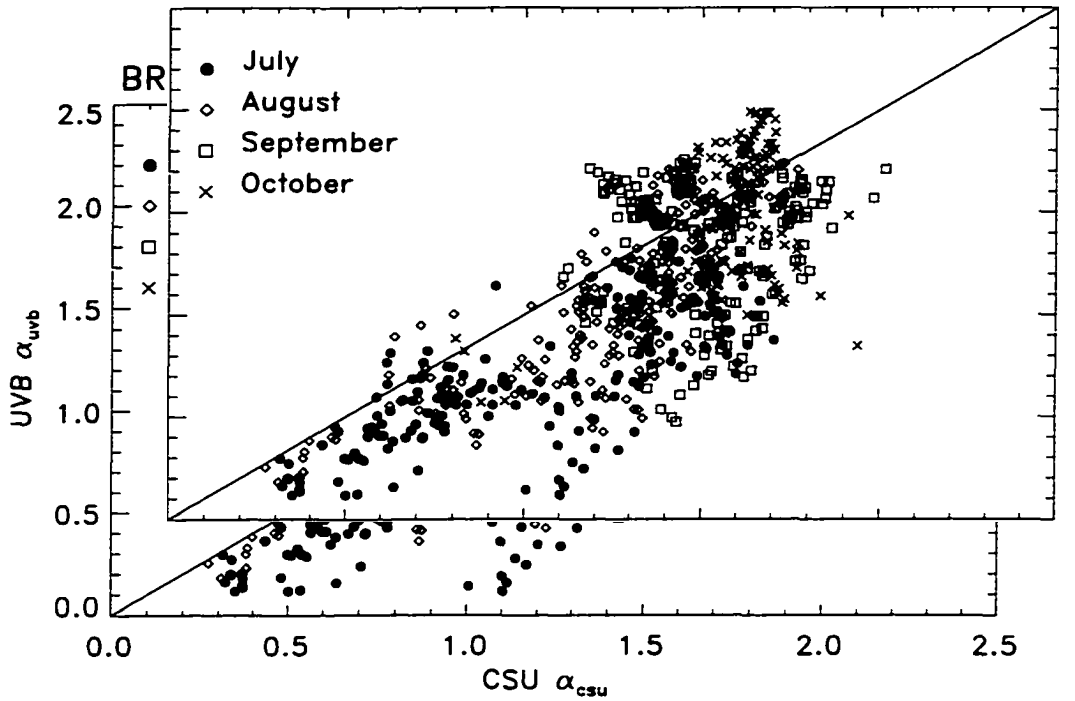

Figure 8.3.5 Comparison of ambient surface-based Ångstrom wavelength exponents (α_{csu}) and column-based Ångstrom wavelength exponents (α_{uvb}).

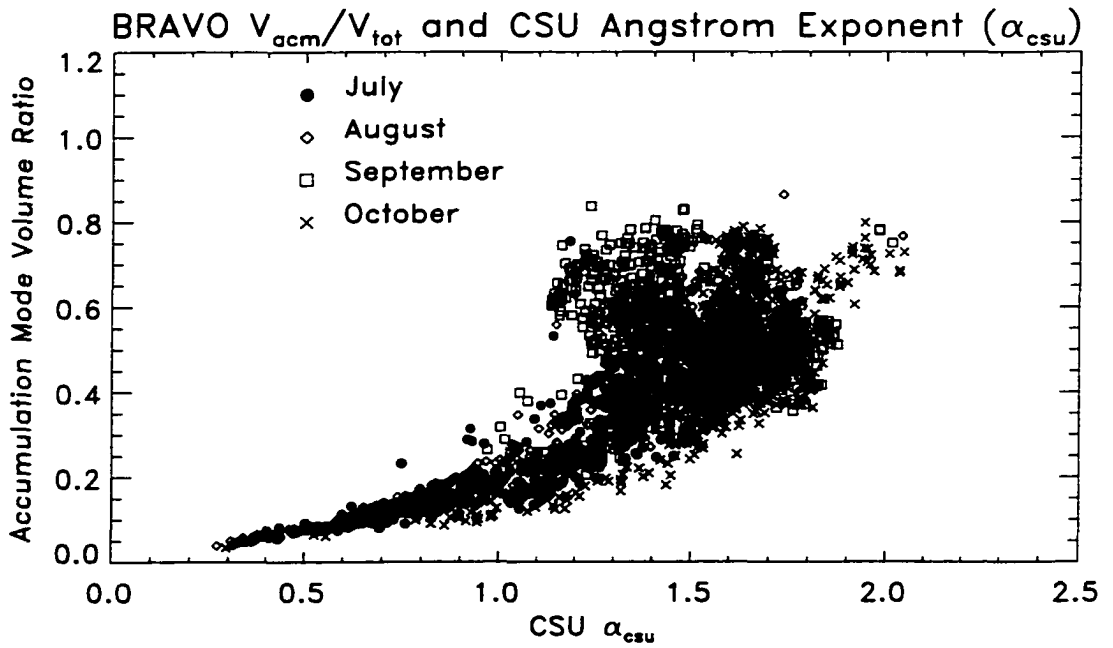

Figure 8.3.6 The fractional contribution of dry accumulation mode volume concentrations to total volume (V_{acm}/V_{tot}) compared with surface-based ambient Ångstrom wavelength exponents (α_{csu}).

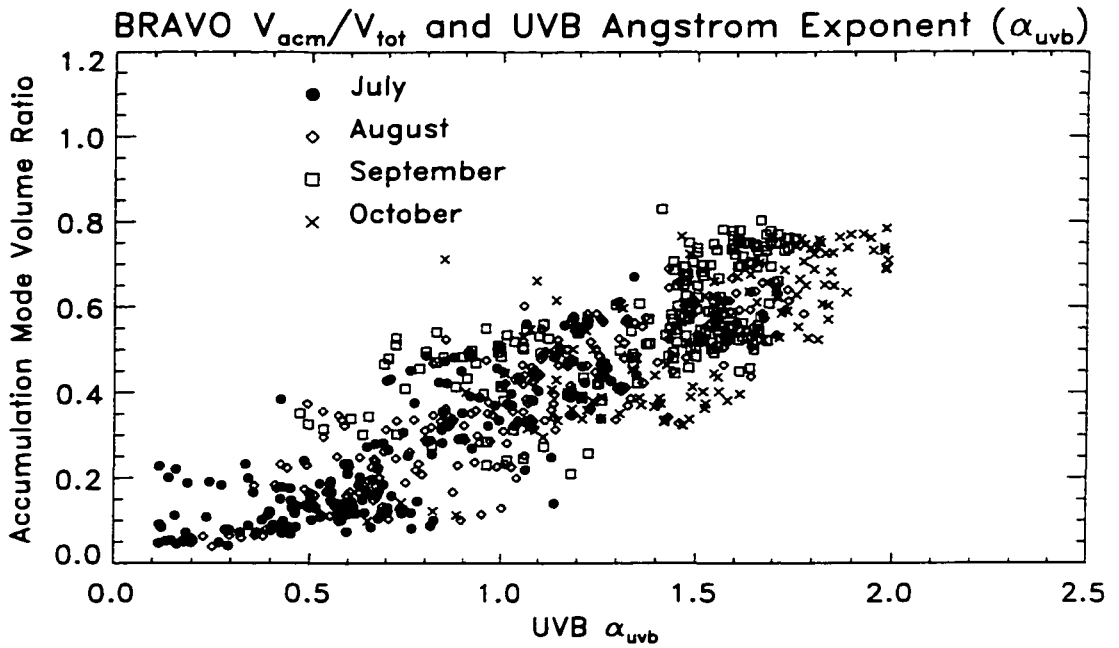

Figure 8.3.7 The fractional contribution of dry accumulation mode volume concentration to total volume (V_{acm}/V_{tot}) compared with column-based Ångstrom wavelength exponents (α_{uvb}).

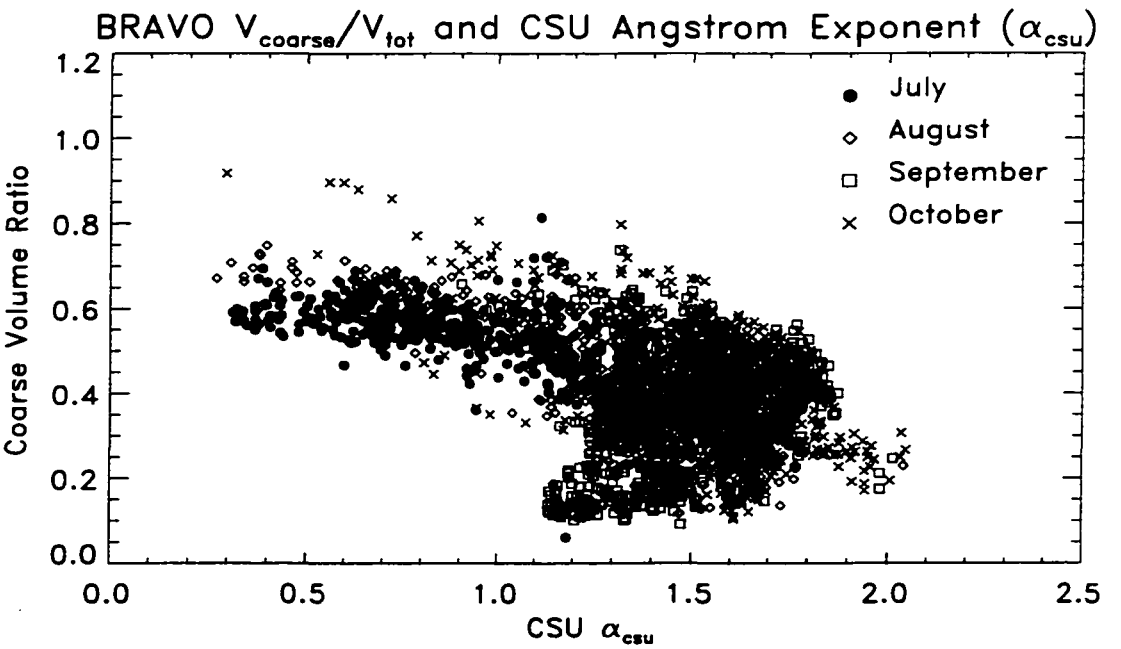

Figure 8.3.8 The fractional contribution of dry coarse mode volume concentration to total volume (V_{coarse}/V_{tot}) compared with surface-based ambient Ångstrom wavelength exponents (α_{csu}).

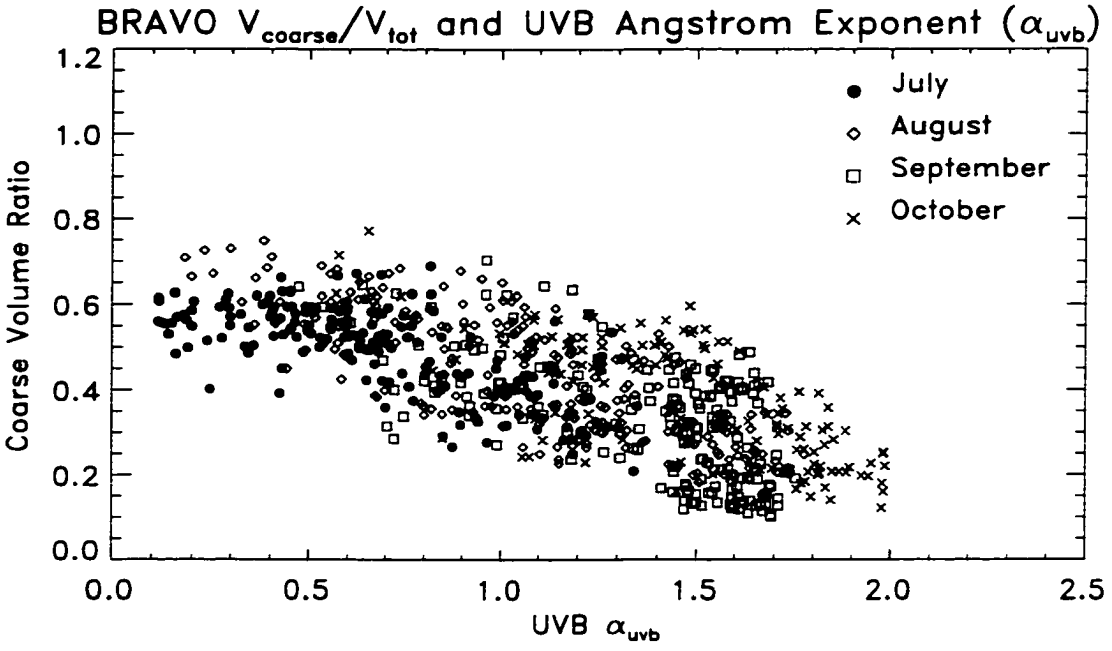

Figure 8.3.9 The fractional contribution of dry coarse mode volume concentration to total volume (V_{coarse}/V_{tot}) compared with column-based Ångstrom wavelength exponents (α_{uvb}).

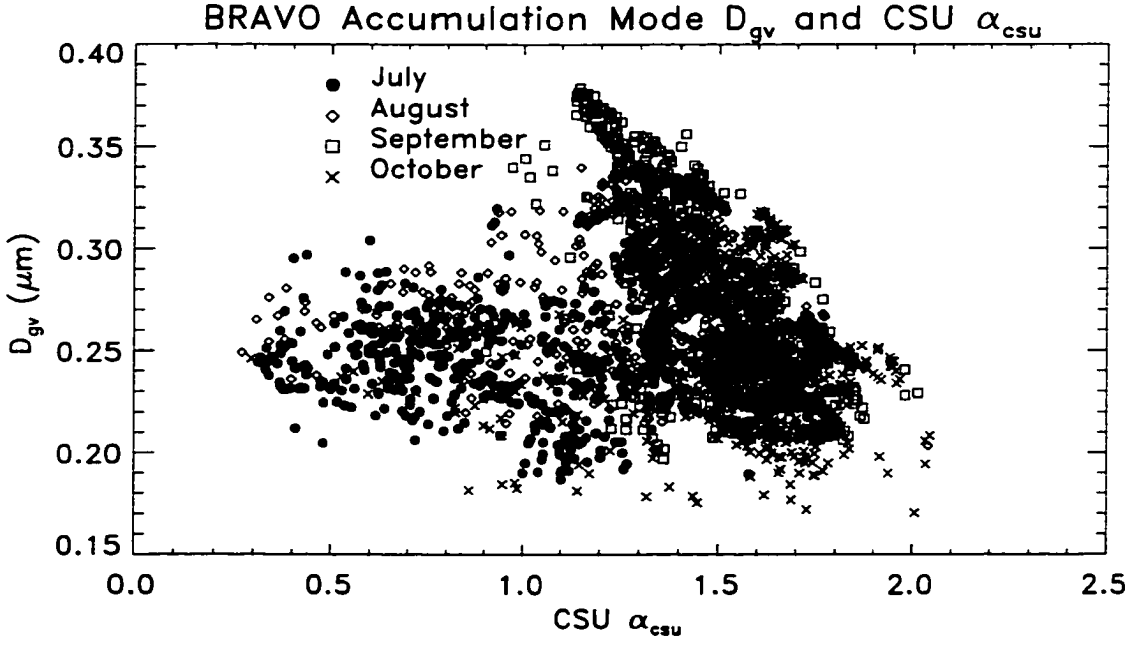

Figure 8.3.10 Comparison of dry accumulation mode volume geometric mean diameter (D_{gv}) (μm) and ambient surface-based Ångstrom wavelength exponents (α_{csu}).

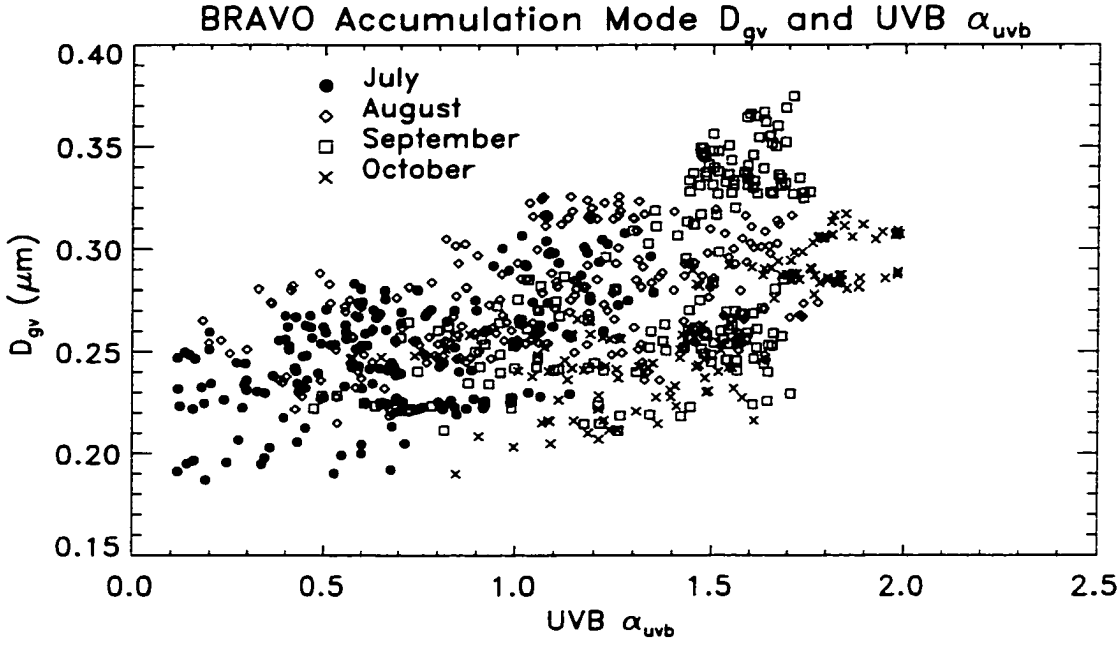

Figure 8.3.11 Comparison of dry accumulation mode volume geometric mean diameter (D_{gv}) (μm) and column-based Ångstrom wavelength exponents (α_{uvb}).

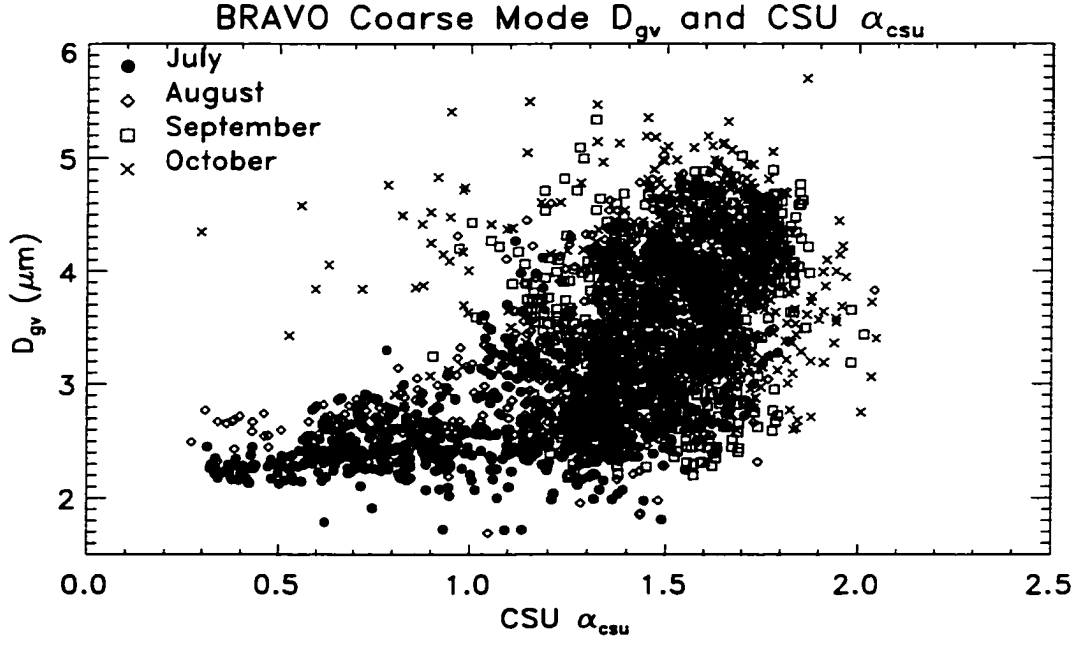

Figure 8.3.12 Comparison of dry coarse mode volume geometric mean diameter (D_{gv}) (μm) and ambient surface-based Ångstrom wavelength exponents (α_{csu}).

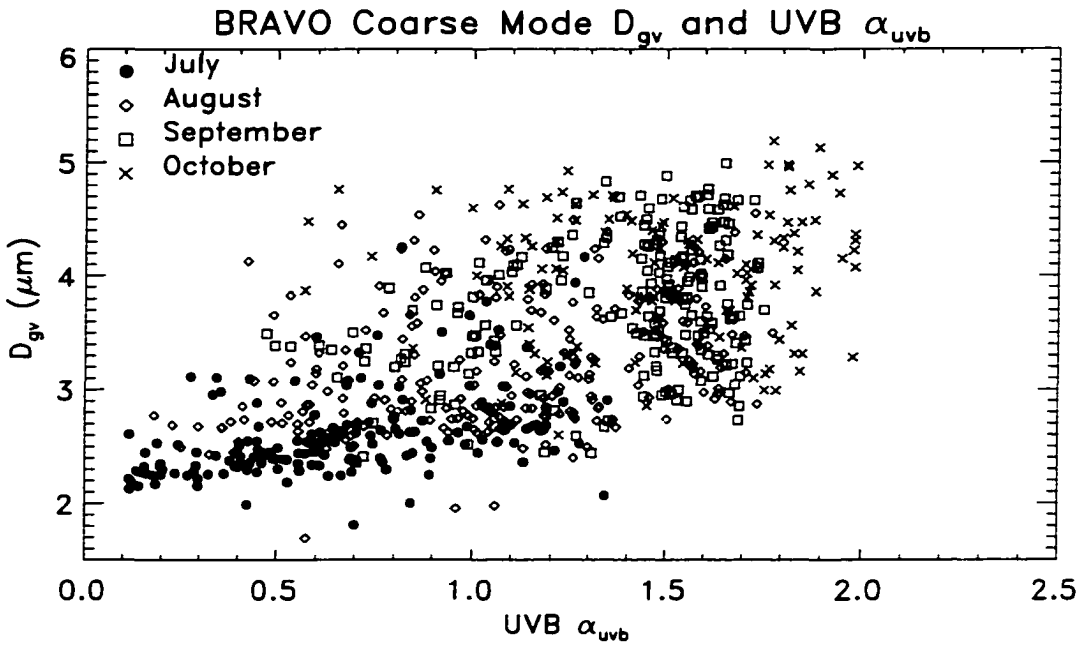

Figure 8.3.13 Comparison of dry coarse mode volume geometric mean diameter (D_{gv}) (μm) and column-based Ångstrom wavelength exponents (α_{uvb}).

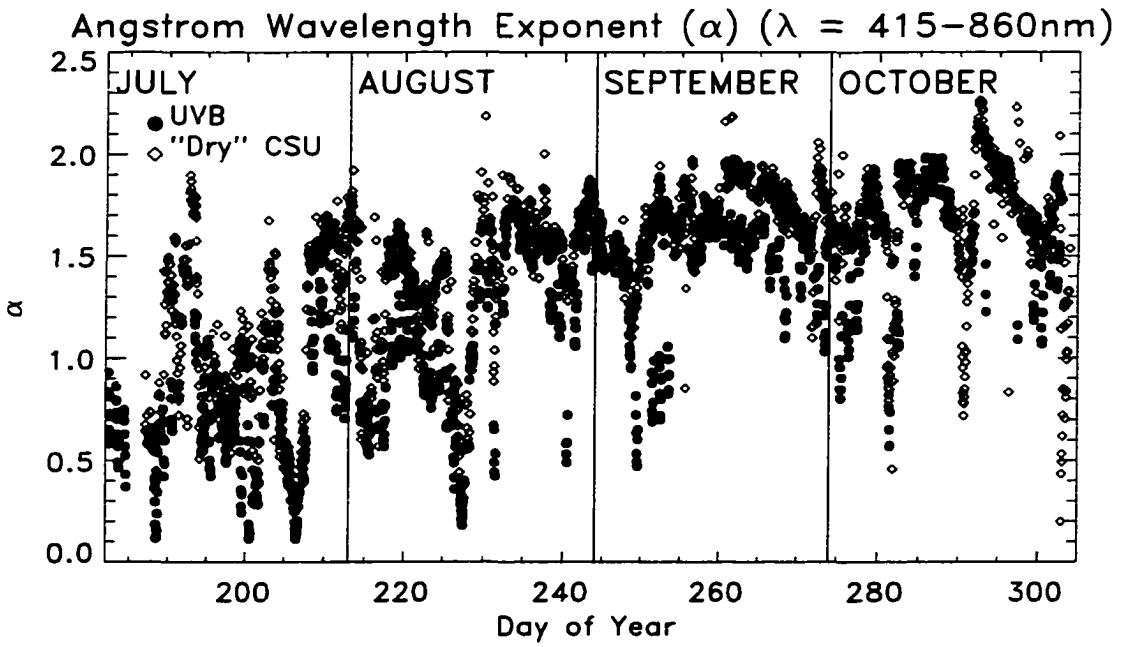

Figure 8.3.14 Timeline of dry surface- and ambient column-based Ångstrom wavelength exponents (α).

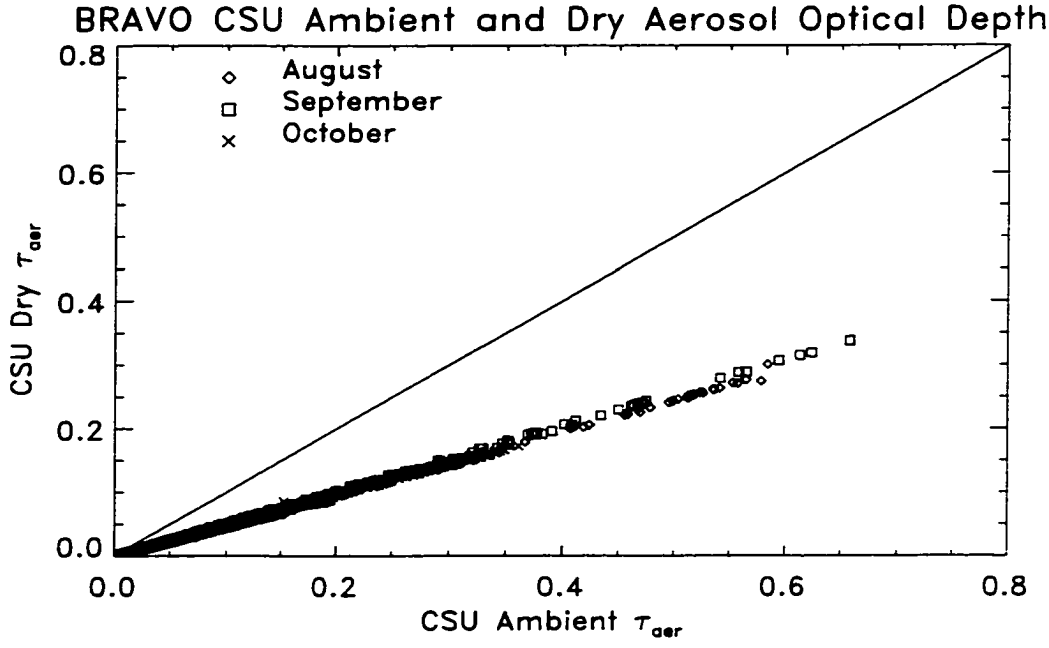

Figure 8.3.15 Comparison of surfaced-based (CSU) aerosol optical depths for dry aerosols and for aerosols corrected for relative humidity effects at RH = 60 %.

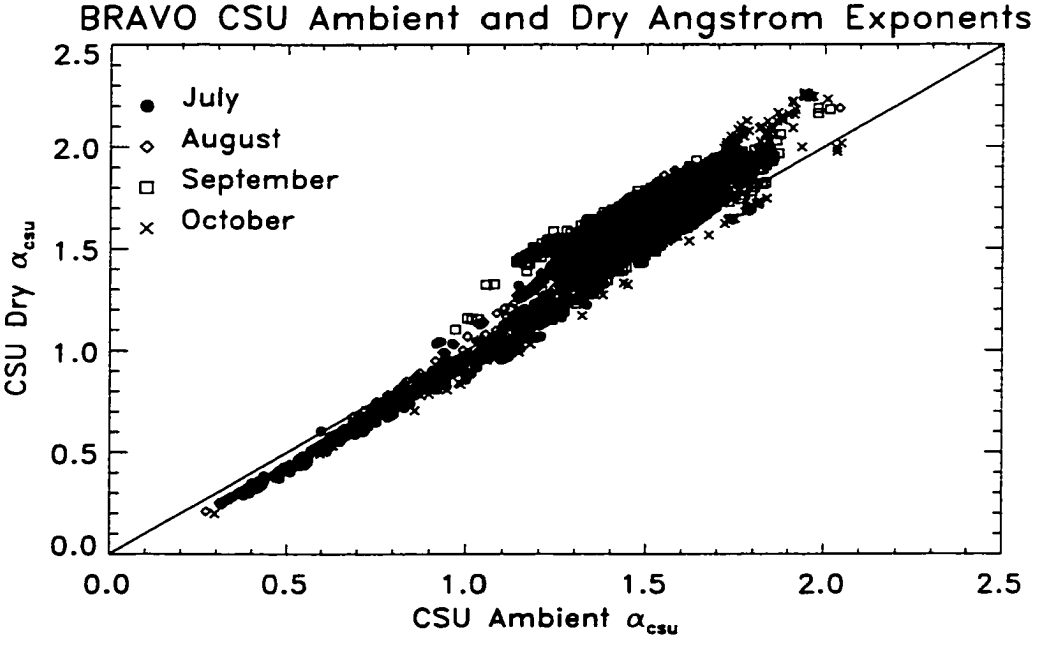

Figure 8.3.16 Comparison of surface-based (CSU) Ångstrom wavelength exponents for dry aerosols and for aerosols corrected for relative humidity effects at RH = 60 %.

CHAPTER 9 SUMMARY AND FUTURE WORK

9.1 SUMMARY

The meteorological conditions during BRAVO provided interesting opportunities to study the chemical, physical and optical properties of aerosols transported to the park from long distances as well as from local sources. Episodes linked to Saharan dust transport into the park in July and early August corresponded to elevated levels of coarse particle volume concentrations, fine soil mass concentrations and relatively high coarse particle scattering coefficients. Later episodes with high loading of coarse particles suggested more local sources with transport from the north and different soil mineralogy. Periods in September and October were dominated by accumulation mode sulfate aerosols that were responsible for increased visibility degradation in the park. During these periods, air flow patterns suggested transport from east Texas and the Texas-Mexico border. The BRAVO study provided an excellent opportunity not only to investigate the varying aerosol properties and their effects on visibility, but to test the methods by which information about the aerosols were obtained.

Dry aerosol size distributions were obtained with three instruments having different measurement techniques and size ranges. The TSI Differential Mobility Analyzer (DMA) measured mobility diameter from 0.05 μm to 0.87 μm. The PMS Optical Particle Counter (OPC) measured optical size from 0.1 μm to 2 μm, and the TSI Aerodynamic Particle Sizer (APS) measured aerodynamic size from 0.8 to 20 μm.

Extensive calibrations were performed on the OPC and APS to characterize instrument response to aerosols of different composition and size. These calibrations were used to construct channel collection efficiencies for each instrument, and the APS was found to have poor collection efficiencies for sizes smaller than 0.8 μm, regardless of composition. To construct a full aerosol size distribution from 0.05 to 20 μm, a new alignment method was devised that reconciled the data in the overlap regions between the instruments and retrieved particle refractive index and effective density (a function of particle dynamic shape factor). The average retrieved real refractive index (and one standard deviation) from this method was 1.566 ± 0.012 and the retrieved effective density was 1.56 ± 0.12 g cm^{-3}. Estimates of dynamic shape factor were also derived and the average was χ = 1.19 ± 0.14, suggesting that in general particles were nearly spherical. Applying this average shape factor to retrieved effective densities resulted in an average retrieved bulk density of 1.87 ± 0.13 g cm^{-3}. The retrieval of refractive index and effective density was most sensitive to the size range over which the data from each instrument were reconciled, and resulted in typical uncertainties of 3 % in refractive index and up to 30 % in effective density. Suggested improvements in experimental design that would reduce these uncertainties will be addressed in Section 9.2.

Fine ($PM_{2.5}$) and coarse ($PM_{10} - PM_{2.5}$) chemical compositions were obtained from 24-hour samples. On average fine aerosols were acidic with an average ammonium to sulfate molar ratio of 1.53 ± 0.3, with ammonium and sulfate as the dominant ionic species. Episodes with enhanced fine soil compositions were observed especially during July and early August and were linked to Saharan dust events. Overall fine ammoniated sulfate contributed approximately 50 % of fine mass concentrations, soil was

approximately 20 %, organic carbon concentrations were approximately 20 %, elemental carbon concentrations were 3 % and sodium nitrate concentrations were on the order of 4 %. The coarse composition was available from late August through October and differed from the fine mass composition in that ammoniated sulfate contributed approximately 20 % to coarse mass concentrations, soil was roughly 40 %, organic carbon was 30 %, elemental carbon was 2 % and sodium nitrate was approximately 7 %.

Complex refractive indices and bulk densities were computed with volume-weighted mixing rules and fine and coarse chemical compositions. The overall average real part of the fine complex refractive index was $m_r = 1.56 \pm 0.02$ and was in good agreement with the retrieved values. The average real part of the complex coarse refractive index was $m_r = 1.58 \pm 0.02$. The imaginary part of refractive index for the fine mode was $k = 0.015 \pm 0.008i$ and for the coarse mode was $k = 0.013 \pm 0.012i$. The average value of computed fine density was 1.85 ± 0.14 g cm^{-3} and coarse density was 1.97 ± 0.15 g cm^{-3}.

Size parameters derived from the complete aerosol size distributions using the alignment method suggested that both accumulation mode and coarse mode particles each contributed approximately 40 % to total volume concentrations during the study, and an observable giant mode existed in July and early August that contributed roughly 20 %. Periods when coarse mode volume dominated total volume were associated with Saharan dust episodes in July and August and flow from the north in October. Aerosols dominated by accumulation mode particles were associated with transport from east Texas, eastern United States and along the Texas-Mexico border. Variations in the position of the accumulation and coarse modes were observed with the average

accumulation volume mean diameter of $D_{gv} = 0.26 \pm 0.04$ μm and an average coarse mode $D_{gv} = 3.4 \pm 0.8$ μm.

Dry light scattering coefficients (b_{sp}) were computed from measured volume distributions and retrieved refractive indices and were evaluated over the same diameter ranges for the accumulation and coarse modes for which the size parameters were computed. On average the total light scattering coefficient (corresponding to the complete size distribution) was $b_{sp} = 0.026 \pm 0.016$ km^{-1}, the average accumulation mode light scattering coefficient was $b_{sp} = 0.021 \pm 0.015$ km^{-1}, and the average coarse mode light scattering coefficient was $b_{sp} = 0.005 \pm 0.005$ km^{-1}. On average accumulation mode particles were responsible for 80 % of total b_{sp}, although periods with significant coarse particle scattering coefficients were observed and corresponded to Saharan dust episodes in July and early August. These higher values of coarse b_{sp} also corresponded to coarse volume modes positioned at smaller sizes ($D_{gv} \sim 2.0$ μm), suggesting these particles were more efficient at light scattering than the average coarse mode size. Comparisons of accumulation mode b_{sp} to nephelometer-measured dry $PM_{2.5}$ b_{sp} demonstrated a high correlation ($R^2 = 0.974$), although estimates of b_{sp} were roughly 15 – 30 % larger than measured b_{sp}. The differences appeared to depend primarily on the characterization of particle losses in the sampling lines.

Dry mass scattering efficiencies for accumulation and coarse mode particles were computed from estimated b_{sp} and mass concentrations derived from integrated volume distributions. The average accumulation mode mass scattering efficiency was $e_{acm} = 3.4 \pm 0.5$ m^2 g^{-1}, similar to the nominal value of 3 m^2 g^{-1} applied in the IMPROVE formula for fine non-soil species. The average coarse mass scattering efficiency was $e_{coarse} = 0.6 \pm 0.2$

m^2 g^{-1}, consistent with the assumed value in the IMPROVE reconstructed scattering formula for wind-blown soil compositions. Higher values ($e_{coarse} \geq 1$ m^2 g^{-1}) were observed during July and corresponded to coarse mode volume distributions shifted to smaller diameters (coarse $D_{gv} \sim 2.0$ μm).

Aerosol optical depths (τ_{aer}) were computed from ground-based remote sensing irradiance measurements from the USDA UVB network over visible wavelengths. The Ångstrom wavelength exponent was computed from $\lambda = 415 - 860$ nm to characterize the spectral dependence of τ_{aer}. Estimates of ambient (RH = 60 %) particle extinction coefficients (b_{ext}) were used to derive aerosol optical depths from surface-based measurements by assuming aerosols were confined to a well-mixed layer and using estimates of this boundary layer height. The average aerosol optical depths from surface- and column-based measurements were $\tau_{aer} = 0.12 \pm 0.12$ (for late August through October) and 0.14 ± 0.06 (July – October), respectively. Overall good agreement was observed between these two estimates; surface- and column-based τ_{aer} were correlated ($R^2 = 0.691$) and agreed within roughly 40 %. A higher correlation was observed between ambient b_{ext} and column-based τ_{aer}, suggesting more realistic boundary layer heights would improve the comparison in aerosol optical depth. This correlation also suggested that during the BRAVO study, τ_{aer} derived from ground-based remote sensing was a good indicator of visibility at the surface. Ångstrom wavelength exponents were computed from ambient b_{ext} calculated over the same wavelengths as the column-based measurements. Ångstrom exponents derived from both methods were correlated ($R^2 = 0.775$) and agreed within roughly 30 %, with an average surface-based estimate of 1.4 ± 0.4 and an average column-based estimate of 1.1 ± 0.5. Variations in Ångstrom

exponents were linked to changing aerosol size distributions. Lower values corresponded to periods with significant coarse mode volume during Saharan dust episodes, and higher values were observed during periods dominated by accumulation mode particles.

The results in this dissertation suggested that the alignment method described in Chapter 4 and Chapter 5 successfully produced realistic aerosol size distributions from $0.05 < D_p < 20$ μm. Chapter 6 included several comparisons of results from this method with estimates from other measurements. Closure within 30 % was obtained between measured and reconstructed aerosol total mass concentrations and derived mass concentrations from integrated volume distributions. Comparisons between MOUDI mass distributions and volume distributions derived here suggested that the positions of the accumulation and coarse modes were consistent. Retrieved refractive indices and effective densities agreed very well with values computed using volume-weighted mixing rules. Chapter 7 and Chapter 8 demonstrated that estimates of optical properties determined entirely with results from the alignment method agreed with direct measurements. This agreement suggested that the alignment method was successful at deriving dry aerosol physical and optical properties from size distributions alone, and did not require estimates from aerosol chemical composition to do so. Furthermore, this method allowed aerosol physical and optical properties to be investigated over the full aerosol spectrum and provided insight into these properties that had yet to be observed. A limitation to this method was that it was applied to dry aerosol size distributions, and estimates of ambient aerosol properties reflecting the true nature of atmospheric aerosols required invoking separate measurements of aerosol chemical composition. Section 9.2 will address this limitation.

9.2 FUTURE WORK

The BRAVO study resulted in such a rich data set that comparisons and investigations into observed aerosol properties will continue for some time. Some of the investigations planned for future work include estimating ambient light scattering and extinction coefficients using dry aerosol size distributions, derived aerosol composition and thermodynamic models. Before estimating ambient light extinction, reconciliation of computed and measured dry light scattering coefficients is important. Currently there is approximately a 30 % difference in the two estimates, and although loss corrections are suspected to be the cause, more investigation is required before ambient light extinction estimates can be made. Ambient extinction coefficients and ambient coarse (PM_{10} – $PM_{2.5}$) scattering coefficients measured with transmissometry and nephelometry will be compared to estimated ambient scattering and extinction coefficients to investigate relative humidity effects on visibility. Comparisons of time-resolved sulfate measurements and aerosol size parameters demonstrated periods of increased sulfate concentrations with increases in small particles ($15 < D_p < 30$ nm) and periods when this trend was not observed (*Hering,* personal communication). These periods will be investigated, as well as the relationship between time-series of sulfate concentrations and light scattering coefficients.

The good agreement between surface- and column-based estimates of aerosol optical depths and Ångstrom exponents encourages further investigations in these types of comparisons at other locations. Relationships between Ångstrom exponents and size parameters can be explored by computing the curvature in the $\ln\tau_{aer}$ versus $\ln\lambda$ and correlating it to particle size. Ångstrom exponents can also be computed over other

wavelength regions to investigate further relationships with particle size. Finally, including these estimates of aerosol optical properties in computations of aerosol radiative direct forcing estimates would be an important aspect of future work. Fine and coarse chemical speciation would allow for the wavelength dependence of aerosol composition in these calculations.

It is possible that the conditions during BRAVO were ideal for the successful employment of the new alignment method. In order to test the general applicability of this method it should be applied in different conditions, for example in more urban areas where absorbing aerosols are more dominant, in marine regions with coarse particles of different composition and in regions with higher relative humidities. One of the major assumptions of the method was that aerosol composition did not vary over the size ranges aligned. Aerosol properties computed with volume-weighted mixing rules in Big Bend suggested that the mean aerosol refractive index and density did not differ greatly between the fine and coarse modes and that this assumption was appropriate during the study. It is important to test the method in regions where this assumption may not be valid, specifically where soil is not as significant in the fine mode and organic carbon is not as predominant in the coarse mode.

One of the major sensitivities in retrieving refractive index and density was the size region used in the data reconciliation. This region was constrained by the sizes corresponding to optimal performance of the instrument as well as the region of overlap between the instruments. Improving the retrieval of effective density will require higher collection efficiencies for the lower size range of the APS so that these data can be reliably included in the retrieval. Although these efficiencies were dependent on the

instrument design, effort into characterizing and applying a correction for the decreased efficiency as a function of composition and size would improve the APS-OPC overlap. The DMA-OPC alignment was performed by adjusting all of the OPC size channels with the same refractive index. It would be possible to adjust each bin with a different refractive index because each OPC bin limit diameter was related to refractive index by a different polynomial. Reconciling the DMA and OPC data by varying refractive index for each bin in the overlap range rather than all bins simultaneously would eliminate the assumption of a constant aerosol composition over the size distribution.

One of the limitations of the alignment method was that it was applied to dry aerosol size distributions to avoid relative humidity effects on particle size due to hygroscopic growth. Operating a similar experimental set-up at higher relative humidities would test the alignment method on size distributions affected by hygroscopic growth. If the method was successful at aligning ambient size distributions, particle refractive index, density and size could be retrieved as a function of aerosol water content. The method could then be used to estimate ambient light scattering coefficients without employing aerosol chemical compositions and thermodynamic models to include aerosol water content.

REFERENCES

Abreu, L. W. and G. P. Anderson, "The MODTRAN 2/3 Report and LOWTRAN 7 Model", *Ontar Corporation for PL/GPOS*, 1996.

Allen, M. D. and O. G. Raabe, "Re-evaluation of Millikan's Oil Drop Data for the Motion of Small Particles in Air", *J. Aerosol Sci.*, **13**, 537-547, 1982.

Ames, R. B., J. L. Hand, S. M. Kreidenweis, D. E. Day, and W. C. Malm, "Optical Measurements of Aerosol Size Distributions in Great Smoky Mountains National Park: Dry Aerosol Characterization", *J. Air Waste Manage.*, **50**, 665-676, 2000.

Ångstrom, A., "On the Atmospheric Transmission of Sun Radiation and on Dust in the Air", *Geogr. Ann.*, **12**, 130-159, 1929.

Arnott, W. P., H. Moosmüller, C. F. Rogers, T. Jin, and R. Bruch, "Photoacoustic Spectrometer for Measuring Light Absorption by Aerosol: Instrument Description", *Atmos. Environ.*, **33**, 2845-2852, 1999.

Arnott, W. P., H. Moosmüller, C. F. Rogers, J. L. Hand, D. E. Sherman, S. G. Brown, S. M. Kreidenweis, and J. L. Collett, "Light Absorption Measurements during the BRAVO Project at Big Bend National Park, Texas, Fall 1999", *Presented at the Conference on Visibility, Aerosols and Atmospheric Optics, Vienna, Austria*, 2000.

Baron, P. A., "Calibration and Use of the Aerodynamic Particle Sizer (APS 3300)", *Aer. Sci. Technol.*, **5**, 55-67, 1986.

Baron, P. A., M. K. Mazumder, and Y. S. Cheng, "Direct-Reading Techniques Using Optical Particle Detection", in *Aerosol Measurement Principles, Techniques and Applications*, edited by Willeke, K. and Baron, P., Van Nostrand Reinhold, NewYork, 1993, 318-409.

Baron, P. A. and K. Willeke, "Gas and Particle Motion", in *Aerosol Measurement Principles, Techniques and Applications*, edited by Willeke, K. and Baron, P., Van Nostrand Reinhold, New York, 23 –40, 1993

Baumgardner, D., J. E. Dye, B. Gandrud, K. Barr, K. Kelly, K. R. Chan, "Refractive Indices of Aerosols in the Upper Troposphere and lower Stratosphere", *Geophys. Res. Letters*, **23**, 749-752, 1996.

Baumgardner, D. and B. Huebert, "The Airborne Aerosol Inlet Workshop- Meeting Report", *J. Aerosol Sci.*, **24**, 835-846, 1993.

Bergin, M. H., S. E. Schwartz, R. N. Halthore, J. A. Ogren, and D. L. Hlavka, "Comparisons of Aerosol Optical Depth Inferred from Surface Measurements with that Determined by Sun Photometry for Cloud-Free Conditions at a Continental U. S. Site", *J. Geophys. Res.*, **105**, 6807-6816, 2000.

Bevington, P. R. and D. K. Robinson, *Data Reduction and Error Analysis for the Physical Sciences*, 2nd Edition, McGraw-Hill, Inc., New York, pp 64, 1992.

Bigelow, D. S., J. R. Slusser, A. F. Beaubien, and J. H. Gibson, "The USDA Ultraviolet Radiation Monitoring Program", *Bull. Amer. Meteor. Soc.*, **79**, 601-615, 1998.

Bohren, C. F., and D. R. Huffman, *Absorption and Scattering of Light by Small Particles*, Wiley Interscience, New York, 1983.

Brechtel, F. J., "Predicting Particle Critical Supersaturaiton from Hygroscopic Growth Measurements in the Humidified Tandem Differential Mobility Analyzer", *Ph.D. Dissertation, Department of Atmospheric Science, Colorado State University, Fort Collins, CO,* 1998.

Brockmann, J. E., "Sampling and Transport of Aerosols", in *Aerosol Measurement Principles, Techniques and Applications,* edited by Willeke, K. and Baron, P., Van Nostrand Reinhold, New York, 77-111, 1993.

Brown, S. G., D. E. Sherman, J. L. Hand, T. Lee, S. M. Kreidenweis, and J. L. Collett, "Aethalometer Measurements of Sub- and Super-Micron Black Carbon during the BRAVO Study", *Presented at AAAR 2000, Paper 11 PJ1,* 2000.

Cahill, T. A., L. L. Ashbaugh, R. A. Eldred, P. J. Feeney, B. H. Husko, and R. G. Flocchini, "Comparisons Between Size-Segregated Resuspended Soil Samples and Ambient Aerosols in the Western United States", in *Atmospheric Aerosol: Source/Air Quality Relationships, Am. Chem. Soc. Symp. Ser.*, **167**, edited by E. Macias, Washington D.C., 1981.

Charlson, R. J., S. E. Schwartz, J. M. Hales, R. D. Cess, J. A. Coakley, J. R. Hansen, and D. J. Hofmann, "Climate Forcing by Anthropogenic Aerosols", *Science*, **255**, 423-430, 1992.

Chen, B. T., Y. S. Cheng, and H. C. Yeh, "Performance of a TSI Aerodynamic Particle Sizer", *Aerosol Sci. and Technol.*, **4**, 89-97, 1985.

Clarke, A. D., J. N. Porter, F. P. J. Valero, and P. Pilewski, "Vertical Profiles, Aerosol Microphysics, and Optical Closure during the Atlantic Stratocumulus Transition Experiment: Measured and Modeled Column Optical Properties", *J. Geophys. Res.*, **101**, 4443-4453, 1996.

Collins, D. R., H. H. Jonsson, J. H. Seinfeld, R. C. Flagan, S. Gasso, D. A. Hegg, P. B. Russell, B. Schmid, J. M. Livingston, E. Ostrom, K. J. Noone, L. M. Russell, and J. P. Putaud, "In Situ Aerosol Size Distributions and Clear Column Radiative Closure During ACE-2", *Tellus*, **52B**, 498-525, 2000.

Crump, J. G. and J. H. Seinfeld, "A New Algorithm for Inversion of Aerosol Size Distribution Data", *Aerosol Sci. Technol.*, **1**, 15-34, 1982.

Dick, W. D., P. H. McMurry, and J. R. Bottiger, "Size- and Composition-Dependent Response of the DAWN-A Multiangle Single Particle Optical Detector", *Aerosol Sci. Technol.*, **20**, 345-362, 1994.

Dick, W. D., "Multiangle Light Scattering Techniques for Measuring Shape and Refractive Index of Submicron Atmospheric Particles", *Ph. D. Dissertation*, Department of Mechanical Engineering, University of Minnesota, 1998a.

Dick, W. D., P. Saxena, P. H. McMurry, "Estimation of Water Uptake by Organic Compounds in Submicron Aerosols Measured During the Southeastern Aerosol and Visibility Study", *J. Geophys. Res.*, **105**, 1471-1479, 2000.

Dick, W. D., P. A. Ziemann, P. F. Huang, and P. H. McMurry, "Optical Shape Fraction Measurements of Submicron Laboratory and Atmospheric Aerosols", *Meas. Sci. and Technol.*, **9**, 183-196, 1998b.

Dzubay, T. G. and H. Hasan, "Fitting Multimodal Lognormal Size Distributions to Cascade Impactor Data", *Aerosol Sci. Technol.*, **13,** 144- 150.

Eck, T. F., B. N. Holben, J. S. Reid, O. Dubovik, A. Smirnov, N. T. O'Neill, I. Slutsker, and S. Kinne, "Wavelength Dependence of the Optical Depth of Biomass Burning, Urban, and Desert Dust Aerosol", *J. Geophys. Res.*, **104**, 31333-31349, 1999.

Ehara, K. C., C. Hagwood, and K. J. Coakley, "Novel Method to Classify Aerosol Particles According to their Mass-to-Charge Ratio: Aerosol Particle Mass Analyser", *J. Aerosol Sci.*, **27**, 217-234, 1996.

Eldering, A., G. R. Cass, and K. C. Moon, "An Air Monitoring Network Using Continuous Particle Size Distribution Monitors: Connecting Pollutant Properties to Visibility via Mie Scattering Calculations", *Atmos. Environ.*, **28(16)**, 2733-2749, 1994.

Eldred, R., "Regional Patterns in Particulate Matter from the National Park Service Network, June 1982 to May 1986", *Visibility Protection, Research and Policy Aspects*, edited by P. S. Bhardwaja, Air & Waste Management Association, Pittsburgh, 386-396, 1986.

Fuchs, N. A., *The Mechanics of Aerosols*, Pergamon, 1964.

Fuller, K. A., W. C. Malm, and S. M. Kreidenweis, "Effects of Mixing on Extinction by Carbonaceous Particles", *J. Geophys. Res.*, **104(D13)**, 15941-15954, 1999.

Gebhart, K. G., W. C. Malm, and M. Flores, "A Preliminary Look at Source-Receptor Relationships in the Texas-Mexico Border Area", *J. Air Waste Manage.*, **50**, 858-868, 2000.

Gebhart, K. G., S. M. Kreidenweis, and W. C. Malm, "Back-trajectory Analyses of Fine Particulate Matter measured at Big Bend National Park in the Historical Database and the 1996 Scoping Study", *Sci. Total. Environ., in press*, 2001.

Gras, J. L., "An Investigation of a Non-Linear Iteration Procedure for Inversion of Particle Size Distributions", *Atmos. Environ.*, **17**, 883-894, 1983.

Gunn, R. and R. H. Woessner, "Measurements of the Systematic Electification of Aerosols", *J. Colloid. Sci.*, **11**, 254-259, 1956.

Hand, J. L., R. B. Ames, S. M. Kreidenweis, D. E. Day, and W. C. Malm, "Estimates of Particle Hygroscopicity During the Southeastern Aerosol and Visibility Study (SEAVS)", *J. Air Waste Manage.*, **50**, 677-685, 2000.

Hand, J. L., "Aerosol Hygroscopicity and Visibility Estimates in the Great Smoky Mountains National Park", *M.S. Thesis, Department of Atmospheric Science, Colorado State University, Fort Collins, CO*, 1997.

Handbook of Chemistry and Physics, 61st Edition, 1980-1981, Edited by R. C. Weast, CRC Press, Inc., Boca Raton, Florida, 1981.

Hanel, G. and J. Thudium, "Mean Bulk Densities of Samples of Dry Atmospheric Aerosol Particles: A Summary of Measured Data", *Pageoph*, **115**, 799-803, 1977.

Hansen, J. E. and L. D. Travis, "Light Scattering in Planetary Atmospheres", *Space Sci. Rev.*, **16**, 527-610, 1974.

Harrison, L., J. Michalsky, and J. Berndt, "Automated Multifilter Rotating Shadow-Band Radiometer: An Instrument for Optical Depth and Radiation Measurments", *App. Optics*, **33**, 5118-5125, 1994.

Harrison, L. and J. Michalsky, "Objective Algorithms for the Retrieval of Optical Depth from Ground-Based Measurements", *App. Optics,* **33,** 5126-5132, 1994.

Hasan, H. and T. G. Dzubay, "Apportioning Light Extinction Coefficients to Chemical Species in Atmospheric Aerosol", *Atmos. Environ.*, **17(8)**, 1573-1581, 1983.

Hasan, H. and C. W. Lewis, "Integrating Nephelometer Response Corrections for Bimodal Size Distributions", *Aerosol Sci. Technol.*, **2**,443-453,1983.

Haywood, J. and O. Boucher, "Estimates of the Direct and Indirect Radiative Forcing due to Tropospheric Aerosols: A Review", *Rev. Geophys.*, **38**, 513-543, 2000.

Haywood, J. M. and V. Ramaswamy, "Global Sensitivity Studies for the Direct Radiative Forcing due to Anthropogenic Sulfate and Black Carbon Aerosols", *J. Geophys. Res.*, **103**, 6043-6058, 1998.

Heffter, J. L., "Air Resources Laboratory Atmospheric Transport and Diffusion Model (ARL-ATAD)", National Oceanic and Atmospheric Administration, Technical Memo, ERL-ARL-81, 1980.

Heidenreich, S., H. Büttner, and F. Ebert, "Investigations on the Behaviour of an Aerodynamic Particle Sizer and its Applicability to Calibrate an Optical Particle Counter", *Part. Part. Syst. Charact.*, **12**, 304-308, 1995.

Heitbrink, W. A., P. A. Baron and K. Willeke, "Coincidence in Time-of-Flight Aerosol Spectrometers: Phantom Particle Creation", *Aerosol Sci. Technol.*, **14**, 112-126, 1991.

Heitbrink, W. A. and P. A. Baron, "An Approach to Evaluating and Correcting Aerodynamic Particle Sizer Measurements for Phantom Particle Count Creation", *Am. Ind. Hyg. Assoc. J.*, **53(7),** 427-431, 1992.

Hering, S. V. and P. H. McMurry, "Optical Counter Response to Monodisperse Atmospheric Aerosols", *Atmos. Environ.*, **25A**, 463-468, 1991.

Hinds, W. C., *Aerosol Technology: Properties, Behavior and Measurement of Airborne Particles*, 2nd Edition, John Wiley & Sons, Inc., New York, pp 42-73, 1999.

Hitzenberger, R., S. G. Jennings, S. M. Larson, A. Dillner, H. Cachier, Z. Galambos, A. Rouc, and T. G. Spain, "Intercomparison of Measurement Methods for Black Carbon Aerosols", *Atmos. Environ.*, **33**, 2823-2833, 1999.

Holben, B. N., et al., "AERONET- A Federated Instrument Network and Data Archive for Aerosol Characterization", *Remote Sens. Environ.*, **66**, 1-16, 1998.

Hoppel, W. A., "Determination of the Aerosol Size Distribution from the Mobility Distribution of the Charged Fraction of Aerosols", *J. Aerosol Sci.*, **9**, 41-54, 1978.

Hoppel, W. A., J. W. Fitzgerald, G. M. Frick, R. E. Larson, and E. J. Mack, "Aerosol Size Distributions and Optical Properties Found in the Marine Boundary Layer over the Atlantic Ocean", *J. Geophys. Res.*, **95**, 3659-3686, 1990.

Horvath, H., "Atmospheric Light Absorption- A Review", *Atmos. Environ.*, **27A**, 293-317, 1993.

Intergovernmental Panel on Climate Change (IPCC), edited by J. T. Houghton et al., Cambridge University Press, New York, 1995.

Intergovernmental Panel on Climate Change (IPCC), edited by J. T. Houghton et al., Cambridge University Press, New York, 1996.

Johnston, J., *Econometric Methods*, 3rd Edition, McGraw-Hill, New York, 428-435, 1984.

Junge, C. E., "The Size Distribution and Aging of Natural Aerosols as Determined from Electrical and Optical Measurements in the Atmosphere", *J. Meteorol.*, **12**, 13-25, 1955.

Kalashnikova O. V., and I. N. Sokolik, "Characterization of the Optical Properties of Irregular Mineral Dust Aggregates Combining Individual Particle Analysis and Modeling", *presented at AMS 2001, paper J1.12, 2001.*

Kelly, W. P. and P. H. McMurry, "Measurement of Particle Density by Inertial Classification of Differential Mobility Analyzer- Generated Mondisperse Aerosols", *Aerosol Sci. Technol.*, **17**, 199-212, 1992.

Kim, Y. J. and J. F. Boatman, "Size Calibration Corrections for the Active Scattering Aerosol Spectrometer Probe (ASASP-100X)", *Aerosol Sci. Technol.*, **12**, 665-672, 1990.

Kim, Y. J, "Response of the Active Scattering Aerosol Spectrometer Probe (ASASP-100X) to Different Chemical Composition", *Aerosol Sci. Technol.*, **22**, 33-42, 1995.

Kinne, S., T. P. Ackerman, M. Shiobara, A. Uchiyama, A. J. Heymsfield, L. Miloshevich, J. Wendell, E. W. Eloranta, C. Purgold, and R. W. Bergstrom, "Cirrus Cloud Radiative and Microphysical Properties from Ground Observations and In Situ Measurements during FIRE 1991 and Their Application to Exhibit Problems in Cirrus Solar Radiative Transfer Modeling", *J. Atmos. Sci.*, **54**, 2320-2344, 1997.

Knutson, E. O., and P. J. Lioy, "Measurement and Presentation of Aerosol Size Distributions", *Air Sampling Instruments for Evaluation of Atmospheric*

Contaminants, 7th Edition, edited by S. V. Hering, American Conference of Governmental Industrial Hygienists, Cincinnati, Ohio, pp 59-71, 1989.

Knutson, E. O., and K. T. Whitby, "Aerosol Classification by Electric Mobility: Apparatus, Theory and Applications", *J. Aerosol Sci.*, **6**, 443-451, 1975.

Kreidenweis, S. M., L. A. Remer, R. Bruintjes, and O. Dubovik, "Smoke Aerosol from Biomass Burning in Mexico: Hygroscopic Smoke Optical Model", *J. Geophys. Res.*, **106**, 4831- 4844, 2001.

Kreisberg N. M., M. R. Stolzenburg, S. V. Hering, W. D. Dick, and P. H. McMurry, "A New Method for Measuring the Dependence of Particle Size Distributions on Relative Humidity, with Application to the Southeastern Aerosol and Visibility Study", *J. Geophs. Res., Accepted for publication,* 2001.

Kaufman, Y. J., "Aerosol Optical Thickness and Atmospheric Path Radiance", *J. Geophys. Res.*, **98**, 2677-2692, 1993.

Lee, T, J. E. Reilly, M. P. Hannigan, D. E. Sherman, J. L. Hand, S. M. Kreidenweis, and J. L. Collett, "Comparison of Observed and Model-Predicted Aerosol Composition During the Big Bend Regional Aerosol and Visibility Observational Study (BRAVO)", *presented at the AAAR 2000, paper 11PJ1,* 2000.

Leinert, S. and A. Wiedensohler, "APS Counting Efficiency Calibration for Submicrometer Particles", *presented at the 2000 European Aerosol Conference*, 2000.

Liu, Y. and P. H. Daum, "The Effectof Refractive Index on Size Distributions and Light Scattering Coefficients Derived from Optical Particle Counters", *J. Aerosol Sci.*, **31(8)**, 945-957, 2000.

Lowenthal, D. H., J. G. Watson, and P. Saxena, "Contributions to Light Extinction During Project MOHAVE", *Atmos. Environ.*, **34**, 2351-2359, 2000.

Lowenthal, D. H., C. F. Rogers, P. Saxena, J. G. Watson, and J. C. Chow, "Sensitivity of Estimated Light Extinction Coefficients to Model Assumptions and Measurement Errors", *Atmos. Environ.*, **29**, 751-766, 1995.

Malm, W. C., "Examining the Relationship between Aerosol Concentration and Particle Scattering Efficiencies near the Grand Canyon", Presented at the 91st Annual Meeting and Exhibition of the Air and Waste Management Association, Pittsburg, PA., 1998.

Malm, W. C., J. F. Sisler, D. Huffman, R. A. Eldred, and T. A. Cahill, "Spatial and Seasonal Trends in Particle Concentration and Optical Extinction in the United States", *J. Geophys. Res.*, **99**, 1347-1370, 1994.

Malm, W. C., and M. L. Pitchford, "Comparison of Calculated Sulfate Scattering Efficiencies as Estimated from Size-Resolved Particle Measurements at Three National Locations", *Atmos. Environ.*, **31**, 1315-1325, 1997.

Malm, W. C. and D. E. Day, "Optical Properties of Aerosols at Grand Canyon National Park", *Atmos. Environ.*, **34**, 3373-3391, 2000.

Malm, W. C., D. E. Day, and S. M. Kreidenweis, "Light Scattering Characteristics of Aerosols as a Function of Relative Humidity: Part I- A Comparison of Measured Scattering and Aerosol Concentrations Using the Theoretical Models", *J. Air Waste Mangage.*, **50**, 686-700, 2000.

Markowski, G. R., "Improving Twomey's Algorithm for Inversion of Aerosol Measurement Data", *Aerosol Sci. Technol.*, **7**, 127-141, 1987.

McMurry, P. H., " A Review of Atmospheric Aerosol Measurements", *Atmos. Environment*, **34**, 1959-1999, 2000.

McMurry, P. H., X. Wang, K. Park, and K. Ehara, "The Relationship Between Mass and Mobility for Atmospheric Particles: A New Technique for Measuring Particle Density", *submitted to Aerosol Sci. and Technol.*, 2000.

Mie, G. "Beitraege zur Optik trueber Medien, speziell kolloidaler Metalosungen", *Ann. Physik*, **25**, 377-445, 1908.

Myhre, G., F. Stordal, K. Restad, and I. Isaksen, "Estimates of the Direct Radiative Forcing due to Sulfate and Soot Aerosols", *Tellus, Ser. B*, **50**, 463-477, 1998.

Nakajima, T. and A. Higurashi, "A Use of Two-Channel Radiances for an Aerosol Characterization from Space", *Geophys. Res. Letters*, **25**, 3815-3818, 1998.

Ouimette, J. R. and R. C. Flagan, "The Extinction Coefficient of Multicomponent Aerosols", *Atmos. Environ.*, **16(10)**, 2405-2419, 1982.

Perry, K. D., T. A. Cahill, R. A. Eldred, and D. D. Dutcher, "Long-Range Transport of North African Dust to the Eastern United States", *J. Geophys. Res.*, **102**, 11225-11238, 1997.

Peters, T. M., H. Chein, D. A. Lundgren, and P. B. Keady, "Comparison and Combination of Aerosol Size Distributions Measured with a Low Pressure Impactor, Differential Mobility Particle Sizer, Electric Aerosol Analyzer, and Aerodynamic Particle Sizer", *Aer. Sci. Technol.*, **19**, 396-405, 1993.

Pinnick, R. G. and H. J. Auvermann, "Response Characteristics of Knollenberg Light-Scattering Aerosol Counters", *J. Aerosol Science.*, **10**, 55-74, 1979.

Pinnick, R. G., J. D. Pendleton, and G. Videen, "Response Characteristics of the Particle Measuring Systems Active Scattering Aerosol Spectrometer Probes", *Aerosol Sci. Technol.*, **33**, 334-352, 2000.

Pitchford, M., R. G. Flocchini, R. G. Draftz, T. A. Cahill, L. L. Ashbaugh, and R. A. Eldred, "Silicon in Submicron Particles in the Southwest", *Atmos. Environ.*, **15**, 321-333, 1981.

PMS Instrument Manual for the LASAIR 1003 Optical Particle Counter, PMS, Boulder, CO.

Press, W. H., S. A. Teukolsky, W. T. Vetterling, and B. P. Flannery, *Numerical Recipes in Fortran 77: The Art of Scientific Computing*, 2nd Edition, Press Syndicate of the University of Cambridge, Cambridge, 1992.

Quinn, P. K., S. F. Marshall, T. S. Bates, D. S. Covert, and V. N Kapustin, "Comparison of Measured and Calculated Aerosol Properties Relevant to the Direct Radiative Forcing of Tropospheric Sulfate Aerosols on Climate", *J. Geophys. Res.*, **100**, 8977-8991, 1995.

Quinn, P. K., D. J. Coffman, V. N. Kapustin, and T. S. Bates, "Aerosol Optical Properties during the First Aerosol Characterization Experiment (ACE-1) and the Underlying Chemical and Physical Aerosol Properties", *J. Geophys. Res.*, **103**, 16547-16563.

Reid, J. S., T. F. Eck, S. A. Christopher, P. V. Hobbs, and B. Holben, "Use of the Angstrom Exponent to Estimate the Variability of Optical and Physical Properties of Aging Smoke Particles in Brazil", *J. Geophys. Res.*, **104**, 27473-27489, 1999.

Reineking A. and J. Porstendörfer, "Measurements of Particle Loss Functions in a Differential Mobility Analyzer (TSI, Model 3071) for Different Flow Rates", *Aer. Sci. Technol.*, **5**, 483-486, 1986.

Sherman, D. E., J. L. Hand, S. M. Kreidenweis, J. L. Collett, T. Lee, D. E. Day, W. C. Malm, and K. A. Gebhart, "The Influence of Meteorological Conditions on Ambient Particle Concentrations during BRAVO", *presented at the AAAR 2000, paper11PJ4*, 2000.

Shettle, E. P. and S.Anderson, "New Visible and Near IR Ozone Absorption Cross-Sections for MODTRAN", in *Proceedings of the 17th Annual Review Conference on Atmopsheric Transmission Models*, 8-9 June 1994, edited by G. Anderson, R. H. Picard, and J. H. Chetwynd, PL-TR-95-2060, Phillips Laboratory, Hanscom AFB, MA, pp 335-345.

Sisler, J. F., "Spatial and Seasonal Patterns and Long Term Variability of the Composition of the Haze in the United States: An Analysis of Data from the IMPROVE Network", CIRA report, ISSN 0737-5352-32, Colorado State University, 1996.

Sloane, C. S., "Effect of Composition on Aerosol Light Scattering Efficiencies", *Atmos. Environ.*, **20**, 1025-1037.

Sloane, C. S., M. J. Rood, and C. F. Rogers, "Reconciliation of Aerosol Particle Measurements", *Transactions Visibility and Fine Particles*, edited by C. V. Mathai, AWMA, Pittsburgh, PA., 1990.

Slusser, J., J. Gibson, D. Bigelow, D. Kolinski, P. Disterhoft, K. Lantz, and A. Beaubien, "Langley Method for Calibrating UV Filter Radiometers", *J. Geophys. Res.*, **105**, 4841-4849, 2000.

Smirnov, A., B. N. Holben, T. F. Eck, O. Dubovik, and I. Slutsker, "Cloud-Screening and Quality Control Algorithms for the AERONET Database", *Rem. Sens. Environ.*, **73**, 337-349, 2000.

Smirnov, A., B. N. Holben, I. Slutsker, E. J. Welton, and P. Formenti, "Optical Properties of Sarahan Dust during ACE 2", *J. Geophys. Res.*, **103**, 28079-28092, 1998.

Sokolik, I. N. and O. B. Toon, "Direct Radiative Forcing by Anthropogenic Airborne Mineral Aerosols", *Nature*, **381**, 681-683, 1996.

Sokolik, I. N. and O. B. Toon, "Incorporation of Mineralogical Composition into Models of the Radiative Properties of Mineral Aerosol from UV to IR Wavelengths", *J. Geophys. Res.*, **104**, 9423-9444, 1999.

Stein, S. W., B. J. Turpin, X. P. Cai, C. P. F. Huang, and P. H. McMurry, "Measurements of Relative Humidity-Dependent Bounce and Density for Atmospheric Particles Using the DMA-Impactor Technique", *Atmos. Environ.*, **28**, 1739-1746.

Stelson, A. W., "Urban Aerosol Refractive Index Prediction by Partial Molar Refraction Approach", *Environ. Sci. Technol.*, **24**, 1676-1679, 1990.

Stolzenburg, M., N. Kreisberg, and S. Hering, "Atmospheric Size Distributions Measured by Differential Mobility Optical Particle Size Spectrometry", *Aer. Sci. Technol.*, **29**, 402-418, 1998.

Straub, D. J. and J. L. Collett, "Numerical and Experimental Performance Evaluation of the 3-Stage FROSTY Supercooled Cloud Collector", *Aer. Sci. Technol.*, **34**, 247-261, 2001.

Tang, I. N., "Chemical and Size Effects of Hygroscopic Aerosols on Light Scattering Coefficients", *J. Geophys. Res.*, **101**, 19245-19250, 1996.

Tegen I., A. Lacis, and I. Fung, " The Influences of Mineral Aerosols from Disturbed Soils on Climate Forcing", *Nature*, **380**, 419-422, 1996.

Trijonis, J.C., "RESOLVE Project Final Report: Visibility Conditions and Causes of Visibility Degradation in the Mohave Desert of California", NWC Tech Paper 6869, Naval Weapons Center, China Lake, CA., 1988.

Trijonis, J. C., W. C. Malm, M. Pitchford, M., W. H. White, R. Charlson, and R. Husar, "Visibility: Existing and Historical Conditions: Causes and Effects", In: State Sci. State Technol. Rep. 24, Natl. Acid Precip. Assessment Program, Washington D.C., 1990.

TSI Instrument Manual for the APS 3320, TSI, Minneapolis, MN.

TSI Instrument Manual for the DMA 3071, TSI, Minneapolis, MN.

TSI Instrument Manual for the CPC 3010, TSI, Minneapolis, MN.

TSI Instrument Manual for the Aerosol Generation System 3075/3076, TSI, Minneapolis, MN.

TSI Instrument Manual for the VOAG 3450, TSI, Minneapolis, MN.

TSI Instrument Manual for the Single Jet Atomizer 9302A, TSI, Minneapolis, MN.

Twomey, S., "Comparison of Constrained Linear Inversion and an Iterative Nonlinear Algorithm Applied to the Indirect Estimation of Particle Size Distributions", *J. Comput. Phys.*, **18**, 188-200, 1975.

van de Hulst, H. C., *Light Scattering by Small Particles*, Dover, Mineola, New York, 1981.

Wang, H.-C. and W. John, "A simple iteration procedure to correct for the density effect in the Aerodynamic Particle Sizer", *Aerosol Sci. and Technol.*, **10**, 501-505, 1989.

Wang, H-C. and W. John, "Characteristics of the Berner Impactor for Sampling Inorganic Ions", *Aerosol Sci. Technol.*, **8**, 157-172, 1988.

Wiedensohler, A., "An Approximation of the Bipolar Charge Distribution for Particles in the Submicron Size Range", *J. Aerosol Sci.*, **3**, 387-389, 1988.

Wilson, J. C., A. Gupta, K. T. Whitby, and W. E. Wilson, "Measured Aerosol Light Scattering Coefficients Compared with Values Calculated from EAA and Optical Particle Counter Measurements: Improving the Utility of the Comparison", *Atmos. Environ.*, **22(4)**, 789-793, 1988.

Winklmayr, W., H-C. Wang, and W. John, "Adaptation of the Twomey Algorithm to the Inversion of Cascade Impactor Data", *Aerosol Sci. Technol.*, **13**, 322-331, 1990.

Zhang, X., B. J. Turpin, P. H. McMurry, S. V. Hering, and M. R. Stolzenburg, "Mie Theory Evaluation of Species Contributions to 1990 Wintertime Visibility Reduction in the Grand Canyon", *J. Air Waste Manage.*, **44**, 153-162.

APPENDIX A. THEORETICAL LOSS CALCULATIONS

Theoretical loss calculations were performed for all the instruments in their experimental configuration to take into account particle losses in the sampling lines. Diffusional losses, gravitational losses, losses in bends, and losses in cyclones and Perma Pure dryers were considered. All of the loss calculations were performed for instrument channel midpoint diameters converted to aerodynamic diameters using a density of 1.6 g cm^{-3}. The Optical Particle Counter channel diameters were converted from optical to geometric diameter with a refractive index of m = 1.55 and then converted to aerodynamic diameter with a density of 1.6 g cm^{-3}. Many parameters are required to perform these calculations. These will be described next.

Many of the parameters required in loss calculations do not depend on the tubing configuration. Air density, ρ_{air} (kg m^{-3}) given by Equation A.1 and was computed according to the site elevation. Ambient pressure (P) was 890 mbar, and the temperature at which the measurements were performed was T = 293 K. The molecular weight of air is given by MW_{air} as 29 g/mol.

$$\rho_{air} = \left(\frac{P}{1013.25}\right) \cdot \left(\frac{MW_{air}}{T \cdot 0.08206}\right) \qquad \text{(A.1)}$$

Dynamic viscosity is a measure of the momentum transfer occurring during molecular collisions. It is usually related to a reference viscosity ($\eta_{23} = 1.83245 \times 10^{-4}$) and reference temperature (T_r = 296.15 K). The conversion to the units of kg m s^{-1} is included in

Equation (A.2) (*Allen and Raabe*, 1985). The Sutherland interpolation constant, S, is 110.4. The temperature T is the same as applied in Equation A.1.

$$\eta = \frac{\eta_{23}}{10}\left(\frac{T_r + S}{T + S}\right)\cdot\left(\frac{T}{T_r}\right)^{3/2} \qquad \text{(A.2)}$$

The mean free path, λ, is the mean distance a molecule travels before colliding with another molecule and was computed with Equation A.3. In Equation (A.3), pressure (P) is in units of mmHg and the reference mean free path, λ_o, is in units of micrometers. The units of mean free path for future use will be meters (*Allen and Raabe*, 1985).

$$\lambda = \lambda_o \cdot \left(\frac{T}{T_r}\right)\cdot\left(\frac{760}{P_{mmHg}}\right)\cdot\left(\frac{1 + S/T_r}{1 + S/T}\right) \qquad \text{(A.3)}$$

Stokes law is a solution to the Navier-Stokes equations assuming inertial forces are negligibly small compared to the viscous forces. Other assumptions include an incompressible fluid, no nearby walls or particles, constant motion, rigid spherical particles and the fluid velocity at the surface of the particle is zero. The last assumption breaks down for very small particles with sizes comparable to the mean free path of the gas. These small particles settle faster than predicted by Stoke's law because there is a "slip" at the surface of the particle. For particles less than 1 μm in diameter this "slip" can be significant. In order to account for this effect, the Cunningham correction factor (C_c) was incorporated into the calculation. (*Hinds*, 1999). For this calculation, the pressure dependent form of the equation was used (pressure in units of cmHg and diameter in micrometers). The Cunningham correction factor is dimensionless (Equation A.4).

$$C_c = 1 + \frac{2}{P_{cmHg} D_p}\cdot\left(6.32 + 2.01\cdot\exp\left(-0.1095\cdot P_{cmHg} D_p\right)\right) \qquad \text{(A.4)}$$

Gas diffusion causes a net movement of molecules from higher concentrations to a lower concentrations and is characterized by the diffusional coefficient, D, in units of $m^2\ s^{-1}$ (Equation A.5) (*Baron and Willeke*, 1993). The Boltzmann constant is given as $k = 1.38\times10^{-23}$ J K^{-1}. Diameter (D_p) has units of meters and the gas viscosity was calculated in Equation A.2.

$$D = \frac{kTC_c}{3\pi\eta D_p} \tag{A.5}$$

The dimensionless Schmidt number, S_c, describes the convective mass transfer relative to Brownian diffusion of particles, and increases with increasing convective mass transfer (Equation A.6) (*Baron and Willeke*, 1993).

$$S_c = \frac{\eta}{\rho_{air} D} \tag{A.6}$$

The settling velocity of a particle is given in Equation A.7 in units of m s^{-1} (*Baron and Willeke*, 1993) where diameter is in units of meters, g is the gravitational constant and ρ_p is particle density in units of kg m^{-3}.

$$v_{ts} = \frac{\rho_p D_p^2 g C_c}{18\eta} \tag{A.7}$$

The following parameters depend on tubing configuration and were calculated for specific tubing configurations for each instrument.

Diffusional losses due to particles diffusing to tubing walls were computed using Equation (A. 8) (*Brockmann*, 1993)

$$\eta_{diff} = \exp(-\xi Sh) \tag{A.8}$$

where

$$\xi = \frac{\pi DL}{Q} \tag{A.9}$$

D is the diffusional coefficient, L is the length of the tubing in meters and Q is the sample flow rate in $m^3\ s^{-1}$. The Sherwood number (Sh) was calculated by Equation A.10 (*Brockmann,* 1993) and is a dimensionless mass transfer coefficient.

$$Sh = 3.66 + \left(\frac{0.0668(d_i/L)R_eS_c}{1 + 0.04[(d_i/L)R_eS_c]^{2/3}} \right) \tag{A.10}$$

The tubing inner diameter (d_i) is in units of meters. Schmidt (S_c) number was given in Equation A.6 and the Reynolds number (R_e), which is a ratio of the inertial force to the frictional force of a gas (*Baron and Willeke,* 1993), is given by Equation A.11.

$$R_e = \frac{\rho_{air} v_{tube} d_i}{\eta} \tag{A.11}$$

where v_{tube} is the velocity in the tube in $m\ s^{-1}$.

Gravitational losses are due to particles settling and depositing on the non-vertical walls of tubing due to gravitational forces. Gravitation losses were calculated using Equation A.12 (*Brockmann*, 1993)

$$\eta_{grav} = 1 - \frac{2}{\pi}\left[2\kappa\sqrt{1-\kappa^{2/3}} - \kappa^{1/3}\sqrt{1-\kappa^{2/3}} + \arcsin(\kappa^{1/3})\right] \tag{A.12}$$

where

$$\kappa = \frac{3}{4}\left(\frac{v_{ts}L}{d_i v_{tube}}\right)\cdot\cos(\theta) \tag{A.13}$$

and θ is the angle of inclination in radians of the tubing with respect to horizontal.

To compute losses in tubing bends, Equation A.14 was used (*Brockmann,* 1993)

$$\eta_{bend} = (1 - S_{tk}\theta)^{nbends} \tag{A.14}$$

where the dimensionless Stokes number, S_{tk}, was given by Equation (A.15) and the angle of the bend (θ) is in radians. The number of bends is given by *nbends*. The Stokes number is the ratio of the stopping distance to a characteristic dimension (*Baron and Willeke*, 1993)

$$S_{tk} = \frac{\rho_p D_p^2 C_c v_{tube}}{18\eta d_i} \qquad \text{(A. 15)}$$

where diameter is in meters.

Gravitational inlet losses are given by Equation A.16 (*Brockmann*, 1993)

$$\eta_{grav\_in} = \exp(-4.7K^{0.75}) \qquad \text{(A.16)}$$

and K is given by Equation A.17:

$$K = Z^{1/2} S_{tk} R_e^{-1/4} \qquad \text{(A.17)}$$

with Z as the gravitational deposition parameter (Equation A.18):

$$Z = \frac{L v_{ts}}{v_{tube} d_i} \qquad \text{(A.18)}$$

The other losses to be considered are due to losses in cyclones or Perma Pure dryers.

Experiments to determine the collection efficiencies for a single 4 foot, 1/8 inch stainless steel Perma Pure dryer were performed for a bank of dryers (*Sherman*, personal communication), and the data were averaged and fit with a second order polynomial with R^2=0.9804. Diameters (D_p) are in nanometers (Equation A.19).

$$\eta_{perma} = -0.1261(\log_{10}(D_p))^2 + 0.6276(\log_{10}(D_p)) + 0.1579 \qquad \text{(A.19)}$$

The cyclone used during BRAVO was a URG 3 liter per minute (LPM) 2.5 μm D_{50} cyclone. No efficiency curves were available for it, so a 16.7 LPM 2.5 μm D_{50} efficiency

curve was used. Efficiencies corresponding to instrument channel midpoint diameters were determined by performing an interpolation to the efficiency curve.

Diffusional losses inside the DMA were also included following *Reineking and Porstendorfer*, 1986. The effective length, L_{eff}, is 13 meters. The DMA polydisperse flow, Q_{DMA}, was 0.3 LPM (Equation A.20).

$$\eta_{DMA} = 0.82\exp(-11.5\beta) + 0.10\exp(-70.0\beta) + 0.03\exp(-180.0\beta) + 0.02\exp(-340.0\beta) \tag{A.20}$$

where β is given by Equation A.21

$$\beta = \frac{600 L_{eff} D}{Q_{DMA}} \tag{A.21}$$

Losses in the TSI condensation particle counter were determined at the Seattle Workshop, August 1995 (provided by A. Wiedensohler) where diameter (D_p) is in nanometers.

$$\eta_{CPC} = 1 - \frac{1.15}{1 + \exp((D_p - 11.3)/2.1)} \tag{A.22}$$

Figure A.1 shows a collection (or penetration) efficiency curve for the drying experimental set-up and the DMA. The total losses included the combined losses from each section of the set-up. For each section, diffusional, gravitational and losses due to bends were combined. Losses due to the Perma Pure dryer were the major contributor to the total losses. The effect of the 2.5 μm D_{50} cut-off cyclone was not shown for the range of aerodynamic diameters plotted. Figure A.2 is similar to Figure A.1 except the losses for the OPC are shown instead of the DMA. Recall that the OPC and DMA used the same particle drying inlet. The effect of the Perma Pure dryer is seen in the OPC losses because its channels extended to large enough diameters. Figure A.3 shows the efficiency curve

for the APS 3320. Because no bends or Perma Pure dryers were used, and because the tubing was oriented 90 degrees with respect to the horizontal, the collection efficiency was 100 % for all sizes.

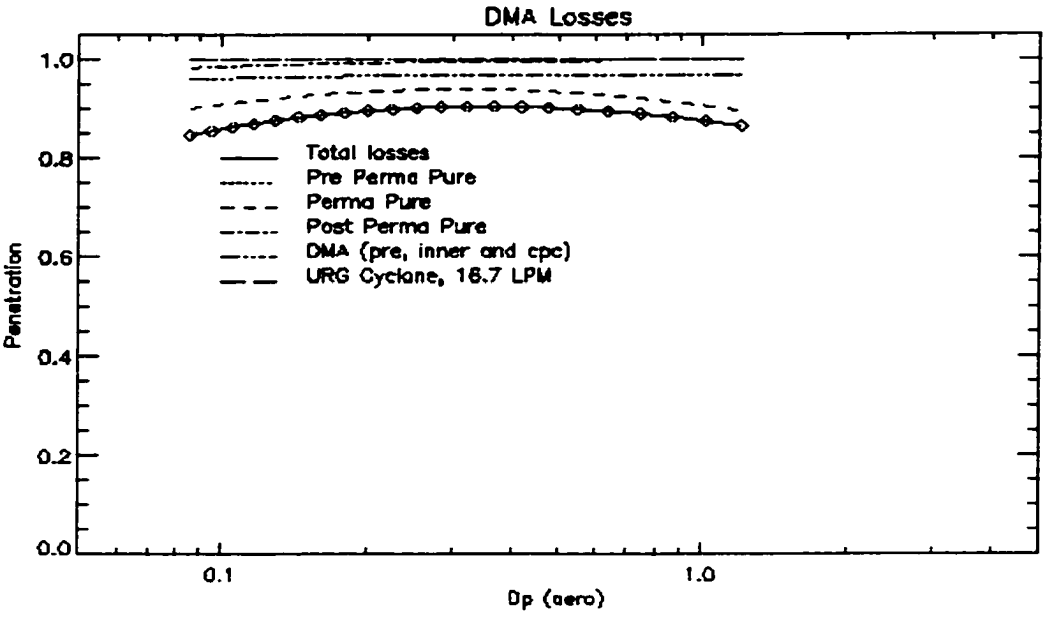

Figure A.1 Particle penetration (collection) efficiency for the DMA experimental set-up as a function of aerodynamic diameter in micrometers (μm). Contributions from each section of the drying system are shown (see Chapter 2). The total losses are given by the diamonds and solid line.

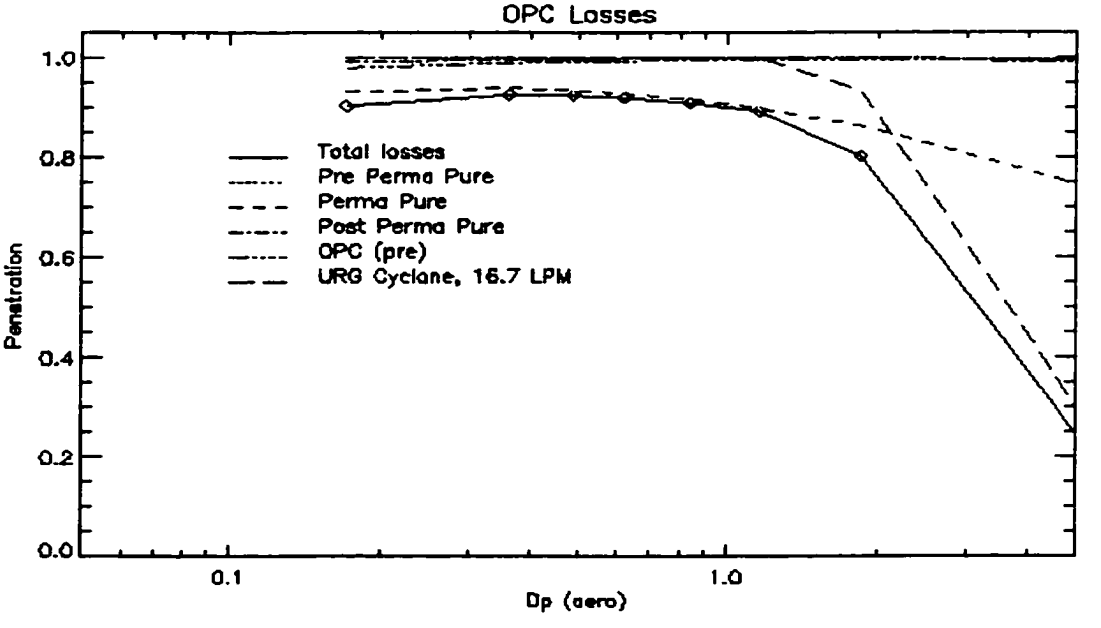

Figure A.2 Particle penetration (collection) efficiency for the OPC experimental set-up as a function of aerodynamic size in micrometers (μm). Contributions from each section of the drying system are shown (see Chapter 2). The total losses are given by the diamonds and solid line.

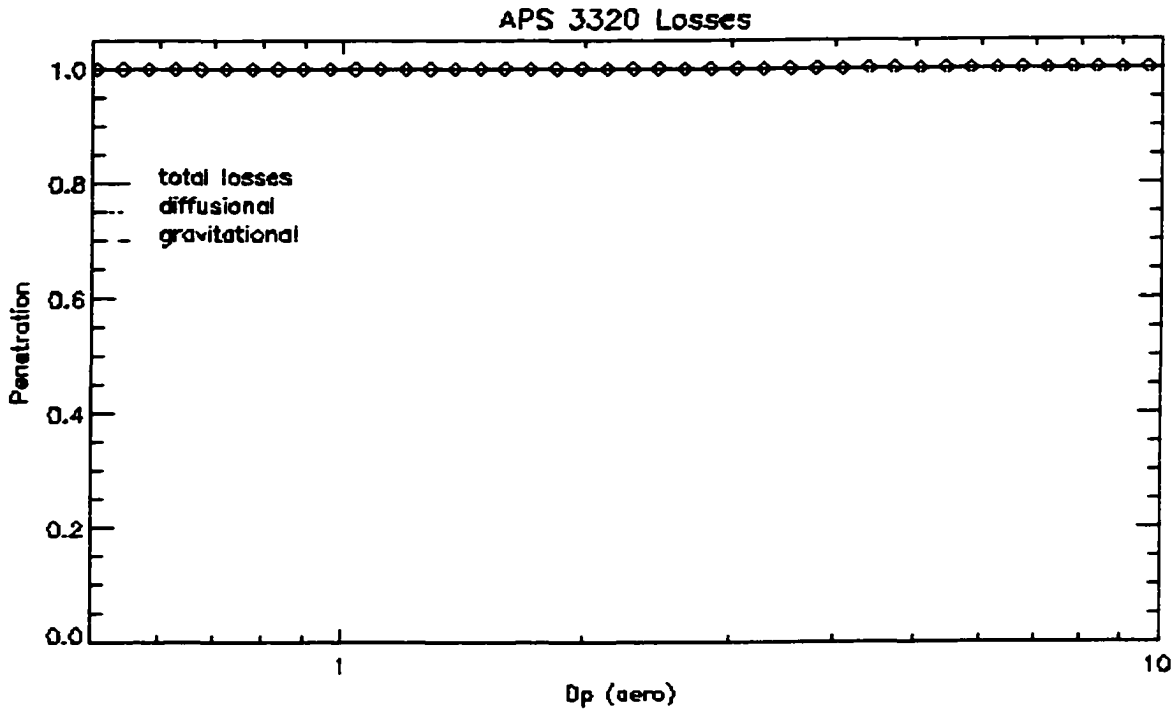

Figure A.3 Particle penetration (efficiency) for the APS experimental set-up as a function of aerodynamic size in micrometers (μm).

APPENDIX B. EXPERIMENTAL UNCERTAINTY CALCULATIONS

Experimental uncertainty in aerosol size parameters and light scattering coefficients will be derived in this Appendix. These uncertainties will be computed following the method of error propagation outlined by *Bevington and Robinson* (1992). We will start with the uncertainty in number concentration. Number concentration (N) is calculated by Equation B.1.

$$N = \frac{c}{Qt} \tag{B.1}$$

where c is the raw counts in a given bin, Q is the instrument flow rate and t is the sample time. Assuming negligible uncertainly in the sample time, the uncertainty in N can be written as Equation B.2

$$\delta N = \left[\left(\frac{\partial N}{\partial c} \right)^2 + \left(\frac{\partial N}{\partial Q} \right)^2 + \left(\frac{\partial N}{\partial L} \right)^2 + \left(\frac{\partial N}{\partial N_{avg}} \right)^2 \right]^{1/2} \tag{B.2}$$

The first term in Equation B.2 is the uncertainty in N due to uncertainty in the counts, determined by Poisson statistics:

$$\frac{\partial N}{\partial c} = \frac{1}{Qt} \delta c \tag{B.3}$$

and $\delta c = c^{1/2}$. The second term is the uncertainty in N due to uncertainty in the flow rate and is given by Equation B.4

$$\frac{\partial N}{\partial Q} = \frac{-c}{Q^2 t}\delta Q \tag{B.4}$$

and δQ is the standard deviation in the flow measurements. The third and fourth terms are due to uncertainty in N due to uncertainty in loss calculations and from averaging distributions together. Both of these uncertainties are negligible compared to the first two terms and will be ignored. By substituting and rewriting, we have Equation B.5 for uncertainty in N in a given instrument channel i:

$$\delta N_i = \left[\frac{N_i}{Qt_i} + \frac{N_i^2}{Q^2}(\delta Q)^2\right]^{1/2} \tag{B.5}$$

The uncertainty in volume concentration can now be calculated. Volume concentration in a given bin (V_I) is determined by Equation B.6 with $D_{p,i}$ as the midpoint diameter of a bin.

$$V_i = \frac{\pi}{6} D_{p,i}^3 N_i \tag{B.6}$$

The uncertainty in V_i is given by Equation B.7:

$$\delta V_i = \left[\left(\frac{\partial V_i}{\partial D_{p,i}}\right)^2 + \left(\frac{\partial V_i}{\partial N_i}\right)^2\right]^{1/2} \tag{B.7}$$

The first term is the uncertain in volume concentration due to uncertainty in diameter:

$$\frac{\partial V_i}{\partial D_{p,i}} = \frac{\pi}{2} D_{p,i}^2 N_i \delta D_{p,i} \tag{B.8}$$

The second term is the uncertain in volume due to the uncertainty in number (Equation B.5)

$$\frac{\partial V_i}{\partial N_i} = \frac{\pi}{6} D_{p,i}^3 \delta N_i \tag{B.9}$$

Substituting in gives the uncertainty in volume concentration (Equation B.10):

$$\delta V_i = \left[\left(\frac{\pi}{2} D_{p,i}^2 N_i\right)^2 (\delta D_{p,i})^2 + \left(\frac{\pi}{6} D_{p,i}^3\right)^2 (\delta N_i)^2\right]^{1/2} \quad \text{(B.10)}$$

For each instrument, the uncertainty in diameter depends on the measurement technique. For the DMA, δD_p depends on how well voltage and shape factor (χ) are known. For the OPC, δD_p depends on how well refractive index is known. For the APS, δD_p depends on knowing density and shape factor. The uncertainty in DMA diameter can be determined in the following way. The mobility (Z_p) of a particle with diameter D_p (meters) is given by Equation B.11 (see Chapter 2) and has units of $m^2\ V^{-1}\ s^{-1}$.

$$Z_p = \frac{neC_c}{3\pi\eta\chi D_p} \quad \text{(B.11)}$$

where n is the number of charges and e is the elementary charge (1.602×10^{-19} J V^{-1}). The dynamic gas viscosity is given by η with units of kg $m^{-1}\ s^{-1}$ and C_c is the Cunningham correction factor given in Equation B.12:

$$C_c = 1 + \frac{\lambda}{D_p}\left[2.514 + 0.8\exp\left(\frac{-0.55D_p}{\lambda}\right)\right] \quad \text{(B.12)}$$

For values of T=20 degrees Celsius and P = 890 mbar, the mean free path (λ) is given as 7.5466×10^{-8} meters and η = 1.8181×10^{-5} kg $m^{-1}\ s^{-1}$. The voltage corresponding to the DMA measurement is given in Equation B.13

$$V = \frac{Q\ln[r_o/r_i]}{2\pi Z_p L} \quad \text{(B.13)}$$

Substituting in for mobility gives Equation B.14

$$V = \frac{3\chi\eta Q\ln[r_o/r_i]D_p}{2LneC_c} \quad \text{(B.14)}$$

To characterize the DMA, we have the column length (L) as 0.4444 meters, the inner rod diameter (r_i) as 0.00937 meters, the outer rod (r_o) diameter as 0.01958 meters and the DMA flow (Q) as 3 LPM converted to $m^3\ s^{-1}$. If C_c is substituted into Equation B.14 and we solve for D_p, we find a transcendental Equation B.15:

$$D_p^2 - \frac{V}{\gamma\chi} D_p - \frac{V\lambda}{\gamma\chi}\left[2.514 + 0.8\exp\left(\frac{-0.55D_p}{\lambda}\right)\right] = 0 \qquad \text{(B.15)}$$

where constants have been grouped into the parameter γ,

$$\gamma = \frac{3\eta Q \ln[r_o/r_i]}{2Le} \qquad \text{(B.16)}$$

where we have assumed n=1. Using Equation B.15 we can determine the sensitivity of diameter to uncertainties in χ and V. We can take the numerical derivative of Equation B.15 to quantify these uncertainties. A $\delta\chi = 0.1$ results in a $\delta D_p = 0.05$ μm. A $\delta V = 3$V corresponds to a $\delta D_p = 1\times10^{-5}$ μm, demonstrating the negligible effects of voltage on diameter. Increasing voltage results in a larger diameter while an increase in shape factor results in a smaller diameter.

For the APS, the geometric diameter is converted from aerodynamic diameter using Equation B.17.

$$D_p = D_{ae}\left[\frac{C_{ae}\chi}{C_p\rho_p}\right]^{1/2} \qquad \text{(B.17)}$$

where C_{ae} is the Cunningham correction factor for aerodynamic diameter. The particle density is given by ρ_p. Solving for geometric diameter gives Equation B.18

$$D_p = D_{ae}\left[\frac{C_{ae}\chi/\rho_p}{1+\frac{\lambda}{D_p}\left(2.514+0.8\exp\left(\frac{-0.55D_p}{\lambda}\right)\right)}\right]^{1/2} \quad \text{(B.18)}$$

and the mean free path, λ, is 7.5466×10^{-8} meters. We can determine from Equation B.18 the effect of particle density and shape factor on derived geometric diameter. To quantify this effect, we can determine the numeric derivative of Equation B.18. An uncertainty in density of $\delta\rho = 0.1$ corresponds to an uncertainty in diameter of $\delta D_p \sim 0.05$ μm. An uncertainty in dynamic shape factor of $\delta\chi = 0.1$ results in an uncertainty in diameter of $\delta D_p = 0.08$ μm. Increasing particle density results in smaller geometric diameter, while increasing shape factor results in a larger geometric diameter.

For the optical particle counter, the geometric diameter depends on refractive index. Because there is no theoretical relationship between instrument response and diameter for the instrument used during BRAVO, empirically derived equations will suffice. Equation B.19 describes the relationship between geometric and optical diameter:

$$D_{p,i} = \frac{D_{opt,i}}{a_i m^2 + b_i m + c_i} \quad \text{(B.19)}$$

For each bin, i, a second order polynomial is used to relate the optical and geometric diameters (see Chapter 3). The polynomial coefficients a, b, and c, are different for each bin. The optical diameter (D_{opt}) is given by the manufacturer calibration for each bin. We can quantify the effects of refractive index on each bin by taking the derivative of Equation (B.19). For higher refractive indices, the derivative of Equation B.19 also increases due to the shape of the polynomials. An uncertainty in refractive index of δm =

0.005 results in a 0.003 μm uncertainty in diameter. An increased refractive index results in a smaller geometric diameter.

Volume mean diameters for each particle mode (see Chapter 6) were computed using Equation B.20.

$$D_{gv} = \exp\left[\frac{\sum V_i \ln D_{pm,i}}{\sum V_i}\right] \tag{B.20}$$

For simplicity, Equation B.20 is rewritten as Equation B.21:

$$D_{gv} = \exp[C_i] \tag{B.21}$$

where

$$C_i = \frac{\sum A_i}{\sum B_i} \tag{B.22}$$

and

$$A_i = V_i \ln D_{pm,i}$$

$$B_i = V_I$$

The uncertainties in the quantities A and B are:

$$\partial A_i = \left[\left(\ln D_{pm,i}\right)^2 (\delta V_i)^2 + \left(\frac{V_i}{D_{pm,i}}\right)^2 \left(\delta D_{pm,i}\right)^2\right]^{1/2}$$

$$\partial B_i = \partial V_i \tag{B.23}$$

Uncertainty in volume concentrations and diameter were described in the previous discussions. The uncertainty in the quantity C was determined with Equation B.24.

$$\partial C_i = \left[\left(\frac{1}{B_i}\right)^2 (\delta A_i)^2 + \left(\frac{-A_i}{B_i}\right)^2 (\delta B_i)^2\right]^{1/2} \tag{B.24}$$

The uncertainty in the volume mean diameter was then computed by Equation B.25:

$$\partial D_{gv} = \exp(C)\partial C \tag{B.25}$$

Light scattering coefficients were computed with volume distributions using Equation B.26 (see Chapter 7) for each bin *i*:

$$b_{sp} = \Sigma \frac{3}{2} \frac{Q_{sp}}{D_{p,i}} V_i \tag{B.26}$$

The uncertainty in b_{sp} was computed using Equation B.27.

$$\partial b_{sp} = \left[\left(\frac{3Q_{sp}}{2D_p} \right)^2 (\delta V)^2 + \left(\frac{-3Q_{sp}V}{2D_p^2} \right)^2 (\delta D_p)^2 \right]^{1/2} \tag{B.27}$$

The uncertainties in the Mie scattering efficiency (Q_{sp}) were assumed to be negligible and the uncertainties in volume and diameter have already been discussed. Uncertaintes in b_{ext} can be calculated following Equation B.27. Finally, aerosol optical depth (τ_{aer}) was computed with Equation B.28 using light extinction coefficients and estimates of boundary layer height (H_B).

$$\tau_{aer} = b_{ext} H_B \tag{B.28}$$

The uncertainty in aerosol optical depth was computed with Equation B.29:

$$\partial \tau_{aer} = \left[H_B^2 (\delta b_{ext})^2 \right]^{1/2} \tag{B.29}$$

No uncertainty in boundary layer height was included because no information was available.

Appendix C. Each entry corresponds to f(bin, charge). The first non zero entry in each column corresponds to a singlet correction and higher multiplet corrections correspond to entries below.

f(25,i)	f(24,i)	f(23,i)	f(22,i)	f(21,i)	f(20,i)	f(19,i)	f(18,i)	f(17,i)	f(16,i)	f(15,i)	f(14,i)	f(13,i)	f(12,i)	f(11,i)	f(10,i)	f(9,i)	f(8,i)	f(7,i)	f(6,i)	f(5,i)	f(4,i)	f(3,i)	f(2,i)	f(1,i)
1	0	0	0	0	0	0	0	0	0	0	0	0	0	0	0	0	0	0	0	0	0	0	0	0
0	1	0	0	0	0	0	0	0	0	0	0	0	0	0	0	0	0	0	0	0	0	0	0	0
0	0	1	0	0	0	0	0	0	0	0	0	0	0	0	0	0	0	0	0	0	0	0	0	0
0	0	0	1	0	0	0	0	0	0	0	0	0	0	0	0	0	0	0	0	0	0	0	0	0
0.08333	0	0	0	0.11315	0	0	0	0	0	0	0	0	0	0	0	0	0	0	0	0	0	0	0	0
0	0.07637	0	0	0	0.12176	0	0	0	0	0	0	0	0	0	0	0	0	0	0	0	0	0	0	0
0.04577	0	0.07474	0	0	0	0.13163	0	0	0	0	0	0	0	0	0	0	0	0	0	0	0	0	0	0
0.03116	0.04797	0	0.07619	0	0	0	0.14236	0	0	0	0	0	0	0	0	0	0	0	0	0	0	0	0	0
0.01974	0.03108	0.04945	0	0.07931	0	0	0	0.15356	0	0	0	0	0	0	0	0	0	0	0	0	0	0	0	0
0.01164	0.01848	0.03023	0.05011	0	0.08311	0	0	0	0.16478	0	0	0	0	0	0	0	0	0	0	0	0	0	0	0
0	0.01008	0.01668	0.02862	0.04985	0	0.08675	0	0	0	0.1756	0	0	0	0	0	0	0	0	0	0	0	0	0	0
0	0	0.00831	0.01447	0.02631	0.04863	0	0.08952	0	0	0	0.18569	0	0	0	0	0	0	0	0	0	0	0	0	0
0	0	0	0.00648	0.01202	0.02343	0.04644	0	0.09093	0	0	0	0.19472	0	0	0	0	0	0	0	0	0	0	0	0
0	0	0	0	0.00475	0.00952	0.02015	0.04336	0	0.09063	0	0	0	0.20245	0	0	0	0	0	0	0	0	0	0	0
0	0	0	0	0	0.00326	0.00715	0.01669	0.03951	0	0.08861	0	0	0	0.20864	0	0	0	0	0	0	0	0	0	0
0	0	0	0	0	0	0.00208	0.00508	0.01328	0.0351	0	0.08493	0	0	0	0.21316	0	0	0	0	0	0	0	0	0
0	0	0	0	0	0	0	0.00122	0.00339	0.01012	0.03036	0	0.07983	0	0	0	0.21592	0	0	0	0	0	0	0	0
0	0	0	0	0	0	0	0	0.00066	0.00212	0.00737	0.02551	0	0.07366	0	0	0	0.21692	0	0	0	0	0	0	0
0	0	0	0	0	0	0	0	0	0.00032	0.00124	0.00511	0.02079	0	0.06674	0	0	0	0.21618	0	0	0	0	0	0
0	0	0	0	0	0	0	0	0	0	0.00014	0.00067	0.00336	0.01639	0	0.05943	0	0	0	0.21379	0	0	0	0	0
0	0	0	0	0	0	0	0	0	0	0	0.00006	0.00034	0.00209	0.01246	0	0.05206	0	0	0	0.20982	0	0	0	0
0	0	0	0	0	0	0	0	0	0	0	0	0	0.00015	0.00122	0.00913	0	0.04484	0	0	0	0.20444	0	0	0
0	0	0	0	0	0	0	0	0	0	0	0	0	0	0.00006	0.00067	0.00642	0	0.038	0	0	0	0.19784	0	0
0	0	0	0	0	0	0	0	0	0	0	0	0	0	0	0	0.00054	0.00431	0	0.0317	0	0	0	0.19016	0
0	0	0	0	0	0	0	0	0	0	0	0	0	0	0	0	0	0.00016	0.00276	0	0.02596	0	0	0	0.1816